High Energy Neutral Emissions from Solar Flares

Mark P. Toner

A thesis for the degree of PhD, submitted to the Physical Sciences Graduate School, Faculty of Science, University of Glasgow, September 2004.

Abstract

Solar flares produce two kinds of high-energy neutral emissions: γ-rays and neutrons (with thanks to Chupp 1984, for this convenient title). These originate in interactions between accelerated ions and ambient nuclei and, between the photons and the neutrons, provide a window into the fast ion population between the energies of a few MeV and a few hundred MeV.

Previously, the γ-ray spectrum has been investigated by Monte Carlo modelling methods and conditions in the flare region deduced by adjusting the models to fit the observed spectra, chiefly from the Solar Maximum Mission Gamma Ray Spectrometer (e.g. Murphy et al. 1991). This provides abundances for accelerated ions and ambient nuclei, and energy distributions for the accelerated ions. However a number of assumptions have to be made in order to keep the model parameter numbers low enough to enable statistical matching to the data in a reasonable amount of processor time and there are some difficulties with the parameters deduced. In particular, there are difficulties in accounting for the brightness of the narrow emission line at 1.63 MeV due to the deexcitation of ^{20}Ne. This demands a steep accelerated ion spectrum and a low abundance for fast α-particles. However, strong emission in the 0.429 MeV and 0.478 MeV features due to the production of lithium and beryllium by fusion of α-particles often contradicts this, demanding an enhanced population of accelerated α-particles.

Fresh approaches to the modelling of some of the narrow lines are presented here in order to explore, and possibly resolve, this contradiction. Two possibilities are examined: the assumptions in previous work of a cold target region and the further assumption that all of the accelerated ions share the same energy distribution. It may be that the accelerated ions pass through a region in which, at least for the lower energy ions, energy loss is experienced in warm target conditions (e.g. Emslie et al. 1997). If they spend a sufficient part of their time in such a region, their energy distribution will be altered to enhance the number of ions at energies of a few MeV. This would preferentially stimulate the 1.63 MeV line due to the particularly low energy sensitivity of ^{20}Ne to proton-excitation, without having to invoke a steep ion spectrum. Previous attempts to apply this analysis did not model the line production in detail and considered only the peak values of the excitation cross-sections. Integrating the excitation in detail allows a resonant spike at 3 MeV in the ^{20}Ne cross-section to have its effect and reduce the required proton energy slope. Even with a large proportion of accelerated α-particles, this approach can

reduce the ion slope and significantly reduce the required ion energy in the flare.

The second assumption challenged here, is that all of the accelerated ions have the same energy distribution, characterized by a single power-law index. Relaxing this assumption and modelling the lines with separate fast proton and fast α-particle power-laws has significant results. It is possible to satisfy the bright 1.63 MeV line and the strong emission from the α-fusion reactions with a steep proton spectrum and a hard α-particle spectrum. This also significantly reduces the required α-particle abundance to values more in line with cosmic abundances.

Rounding out this work on high-energy neutral emissions, the GUIPS software has been applied to correctly inverting a Compton Gamma Ray Observatory COMPTEL neutron spectrum from the solar flare of 15 June 1991. Maximum entropy and quadratic inversion techniques are applied to the instrument data to produce an improved neutron spectrum. Previous simplified approaches have underestimated the sensitivity of the instrument as well as distorting the neutron spectrum. A dip in the spectrum has been confirmed but the overall number of neutrons detected has to be reduced to 73% of the previous value obtained by Kocharov et al. (1998). Further investigation of COMPTEL neutron spectra awaits the preparation of the data. This depends on extensive work modelling the passage of the solar neutrons through the instrument using the Los Alamos LAHET and MCNP software.

Dedication and Acknowledgements

To my wife, Ann, and my children, Lucy and Simon, without whose patience this work would never have got started, let alone finished. Also to my mother, who still believes in me after all these years, and to my father who saw it finished before he died.

I would like to thank my supervisors, Alec and John, for the great support they have given. This was especially important due to the novel mode of study that I adopted for this work. Thanks are also due to a great many people and to name some would be unfair on the rest. However I must thank Ron Murphy for his generous help throughout this work, Keith Macpherson for getting me started with GUIPS and Daphne Davidson for keeping me right on all that paperwork.

Contents

1 Solar Flares and Accelerated Particles 1
- 1.1 Introduction . . . 1
- 1.2 The Sun . . . 2
- 1.3 The Solar Atmosphere . . . 2
- 1.4 Solar Flare Phenomena . . . 7
  - 1.4.1 The Cycle of Solar Activity . . . 7
  - 1.4.2 Electromagnetic Radiation . . . 8
  - 1.4.3 Energetic Particles . . . 11
- 1.5 γ-ray Spectroscopy . . . 11
- 1.6 De-excitation Lines to Consider . . . 12
- 1.7 Neutron Emission . . . 13
- 1.8 The Source . . . 13
- 1.9 Species Differentiation in the Accelerated Particle Spectrum . . . 16
- 1.10 Data . . . 16
  - 1.10.1 Early γ-ray Observations . . . 18
  - 1.10.2 Early Solar γ-ray Observations . . . 20
  - 1.10.3 Supporting Space Observations . . . 22
  - 1.10.4 Solar Maximum Mission . . . 27
  - 1.10.5 Yohkoh . . . 28
  - 1.10.6 Compton Gamma Ray Observatory . . . 31
  - 1.10.7 Reuven Ramaty High Energy Spectroscopic Solar Investigator 34

2 γ-ray Spectroscopy of Solar Flares 37
- 2.1 Introduction . . . 37
- 2.2 A γ-ray Spectrum . . . 37
- 2.3 Cross-sections . . . 39
  - 2.3.1 Cross-section Modelling . . . 40
  - 2.3.2 Laboratory Measurements . . . 44
  - 2.3.3 Filling The Gaps . . . 46
- 2.4 Ambient Particle Abundances . . . 48
  - 2.4.1 Supporting Abundance Measurements . . . 49
  - 2.4.2 Abundances from γ-ray Spectra . . . 50
- 2.5 Energy Distributions . . . 53
  - 2.5.1 Stochastic Acceleration . . . 53
  - 2.5.2 Shock Acceleration . . . 58
  - 2.5.3 Direct Measurement of Accelerated Ion Distributions . . . 59
  - 2.5.4 Energy Distributions from γ-ray Spectra . . . 60

3 Source Model **65**
3.1 Introduction 65
3.2 Thick and Thin Targets 65
3.3 Cold Neutral Targets 68
3.4 Software 73
3.5 A Cold Target Application: ^{24}Mg 1.37 MeV Line 76
3.5.1 The 1.37 MeV ^{24}Mg Line and Proton Excitation 78
3.5.2 The 1.37 MeV ^{24}Mg Line and Combined Proton and α-particle Excitation 79
3.5.3 Correlation Between the 1.37 MeV and 1.63 MeV Line Fluences 81
3.5.4 The 1.37 MeV-to-1.63 MeV Fluence Ratio as a Diagnostic 83

4 Warm Ionized Targets **84**
4.1 Feeding the Low-energy Sensitivity of ^{20}Ne 84
4.2 Why Warm Targets? 84
4.3 Proton Containment in the Corona 85
4.4 γ-ray Line Flux in a Target of Arbitrary Temperature 88
4.5 Role of α Particles 91
4.6 Results 93
4.7 Examples of Applications 96
4.8 ^{20}Ne Abundance and Partial Trapping 98
4.9 Conclusions and Discussion 101

5 Unravelling α-particle and Proton Energies **104**
5.1 Introduction 104
5.2 Diagnosis of Fast Proton and α Distributions: Method 104
5.2.1 Calculation of Line Fluences 104
5.2.2 De-excitation Line Ratio Diagnostics Without Assumption A106
5.3 Application to Flares Observed by SMM/GRS 110
5.4 Summary and Discussion 116
5.5 An Application to the RHESSI Flare of 23 July 2002 120

6 Solar Flare Neutron Emission **123**
6.1 Another Neutral Emission 123
6.2 Solar Flares and Energetic Neutrons 124
6.3 COMPTEL 125
6.4 COMPTEL Neutron Response 127
6.4.1 Principles 127
6.4.2 Simulation 127
6.5 Statistical Regularization 129
6.5.1 GUIPS 129
6.5.2 Quadratic Regularization 130
6.5.3 Maximum Entropy Regularization 131
6.5.4 The Lagrangian Multiplier λ 133
6.6 15 June 1991 Solar Flare 134
6.6.1 Previous Neutron Analysis 135
6.6.2 Solutions to the Inverse Problem 136
6.6.3 Neutron Emissivity 137

6.6.4 Results and Conclusions 139

7 Future Work **142**
7.1 Summary 142
7.2 Temporal Behaviour of Flare γ-ray Spectra 145
7.3 Inversion Techniques 146
7.4 Neutron Production 147
7.5 Conclusion 147

A The 'Effective Coulomb Logarithm' **149**

B γ-ray Nuclear Excitation Cross-sections **151**

C Ion Energies from the 19 SMM/GRS-observed Flares **163**

List of Figures

1.1 A group of sunspots in the solar atmosphere. Sunspots are the focus of intense magnetic activity and are a marker in visible light of the position of active regions on the Sun. These are the areas where solar activity is likely and where we expect to find solar flares (Covington & Myers 2000). 3

1.2 Temperature profile of the solar atmosphere. This graph shows the usual definitions of the layers above the photosphere: the chromosphere, the transition region and the start of the hot corona (l'Observatoire de Paris 2004). 4

1.3 TRACE images showing the ubiquitous loop structure of the solar transition region and corona. From left to right, top to bottom, these show the active regions of 1998 May 19 and 1998 August 19, in 171 Å light, and the post-flare loops of 1998 August 16, in 195 Å light (NASA Goddard Space Flight Centre). The fourth image is a cartoon of the underlying magnetic structure with a hypothetical accelerated ion path. 6

1.4 The solar cycle as revealed in the sunspot record. Essentially this graph shows the frequency of sunspots on the visible solar disk over time. Although the sunspot number does not repeat exactly, it cycles from minimum to maximum over a fairly regular period of about 11 years (Covington & Myers 2000). 8

1.5 The γ-ray background showing the Apollo and Ranger contributions. 19

1.6 The Russian GRANAT X-ray observatory. 22

1.7 The 'halo' orbit exploited by SOHO and other solar observatories. 24

1.8 The Transition Region and Coronal Explorer (TRACE). Image courtesy of http://sunland.gsfc.nasa.gov/smex/trace. 25

1.9 This GOES X-ray flux plot contains 1 minute averages of solar X-ray output in the 0.1 to 0.8 nm and 0.05 to 0.4 nm passbands. Data from both operational GOES satellites are included. Image is from the Space Environment Centre (Centre 2004). 26

1.10 The Solar Maximum Mission (SMM) Spacecraft 27

1.11 Spectra recorded by the Gamma Ray Spectrometer (GRS) on board the SMM spacecraft for four different flares. 29

1.12 The Japanese Yohkoh high-energy solar observatory. 30

1.13 The Compton Gamma Ray Observatory showing the main instruments. 31

1.14 The COMPTEL γ-ray telescope which flew on board the Compton Gamma-Ray Observatory. 32

1.15 The Reuven Ramaty High Energy Spectroscopic Solar Investigator spacecraft, showing the instrumentation and the axis of rotation which enables Fourier decoding of image data. 35

2.1 OSSE spectrum from the 4 June 1991 solar flare (Murphy et al. 1997). 38
2.2 Calculated total scattering cross-sections for protons interacting with ^{16}O nuclei from Deb & Amos (2003). These include all excitations of the nucleus. 41
2.3 The energy-dependent cross-sections for γ-ray excitation of ^{24}Mg at 1.37 MeV, ^{20}Ne at 1.63 MeV, ^{12}C at 4.44 MeV and ^{16}O at 6.13 MeV by protons. 43
2.4 Energy-dependent cross-sections as in 2.3 except that excitation is caused by α-particles. 43
2.5 Excitation cross-sections for ^{12}C, ^{14}N and ^{16}O that all lead into the excited state of ^{12}C responsible for the 4.438 MeV prompt deexcitation line. These result from collisions with protons and α-particles. 44

3.1 A comparison between the cross-sections used in this present work (Toner 2004) with the coarser cross-sections used by Kozlovsky et al. (2002) in Monte Carlo simulations. These show the cross-section for excitation of 1.63 MeV ^{20}Ne by fast protons. Note that my methods allow finer energy resolution but that the coarser resolution is necessary for the computational intensity of a Monte Carlo approach. 73
3.2 The excitation cross-sections of ^{20}Ne at 1.63 MeV and ^{24}Mg at 1.37 MeV showing how they both have fairly low-energy sensitivity to proton excitation. 78
3.3 Comparison of the fluences of the ^{24}Mg and ^{20}Ne line emission at 1.37 and 1.63 MeV respectively. These are calculated for various values of the relative α-particle abundance in the accelerated ions given relative to the protons as α/p, and for accelerated particle spectral slopes δ. The ratio of the two fluences is given for each combination of α/p and δ. 80
3.4 Pearson's correlation coefficient of the fluences in the 1.37 and 1.63 MeV lines in 1000 simulated flares, in three different ranges of accelerated proton power laws. A Monte Carlo simulation has produced these fluences while varying relative abundances of the ambient ^{24}Mg and ^{20}Ne and the power law index of the accelerated protons. The accelerated ion population in this example consists only of protons. 82

4.1 Dependence of the ratio of line fluxes $\Phi_{1.63}/\Phi_{6.13}$ on T for injected ion energy distributions characterized by various values of ion energy spectral index δ. The fast α-particle abundance relative to protons is $\alpha/p = 0.1$. 92
4.2 As Figure 4.1 except α's are over-abundant: $\alpha/p = 0.5$. 95

4.3 The maximum value of $\Phi_{1.63}/\Phi_{6.13}$ enhanced by the warm target model as it depends on the accelerated particle spectrum index delta, for a range of values of fast α-particle abundance relative to protons. 96

5.1 Contours of constant $\Phi_{1.63}/\Phi_{6.13}$ for (a) $F_{0,\alpha}/F_{0,p} = 0.1$ (b) $F_{0,\alpha}/F_{0,p} = 0.5$. Each contour is labelled with the value of $\Phi_{1.63}/\Phi_{6.13}$ it represents. 106
5.2 A comparison plot of the nuclear excitation cross-sections for interactions between α-particles and ^{56}Fe nuclei, giving rise to the 0.339 and 1.02 MeV lines, and for the $\alpha - \alpha$ fusion reactions that produce the spectral feature between 0.4 and 0.5 MeV. 107
5.3 Total yield of photons in the two lines at 0.429 and 0.478 MeV, as a function of α particle energy spectral index δ_α. The yield is normalized to one α above 10 MeV.nucl^{-1}. 108
5.4 The accelerated particle power law index δ as a function of the fluence ratio of the 1.63 and 6.13 MeV lines making Assumption A. The curves show different assumed values for α/p. 113

6.1 An image of the neutron source of the 15 June 1991 solar flare made with COMPTEL, on board the CGRO. This was made from the same data-set analyzed here to obtain the neutron emissivity spectrum, but the reduction was to trace each neutron back to its point of origin. This is the first image of an astrophysical object produced in particles other than photons (Arndt et al. 1998; McConnell 1994). 124
6.2 How COMPTEL worked. Path nn' shows how a solar neutron enters the front detector array D1 at angle ϕ to the instrument axis, interacts to deposit energy in D1 and produce secondary neutron n' which travels on to be detected by the back array D2. Path $\gamma\gamma'$ shows the similar path of a high-energy photon. The telescope length was 2.61 m. After McConnell (1994). 126
6.3 Maximum entropy and quadratic regularised solutions for the energy spectrum of neutrons arriving at the COMPTEL instrument during 15 June 1991 solar flare, using a Bayesian method for choosing the smoothing parameter. Error bars are set at the 66.7% confidence level. 136
6.4 As 6.3 except that both solutions use global maximum entropy as the smoothing function and differ only in the method of choosing the smoothing parameter, either Bayesian or χ^2. 137
6.5 A comparison of a diagonal-elements-only inversion by Kocharov et al. (1998) with the full inversion with local maximum entropy smoothing function. Both of these data sets have been converted to source neutron energy distributions at the Sun (after Kocharov et al. (1998)). 140

B.1 Cross-sections for the 0.847 MeV excitation of ^{56}Fe. 152
B.2 Cross-sections for the 1.37 MeV excitation of ^{24}Mg. 152
B.3 Cross-sections for the 1.63 MeV emission. 155
B.4 Cross-sections for the 1.78 MeV excitation of ^{28}Si. 155

B.5 Cross-sections for the 4.44 MeV excitation of ^{12}C. 159
B.6 Cross-sections for the 6.13 MeV emission. 159

List of Tables

2.1 Compiled abundances from different sources. (1) Murphy et al. (1991); VanHollebeke et al. (1990); Breneman & Stone (1985) but Ramaty et al. (1996a) use the values from Reames (1995) for those marked ★. (2) Murphy et al. (1991); VanHollebeke et al. (1990); Anders & Grevesse (1989). (3) Meyer (1985a). (4) Best fit from Murphy et al. (1991), giving equal numbers of accelerated α-particles and protons, renormalized relative to H. (4a) Murphy et al. (1991) with accelerated α-particle to proton ratio set to 0.5. ^{4}He abundances are uncertain (e.g. Meyer 1993) and are set to the cosmic value of 0.1 here, and used to infer the coronal H abundance for which evidence is conflicting. This is supported by Share & Murphy (1998) who find that γ-ray spectra (which tend to be more coronal in relative abundances) are consistent with a photospheric abundance of 8% in the ambient medium, although accelerated ^{4}He might be enhanced in some flares. 48

3.1 The line fluences modelled with the software used in this work, together with the nuclear excitation reactions that contribute to each. The reactions are given in the standard notation where the first nucleus is the target, the bracketed particles are, first, the incident ion and, second, the ejected particle and the last nucleus, marked with an asterisk, is the resultant excited nucleus. This excited nucleus de-excites almost instantly to produce the observed photon. Any intermediate reactions, such as in the second reaction for the 0.478 MeV line, list in the middle. The ^3He-induced reactions complicate the interpretation of the 1.02 MeV complex as discussed in Chapter 5. For more details of all of these reactions see the summary in Kozlovsky et al. (2002) and the discussion in Section 2.3. 75

4.1 Illustrative sets of parameters consistent with $\Phi_{1.63} = 18$ cm^{-2} and $\Phi_{6.13}/\Phi_{1.63} = 1.4$ 98

5.1 Solutions for SMM/GRS flare spectra, choosing a range of values for δ_α and using the fluences given in Share & Murphy (1997). Above the largest δ_α shown for each flare, there was insufficient line fluence to accommodate the α-induced emission, except in the case of the 1986 February 6 flare for which solutions were possible throughout the range of δ_α investigated. Linear propagation of the quoted observation error bars led to the errors quoted here. A '?' in the error indicates that the value was not obtainable by this method. A more complete statistical treatment of errors is beyond the scope of the present work. For comparison, the last line for each flare, labelled 'A', gives the result which would have been obtained from $\Phi_{1.63}$, $\Phi_{6.13}$ and Assumption A with $\alpha/p = 0.5$ 112

5.2 An analysis of the same group of flares in Table 5.1 except that we make Assumption A and assume the protons and α-particles have the same energy distributions. Only the 1986 February 6 data provided a good enough fit to set meaningful error bars at the usual 67% confidence level. The 1981 April 27 fit is only 0.002% confident, while the 1986 May 3 and 1989 November 15 fits are 18% and 14% confident respectively. The 1986 February 6 fit is in excellent agreement with the fit with Assumption A relaxed, but this is not surprising since the relaxed fit does not rule out two identical energy spectra. This is the flare with a non-detection of $\Phi_{0.4-0.5}$ and so there is no more to go on than the ratio of the 1.63 and 6.13 MeV line fluences. The other flares present more of a problem as Assumption A is ruled out by our separate energy spectra in these cases and so we now have difficulty in making a good fit with Assumption A restored. 115

5.3 γ-ray line emission as measured by RHESSI for the 23 July 2002 flare (Shih 2004). The emission has been divided into two parts over the time that γ emission was detected. 120

B.1 Digitized cross-section for 0.847 MeV excitation of ^{56}Fe by α-particles and protons. 153

B.2 Digitized cross-sections for 1.369 MeV excitation of ^{24}Mg by α-particles and protons. 154

B.3 Digitized cross-sections for 1.634 MeV excitation of ^{20}Ne by α-particles and protons. 156

B.4 Digitized cross-sections for 1.635 MeV excitation of ^{14}N by α-particles and protons. 157

B.5 Digitized cross-sections for 1.779 MeV excitation of ^{28}Si by α-particles and protons. 158

B.6 Digitized cross-sections for 4.438 MeV excitation of ^{12}C by α-particles and protons. 160

B.7 Digitized cross-sections for 6.129 MeV excitation of ^{16}O by α-particles protons. 161

B.8 Digitized cross-section for production of 6.129 MeV ^{16}O by spallation reaction on ^{20}Ne by protons. 162

C.1 Solutions for SMM/GRS flare spectra, choosing a range of values for δ_α and using the fluences given in Share & Murphy (1997). . . 164

Chapter 1

Solar Flares and Accelerated Particles

1.1 Introduction

In this chapter, I review background information about the active Sun and the methods used to gather data from high energy phenomena. Particular attention is paid to high-energy emissions from solar flares such as neutrons and γ-rays. Chapter 2 continues with a review of γ-ray spectroscopy. This includes a summary of research into the main factors that give rise to nuclear deexcitation line emission: the accelerated ion spectrum and methods of acceleration, cross-sections for excitation of nuclei and the ways in which these are measured and calculated, and the evidence used to estimate the relative abundances within the target region and the accelerated ions.

My original work begins with Chapter 3, in which I describe my methods of modelling γ-ray emission. This is continued in Chapter 4 in which I extend the usual model of a cold, neutral target region to include the possibility of a warm, ionized target. Further extension of the model is presented in Chapter 5 in which I discuss a more sophisticated model of the accelerated ions that allows for differences in the energy distribution of different types of ions.

My own work on analyzing the energy distribution of flare neutrons using sounder statistical methods is presented in Chapter 6. This looks at a particular set of data with the Glasgow University Inverse Problem Software (GUIPS) and explores a method that can be applied to observations with future instruments.

Chapter 7 concludes this thesis with suggestions as to where this work could lead. There are a number of interesting directions that can be pursued based on the extensions to the γ-ray spectrum models presented here and on the statistical methods demonstrated in the analysis of neutron observations. Good statistical

approaches may help in understanding γ-ray spectra and the variations observed over time in deexcitation lines could be a useful probe into the history of the accelerated ions.

1.2 The Sun

There is only one star sufficiently close to the Earth to be relatively easily observed in all wavelengths at very high resolution and that is our Sun. It is the first step in a chain of reasoning whereby we can study the detailed workings of a star and then extend our knowledge out to try and understand the stars of our galaxy in general. For example, Fraunhofer's solar spectrum (see e.g. Golub & Pasachoff 2001) showed that absorption lines could be used to establish the chemical composition of a star's atmosphere and that the photosphere emits radiation in a pattern close to that of a theoretical black body, allowing spectroscopic investigation of the temperature and composition of all other stars, and providing clues to be used in the development of physical models of stars.

Although the Sun's energy originates from its bulk properties, the balance between gravitational energy and the heat produced by nuclear fusion in its core, there are secondary processes of energy conversion that go on in its outer layers and which are observed in its atmosphere in the form of active regions, prominences and filaments, solar flares and coronal mass ejections. The energy produced in the core moves upward through the interior by radiative transport initially but, above 500,000 km, convective processes take over, working the solar material and giving rise to electric currents and magnetic fields. Useful reviews of current information about the solar atmosphere and activity can be found in Golub & Pasachoff (2001); Lang (2001); Weiss (2001) with further coverage of solar magnetic fields in Weiss (2002); Cattaneo & Hughes (2001).

1.3 The Solar Atmosphere

The visible surface of the Sun is the photosphere. Intuitively this is defined as the maximum depth in the solar atmosphere from which visible-wavelength photons escape unhindered. In practice the base of the photosphere is set as the depth at which optical opacity is 2/3 and it extends upwards from there to a height of a

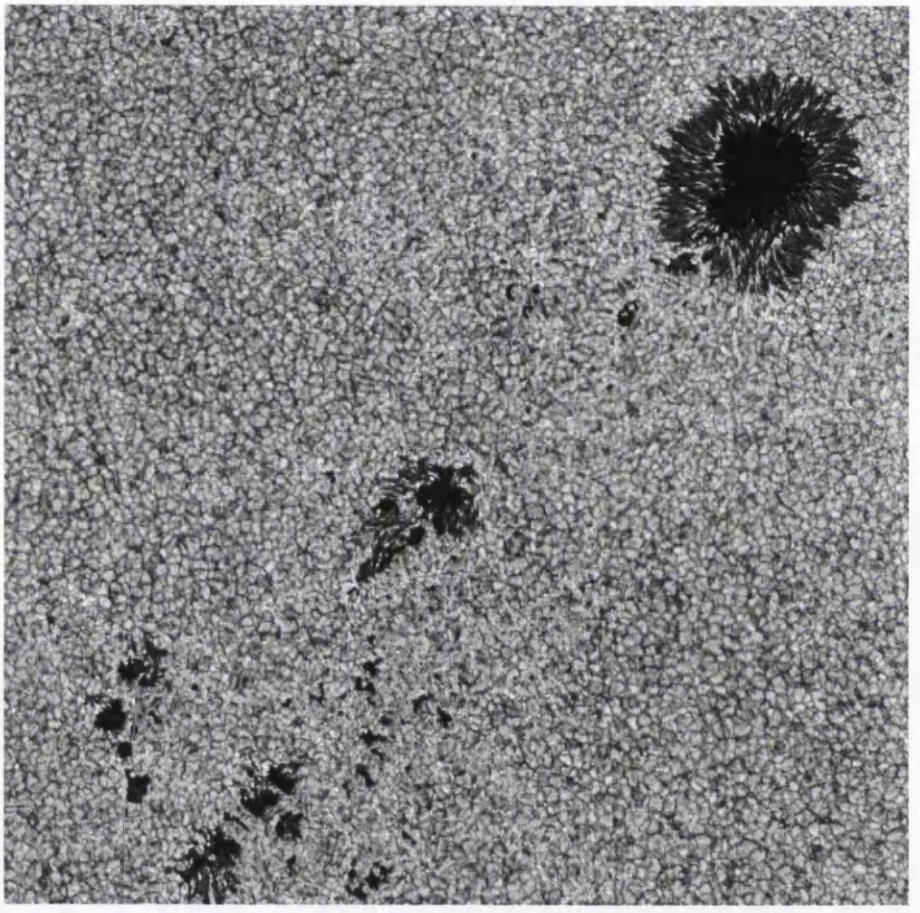

Figure 1.1: A group of sunspots in the solar atmosphere. Sunspots are the focus of intense magnetic activity and are a marker in visible light of the position of active regions on the Sun. These are the areas where solar activity is likely and where we expect to find solar flares (Covington & Myers 2000).

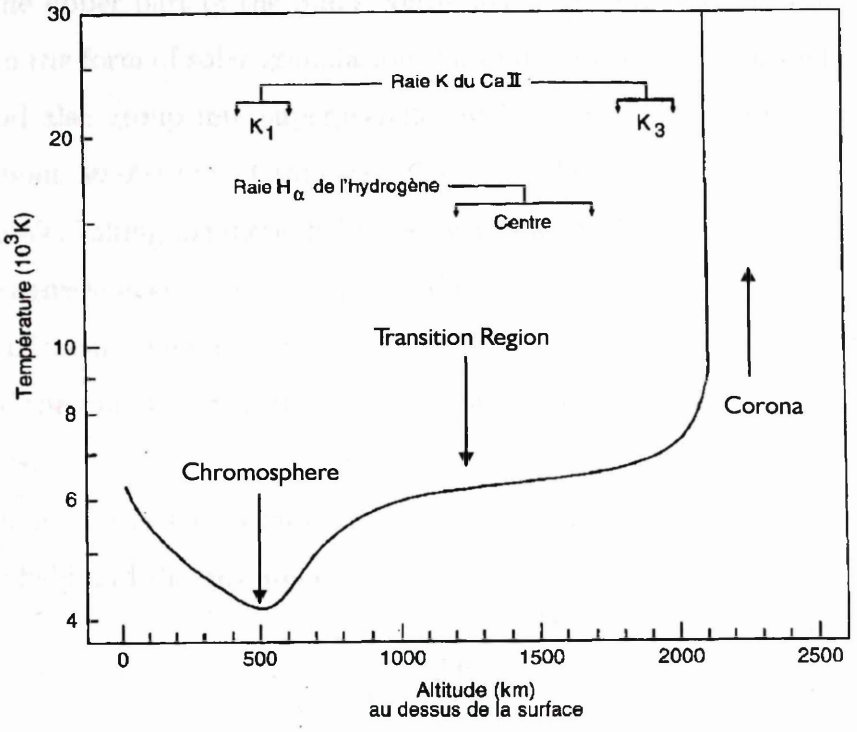

Figure 1.2: Temperature profile of the solar atmosphere. This graph shows the usual definitions of the layers above the photosphere: the chromosphere, the transition region and the start of the hot corona (l'Observatoire de Paris 2004).

few hundred kilometres. This is the region where the optical continuum emission originates providing an average temperature estimate of 5800 K and corresponds to a radius of about 700,000 km. Above the photosphere there is a cooler region as evidenced by the absorption lines in the visible spectrum. This is the chromosphere which extends up for another few thousand kilometres. Figure 1.2 shows this dip in temperature with height. With higher energy radiation, such as ultraviolet (UV) and x-rays, a large temperature rise is observed above the chromosphere. This is also the level at which the hydrogen density drops from $\sim 10^{17}\ cm^{-3}$ at the photosphere down to $\lesssim 10^{9}\ cm^{-3}$ out in this thin hot region, the corona. Where the solar material sharply drops in density and increases in temperature between the chromosphere and corona is called the transition region. The corona extends well out into the solar system. Motion of magnetic fields in the photosphere is probably the main cause of this extreme heating in the corona (Weiss 2001).

As well as sunspots, there are other structures to be seen on the photosphere.

This is the upper part of the Sun's convective zone and convection cells bubble up here in the form of solar granulation. Granules are several hundred kilometres across and also group into supergranules which are a flow pattern with a scale size of about 30,000 km. Granules move from the centre out to the edge of a supergranule, taking magnetic field lines with them. This produces a concentration of magnetic energy at the edges of the supergranules which can be detected in Ca^+ emission. This is the most conspicuous source of energy at the visible surface of the Sun and it features prominently in theories of coronal heating and solar flares.

Throughout the solar atmosphere there is a change in balance between the magnetic field and the gas pressure (see, e.g., Lang 2001).

$$P_m = \frac{B^2}{2}, \tag{1.1}$$

where B is the magnitude of the magnetic field.

$$P_g = NkT, \tag{1.2}$$

where N is the particle density, k is Boltzmann's constant and T is the gas temperature.

Equation 1.1 defines the pressure exerted by the magnetic field on the plasma perpendicular to the field lines and Equation 1.2 gives the competing pressure of the gas. Below the photosphere, P_g dominates over P_m and the gas tends to move the field lines around. Above the photosphere and especially out into the corona, P_m dominates and the field controls the plasma. Low in the corona, the two pressures become equal when the magnetic field is

$$B = \sqrt{2kNT} = \sqrt{2.76 \times 10^{-16} NT} \tag{1.3}$$

Extreme ultraviolet (EUV) images, especially those recorded with the TRACE satellite (see Section 1.10.3 and Figure 1.3), show the low corona and transition region lit by a complex structure of loops. The hot plasma indicates where the magnetic field threads through this part of the solar atmosphere. In a coronal loop, $N \approx 10^{11}$ cm^{-3} and $T \approx 10^6$ K. So Equation 1.3 gives a coronal loop field strength of ~ 5 gauss.

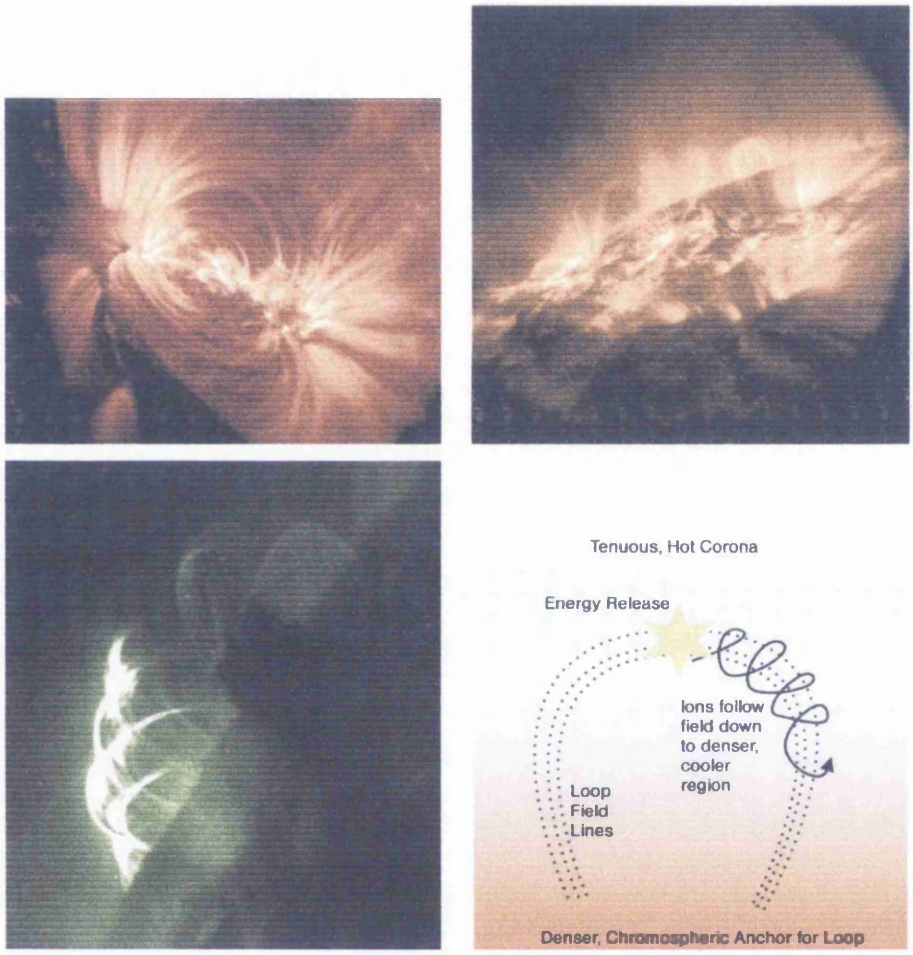

Figure 1.3: TRACE images showing the ubiquitous loop structure of the solar transition region and corona. From left to right, top to bottom, these show the active regions of 1998 May 19 and 1998 August 19, in 171 Å light, and the post-flare loops of 1998 August 16, in 195 Å light (NASA Goddard Space Flight Centre). The fourth image is a cartoon of the underlying magnetic structure with a hypothetical accelerated ion path.

Attempts to understand emission from solar flares and other activity centre on the increased magnetic field available in loops. The solar plasma threaded by such fields can provide sufficient energy to drive flares and magnetic loops are capable of accelerating the ions that excite γ-ray line spectra (e.g. Hua et al. 1989).

1.4 Solar Flare Phenomena

A solar flare is an explosion in the solar atmosphere. The study of flares focusses on where the energy to drive the explosion comes from and how this energy comes to be manifest in the explosion itself. A broad range of electromagnetic radiation is produced along with accelerated particles such as electrons, protons, neutrons and atomic nuclei. In the course of the explosion large quantities of matter can be ejected from the solar atmosphere and shock waves are detected. Solar flares are always associated with regions of magnetic activity, usually occurring in the magnetically neutral region between positive and negative fields in an active region (the 'neutral line'), and are likely driven by the interaction of motions in the solar atmosphere and the local magnetic field. Phenomena observed in a flare generally divide into an 'impulsive' component, lasting for tens of minutes, and a 'gradual' component, lasting for hours.

Flare energies can be as great as 10^{32} ergs. The effects are felt far out in space where they impact on human activities. Damage to satellites, power grids and communication networks is not uncommon and provides an economic motivation to understanding flares. Also the Sun is a fairly typical star, and even larger flare activity can be detected on other stars. The Sun provides a close-by laboratory for the study of a general astrophysical phenomenon.

1.4.1 The Cycle of Solar Activity

Over a period of eleven years, events in the solar atmosphere unfold so that many phenomena involving high energy and strong magnetic fields increase in intensity or frequency of occurrence, reaching a maximum and then dying down again into the relative quiescence of solar minimum. The cycle can be observed in many ways ranging from the sunspot count (see Figure 1.4) through high-energy radiation (ultra-violet and, X-rays) to solar flare frequency and coronal mass ejections and

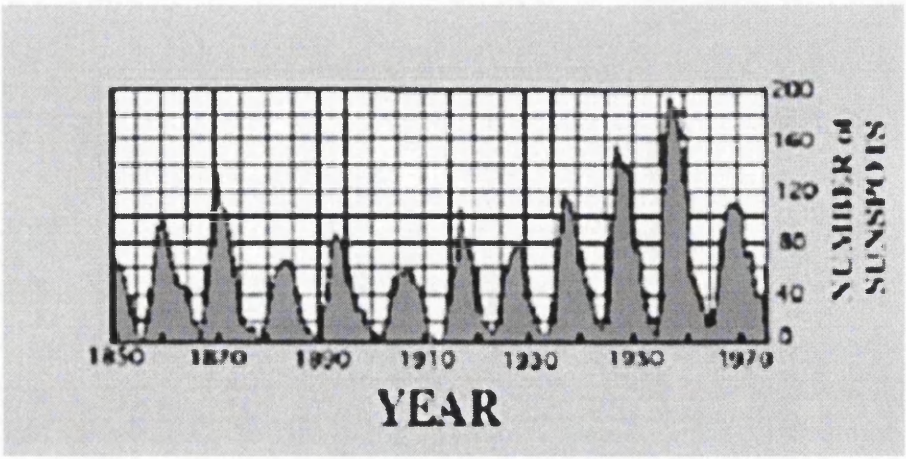

Figure 1.4: The solar cycle as revealed in the sunspot record. Essentially this graph shows the frequency of sunspots on the visible solar disk over time. Although the sunspot number does not repeat exactly, it cycles from minimum to maximum over a fairly regular period of about 11 years (Covington & Myers 2000).

all of these phenomena originate in active regions marked by high concentration of sunspots (and hence magnetic fields). Although flare frequency follows the cycle, the energy in each flare does not. It is often the case that very large flares occur during the declining part of the cycle following solar maximum.

1.4.2 Electromagnetic Radiation

There are five types of metre-wavelength radio emissions as defined by Wild et al. (1963). Type I are associated with an active region but not with a flare. A typical Type I noise storm produces a long series of bursts (at several hundred MHz) with, sometimes, a weak background. Type II bursts come in two bands a few MHz wide, with a 2:1 frequency ratio. The lower frequency starts at about 100 MHz and drifts down in frequency, fading out below 30 MHz. This may be due to a shock wave spreading out from the flare and exciting plasma oscillations. The frequency would then change with conditions in the plasma at different levels in the solar atmosphere. Durations of 5 to 10 minutes are usual. Type III bursts display characteristic spikes of intense emission that drift from high to low frequencies (100s of MHz to 10s of kHz) in a few seconds. This is due to a stream of fast electrons moving out from the base of the corona to the distance of the Earth,

again exciting plasma oscillations on the way like the shock waves in the Type II bursts. Type IV bursts usually follow Type II in long-duration flares (defined by the soft X-ray emission) and present a complex continuum. They correlate well with emission of protons into interplanetary space (see Sections 2.4.1 and 2.5.3 for SEPs). They are generally associated with coronal mass ejections (CMEs). Type V bursts are also continuum emissions but follow Type III bursts in impulsive soft X-ray flares. They may be due to Langmuir waves from electrons ejected by the Type III event. See Section 2.5 for a more detailed account of the various plasma waves.

Impulsive microwave bursts ($\gtrsim$1 GHz) are similar to hard X-ray and EUV bursts and occur simultaneously. They are characterized by a broad-band continuum with a maximum between 3 and 10 GHz. The maximum occurs at higher frequencies for stronger bursts. This appears to be gyrosynchrotron emission from non-thermal electrons ($\gtrsim$100 keV). Gradually increasing microwave emissions are often associated with soft X-ray bursts, possibly produced in thermal bremsstrahlung, like the X-rays (Murphy 1985).

Optical and UV emission is exhibited mostly in spectral lines. Rare continuum emission is most likely due to high-energy particles heating the photosphere by a few hundred K and enhancing recombination continuum (Murphy 1985, and references therein). These are comparatively low temperature emissions. Optical imaging of solar activity has long been successful in the Hα emission line at 6563 $\AA$. Hα brightening either side of the magnetic neutral line indicates the precursor and this emission also shows wave motions on the disk and coronal mass ejections at the limb.

EUV bursts are usually simultaneous with the non-thermal hard X-rays and microwaves. When there is no non-thermal burst, a more gradual EUV emission can often be detected. There are EUV lines and a recombination continuum. Spectroscopic analysis reveals that the impulsive burst emission originates in conditions compatible with the chromosphere and transition region while the more gradual emission appears coronal. EUV imaging is proving to be a powerful tool for investigating the active Sun (see Section 1.10.3 and Figure 1.3).

Soft X-rays ($\lesssim$10 keV) also accompany the Hα emission from the flare itself and produce a spectrum that is most likely due to thermal bremsstrahlung from

plasma at around 10^7 K. This emission grows over a period of a few minutes (impulsive phase) and then decays over a longer time, up to several hours (gradual phase) (Murphy 1985). Hard X-rays ($\gtrsim$10 keV) often accompany the rising part of the soft X-ray emission. The time-scale of soft X-ray emission is used to classify flares as 'impulsive' or 'long-duration.' The thermal X-ray plasma is much denser than the surrounding corona, possibly supplied by heated chromospheric plasma 'evaporating' into the corona (Murphy 1985).

Hard X-rays, between 30 and 300 keV, usually follow closely on the soft X-ray burst. This is usually a short burst lasting between a few seconds and a few minutes. The hard X-rays are usually attributed to non-thermal bremsstrahlung emission because the X-ray spectrum usually follows a power law, has a very short-scale time variation (seconds or less) and occurs simultaneously with the impulsive microwave bursts (also thought to be non-thermal). See, for example, Brown (1971); Lin & Hudson (1976); Hoyng et al. (1976).

Lines and continuum are observed in γ-rays (Chupp 1984, and see Figure 2.1). Spectral lines are produced in nuclear interactions between flare-accelerated ions and ambient nuclei in the solar atmosphere. Many are due to the deexcitation of nuclei excited in collisions with fast ions, the narrow lines being produced by light fast ions hitting heavy nuclei. These are a major topic in this present work and need fast ions with energies ranging from a few MeV up to tens of MeV to excite the nuclei. This gives us a window onto the ions accelerated by the flare in this energy band. There are also lines produced by the capture of neutrons on hydrogen (at 2.223 MeV) and by the annihilation of positrons (at 0.511 MeV).

There is a γ-ray continuum due mainly to very broad lines emitted by heavy accelerated nuclei interacting with lighter ambient particles, producing large doppler broadening, and from the decay of neutral pions (at photon energies $\gtrsim$30 MeV) and also to bremsstrahlung emission from relativistic electrons. There are often many unresolved lines that add to the continuum. The nuclear deexcitation lines are the main component of the continuum between 4 and 7 MeV (Murphy et al. 1990b, 1991). γ-rays are often associated with impulsive flares.

1.4.3 Energetic Particles

Solar Energetic Particles (SEPs) are often emitted in flares and, especially in Coronal Mass Ejections (see Sections 2.4.1 and 2.5.3). These are fast ions with energies up to 10 GeV and electrons with energies up to tens of MeV. Large SEP events are usually associated with long-duration flares. With careful study, the distribution of SEPs with energy can provide clues as to the energy distributions of the accelerated ions that produce the γ-ray emission. They can also help with studying the relative abundances within the various accelerated ions. However these particles can experience further acceleration by shocks on their way from the Sun. Interactions along the way and simple decay will complicate their use in determining abundances.

Neutrons are also ejected from flares. See Chapter 6 for detailed discussion of neutrons and their relationship with the accelerated ions that excite the γ-ray emission. Again these have to be studied with care. They suffer decays to protons as they come to us from the Sun and their interaction with the detector system can be involved. They originate in the nuclear reactions that also produce the γ-ray emission but are produced by fast ions in the tens to hundreds of MeV energy range. Thus they extend our window into the energy distribution of the fast ions and hence into their acceleration mechanisms.

1.5 γ-ray Spectroscopy

When highly energetic ions, with energies of a few MeV or more, move through ambient material, they can interact with it in nuclear reactions that produce nuclei in excited states. The lifetimes of the excited states are very short-lived, of order 10^{-12} seconds. Therefore they quickly de-excite and release the excess energy in γ-ray photons. The same result is achieved when heavy nuclei are the accelerated ions except that, because these fast-moving heavy nuclei are also emitting the γ-rays, the resulting lines are broader due to a greater Doppler effect. This broad-line component combines with the highest energy electron bremsstrahlung emission to create the γ-ray continuum and the broad lines dominate the continuum at the highest energies. All of these mechanisms makes a rich gamma-ray spectrum, providing probes into the energies of the exciting particles

and the relative abundances of the emitting species. Indeed, the γ-ray lines are the only direct signature of the ions accelerated in solar flares.

Dolan & Fazio (1965) predicted that the 2.22 MeV neutron recapture line should be observable in solar flares. Richard Lingenfelter and the late Reuven Ramaty made the first detailed calculations of the expected nuclear line fluxes at the Earth due to a solar flare and suggested that gamma-ray line spectra could be useful tools to investigate solar flares (Lingenfelter & Ramaty 1967) and they and their collaborators have provided most of the techniques necessary to exploit it. After many Ramaty and Lingenfelter papers, showing that γ-rays should be there to find, Chupp et al. (1973); Meliorensky et al. (1975) finally reported their detection in solar flares (see Section 1.10.1).

These de-excitation lines are one component of a rich spectrum, stretching from 1 MeV to 7 MeV. At 2.223 MeV there is a line due to the capture of neutrons by hydrogen nuclei to produce deuterium by the reaction ^{1}H(n,γ)^{2}H. The fast neutrons arise in a variety of spallation reactions that contribute to the de-excitation lines. The spallation reactions are caused by protons with energies in excess of 30 MeV, extending the proton energy coverage of the γ-ray spectrum. Together with other signatures such as pion decay continuum, secondary neutrons and the 0.511 MeV positron annihilation line, these lines yield a fairly complete picture of flare ion acceleration from about 3 MeV.nucleon^{-1} to several GeV.nucleon^{-1} (e.g. Murphy (1985); Kocharov et al. (1998); Vilmer & MacKinnon (2003)).

1.6 De-excitation Lines to Consider

The choice of lines to observe is mainly decided by their observability and the availability of laboratory-measured cross-sections. The strongest lines (Kozlovsky et al. 2002) arise between photon energies of 1 MeV and 7 MeV due to excited states of the nuclei of carbon, nitrogen, oxygen, neon, magnesium, silicon and iron (Ramaty 1986; Chupp 1984). Many others are known but have not been observed. The cross-sections of these lines are discussed in detail in 2.3. The intensities of these lines depend on the abundance of these elements in the source as well as the detailed nuclear physics and some difficulties have arisen in matching these

to known abundances in likely source regions (the corona, chromosphere and photosphere). The abundance of ^{20}Ne is a particular problem that is addressed in the work presented in this thesis.

1.7 Neutron Emission

Hard X-ray and γ-ray observations reveal the presence of electrons of energies sometimes in excess of 10 MeV; and of ions of energies sometimes exceeding 1 GeV/nucleon. Fast neutrons, secondary products of various nuclear reactions involving the accelerated ions, are a valuable diagnostic of the solar flare accelerated ion distribution, filling the diagnostic gap between the nuclear de-excitation γ-ray lines which tell us about ions at 10 to 100 MeV.nucleon^{-1}, and pion decay continuum around 100 MeV photon energy, which carries information on ions with more than 300 MeV energy. Solar flare secondary neutrons were first detected by SMM (Chupp et al. 1982), but with no energy discrimination. Initial assumptions about the impulsive production of neutrons were later found to be false (Chupp et al. 1987). COMPTEL could perform neutron imaging and spectroscopy in the energy range 10 to 120 MeV (e.g. McConnell (1994)) and has provided the first neutron spectra and images. Interpreting the COMPTEL neutron data presents some difficulties in ensuring that meaningful neutron counts are obtained. An inversion of a COMPTEL neutron spectrum, using a full instrument response matrix is presented here. This is an improvement on previous approaches which applied only diagonal elements of this matrix and lost some of the detected neutrons.

1.8 The Source

The γ emission and neutron observations together can test the available models for particle acceleration. Constraints can be placed on the rapidity of particle acceleration, or the greatest individual particle energies of which the accelerator must be capable. Accelerated, non-thermal particles are a primary product of the energy release process in solar flares. We have known for decades that the energy content of electrons above about 20 - 25 keV appears to constitute several tenths of the total energy manifested in the flare (e.g. Hoyng et al. (1976), Lin & Hudson

(1976)). However, the overall role of fast ions in flares remains uncertain. Early, SMM era estimates of the energy content of ions above 1 - 10 MeV.nucleon^{-1} (e.g. Murphy & Ramaty (1984), Ramaty (1986)) indicated values modest compared to those of electrons.

The strong de-excitation lines are all produced by particles with higher energies than a few MeV.nucleon^{-1}, more energy than is available thermally in the corona. In the observable range, fast ion numbers decrease with energy and so the total energy in these ions must be dominated by the form of the energy distribution at lower energies. Yet this is below the window afforded by γ-ray spectroscopy. If the energy distribution deduced from gamma-ray lines is flatter below about 1 MeV, the total fast ion energy distribution will be small. Fast ions would not then be a major element in the transport of flare energy. Since the Ramaty-Lee model of particle acceleration (Ramaty et al. 1979) predicts just such a distribution, fast ions have long been discounted. Now, if the distribution continued to increase in number as energy decreased down to energies of, say 25 keV/nucleon, fast ions would be a major product of the energy release process. The accelerated ions would then need to be considered if flare radiation signatures at other wavelengths were to be understood. This component and its importance in the flare mechanism remains problematic and Dennis (1988) compares it to the Loch Ness Monster (also Brown et al. (1990)). This is in contrast to the role of electrons, for which the thick target interpretation of deka-keV bremsstrahlung X-rays provides estimates of total energy content, assuming a power law for their energy distribution (e.g. Hoyng et al. (1976); Lin & Hudson (1976)). However there are still uncertainties here over the minimum energy to which this power law extends (Kane et al. 1992; Emslie 2003; Galloway et al. 2004).

More recent work has begun to offer new insights. Share & Murphy (1995) pointed out the unexpectedly bright intensity of the 1.63 MeV line that arises from de-excitations of the first excited state of ^{20}Ne. There is uncertainty in estimates of neon abundance in the corona and other situations (e.g. Widing & Feldman (1995); McKenzie & Feldman (1992); Saba & Strong (1993)), and ^{20}Ne abundance variations between flares appeared to be part of the explanation. However, Share & Murphy (1995) demonstrated that there must be some other factor. One possibility lies in the sensitivity at lower proton energy of the cross-

section for excitation of the 1.63 MeV ^{20}Ne state. Protons of energies as low as 2 MeV can contribute to this line, while most other de-excitation lines need protons of at least 4 MeV for their production. A strong 1.63 MeV line would imply that the distribution of accelerated protons remains steep down to 2 - 3 MeV. This finding does not agree with the Ramaty-Lee Bessel function K_2 in momentum, which flattens off at low proton energies, and seems to suggest a higher proportion of accelerated ions at lower energies without revealing more about ions below 1 MeV.nucleon^{-1}. It may be that deduced power-law type distributions extrapolate to sub-MeV energies, implying a very large total ion content (Ramaty et al. 1996b).

All of these discussions also assume *thick target* production of γ-rays, i.e. that the accelerated ions stop completely in the source. Then the energy loss rate of the fast ions also enters the discussion, because it determines how long they stay above any particular energy and thus the number of photons they can produce while slowing down. Ions may interact resonantly with magnetohydrodynamic (MHD) waves but this results primarily in pitch-angle scattering, at least to first order (e.g. Miller & Ramaty (1987)), rather than any change in energy. Thus the necessary energy loss rates are given by test particle treatments of binary interactions (e.g. Spitzer (1956), Trubnikov (1965)). Emslie et al. (1997) pointed out that all the existing treatments assumed 'cold target' energy loss rates, assuming test particle speeds are very much greater than target particle speeds. For temperatures above 10^7 K and proton energies around a few MeV, however, this may no longer be the case. In this 'warm target' regime fast ions lose less energy in each binary collision, their effective lifetimes in the source are longer, and their photon yields potentially enhanced. Thus the stronger than expected 1.63 MeV line might reflect a reduced, warm target energy loss rate near threshold, rather than a greater number of fast protons.

However, Emslie et al. (1997) eventually concluded that warm target effects could not account for the brighter ^{20}Ne line. The reduction in energy loss rate over cold target conditions simply made it easier for the protons to leave the hot coronal region. They would produce their cold target photon yields, after quickly passing into the chromosphere. Emslie's conclusion neglects any other mechanisms that could keep the protons in the corona. Accordingly any treat-

ment of a fully-contained source was carried out only in a semi-quantitative way, approximating that the energy of the cross-section peak (close to 6 MeV) was characteristic of the protons and neglecting those at 3 MeV which can still contribute to the emission.

In Chapter 4 I re-evaluate the possible effect of warm target energy losses on the 1.63 MeV ^{20}Ne line (MacKinnon & Toner 2003). I look at the effect of warm target energy losses on the yield of the 1.63 MeV line in a hypothetical, fully-contained source. This illustrates the importance of considering all relevant proton energies. Such a hypothetical source is not a real flare but it does set the maximum influence warm target effects could ever have on estimates of ion energy distribution and total energy content. A brief Appendix reviews theoretical and experimental results on ion energy loss rates in neutral and ionized targets.

1.9 Species Differentiation in the Accelerated Particle Spectrum

Nuclear de-excitation γ-ray lines yield diagnostic information on ion acceleration in solar flares. Deductions using these lines of flare site ion distributions generally assume that all accelerated ion species have energy distributions of the same form. Particularly high total energy contents for fast ions result. In Chapter 5, I show how this assumption may be relaxed. Sufficiently precise measurements of a key set of lines may be combined to deduce separately the distributions of the fast protons and α-particles that produce the narrow de-excitation lines.

I apply the resulting procedure to the SMM/GRS observations. This provides two sorts of illustration, one assuming the relative abundance of fast α's and protons, and the other delineating regions of the parameter space consistent with the lines that are observed. Implications for flare ion total energy content may be dramatic.

1.10 Data

Spectra of solar activity in the γ-ray range, have to be collected from high altitude, since the Earth's atmosphere blocks most of this radiation. Early balloon flights provided images of the sky in X-rays and γ-rays. The first solar γ-ray photons

were detected in 1958 (Chupp 1984; Peterson & Winckler 1959). These balloons were able to operate at high altitudes for hours or days at a time and modern long-duration balloon flights continue to add to our knowledge of the high-energy sky. However, most solar γ-ray data now come from spacecraft.

These are of two main types: Earth satellites, which are typically placed in a low polar orbit, chosen to minimize the time spent in the Earth's shadow, and interplanetary spacecraft, often placed in orbit around the L1 Lagrange point between the Earth and the Sun, a 'halo' orbit (see Figure 1.7). The halo orbit is reserved for durable spacecraft that can constantly monitor the Sun for a long time without servicing. Satellites in low Earth orbits have benefitted from regular servicing by Space Shuttle flights, allowing for extended missions and equipment upgrades. Spacecraft can gather whole-sun flux measurements, detailed images and spectra in γ-rays. They also monitor other electromagnetic frequencies, especially ultra violet and X-rays, and also observe particle fluxes from solar events such as protons, electrons, neutrons and α-particles.

Detection of γ-rays usually depends on technology borrowed from nuclear physics. A volume of material, either plastic or crystal, that scintillates on passage of a high-energy photon or particle (they often detect neutrons simultaneously) acts as the first stage of detection. The larger this scintillator the more likely it is to stop a photon and therefore the more sensitive the instrument. The scintillation photons are then observed by photomultipliers. This count of scintillation photons is what we need to interpret to discover the nature of the γ-ray detection. Not all of these detections will be solar in origin. High-energy radiation interacts with the spacecraft and can produce interesting γ-ray emission. Shielding and a good knowledge of the spacecraft's contribution help to isolate the solar data. There are also local sources which interfere, particularly in Earth orbit. Solar activity stimulates the Earth's upper atmosphere causing it to emit its own rich γ-ray spectrum. Also, energetic particles are captured by the geomagnetic field and cause interference when the satellite passes through them. A major concentration is formed in the South Atlantic Anomaly (SAA) and care has to be taken to avoid data gathered in such a location.

When observing cosmic γ-ray sources, the background is often removed by subtracting a spectrum observed in a nearby region of the sky around the same

time as the main observation. However, this is difficult when observing a complex extended source like a solar flare. The accepted method of removing background interference from a solar flare spectrum is to look at spectra from a previous orbit and a subsequent orbit that placed the spacecraft in similar positions to the one when the flare was observed. Sometimes this process can be summed over many previous and subsequent orbits. This creates a background spectrum which is then removed from the solar flare data (Murphy et al. 1990a, 1997).

1.10.1 Early γ-ray Observations

Explorer 11, or S 15, was the first γ-ray detection satellite flown (High Energy Astrophysics Science Archive Research Centre 2004). It was launched on 27 April 1961 and the instrument aboard was designed to detect γ-rays above 50 MeV. It was intended to map the positions of γ-ray sources. These were found to originate from solar flares, the Van Allen belts and from an isotropic cosmic background (Arnold et al. 1962; Mechau 1962; Miller 1962). The satellite operated well until early September 1961, when power supply problems became noticeable and soon no more useful data could be collected.

The Ranger probes were intended to crash-land on the Moon, transmitting close-up photographs of the lunar surface on the way (High Energy Astrophysics Science Archive Research Centre 2004). However not all of them completed their mission as intended. In particular Ranger 3 and Ranger 5, both launched in 1962, missed the Moon and went into heliocentric orbits. They were both equipped with γ-ray instruments for measuring radiation from the lunar surface. The detector in each of these was a CsI crystal surrounded by a plastic scintillator. A photomultiplier tube detected each event which was then recorded in a 32-channel pulse height analyzer. This provided spectra over the energy ranges 0.1 to 3.0 MeV and 20 to 600 keV (National Space Science Data Centre 2004). These instruments were instead used to measure the γ-ray background before they were lost to telemetry.

Over this period there were a number of satellite series (High Energy Astrophysics Science Archive Research Centre 2004) which included γ-ray instruments such as OGO (Orbiting Geophysical Satellites), Cosmos and the military Vela satellites. The Vela series were intended to monitor for violations of the 1963

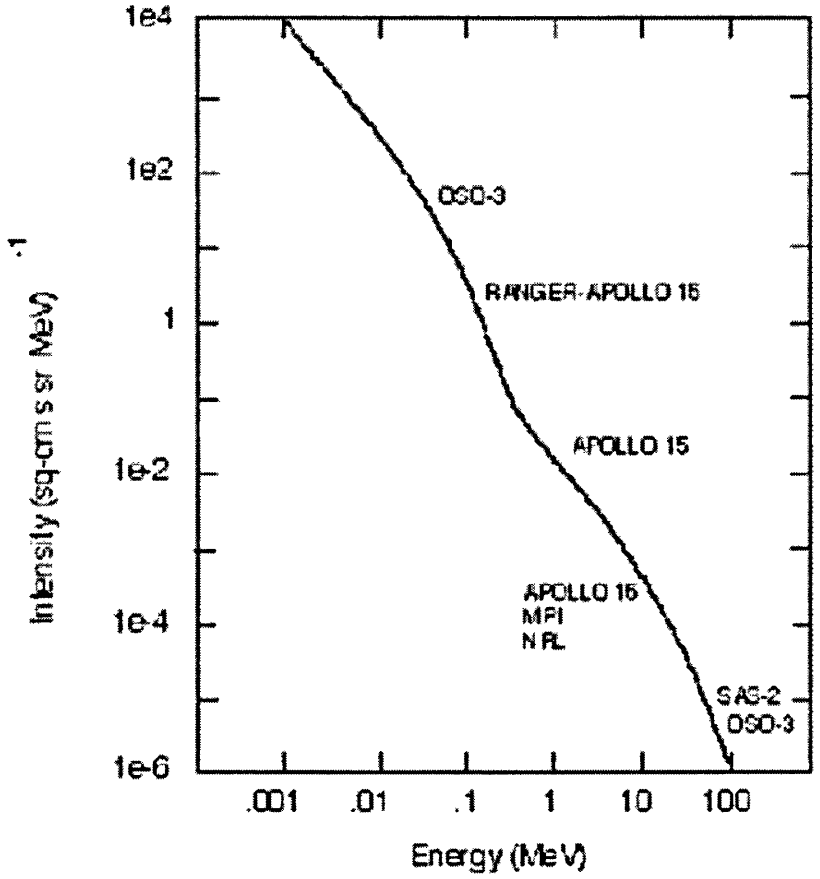

Figure 1.5: The γ-ray background showing the Apollo and Ranger contributions.

Limited Test Ban Treaty, but they also detected extra-terrestrial sources of radiation, and discovered γ-ray bursts, although the discovery was kept secret at the time in the interests of national security. They were fitted with CsI γ-ray detectors sensitive to photons in the energy range 150 to 750 keV. The IMP-6 (Interplanetary Monitoring Platform) satellite was launched in 1971. While this instrument was monitoring for solar flares, it unexpectedly detected γ-ray bursts.

The cosmic γ-ray background was the focus of the SAS-2 (Small Astronomical Satellite; SAS-1 was the Uhuru X-ray satellite), launched in 1972 by NASA and lasting seven months, and ESA's COS-B, which flew between 1975 and 1982 (High Energy Astrophysics Science Archive Research Centre 2004). These confirmed the early detections of the background and discovered a number of γ-ray point sources.

Apollo 15 and 16 (1971 and 1972 respectively) released sub-satellites while in orbit around the Moon to do studies on lunar gravity and magnetic fields. Apollo 16 astronauts John Young and Charles Duke deployed a UV electrographic

camera and spectrograph on the lunar surface. The instrument observed the Sun, the Earth's geocorona and various astronomical objects. Both Apollo 15 and 16 Command and Service Modules carried γ-ray spectrometers. They contained a NaI(Th) scintillation crystal in a plastic scintillator shield, which prevented interference from charged particles, and could be extended on a boom, 7.6 m long, to reduce interference from the spacecraft. γ-rays could be studied between 0.5 and 30 MeV with an energy resolution of 8.5%. These spectrometers studied the lunar surface in a 2° to 3° field and the γ-ray background (see Figure 1.5 and Lindstrom et al. (1971); National Space Science Data Centre (2004)).

1.10.2 Early Solar γ-ray Observations

Launched in 1962, Orbiting Solar Observatory 1 (OSO 1) was the first of a series of nearly identical satellites intended to cover an entire 11-year solar cycle (e.g. Ramaty 1974; Datlowe et al. 1974). The primary mission objectives were to measure the solar electromagnetic radiation in the UV, X-ray, and gamma-ray regions. OSO-3, was launched in 1967 and the series continued until OSO-8 which flew between 1975 and 1978 (High Energy Astrophysics Science Archive Research Centre 2004). For solar γ-ray workers the high point of this series was OSO-7 which detected the first γ-ray spectrum of a solar flare on 4 August 1972 (Chupp et al. 1973; Chupp & Dunphy 2004). This spectrum included lines at 0.511 MeV (positron annihilation), 2.22 MeV (neutron capture), 4.44 MeV (^{12}C nuclear line) and 6.13 MeV (^{16}O nuclear line). The positron and neutron lines were seen again in the 7 August 1972 flare. The same flares were also seen by the Prognoz-2 satellite.

The SIGNE program (Solar International Gamma-Ray and Neutron Experiments) was a joint French-Soviet program which first went into space in 1972 with the Prognoz-2 satellite and completed with the Prognoz-9 satellite in 1983. The scientific objectives of all of the Prognoz missions was the study of particles and fields and solar electromagnetic radiation (see, e.g., Volodichev et al. 1983; Zastenker et al. 1985). Prognoz-2 carried the Signe-1 instrument which was sensitive to γ-rays in the range 0.4 to 11.8 MeV in eight bands. It detected emission from the 4 and 7 August 1972 flares in the 3.9 to 8.1 MeV band, consistent with the OSO-7 detection of the 4.44 MeV and 6.13 MeV lines (Meliorensky et al.

1975; Talon et al. 1975). Talon et al. (1975) also looked at data from a flare on 2 August 1972 but did not find conclusive evidence of γ-ray line emission.

The next solar γ-ray detections following OSO-7, were made by the first High Energy Astrophysical Observatory satellite (HEAO-1) on 11 July 1978, using its A4 detector, the UCSD/MIT Hard X-ray/Low-Energy Gamma-Ray Experiment (Hudson et al. 1980). This could detect X-rays and γ-rays between 80 keV and 10 MeV and found the neutron capture line at 2.22 MeV and the ^{12}C line at 4.44 MeV and measured the 1 to 5 MeV continuum emission .

This was followed by HEAO-3 which carried the Gamma Ray Spectroscopy Experiment which could detect X-rays between 50 keV and 10MeV. It measured the 2.22 MeV line and the continuum above 80 keV and above 3.8 MeV during the short 9 November 1979 flare (Prince et al. 1982). This period also saw the first part of the Solar Maximum Mission (SMM) (Section 1.10.4) and also the Japanese satellite Hinotori. Hinotori carried a γ-ray spectrometer sensitive to the energy range 0.21 to 6.67 MeV. It observed many γ-ray flares after its launch in 1981 and detected several γ-ray lines, including 0.85 MeV ^{56}Fe, 1.24 MeV ^{56}Fe, 1.63 MeV ^{20}Ne, 1.78 MeV ^{2}8Si, 2.22 MeV neutron capture, 4.44 MeV ^{12}C, and 6.14 MeV ^{16}O. It could not discriminate between the $\alpha - \alpha$ lines at 0.43 MeV and 0.48 MeV and the 0.51 MeV positron emission but did detect a broad peak in that range (Yoshimori et al. 1983).

GRANAT was launched by Russia in 1989 and made observations up until 1998 (Figure 1.6). It was created in collaboration with a number of European countries, particularly France, where the SIGMA X-ray telescope and PHEBUS high-energy γ-ray experiment were developed. The other γ-ray instruments were KONUS-B, which added a lower energy range to PHEBUS' γ-ray burst monitoring (0.02 to 100 MeV in all), and TOURNESOL, which was used view a 5° field in the energy range 0.002 to 20 MeV. GRANAT was primarily a cosmic X-ray observatory but also was used to study solar activity in X-rays, γ-rays and charged particles (Chupp & Dunphy 2004; Trottet et al. 2003; Vilmer & MacKinnon 2003; Lentners et al. 1999; Murphy et al. 1999; Ramaty & Mandzhavidze 1997; Vilmer 1994; Terekhov et al. 1993; Pelaez et al. 1992; Chuchkov et al. 1991).

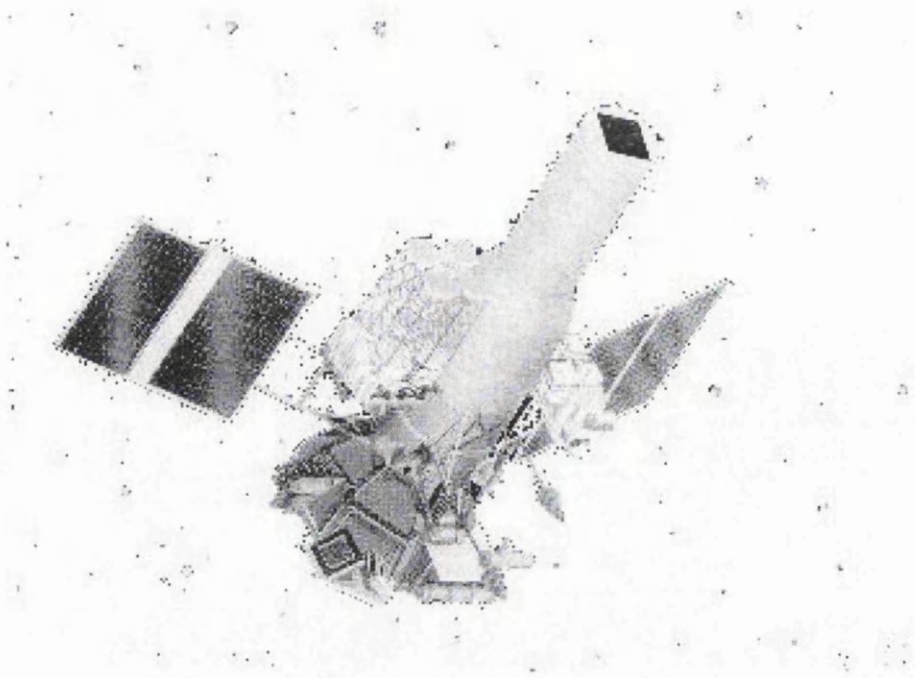

Figure 1.6: The Russian GRANAT X-ray observatory.

1.10.3 Supporting Space Observations

In addition to observing the γ-ray spectra and γ-ray emissions, we also need to know about the composition of the source, the species abundances. There is a long history of space probes investigating interplanetary particles and solar energetic particles which give a window onto the composition of material from flares. We also get good imaging from other wavebands such as extreme ultra-violet and X-rays.

The Helios pair of satellites were put into solar orbits by NASA for the Federal Republic of Germany. Helios-A was launched in 1974 and Helios-B was launched in 1976. The Helios satellites investigated many features of the interplanetary medium and solar activity and, in particular, Solar Energetic Particles using magnetic particle spectrometers. These could detect protons above 80 keV and electrons above 15 keV (McDonald & Van Hollebeke 1985; Sanahuja et al. 1983).

The International Sun-Earth Explorer (ISEE) program consisted of 3 satellites– ISEE-1 and ISEE-3 were the principal US contribution to the International Magnetospheric Study, and ISEE-2 which was built and managed by ESA. ISEE-3 was launched in 1978. It was inserted into a 'halo' orbit about the libration point some 240 Earth radii upstream between the Earth and Sun. Three proton tele-

scopes on board detected particles in the energy range 35 to 1600 keV and were used to investigate the interplanetary medium and particles produced in solar flares (e.g. Reames et al. 1990; Kunz et al. 1983; Sanahuja et al. 1983). ISEE-3 was renamed ICE (International Cometary Explorer) when, after completing its original mission in 1982, it was gravitationally maneuvered to intercept the comet P/Giacobini-Zinner. In 1985, the veteran NASA spacecraft flew through the tail of the comet. An extended ICE mission was approved by NASA in 1991 for the continued investigation of coronal mass ejections and cosmic rays, and coordinated observations with Ulysses. It will return to the vicinity of the Earth-moon system in 2014.

The Ulysses mission is a joint mission with NASA and ESA to explore the solar environment at high ecliptic latitudes. It was launched in 1990, and reached Jupiter for its 'gravitational slingshot' in 1992. It passed the south solar pole in 1994 and crossed the ecliptic equator in 1995, during solar minimum. In addition to its solar environment instruments, Ulysses also carries plasma instruments to study the interstellar and Jovian regions, as well as two instruments for studying X-rays and gamma-rays of both solar and cosmic origins (Trottet et al. 2003). Its mission was extended for an additional thirteen years and will now continue until 2008, allowing measurements with the same instruments at the next solar minimum in 2006. Recently problems with the satellite heating system have developed and engineers are having to be careful about loading the power system until the spacecraft moves close enough to the Sun to prevent fuel lines from freezing. This will be in 2007 (Phillips 2004).

After launch in 1994, NASA's Wind satellite took up a 'halo' orbit between the Sun and the Earth (similarly to SOHO, Figure 1.7), where it can observe the solar wind. Onboard are the hot plasma and charged particles Three-Dimensional Plasma analyzer (3DP) experiment, the Transient Gamma-Ray Spectrometer (TGRS), the Magnetic Fields Instrument (MFI), the Plasma and Radio Waves (WAVES) experiment, the Solar Wind Experiment (SWE), the Energetic Particle Acceleration, Composition and Transport (EPACT) experiment, the Solar Wind and Suprathermal Ion Composition Studies (SWICS/STICS) experiment and the Gamma Ray Burst Detector (KONUS).

SOHO was launched in 1995. It sits in a 'halo' orbit around a Lagrange point

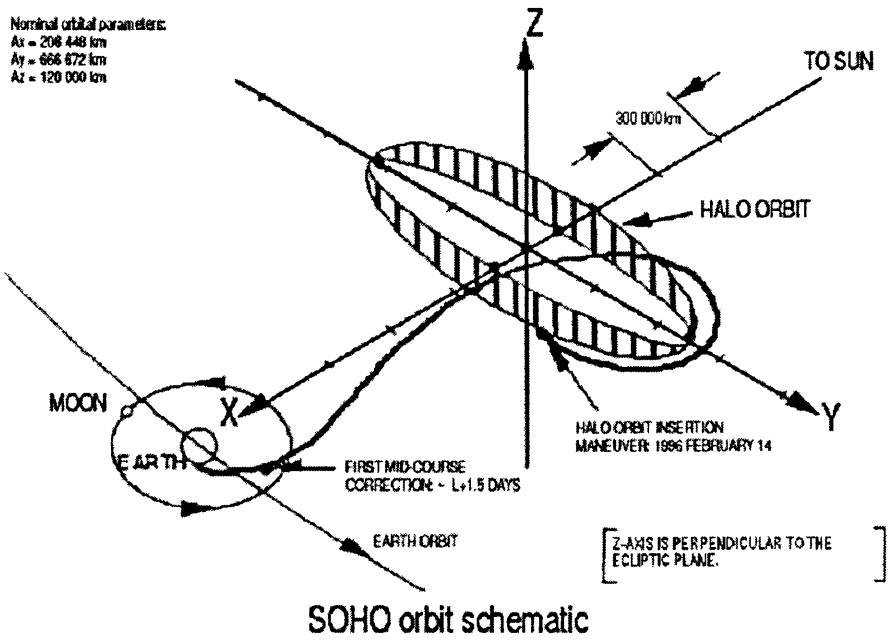

Figure 1.7: The 'halo' orbit exploited by SOHO and other solar observatories.

$^1/_{100}$ of the distance between the Earth and the Sun (see Figure 1.7) and monitors solar activity. The instruments are designed to explore three aspects of the Sun and its environment. GOLF (Global Oscillations at Low Frequencies), VIRGO (Variability of Solar Irradiance and Gravity Oscillations) and MDI/SOI (Michelson Doppler Imager/Solar Oscillations Investigation) monitor oscillations at different temporal and spacial scales to allow study of the solar interior; SUMER (Solar Ultraviolet Measurements of Emitted Radiation), CDS (Coronal Diagnostic Spectrometer), EIT (Extreme ultraviolet Imaging Telescope), UVCS (Ultra Violet Coronagraph Spectrometer) and LASCO (Large Angle and Spectroscopic Coronagraph) observe the corona; and CELIAS (Charge Element and Isotope Analysis System), COSTEP (Comprehensive Suprathermal and Energetic Particle Analyzer) and ERNE (Energetic and Relativistic Nuclei and Electron Experiment) allow study of the *in situ* solar wind while SWAN (Solar Wind Anisotropies) maps hydrogen in the heliosphere from ten solar diameters outwards. Between them it is hoped to develop an early warning system for extreme solar activity leading to adverse space weather at the Earth.

In 1997, the Advanced Composition Explorer (ACE) joined SOHO and WIND at the Lagrange point. It is equipped with a battery of particle-detection instruments and was specifically designed to investigate questions of chemical abun-

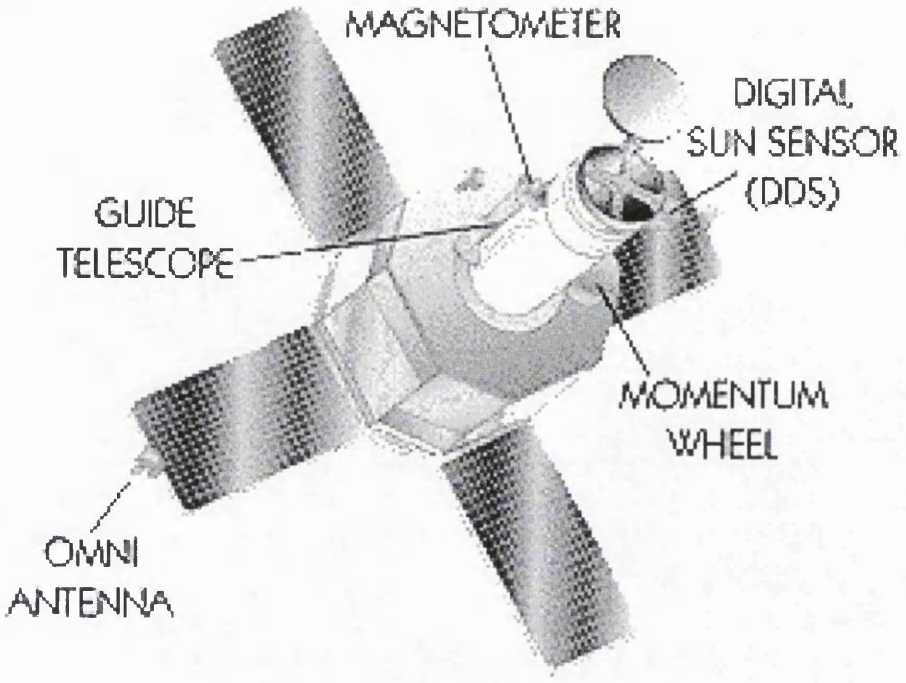

Figure 1.8: The Transition Region and Coronal Explorer (TRACE). Image courtesy of http://sunland.gsfc.nasa.gov/smex/trace.

dance in the solar wind and in coronal mass ejections. It is still functioning well and contributing to our knowledge of solar energetic particles (see Section 2.4).

The Transition Region and Coronal Explorer (TRACE) is equipped with a telescope, filters and CCD detector allowing it to image parts of the solar atmosphere in emission lines of Fe, H and C at 171, 195, 284, 1216 and 1550 Å and in the continuum at 1600 Å (Figure 1.8). This emission originates from regions stretching from the upper photosphere out into the lower corona and allows imaging of plasma loops and flares. These close-up images complement the larger-scale pictures provided by SOHO.

Probably one of the most important support systems for solar physics observations is provided by the Geostationary Operational Environmental Satellites (GOES) operated by the US National Oceanic and Atmospheric Administration (NOAA). At all times there are two of these satellites operating in the GOES-East (over the Pacific basin) and GOES-West (over North and South America and the Atlantic Ocean) positions and their primary purpose is meteorological monitoring of the Earth's atmosphere. At present GOES-10 is the GOES-West satellite and GOES-12 is the GOES-East satellite. There are two other GOES

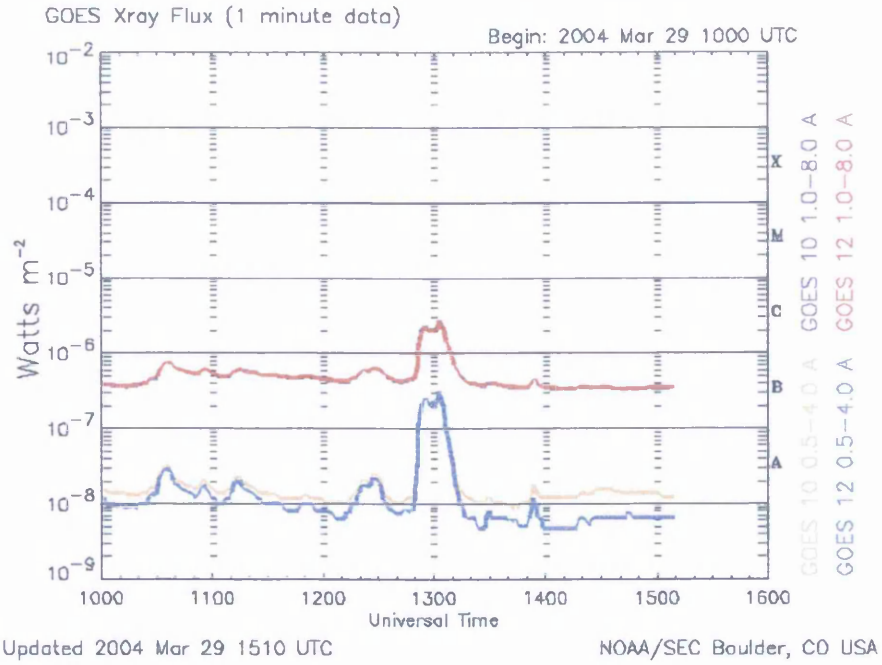

Figure 1.9: This GOES X-ray flux plot contains 1 minute averages of solar X-ray output in the 0.1 to 0.8 nm and 0.05 to 0.4 nm passbands. Data from both operational GOES satellites are included. Image is from the Space Environment Centre (Centre 2004).

satellites in orbit: GOES-11 is on standby in case of a failure of either GOES-10 or GOES-12 and GOES-9 is being used by the Japanese Meteorological Agency. The importance of these satellites for solar physics lies in their secondary objective as space weather monitors using their Space Environment Monitor (SEM) instrument. These provide real-time warnings of events on the Sun which can signal high-energy observatories to begin observations.

Up until GOES-12, the SEM provided a measure of solar X-ray flux using the X-ray Sensor (XRS), useful as a warning of the start of activity and after the event for finding the time of onset to look for in other observations. It provides a time series of total solar flux in the 0.5 to 4 Å and 1 to 8 Å bands in a 3.06 s time resolution (see Figure 1.9). Now the GOES-12 has a Solar X-ray Imager (SXI) which provides images of the whole solar disk in these wavebands.

In addition to X-rays, GOES SEM can also detect protons, electrons and α-particles with its particle sensor (EPS) and it can monitor the Earth's magnetic field with its magnetometer, sensitive to changes as small as 0.2 nT.

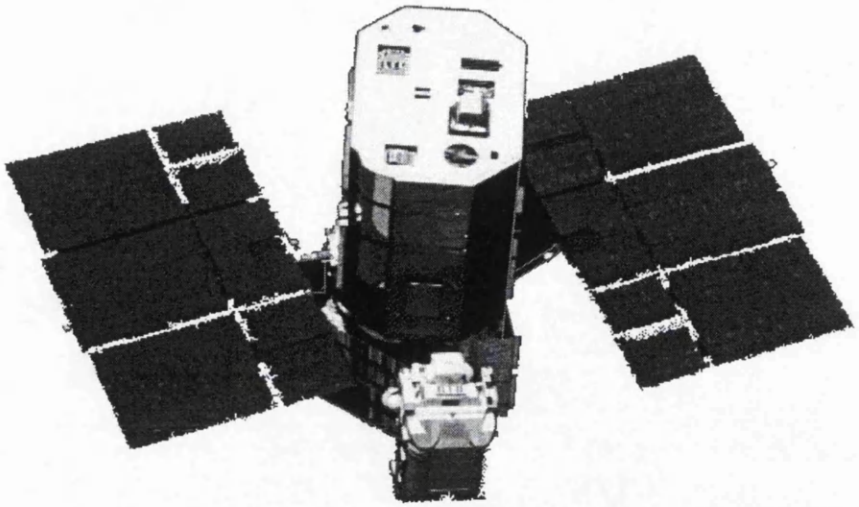

Figure 1.10: The Solar Maximum Mission (SMM) Spacecraft

1.10.4 Solar Maximum Mission

The Solar Maximum Mission (SMM) was launched by NASA in 1980 and was a dedicated high-energy solar observatory (Figure 1.10). It was intended to observe the Sun in ultra-violet, X-rays and γ-rays during the subsequent maximum phase of the solar cycle (Chupp et al. 1981; Ryan et al. 1981; Forrest & Chupp 1983; Chupp 1984). However, maintenance by NASA Space Shuttle astronauts extended the mission's life and it gathered data until 1989.

SMM's instruments were the Coronagraph/Polarimeter (SMMCP) the Ultra-violet Spectrometer and Polarimeter (UVSP), the Hard X-Ray Burst Spectrometer (HXRBS) and the Gamma Ray Spectrometer (GRS). The SMMCP recorded corona images in the green optical band (500 to 535 nm) with some images in the FeXIV line at 530.0 to 530.6 nm band and the Hα line between 654.3 and 658.3 nm. Images usually had a resolution of 12" but some were recorded at 6" and a catalogue of coronal mass ejections was compiled. UVSP was a Gregorian telescope with resolution of 2" equipped with an Ebert-Fastie spectrometer and five detectors. The detectors consisted of four CsI photocathode tubes that recorded emission between 117 and 190 nm, and one CsTe photocathode tube for longer wavelengths up to 360 nm. It was able to produce images of regions on the Sun 256" on a side. It was used to point and time observations with the other instruments and also recorded ozone concentrations in the Earth's atmosphere.

HXRBS was used to investigate energetic electrons by examining hard X-ray flux in fifteen channels between 25 and 500 keV at time resolutions of between 1 and 128 ms. It employed a CsI(Na) scintillation detector collimated to a 40° field of view.

The GRS used an array of seven NaI(Tl) detectors to record nuclear line spectra between 0.3 and 0.9 MeV with an energy resolution of about 7%. In combination with a thick CsI(Na) crystal, their sensitivity could be extended to γ-rays between 10 and 140 MeV and neutrons above 20 MeV. Hard X-rays between 10 and 140 keV could be detected by another two NaI detectors. Time resolution in GRS data is between 64 ms (for 300 to 340 keV) and 16 s, with typical measurements being at around 2 s resolution. The field of view covered half of the sky and GRS recorded many cosmic events as well as solar data. The GRS database of solar flare spectra still remains as an important research tool (e.g. Chupp & Dunphy 2004) as we wait for reduction of CGRO data and for new RHESSI data. It is used in this present work, particularly in chapters 3 and 5. Convenient line intensities taken from this database are available in Share & Murphy (1995, 1997, 1998) and example GRS spectra are shown in Figure 1.11.

1.10.5 Yohkoh

Yohkoh ('sunbeam') was launched by Japan in 1991 and was a collaboration with the US (on the Soft X-ray Telescope and the Bragg Crystal Spectrometer) and the UK (on the Bragg Crystal Spectrometer). Its principal mission was to study solar X-ray and γ-ray emissions which it did successfully until 2001 (Institute of Space and Astronautical Science 2004; NASA Goddard Space Flight Centre 2004).

The instruments on board Yohkoh (Figure 1.12) were the Bragg Crystal Spectrometer (BCS), the Wide Band Spectrometer (WBS), the Soft X-ray Telescope (SXT) and the Hard X-ray Telescope (HXT). The BCS was a composite of four bent germanium crystal spectrometers, each covering a specific band of soft X-rays to be able to sample lines produced by FeXXVI, CaXIX and SXV with a resolution of $\frac{\lambda}{\Delta\lambda}$ between 3000 and 6000. Its field of view covered the whole Sun and it was used to investigate hot plasmas ($\sim 10^7$ K) produced in solar flares.

The WBS consisted of a soft X-ray spectrometer (SXS), a hard X-ray spec-

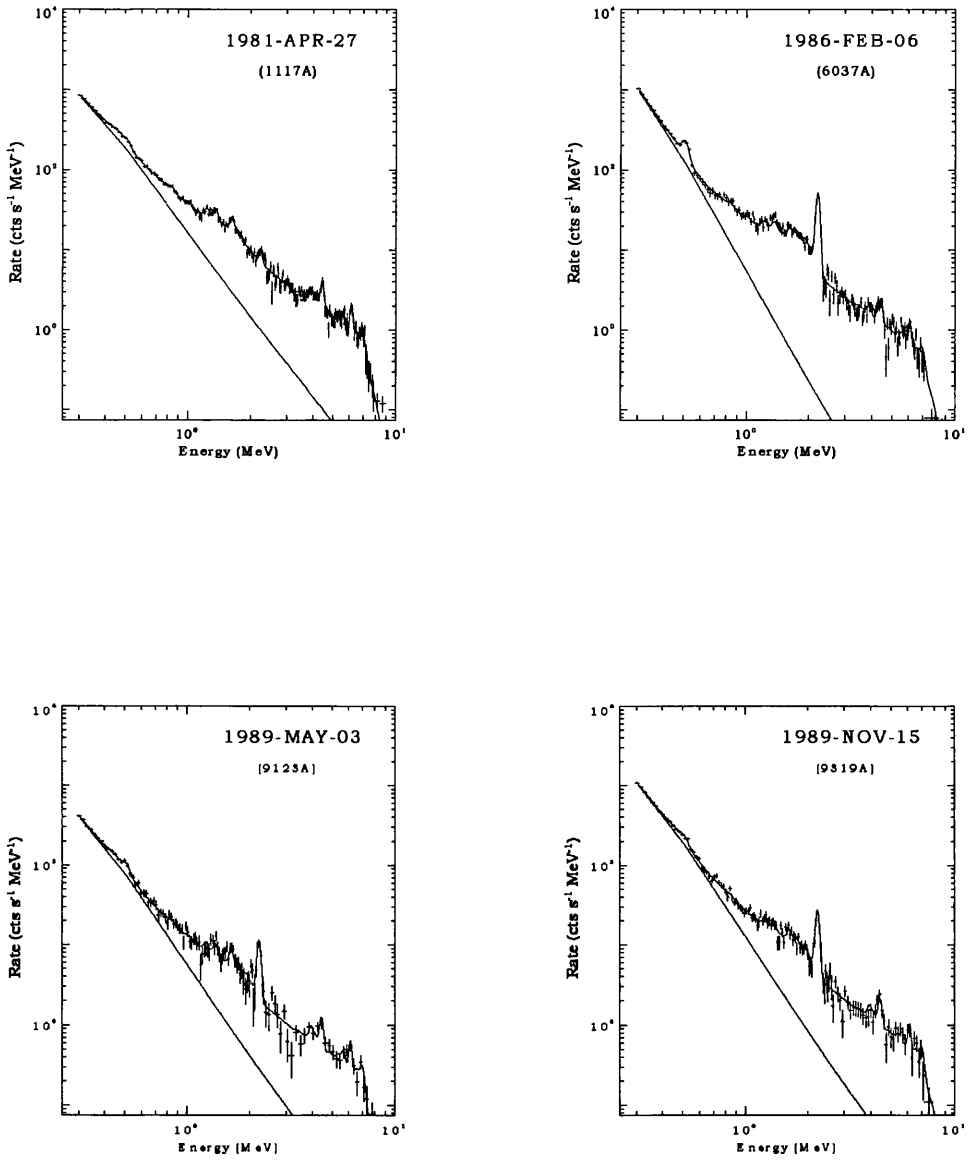

Figure 1.11: Spectra recorded by the Gamma Ray Spectrometer (GRS) on board the SMM spacecraft for four different flares.

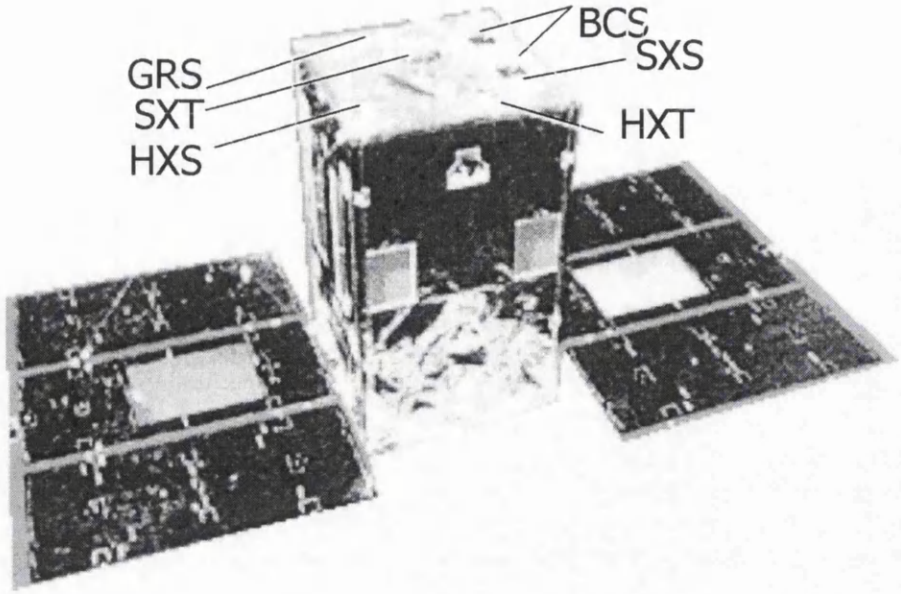

Figure 1.12: The Japanese Yohkoh high-energy solar observatory.

trometer (HXS) and a γ-ray spectrometer (GRS). SXS had two proportional counters sensitive in the 2 to 30 keV range and was used to make time series of electron temperatures and emission measures throughout a flare. HXS used a NaI scintillator to detect photons between 20 and 400 keV and was used to make time series of the electron spectrum. GRS had two BGO scintillation detectors detecting in the 8 to 100 MeV energy range for producing time series of nuclear line spectra (e.g. Chupp & Dunphy 2004).

The SXT was a glancing incidence instrument that could produce X-ray images in the 0.25 to 4.0 keV energy range. The detector was a 1024×1024 CCD array. Metal filters could be used to separate various X-ray bands and the same detector could take optical images using a visible-light telescope when the metal filters were replaced by a glass filter. The HXT used a Fourier synthesis method for imaging X-rays with energies between 14 and 93 keV (in bands L, M1, M2 and H). It had 64 sub-collimators, each fitted with a NaI(Tl) scintillator. Each of these provided a modulated count rate signal with a resolution down to 0.5 s which was used as a spatial Fourier component. This set of data could be processed later to synthesize an X-ray image $2.1' \times 2.1'$ with a resolution element as small as 5". The instrument's complete field of view was $35' \times 35'$, covering the whole Sun, which made it possible to acquire an image of a flare site without needing to repoint the telescope.

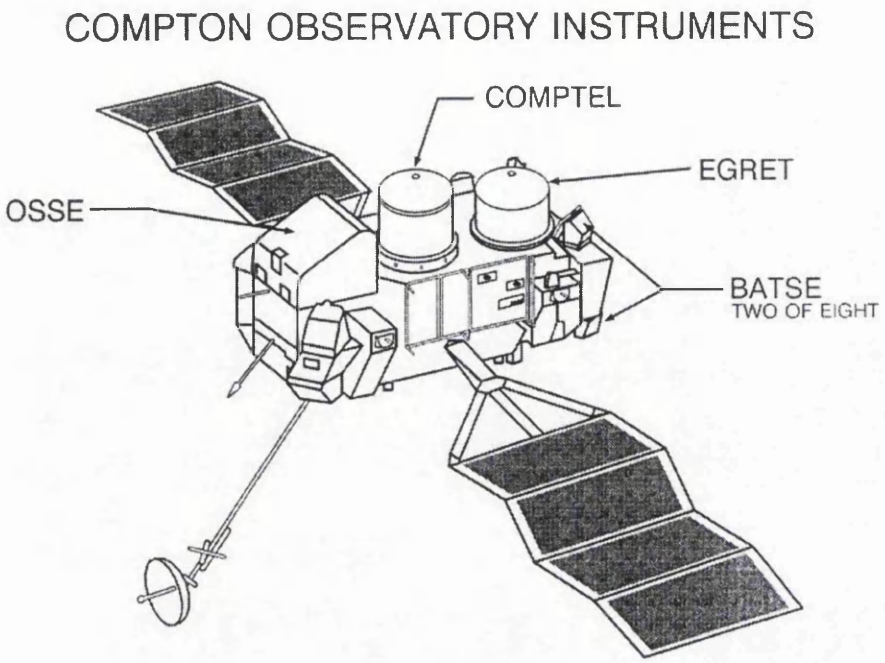

Figure 1.13: The Compton Gamma Ray Observatory showing the main instruments.

Yohkoh images have provided spatial references for a number of γ-ray observations with other satellites such as RHESSI. However, the multiwavelength capability of this satellite has provided much useful data by itself (e.g. Morimoto 1996; Alexander et al. 1994; Yoshimori et al. 1994).

1.10.6 Compton Gamma Ray Observatory

The Compton Gamma Ray Observatory (CGRO) was launched by NASA in 1991 from Space Shuttle Atlantis. It was the second Great Observatory (the Hubble Space Telescope was the first) and was designed to be a general purpose γ-ray observatory, investigating both solar and cosmic phenomena. It took its name from Arthur Holly Compton whose work on the scattering of high-energy photons underlies the technology of CGRO's instruments. CGRO finished its mission when it was deorbited in 2000.

There were four instruments on CGRO: the Burst and Transient Source Experiment (BATSE) designed to investigate γ-ray bursts and similar transient sources; the Oriented Scintillation Spectrometer Experiment (OSSE) which has gathered nuclear line spectra from solar flares as well as γ-ray spectra from cosmic sources such as supernova remnants; the imaging Compton Telescope (COMP-

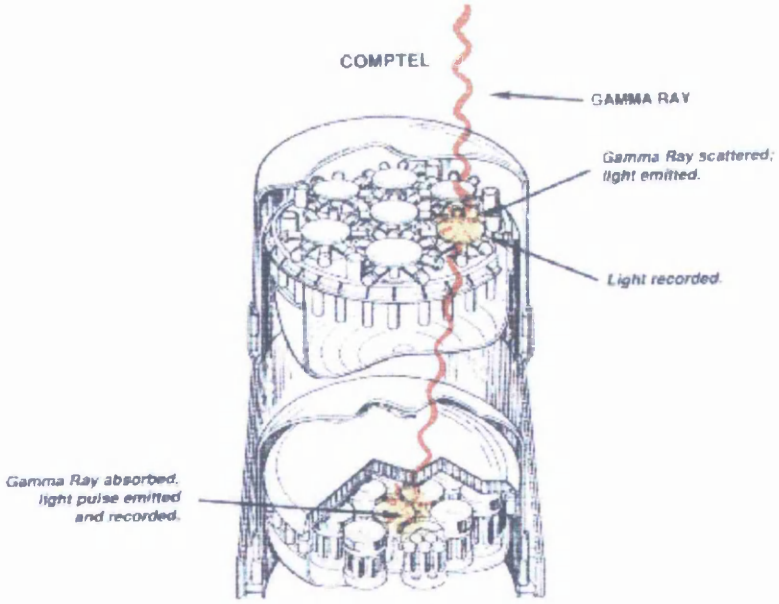

Figure 1.14: The COMPTEL γ-ray telescope which flew on board the Compton Gamma-Ray Observatory.

TEL) which produced γ-ray images of solar flares and also detected solar flare neutrons (see Chapter 6) in addition to providing locations for cosmic sources; the Energetic Gamma Ray Experiment Telescope (EGRET) could make images from γ-rays with energies as high as 30 GeV (Figure 1.13).

BATSE was not really a solar instrument, being mainly used to detect γ-ray burst sources, but it could detect the occurrence of a solar flare. It took the form of eight NaI scintillator detection modules mounted on the corners of the spacecraft. This provided whole-sky coverage in the energy range 20 to 1000 keV. There were two detectors in each module: one sensitive to very faint transient events and the other capable of spectroscopic analysis of stronger events.

OSSE had four NaI scintillators which could be pointed independently, to allow background subtraction, and were sensitive to photons between 50 keV and 10 MeV. As well as investigating the γ-ray spectra of cosmic sources, OSSE also provided spectra of solar flares. This data is now beginning to emerge from the large CGRO archive (e.g. Chupp & Dunphy 2004; Murphy et al. 1997,see Figure 2.1).

EGRET extended the energy-range of CGRO and could detect γ-ray photons

from 30 MeV up to 30 GeV (Kanbach et al. 1993). This was made possible by capturing the photons in high-voltage, gas-filled spark chambers where each produced an electron-positron pair. The paths of these particles through the spark chambers would be recorded and enabled the calculation of the direction of the original photon. Its energy could be deduced from the amount of energy deposited by the electron and positron in a NaI crystal at the rear of the system.

The COMPTEL instrument could image γ-ray sources by exploiting Compton scattering. It is shown in Figure 1.14. The front detector array (D1) was made up of seven liquid Ne213A scintillators, each 27.6 cm in diameter and 8.5 cm deep, while the rear array (D2) had fourteen NaI detectors, each 28 cm in diameter and 7.5 cm deep. Ne213A was chosen for the D1 detectors because its low density and low atomic number increase the probability that a γ-ray photon will scatter singly and the scattered photon will escape. Conversely, the D2 detectors had to completely absorb the energy of the scattered photon. This made it possible for photon energies and arrival directions to be deduced from Compton scatter events in the D1 array, and scattered photon energy measured in D2. Figure 6.2 in Chapter 6 shows more clearly how a photon (γ) or neutron (n) comes from the Sun and passes through the telescope. In order to correctly image the incoming solar γ-rays, COMPTEL has to capture all of the energy of the photons and only events which inferred a direction from the Sun were considered in making images, in an attempt to discount photons that did not scatter ideally or belonged to some background source.

If a solar photon, γ, enters the telescope at angle ϕ to the instrument axis and deposits energy E_1 in array D1, a scattered photon, γ', will continue on to deposit energy E_2 in array D2 (McConnell 1994). In this case the energy of the original solar photon can be deduced simply as the total of E_1 and E_2, and its direction of entry into the telescope can be inferred from the Compton kinematic formula (ε is the electron rest mass energy).

$$\phi = \cos^{-1}(1 - \frac{\varepsilon}{E_2} + \frac{\varepsilon}{E_1 + E_2}) \tag{1.4}$$

The same system could detect and image a neutron source and the details of how it did this are described in Chapter 6. Figure 6.1 shows the results of this imaging technique. This shows the source of the neutrons emitted during the

15 June 1991 solar flare, which turns out to be a point source in COMPTEL's resolution. COMPTEL's great sensitivity in telescope mode enabled it to detect neutrons for over one hour after the X-ray maximum of this flare. Although it missed the start of the *gamma*-ray flux from this flare (the Sun was out of COMPTEL's field of view for the first 39 minutes) COMPTEL was able to follow the γ-ray emission as it declined until 70 minutes after the initial peak, showing that the supply of accelerated protons lasted for at least this long (McConnell 1994). GAMMA-1 also recorded this long duration tail at high energies, observing γ-rays in the range 30 MeV to 2 GeV for more than two hours (Leikov et al. 1993). This long sustained γ-ray emission was also a feature of the previous flare on 11 June which was observed with COMPTEL, EGRET and OSSE. In particular, EGRET (Ramaty & Mandzhavidze 1994) recorded 0.05 to 2 GeV emission for eight hours from this flare.

1.10.7 Reuven Ramaty High Energy Spectroscopic Solar Investigator

The Reuven Ramaty High Energy Spectroscopic Solar Investigator (RHESSI) was launched by NASA in 2002 (Figure 1.15). This was just after solar maximum but in time to observe some of the large flares that often occur in this phase of solar activity. It was put into a low Earth orbit to avoid damage to its germanium sensors which could be inflicted by the radiation belts. RHESSI is relatively unshielded as a trade-off in weight to allow for its imaging capability.

RHESSI can form images of γ-ray and X-ray sources using nine rotational modulation collimators (RMCs) each made up of two fine grids. The photons that pass through these collimators are detected by hyper-pure germanium (HPGe) detectors, each 7.1 cm in diameter and 8.5 cm long and cooled to 75 K. The front 1 cm thickness detects hard X-rays while the rear 7 cm detects γ-rays, giving an energy range of 3 keV to 20 MeV. The spaceship rotates around an axis parallel to the RMC axes at about 15 rpm providing modulation of the signals from the detectors that produces a set of Fourier elements, each half rotation, that can be decoded into an image, a process which has already produced the first γ-ray image of a solar flare (Hurford et al. 2003). Additionally, these detectors have an energy resolution of about 1 keV allowing high resolution spectroscopic

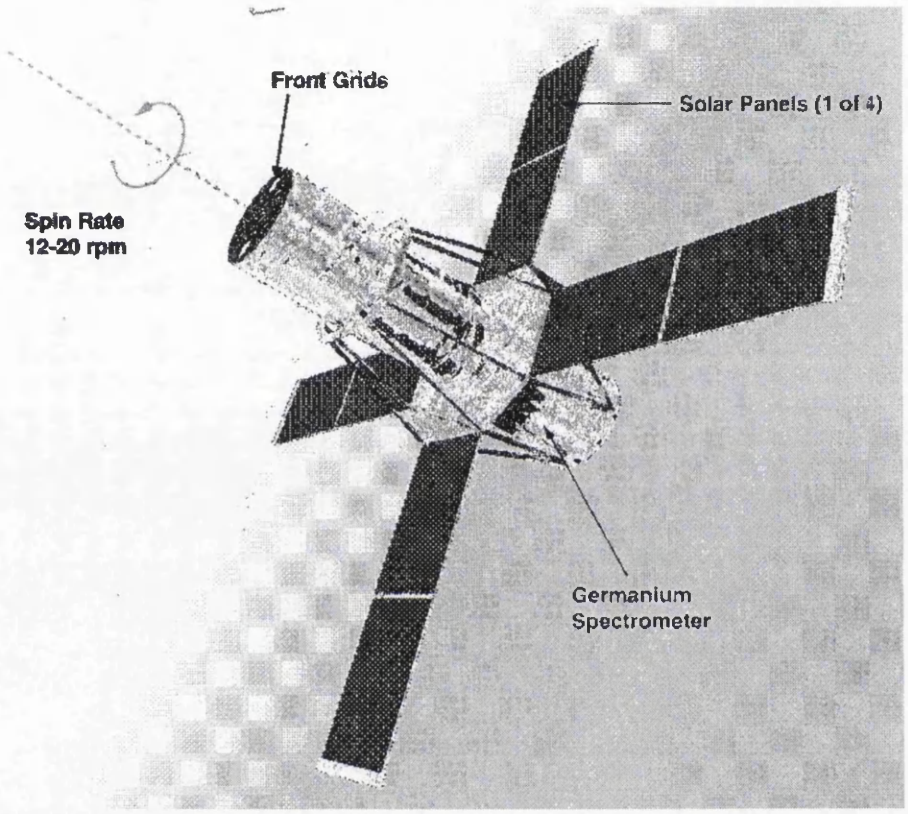

Figure 1.15: The Reuven Ramaty High Energy Spectroscopic Solar Investigator spacecraft, showing the instrumentation and the axis of rotation which enables Fourier decoding of image data.

observations, too. Although not as sensitive as the CGRO instruments, RHESSI should give much finer spectroscopic resolution provided a strong enough source is observed.

Chapter 2

γ-ray Spectroscopy of Solar Flares

2.1 Introduction

Interpretation of γ-ray spectra requires some supporting work, not least the observations of the spectra themselves. I have already reviewed the sources of solar γ-ray data, in Section 1.10. Before moving on to consider how the observed γ-ray nuclear line spectra can tell us about the acceleration of ions in a solar flare, in Chapter 3, I now look at the work that supports modelling of nuclear emission lines, namely measurement of nuclear excitation cross-sections (Section 2.3) and determining nuclear species abundances in the γ-ray source (Section 2.4).

2.2 A γ-ray Spectrum

A solar γ-ray spectrum is a complex set of data with contributions from a number of sources. Figure 2.1 shows a spectrum recorded by the Oriented Scintillation Spectrometer Experiment on the Compton Gamma Ray Observatory (Murphy et al. 1997). The overall downward slope towards higher energy is due to the bremsstrahlung emission from accelerated electrons. This can often be approximated by a single power law with photon energy (Murphy et al. 1990b, 1997). However this does not completely describe the γ-ray continuum. There is also a large contribution from accelerated heavy ions which produce doppler-broadened lines that merge into a continuum between $\sim$0.5 to $\sim$8 MeV, also visible in Figure 2.1. These heavy ions are excited in collisions with ambient protons and α-particles to produce prompt deexcitation lines, either from excited states of the original nuclei or by spallation to another species (Kozlovsky et al. 2002; Ramaty et al. 1979). In principle, these broad lines could provide information about the acceleration of ions but, in practice, any one broad line is difficult to extract

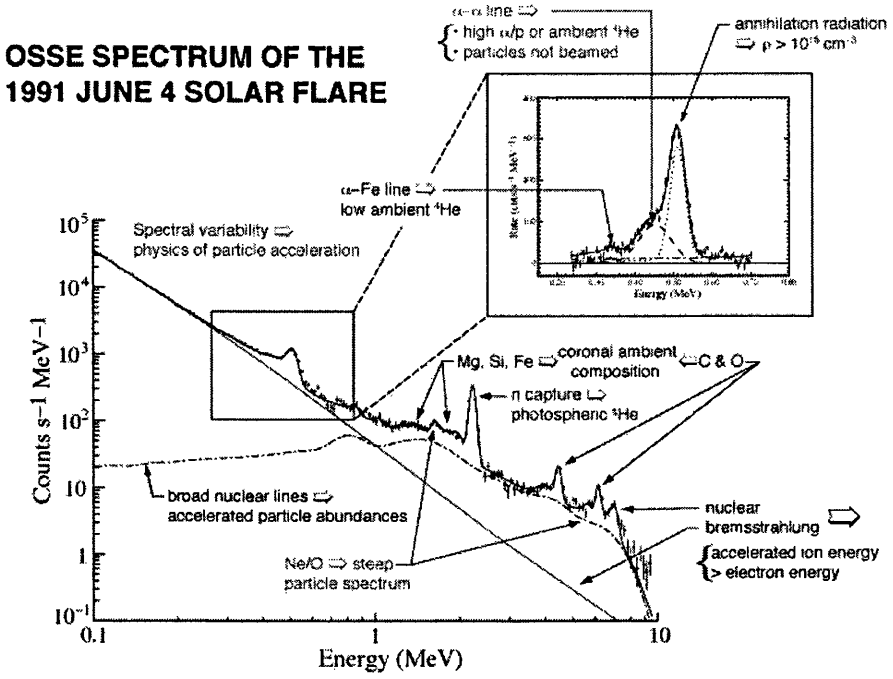

Figure 2.1: OSSE spectrum from the 4 June 1991 solar flare (Murphy et al. 1997).

from the rest of the continuum (Murphy et al. 1990b, 1991).

On top of the broad lines there are the narrow nuclear deexcitation lines. These are produced from the same excited nuclear states as the broad lines, but the excited nuclei are in the ambient medium and the collisions are with protons and α-particles in the accelerated material (see Chapter 3). The heavier ions absorb all of the collision energy and there is very little broadening. This part of the spectrum is of interest in examining the energies of the light accelerated ions (protons and α-particles) and the abundances of the heavy ambient ions in the source regions (Ramaty et al. 1996b).

There are two other features of interest. Fast neutrons are produced in the flare, probably from accelerated protons with energies greater than 30 MeV in interactions with He, C, N and O, and they can be captured on ambient hydrogen to produce strong emission at 2.223 MeV (Murphy et al. 1997; Murphy 1985; Dolan & Fazio 1965). This is clearly visible in Figure 2.1. Also radioactive nuclei and pions produced in the nuclear interactions can decay to make positrons. These annihilate to produce line emission at 0.511 MeV and a continuum to the lower-energy side of this line (Murphy 1985; Murphy et al. 1997). The inset in Figure 2.1 shows the profile of this feature.

2.3 Cross-sections

The γ-ray line spectrum observed in solar flares is due to the prompt de-excitation of nuclei excited in collisions with highly energetic (1-20 MeV) accelerated ions, chiefly protons and α-particles. The excitation of a given nucleus will depend on the energy of the incident particle and the cross-section for exciting the nucleus to the required energy state. If we consider a single incident particle and its journey along path $r(t)$ through a region filled with target nuclei of type x, we obtain Equation 2.1.

$$\phi = \int_0^{t_{th}} \sigma(E(t))n(r(t))a_x v(E(t))dt \tag{2.1}$$

where ϕ is the photon yield per particle, t_{th} is the time when the particle runs out of sufficient energy to excite the nucleus, $\sigma(E)$ is the energy-dependent cross-section for excitation of nucleus x by the particle, n is the hydrogen density, a_x is the relative abundance of nucleus x and $v(E)$ is the speed of the particle. As already mentioned, there is no reason why a_x should not vary with $r(t)$, too, but this introduces another layer of complexity.

We cannot know the energy of every individual accelerated ion. Yet, we can say something about the distribution of these ions with energy. So, provided all of the incident particles follow sufficiently similar energy histories, with energy decreasing monotonically with time, i.e. cooling always outweighs any heating effects, Equation 2.1 can be usefully integrated over all incident particles to arrive at a total line fluence. This is the case where the fast ions encounter a cooler target region such as the cold, neutral target discussed in Section 3.3, but a warm target could complicate the issue. In Chapter 4, we take a statistical approach to this, but there is room for some refinement in dealing with, for example, protons that are occasionally warmed-up by the target, increasing in energy again.

Obviously the energy distribution of the exciting particles is what we would like to measure using the gamma spectrum. The cross-section comes from the nuclear physics laboratory and it is the availability and quality of the cross-sections that ultimately limits the usefulness of gamma-ray spectra as astrophysical tools.

2.3.1 Cross-section Modelling

Carlson et al. (1985) outline the general parameters of a nuclear excitation cross-section. The incident particle has charge ze and centre-of-mass energy E. It interacts with a nucleus that has charge Ze and mass number A. The relative motion of these two objects can be characterized by its reduced wavelength $\overline{\lambda}$ and radius parameter r_0. This is sufficient to express the geometry of the interaction. Effectively the size of the target, r_0 is not entirely independent of energy. A further parameter, T, the nuclear transparency which depends on the mean free path of the incident particle within the nucleus, expresses the energy dependency. In these terms a generic expression for $\sigma(E)$ can be derived.

$$\sigma(E) = \pi(r_0 A^{1/3} + \overline{\lambda}(E))^2(1 - \frac{zZe^2}{r_0 A^{1/3} E})(1 - T(E)) \tag{2.2}$$

The values for the parameters r_0 and T are derived from observations made in the laboratory of the particular excitation of interest. Equation 2.2 is solved with T set to zero, using experimental measurements of σ. The largest r_0 derived in this way is taken as the constant value for that particular nucleus. With r_0 known, values of $\sigma(E)$ can be calculated at any given E, with T still set to zero. This gives σ values for a completely absorbing 'black' nucleus. Experimental values are then compared and the difference between these and the 'black' nucleus values allows T, the nuclear transparency, to be derived.

This expression does not show how the Coulomb barrier reduces the cross-section at lower energies, producing a low-energy cut-off. However it does model how the cross-section increases steadily with increasing energy up to a broad maximum, often around 10 to 20 MeV, and then slowly drops to a minimum above 100 MeV (see Figures 2.3 and 2.4 for examples of real cross-sections and, also Appendix B for detailed digitizations.).

Deb & Amos (2003) have derived an empirical model which can be used to calculate good approximations to measured cross-sections up to incident particle energies of 300 MeV, useful for interpolating between the measured values. They calculate the total reaction cross-section as a sum of partial cross-sections $\sigma_l(E)$.

$$\sigma_l(E) = \frac{2l+1}{1+e^{(l-l_0)/a}} + \frac{\epsilon(2l_0+1)e^{(l-l_0)/a}}{(1+e^{(l-l_0)/a})^2} \tag{2.3}$$

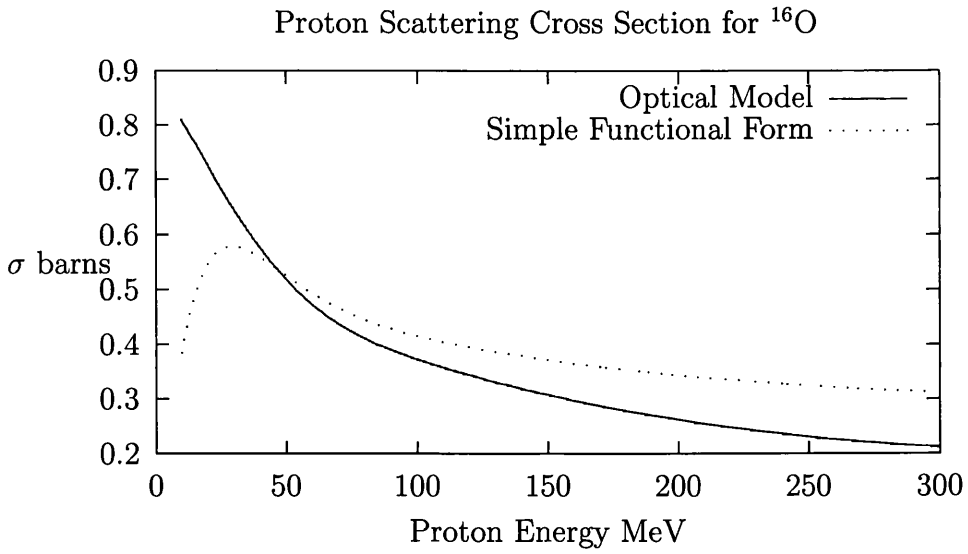

Figure 2.2: Calculated total scattering cross-sections for protons interacting with ^{16}O nuclei from Deb & Amos (2003). These include all excitations of the nucleus.

The functions $l_0(E, A)$, $a(E, A)$ and $\epsilon(E, A)$ are smoothly varying functions of particle energy E and nuclear mass A. An upper limit is chosen for l so that the chosen functions give a σ close to the known high energy limit and the other parameters set to give a close fit to the observed values of $\sigma(E)$ for a given scattering reaction, while maintaining as smooth a variation with E as possible. Deb & Amos (2003) set ϵ to be a constant, independent of E and A, and choose $a(E, A) \sim 1.02k - 0.25$, with $k = \frac{1}{\hbar c}\sqrt{E^2 - m^2c^2}$. This leaves a choice for $l(E, A)$ to match the particular measured values for the given reaction.

A more physical approach produces the 'optical' model (e.g. Carlson et al. 1985; Arellano & von Geramb 2002). This takes its name from the optical potential U used to describe the collision between the incident particle and the nucleus viewed from their centre-of-mass reference frame. The optical potential can be expressed in momentum space as shown in Equation 2.4.

$$U(\mathbf{k}', \mathbf{k}; E) = \sum_{\alpha \leq \epsilon_F} \int \int d\mathbf{p}' d\mathbf{p} \phi^{\dagger}_{\alpha}(\mathbf{p}') \times \langle \mathbf{k}'\mathbf{p}'|T(\Omega_{\alpha})|\mathbf{k}\mathbf{p}\rangle_{A+1} \phi_{\alpha}(\mathbf{p}) \qquad (2.4)$$

ϕ_{α} represents the wave functions of the nucleus ground state at energies ϵ_{α}, where α is limited to below ϵ_F, the Fermi surface. The T matrix describes the system at the starting energy Ω_{α} and its exact form is chosen depending on the energy range required of the incident particle. Arellano & von Geramb (2002)

have recently extended this into the relativistic regime to be able to predict cross-sections at incident particle energies up to 1.5 GeV. They have been successful in producing theoretical cross-sections which match laboratory data up to energies of 600 MeV for a number of nuclei under neutron scattering. Figure 2.2 shows the energy dependence of these two models. The cross-sections calculated by Deb & Amos (2003) are total scattering cross-sections including all of the excitations of the target nucleus. However, the general shape of their 'simple functional form' is clearly similar to the actual cross-sections shown in figures 2.3 and 2.4. The optical model works from the peak cross-section up to higher energies.

At higher energies, we need to consider the integrity of the target nucleus under such heavy abuse. At a few tens of MeV energies, the target reacts with the accelerated ion to produce a different excited nucleus which then contributes to another γ-ray line. Examples of such spallation line contributions are shown in Figure 2.5. The cross-section for fission of the nucleus under bombardment by the incident particles is a similar shape to the excitation cross-section (Guessoum & Gould 1989). However it rises more slowly above the Coulomb barrier energy and break-up of nuclei does not dominate over excitation until much higher energies, above 100 MeV where the excitation cross-section is not so sensitive. Data show that the excitation cross-section is tailing off at these energies for all nuclei investigated so far (Ramaty, Kozlovsky, & Lingenfelter 1979; Kozlovsky, Murphy, & Ramaty 2002). Optical models (Arellano & von Geramb 2002; Deb & Amos 2003) show cross-sections that appear to level off asymptotically to a low, constant value at higher energies and the utility model of Deb & Amos (2003), which is a good fit to the data, drops off monotonically at high energies. The effect is to reduce emission from higher energy excitations. In practice, we cut off the cross-section beyond 1 GeV. This produces an error of no more than 5% in the calculated line emission.

This is not the whole story. We see here that nuclear fission is a possible outcome of interaction between accelerated particles and nuclei. It is possible to populate the excited state of one nucleus by transmutation of another nucleus in just such a spallation reaction. This makes some deexcitation lines more useful than others. Figure 2.5 shows six different cross-sections which will populate the 4.438 MeV excited state of ^{12}C. Two of these involve carbon itself and are due to

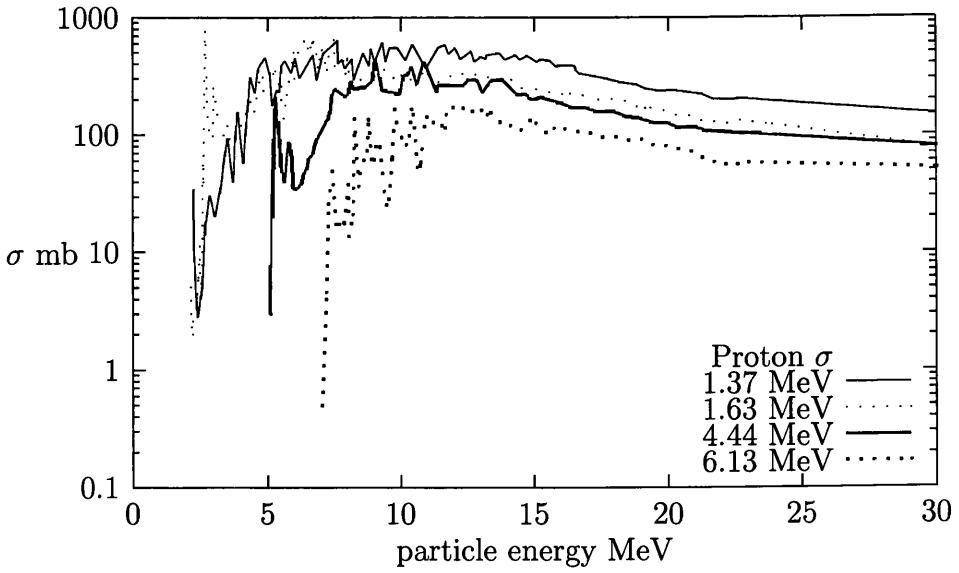

Figure 2.3: The energy-dependent cross-sections for γ-ray excitation of ^{24}Mg at 1.37 MeV, ^{20}Ne at 1.63 MeV, ^{12}C at 4.44 MeV and ^{16}O at 6.13 MeV by protons.

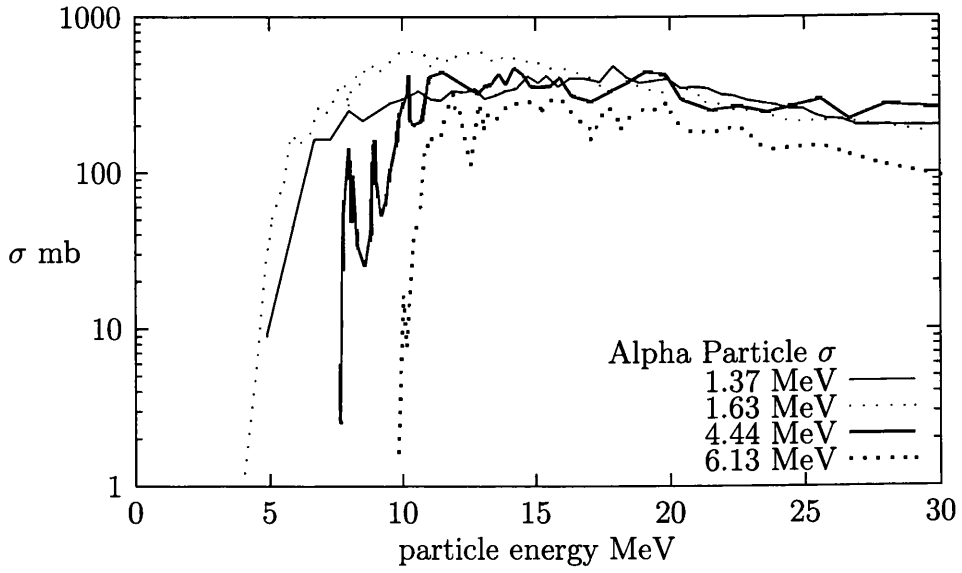

Figure 2.4: Energy-dependent cross-sections as in 2.3 except that excitation is caused by α-particles.

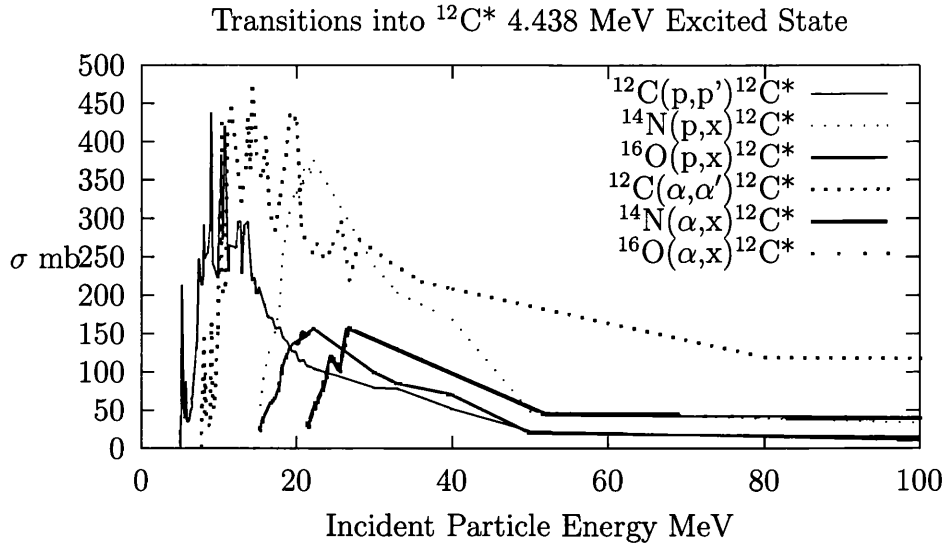

Figure 2.5: Excitation cross-sections for ^{12}C, ^{14}N and ^{16}O that all lead into the excited state of ^{12}C responsible for the 4.438 MeV prompt deexcitation line. These result from collisions with protons and α-particles.

direct excitation by protons and α-particles. The other routes to this state come from ^{14}N and ^{16}O which can both be converted to excited carbon by interaction with protons and α-particles. Although abundances of nuclear species are usually tabulated in terms of relative abundance to ^{12}C, it is often better to convert these to a less contaminated reference line such as the 6.13 MeV ^{16}O line when trying to decipher the information in a γ-ray spectrum.

In general, while much progress is being made in theoretical cross-sections and in semi-empirical models, the best available are those taken from experiments in the laboratory. These are what we use at present, informed by the models when we find gaps in the data.

2.3.2 Laboratory Measurements

A good review of cross-sections for the most useful astrophysical lines was written by Ramaty, Kozlovsky, & Lingenfelter (1979) with a recent update by Kozlovsky, Murphy, & Ramaty (2002) which features machine-readable cross-section data in the electronic edition of the journal. As presented in these papers, the cross-sections are in fairly low energy-resolution to enable their use in Ramaty's Monte Carlo code, which is available on the Internet (Ramaty 2002). This has the

advantage of allowing statistical fits to data of complete spectra including many lines and the continuum.

However, if a more detailed study of the conditions affecting one or two lines is required, the original cross-section data is of much higher energy-resolution and the high-resolution cross-sections used in this present work are listed in Appendix B. Figures 2.3, 2.4 and 2.5 show examples of this cross-section data. Much of this was produced by Dyer, Seamster and their collaborators (Dyer et al. 1981; Seamster et al. 1984; Dyer et al. 1985) by bombarding various target species with a beam of protons or α-particles and observing the emitted γ-rays.

An accelerator was used to produce a beam of protons or α-particles that was directed at the target. The target material was mounted in a thin-walled aluminium chamber. Gas targets were held in a small gas cell within the chamber. Great care had to be taken in measuring the purity of the target materials so that the cross-section for a single isotope could be measured. The emitted γ-rays were detected by lithium-doped germanium detectors, sensitive to the range 0.8 to 12 MeV. Two of these detectors could be moved around the target on rails to gather measurements over a sufficient range of angles to integrate a complete cross-section. The detectors were masked by lead absorbers to reduce counts from x-rays and lower-energy γ-rays. Using this method, cross-sections were obtained in the energy range 2 to 24 MeV (Dyer et al. 1981; Seamster et al. 1984).

Cross-section measurements have been obtained at higher energies by Lesko et al. (1988) and Carlson et al. (1985), using a similar bombardment method. Their cross-sections have lower energy resolution but cover the range 8 to 50 MeV.

At higher energies than these, the data is sparse but some additional points can be found. For example, Neu et al. (1989) investigated α-bombardment of ^{24}Mg, measuring the spectrum of scattered α-particles. A beam of α-particles was directed at a ^{24}Mg target and the reflected α-particles measured by a multi-gap magnetic spectrograph (Enge 1979). By modelling the scattering it was possible to derive the cross-section (Neu et al. 1989). This provided cross-section measurements between 22 and 120 MeV.

2.3.3 Filling The Gaps

Given the enormous effort that has to go into measuring cross-sections it is no surprise that the current catalogue is incomplete. Nuclear physicists have concentrated their efforts on nuclei that produce bright emission and are most often observed in astrophysical contexts. However one should be aware of the gaps in our current knowledge when attempting to use them.

Many excitation cross-sections have never been measured while their contributions to γ-ray lines are known to exist. In these cases, nuclear theory is invoked and a cross-section is created by scaling a measured cross-section that should be similar.

An example of this is the case of the very useful ^{4}He lines at 0.429 and 0.478 MeV (Kozlovsky, Murphy, & Ramaty (2002); Murphy et al. (1990a); Ramaty, Kozlovsky, & Lingenfelter (1979)). The 0.429 MeV line arises from the first excitation state of ^{7}Be. This state is populated by the nuclear reaction of an α-particle on a ^{4}He nucleus producing a neutron and a ^{7}Be nucleus in the excited state. The usual notation expresses this as $^4He(\alpha,n)^7Be*0.429$. However the same reaction also produces ^{7}Be in its ground state and the cross-section has only been measured for the total production of ^{7}Be (King et al. 1975, 1977) between 39 and 140 MeV.

The 0.478 MeV line arises from the first excited state of ^{7}Li. This can be populated by two different routes. There is a 'prompt' reaction $^4He(\alpha,p)^7Li*$ 0.478, that takes place on a similar timescale to the de-excitation that produces the γ-ray line and also produces ground-state ^{7}Li, and a delayed route through the slow decay of ^{7}Be to the first excited state of ^{7}Li. This decay takes about 77 days and 10.5% of the beryllium decays to this state of lithium. This ^{7}Be also comes from the reaction described above which produces both ground-state and first-excited-state ^{7}Be. With solar abundances, there is a negligible amount of ^{7}Li and ^{7}Be that is also produced from carbon, nitrogen and oxygen. So these reactions are ignored.

Collisions between α-particles and ^{4}He also produce ^{7}Li in its ground state and a total cross-section for both reactions has been measured for α-particle energies between 37 and 620 MeV (Slobodrian & Conzett (1982); King et al. (1975, 1977);

Mercer et al. (2001)). However, the cross-section of interest that produces the excited state has only been measured between 37 and 50 MeV (Slobodrian & Conzett (1982) and King et al. (1975, 1977)). The cross-section at higher energies is assumed to be in the same ratio to the total cross-section as the highest four energies actually measured. It is taken as energy-independent and so the desired cross-section is extended to a useful range (Kozlovsky, Murphy, & Ramaty 2002). This is important when we are modelling lines excited by α-particles with a very 'hard' energy spectrum (a spectrum with a very flat dependence on particle energy) as the contribution from high energy interactions is greater.

The delayed line cross-section can be inferred from the measurement of the total cross-section for ^{7}Be production (ground state and first excited state) measured by King et al. (1975, 1977) and Mercer et al. (2001). Since the excited state of ^{7}Li is produced 10.5% of the time, this ratio is used to calculate the delayed component of the line (Kozlovsky, Murphy, & Ramaty 2002).

This is all worrying enough and would be something to be concerned about in analyzing the 0.478 MeV line. However, early detections of these lines in solar flares cannot resolve the two lines one from another. See for example the analysis of Solar Maximum Mission data by Murphy et al. (1990a). So we must include the unknown cross-section for $^4He(\alpha, n)^7Be * 0.429$ in any useful model. Since we have the cross-section for total ^{7}Be production (King et al. 1977; Mercer et al. 2001) we assume that the ratio for production of the first excited state is the same for ^{7}Be as it is for ^{7}Li and create a 'theoretical' cross-section that can be used (Kozlovsky, Murphy, & Ramaty 2002).

Similar reasoning has to be applied to a number of other reactions that are important for understanding the creation of γ-ray spectra. So workers in this field watch the nuclear physics literature closely and try to work with nuclear physicists whenever possible.

Most of the structure in the cross-sections is to be found in the range 2 to 20 MeV, but it is important to know how they behave at higher energies and Kozlovsky, Murphy, & Ramaty (2002) cite many individual measurements at higher energies up to, for example, 1 GeV (Alard 1974). These allow some extrapolation to account for the contribution from higher energy protons and α-particles. However, when the number of accelerated ions falls off with higher energy, the 2

Nucleus	*Coronal*[1]	*Photospheric*[2]	*Solar Energetic Particles*[3]	$\gamma - rays$[4]	$\gamma - rays$[4a]
H	$\equiv 1$	$\equiv 1$	–	$\equiv 1.00 \pm 0.138$	$\equiv 1.00 \pm 0.139$
^4He	0.1	0.1	–	0.1 ± 0.014	0.1 ± 0.014
^{12}C	5.75×10^{-4}	3.72×10^{-4}	2.90	$(12.12 \pm 2.42) \times 10^{-4}$	$(9.26 \pm 1.76) \times 10^{-4}$
^{14}N	1.72×10^{-4}	1.15×10^{-5}	0.81	$(1.58 \pm 6.18) \times 10^{-4}$	$(2.13 \pm 4.44) \times 10^{-4}$
^{16}O	13.91×10^{-4}	8.70×10^{-4}	6.50	$(29.09 \pm 3.27) \times 10^{-4}$	$(21.94 \pm 2.50) \times 10^{-4}$
^{20}Ne	1.90×10^{-4}	1.26×10^{-4}	0.84	$(12.0 \pm 1.93) \times 10^{-4}$	$(8.43 \pm 1.39) \times 10^{-4}$
^{24}Mg	2.64×10^{-4} ★	0.39×10^{-4}	1.23	$(5.58 \pm 1.94) \times 10^{-4}$	$(3.24 \pm 1.20) \times 10^{-4}$
^{28}Si	2.47×10^{-4} ★	0.36×10^{-4}	$\equiv 1$	$(7.64 \pm 2.06) \times 10^{-4}$	$(4.82 \pm 1.39) \times 10^{-4}$
^{56}Fe	3.10×10^{-4} ★	0.48×10^{-4}	0.99	$(5.09 \pm 1.58) \times 10^{-4}$	$(3.43 \pm 1.11) \times 10^{-4}$

Table 2.1: Compiled abundances from different sources. (1) Murphy et al. (1991); VanHollebeke et al. (1990); Breneman & Stone (1985) but Ramaty et al. (1996a) use the values from Reames (1995) for those marked ★. (2) Murphy et al. (1991); VanHollebeke et al. (1990); Anders & Grevesse (1989). (3) Meyer (1985a). (4) Best fit from Murphy et al. (1991), giving equal numbers of accelerated α-particles and protons, renormalized relative to H. (4a) Murphy et al. (1991) with accelerated α-particle to proton ratio set to 0.5. ^{4}He abundances are uncertain (e.g. Meyer 1993) and are set to the cosmic value of 0.1 here, and used to infer the coronal H abundance for which evidence is conflicting. This is supported by Share & Murphy (1998) who find that γ-ray spectra (which tend to be more coronal in relative abundances) are consistent with a photospheric abundance of 8% in the ambient medium, although accelerated ^{4}He might be enhanced in some flares.

to 20 MeV part of the cross-section dominates the γ-ray emission. Figures 2.3, 2.4 and 2.5 show example cross-sections for ^{24}Mg, ^{20}Ne, ^{12}C and ^{16}O derived from the sources above. Note that there is a much higher cross-section value in the lower-energy ranges and it falls off to higher energies, features reproduced by the optical model and the simple functional form of Deb & Amos (2003). Appendix B lists all of the cross-section data used in the work presented here.

2.4 Ambient Particle Abundances

A difficulty in forward-modelling γ-ray spectra lies in deciding on an appropriate elemental composition for the medium in which the lines are produced. Clearly

it is more difficult to establish the effects of the underlying accelerated particle spectrum if the relative contribution to the emission from the different ambient nuclei is unknown.

2.4.1 Supporting Abundance Measurements

There are a number of circumstantial leads that can be followed to try and construct a model of abundances in the flare region. These come from spectroscopic studies of the solar corona and photosphere and from solar wind studies and solar energetic particle observations. Solar energetic particles are usually referred to by the acronym SEP but some authors use this to mean 'solar energetic protons.' So read with care. They are ejected from the Sun during flares and can be detected by spacecraft (Slocum et al. 2003; Mason et al. 2002; Cane et al. 2003; Reames et al. 1990; VanHollebeke et al. 1990; Cliver et al. 1989; Kahler et al. 1984; von Rosenvinge et al. 1978,and see Section 1.10.3) if the interplanetary magnetic field is favourable for connecting the emission event to the spacecraft. The SEP work has led to classifications of flare events according to the abundances of protons and ^{3}He in the emitted particles. Large proton flares (LPFs) are distinguished by an overabundance of accelerated protons in the SEP and are often lengthy events with a large gradual phase. ^{3}He-rich events are characterized by an enhanced ^{3}He/^{4}He ratio and tend to be smaller flares, dominated by the first impulsive phase (e.g. VanHollebeke et al. 1990; Murphy 1985). Reames (1999) shows that SEPs detected in the gradual events are likely to be from coronal material pushed out in Coronal Mass Ejections (CMEs) which are associated with flares but driven by a shock wave. Actual flare material may only be present in SEPs from ^{3}He-rich, impulsive events.

Compositions for the transition zone and corona can be derived from extreme ultra-violet (EUV, e.g. Feldman et al. 1998; Sheeley, Jr. 1996; Spadaro et al. 1996; Noci et al. 1988) and X-ray spectroscopy (e.g. Parkinson 1977; Veck & Parkinson 1981; Schmelz et al. 1996). These observations are also made from spacecraft, to gain access to these higher-energy portions of the electromagnetic spectrum. Spacecraft also investigate the solar wind, capturing material in foil detectors or electrostatic analyzers (e.g. Bame et al. 1975, 1979; Kunz et al. 1983). Foils were also exposed on the Moon by Apollo astronauts and these have been

analyzed to investigate solar wind composition, as have lunar soil samples that they brought back to Earth (e.g. Wieler & Baur 1995, and Sections 1.10.1 and 1.10.3).

There is a very useful review by Meyer (1985a) which pulls together the SEP data available to that date, for events in which no ^{3}He enhancement is observed, and establishes a baseline set of relative abundances for SEP material. There is a companion review (Meyer 1985b) that also covers solar wind and solar corona compositions and compares these with the galactic cosmic ray composition. These provide a good set of models as a starting point in analyzing the flare region and some of these are listed in Table 2.1. However we have to keep in mind that we do not know whether the flare γ-ray source has the same chemical composition as any of these other sources.

2.4.2 Abundances from γ-ray Spectra

Murphy et al. (1991) examined the γ-ray spectra of the 27 April 1981 flare observed by the Gamma Ray Spectrometer on SMM. They attempted to find the abundances of the major γ-ray emitting nuclei in the ambient medium and did this by making a statistical investigation of model fits to the γ-ray spectrum and looking at the best fit for the narrow lines based on a range of assumed abundance ratios (Murphy et al. 1990b,and see Chapter 3). They assumed a cold, thick target and modelled the continuum and the broad and narrow emission lines. This method has difficulties with deciding the composition of the continuum and subtracting it and this is the main contribution to uncertainties in the results.

There were 23 parameters in all in their model which included 16 different relative abundances between the ambient medium and the accelerated ions, two normalization parameters that scaled these to actual abundances, fluxes for the neutron capture line and positronium feature, two parameters to fix the bremsstrahlung continuum and a last parameter which fixed a Bessel function for the accelerated ion spectrum. They attempted five cases. One was a completely free fit to the data allowing all parameters to vary until a χ^2 parameter is minimized. Two fixed the relative abundances in the ambient medium to known photospheric (Anders & Grevesse 1989) or chromospheric (Breneman & Stone

1985) values and varied everything else. A fourth fixed only the abundance ratios within the accelerated ions, to tie down the continuum model, using spacecraft SEP measures from a large proton flare (Breneman & Stone 1985,LPF,). Finally, they fixed both the ambient and accelerated ion abundances to photospheric and LPF values, respectively.

None of the assumed abundance ratios produced particularly good fits and the best results were achieved with the free fit, particularly when there were a lot of α-particles in the accelerated ions, as much as there were protons. This quantity of αs was much more than had ever been observed in SEP investigations and Murphy et al. (1991) backed off from this extreme value and attempted a fit, which was almost as good, with half as many α-particles as protons in the accelerated ions (but see Toner & MacKinnon 2004,and Chapter 5). Their best-fit ambient abundances, and the best fit with half as many accelerated α-particles, are shown in Table 2.1, these are their Case 1 and Case 1a. Note that the closest matched sets of abundances are Case 1a with coronal, but ^{16}O and ^{20}Ne are still overabundant. Murphy et al. (1991) conclude that the flare emission is mostly located in the chromosphere, but this particular extended flare could have had significant emission from the corona too.

An anomalous abundance of ^{20}Ne has been observed by other methods too, where photospheric abundances are taken as normal since they match up with abundances observed outside the solar system, in our Galactic neighbourhood (e.g. Meyer 1993). Ironically, ^{20}Ne abundance is not directly observable in the photosphere, which is too cool to excite ^{20}Ne emission (Sheeley, Jr. 1996), but is inferred from other events which appear to involve photospheric material, by virtue of the other elemental abundances observed, for example in erupting prominences or very compact flares (again reviewed by Meyer 1993). Flare-to-flare variations in the abundances of elements seem to be characterized by two groups of elements distinguished by their first ionization potential (FIP). If we divide elements into low-FIP (< 10 eV) and high-FIP (> 11 eV), there is a consistency between flares of abundances within each group, but the low-FIP to high-FIP abundance ratio can vary by anything up to a factor of four from one flare to another (Share & Murphy 1995; Ramaty et al. 1995; Marsch et al. 1995). However, ^{20}Ne, which should belong with the high-FIP group (21.6 eV), can show large

abundance variations relative to the high-FIP elements. Large variations in ^{20}Ne abundances are not isolated to solar flares and are seen in all solar abundance investigations, for example, in EUV spectra (Sheeley, Jr. 1996,finds ^{20}Ne abundance enhanced over sunspot umbras and reduced over sunspot penumbras), in X-rays (Schmelz et al. 1996,find a factor of two variation above and below high-FIP values, even in quiescent active regions), SEPs (e.g Meyer 1993,reviews high ^{20}Ne abundances possibly due to preferential acceleration) and in the solar wind (Kunz et al. 1983,find a factor of two enhancement over coronal values).

Ramaty et al. (1996b) attempted to derive self-consistent particle abundances from all nineteen of the SMM γ-ray spectra. Assuming a thick, cold target (see Chapter 3), they calculated line ratios for the 2.22 MeV / 4.44 MeV line fluences (neutron capture and ^{12}C emission) and used the SMM data with these to derive a power-law energy spectrum for the accelerated ions. This was possible with nine of the SMM flares that had strong 2.22 MeV emission. With this fixed, only relative abundances of the accelerated ions and the target species are then required to model the measured emission fluences. In particular, they wanted to investigate whether ^{20}Ne is actually overabundant in the flare region as appears to be the case in the previous analysis of Murphy et al. (1991).

Concentrating on the ratio of the 6.13 MeV to the 1.63 MeV lines due chiefly to ^{16}O and ^{20}Ne, they tried to fix a value of the ^{20}Ne/^{16}O abundance ratio that was consistent with the rest of the spectrum. There is a small contribution to these lines from ^{24}Mg and ^{28}Si and they set these abundances and those of all other species save ^{20}Ne equal to coronal values taken from Reames (1995), following on from the findings of Murphy et al. (1991). This leaves just the shape of the accelerated ion spectrum and the relative abundance of α-particles and protons in the accelerated ion stream. The power-law slope for the accelerated ions could be calculated from the ratios of the 6.13 MeV and 1.63 MeV lines, the 4.44 MeV (^{12}C which has the same relative abundance in coronal and photospheric measurements) and 1.63 MeV lines, and the 2.22 MeV and 4.44 MeV lines, assuming various values for the ratio of accelerated αs to protons and for the relative abundance of ^{20}Ne. With three sets of data constraining the calculations, a self-consistent value for the remaining two parameters emerged. The nine SMM flares that were eligible for this analysis constrained the models to give an

average relative abundance of $^{20}Ne/^{16}O$ of 0.25 with αs/protons between 0.1 and 0.5, which really is enhanced over coronal or photospheric values.

Murphy et al. (1997) employed a similar analysis to Ramaty et al. (1996a) when investigating CGRO/OSSE data from the 4 June 1991 solar flare. Again, an enhanced $^{20}Ne/^{16}O$ abundance ratio of 0.25 provided a self-consistent accelerated ion spectrum with index 4.4 ± 0.3 when the α-particle to proton ratio is 0.5. In Chapters 4 and 5 I explore possible explanations for the bright 1.63 MeV line without resorting to an enhanced ^{20}Ne abundance.

2.5 Energy Distributions

The energy distribution of the incident particles depends on the acceleration mechanism encountered by these particles in the flare. However, since the γ-ray spectrum is the probe of the energy distribution, this information is not available a priori. Ideally we would like to derive the energy distribution directly from observations of the γ-ray lines and with sufficiently good data this might be possible using inverse problem techniques as in the COMPTEL solar flare neutrons data inversion discussed in Chapter 6. This is not yet possible and we need some trial parametric forms to work with initially. Miller et al. (1997) summarize possible particle acceleration processes. These models give clues as to likely accelerated ion distributions.

2.5.1 Stochastic Acceleration

Stochastic acceleration arises in systems where a particle both gains and loses energy on short timescales but will only gain energy on longer timescales. The most important in this context are systems where particles are accelerated by resonance in waves. In the solar atmosphere plasmas, which are threaded by complex magnetic fields, there are many possible sources of waves that are capable of interacting with ions in such a way. Those considered in detail arise in cold magnetic plasmas, in keeping with the assumption of a cold target (Section 3.3 but see Chapter 4 for some discussion on this) and are characterized chiefly by the wave frequency ω and the wave vector $\vec{k}$. Critical values for ω that separate different wave modes are the hydrogen gyrofrequency Ω_H and the electron gyrofrequency Ω_e. We define the Alfvén speed (Dendy 1994) as the root of the ratio

of the magnetic field energy density $\mathbf{B}/\mu_0$ to the mass density ρ

$$\mathbf{v}_A = \frac{\mathbf{B}}{(\mu_0\rho)^{\frac{1}{2}}}.$$

We can now identify a range of electromagnetic modes. For $\omega \ll \Omega_H$, the Alfvén branch has dispersion relation

$$\omega = v_A|k_\parallel|, \tag{2.5}$$

where $k_\parallel$ is the field-aligned component of the wave vector, and the fast mode branch has dispersion relation

$$\omega = v_A k,$$

where k is the magnitude of the wave vector. As ω approaches Ω_H, the Alfvén branch phase velocity approaches zero (producing H^+ electromagnetic ion cyclotron waves) while the fast mode phase velocity increases. For parallel propagation, Alfvén waves are left-hand polarized and all fast mode waves are right-hand polarized. In the range $\Omega_H \ll \omega \ll \Omega_e$, the waves are called whistlers and the dispersion relation is

$$\omega = \frac{k_\parallel^2 c^2 \Omega_e}{\omega_{pe}^2},$$

where ω_{pe} is the electron plasma frequency, the natural frequency at which an electron oscillates in a neutral plasma. When the wave frequency approaches Ω_e, the whistler phase speed approaches zero and the waves are called electromagnetic electron cyclotron waves.

There are also electrostatic modes. When ions drift across the electric field or relative to electrons, lower hybrid waves are generated with frequency

$$\omega_{LH} = \sqrt{1 + \frac{m_p}{m_e}(\frac{k_\parallel}{k_\perp})^2},$$

where $k_\perp$ is the component of the wave vector perpendicular to the field. Electron-ion drift also generates electrostatic ion cyclotron waves with frequency above the ion cyclotron frequency. Langmuir waves are electron plasma waves that originate with streaming electrons and have $\omega = \omega_{pe}$.

Given these waves, we only need a resonant wave-particle interaction and we can start to accelerate the particles by stochastic means. If $v_\parallel$ is the parallel particle speed and Ω is the particle's cyclotron frequency, we can define the frequency mismatch parameter x.

$$x \equiv \omega - k_{\parallel} v_{\parallel} - \frac{l\Omega}{\gamma}, \tag{2.6}$$

where l is a harmonic number and γ is the Lorentz factor for the particle. When the wave has a small amplitude, resonance will occur when $x = 0$. When $l = 0$, Equation 2.5.1 specifies matching between the parallel components of the wave phase velocity and the particle velocity to achieve resonance. This is usually called Landau or Cerenkov resonance. When $l \neq 0$, we have gyroresonance through various harmonics. Equation 2.5.1 then specifies a match between the cyclotron frequency of the particle and its Doppler-shifted wave frequency in the frame of its guiding centre. $l = 1$ gives the most effective gyroresonance, cyclotron resonance.

A particle in resonance with a single low-amplitude wave oscillates across the wavefront in simple harmonic motion that satisfies Equation 2.5.1. There is no net gain in energy. The amplitude and frequency ω_b (the bounce frequency) of this oscillation are both proportional to the square root of the wave amplitude. Equation 2.5.1 does not have to be satisfied exactly for resonance to occur. It is sufficient for $|x| \leq 2\omega_b$. This less-strict requirement for strong resonance is where the stochastic mechanism for acceleration lies. Imagine the situation where two neighbouring waves have overlapping resonance criteria. A particle resonating with the lower-frequency wave will occasionally increase or decrease $v_{\parallel}$. If it manages to increase $v_{\parallel}$ sufficiently it will achieve resonance with the next wave. The jump between waves results in an increase in the particle's energy. A sequence of such jumps can result in a large increase in energy. A discrete wave spectrum makes strong demands on the wave spacing to achieve this energy change, but with a continuous wave spectrum this process is automatic. Over time there are gains and losses of energy but, in the long run, energy is gained by the particles and stochastic acceleration is the result. When amplitudes are low, a broad spectrum of waves is required to accelerate the particles, but a single large-amplitude wave can accelerate particles through its own harmonics.

Miller et al. (1997) summarize a number of combinations of wave modes that can accelerate protons from the higher Boltzmann tail of thermal speeds up to the energies necessary to excite γ-rays. It is quite possible to generate Alfvén waves with small k by reconnection or large-scale perturbations to the magnetic

field. Over a short time these cascade to larger k, capable of accelerating thermal protons. As the initial number of protons that will resonate with the waves is small, damping is negligible. However, as the acceleration process continues, eventually a sizeable population of fast protons emerges and damps the high-k waves out. This releases these protons to the low-k waves for further acceleration. Once the initial acceleration has produced a faster, suprathermal population of protons, these can be accelerated up to GeV energies in timescales as small as 1 to 10 s.

Miller & Roberts (1995) have developed a computer code for this type of mechanism. If they inject about 400 ergs cm^{-3} in the form of Alfvén waves, it takes about 1 s to accelerate more than 3×10^5 protons cm^{-3} to energies above 30 MeV. This gives a consistent proton number for γ-ray emission from a flare in a volume of 10^{27} cm^3 but produces proton energy spectra that are either too soft or too hard to account for the details of nuclear deexcitation lines. However, the form of the distribution is a power law over a wide energy range.

$$N_j(E)dE \propto E^{-\delta}dE \tag{2.7}$$

N_j is the differential density of particle type j with particle energy E, so that $N_j dE$ is the number of particles of type j between E and $E + dE$, and δ is the index, high values indicating a steep spectrum and low values a flatter spectrum.

There may or may not be a lower-energy cut-off in this distribution (e.g. see the shapes of the SEP energy distributions in Sanahuja et al. 1983). Particle energy is expressed here as the energy per particle. In other approaches (Ramaty, Kozlovsky, & Lingenfelter 1979; Kozlovsky, Murphy, & Ramaty 2002) E is taken to be the energy per nucleon for computational convenience. Either approach will work, provided the cross-sections are chosen assuming the same energy units. The slope of the energy distribution given by δ has been taken to be independent of particle type (Ramaty et al. 1979; Murphy et al. 1991; Share & Murphy 1995; Ramaty et al. 1996b), but there is no reason to assume that all particles share the same energy distribution and it is important to realize this when trying to derive particle energies from actual γ-ray line spectra.

The momentum distribution of stochastically accelerated ions can be modelled by a modified Bessel function and this form has been used to derive the

energy spectrum in a number of applications to γ-ray spectra (Ramaty et al. 1979; Murphy 1985; Murphy et al. 1988, 1990b, 1991; Share & Murphy 1995).

$$\bar{N}_j(p_j) \propto K_2(2(\frac{3p_jc}{m_jc^2\alpha T})^{\frac{1}{2}}) \tag{2.8}$$

where p_j is the particle momentum per nucleon, m_j is the mass of the accelerated particle, α is the acceleration efficiency and T is the escape time from the acceleration region. α is proportional to the square of the relative particle velocity and inversely proportional to the diffusion mean free path. In practice, all parameters except α and T are known and the product αT is taken as the single number which defines the shape of the energy spectrum.

MacKinnon (1991) derives the distribution of accelerated protons with momentum and over time, $f(p,t)$ under acceleration by Alfvén turbulence (fast turbulence mode is not included). Initially the protons are injected isotropically with a uniform energy into some region of the corona, where they encounter a magnetic loop. These are trapped in the magnetic field, where energy is transferred from the turbulence to the fast ion energy. They remain trapped until the pitch-angle scattering time increases to be equal to the loop crossing time at which point they escape into the flare region with their final energy and momentum distribution. MacKinnon (1991) shows that this distribution is dependent on an imaginary Bessel function in momentum.

The benefit of this model is in reducing the spectrum shape to a single parameter αT to replace the index and low-energy cut-off of the power-law, an advantage when a statistical fit to γ-ray data is required and some observations support the use of the Bessel function distribution, particularly measurements of neutron arrival times. However a power law is a better fit to the gamma-ray spectra obtained so far (e.g. Ramaty et al. 1996b). The line due to ^{20}Ne at 1.63 MeV shows up very strongly in most spectra, so that the abundance of ^{20}Ne is very high if a Bessel function or a power law with a moderately high cut-off energy is chosen (Murphy et al. 1991). However, since the cross-section for excitation of ^{20}Ne into this state is unusually sensitive to protons in the few MeV energy range (Figure 2.3) a less severe abundance enhancement is derived from a power law model with a low cut-off energy (Share & Murphy 1995).

Stochastic acceleration also presents a possibility of explaining enhanced abun-

dances of particular ions in the accelerated material. It is possible for gyroresonance to preferentially accelerate an ion species whose cyclotron frequency is close to the frequency of the waves.

2.5.2 Shock Acceleration

Miller et al. (1997) also review shock acceleration. There are two types: drift acceleration and diffusive acceleration (see also Forman et al. 1986). In drift acceleration, the particles move along the shock front and gain energy from the electric field in the shock. This happens quickly but the particles soon escape along the upstream magnetic field. However some turbulence upstream can confine ions sufficiently for acceleration to energies of a few MeV. The effect is still limited because the shock has to move almost exactly perpendicularly to the magnetic field.

Diffusive shock acceleration occurs in fast shocks and is similar to stochastic acceleration in that the particles are accelerated by interaction with moving scattering centres. In this case the scattering centres move towards each other with respect to the shock producing fast acceleration. The effect is quite efficient for ions as they heat up in the shock and then are accelerated quickly upstream. There the hot plasma from the shock stimulates low-frequency electromagnetic waves which are sufficient to further accelerate the ions by resonant scattering. This turbulence also helps trap the ions in the shock allowing them to attain energies of up to 100 MeV in less than 1 s.

We can gather some clues about shock acceleration from solar energetic particle observations and Reames (1999) gives a good review of work on the acceleration of these particles. It is likely that SEPs are actually accelerated in interplanetary shocks driven by coronal mass ejections (CMEs) and not in flares, or, at least, not entirely in flares. However there are good insights here into observational characteristics of shock-accelerated particles.

As reviewed by Reames (1999) a power law energy distribution arises naturally when non-relativistic ions are accelerated in a large-scale planar shock (Forman, Ramaty, & Zweibel 1986; Murphy 1985). The power law index, δ, is given by $(r +^1 /_2)/(r - 1)$ where r is the compression ratio of the shock. This gives a minimum value for δ of $^3/_2$, with r=4. Reames (1999) makes the case, and Miller

et al. (1997) agree, that most gradual events strongly correlate with CMEs and exhibit coronal abundances, and so we can expect that shock acceleration in the corona is highly likely in this class of event. However that does not help with impulsive events, which show significant ion enhancements and rarely occur with CMEs. These probably originate in a more compact zone closer to the chromosphere. The ion enhancements possibly imply a stochastic acceleration method.

Shocks also generate d.c. electric fields which can directly accelerate ions providing a seed population for further acceleration by a different mechanism.

2.5.3 Direct Measurement of Accelerated Ion Distributions

Spacecraft data contain measurements of particle abundances and energies taken directly from the material ejected from the Sun. For example, McDonald & Van Hollebeke (1985) looked at the Helios I energetic particle observations of the 3 and 21 June 1980 solar flares (see also Evenson et al. 1984, for electron spectra). They derived particle energy spectra for protons and electrons. Both particle types appear to follow well-defined power-laws from a few up to 200 MeV, in both of these flares. The protons have a very flat spectrum in the 3 June flare, with an index δ of 1.2, close to the minimum for shock acceleration. In the 21 June event, the index is 2.6. VanHollebeke et al. (1990) looked at other particles in this same data and found power law distributions for helium, carbon, oxygen, neon and iron. In a multispacecraft observation that established the link between the large particle event of 23 to 27 April 1979 and a filament eruption on 22 April, Sanahuja et al. (1983) measured proton energy spectra using ISEE-3. Again these are consistent with power laws, especially above $\sim$200 keV and also later in the event. They also show a low-energy turnover, mid-event, or a discontinuity in the slope $\sim$200 keV. We need to keep this in mind when modelling with power laws. We cannot assume that they continue down to very low energies, with the implication of very large energies in the slower ions.

2.5.4 Energy Distributions from γ-ray Spectra

Most recent work in deriving energy distributions for the accelerated ions assumes a power law because it is mathematically simple and the acceleration models produce distributions not far from this simple function. Theoretical approaches may generate different functions for the accelerated particle spectra but these are then compared with the nearest power law to allow comparison with the data. There is also a distinction between the original energy distribution of the protons injected into the source region predicted by theory and their distribution at the time they interact with the source nuclei. It is only this final distribution that can be inferred from the γ-ray line spectra. We only see what emerges from the acceleration region, not what goes on inside it. Murphy et al. (1991) demonstrate the difficulty of achieving a best fit model γ-ray spectrum to SMM data and, although the current RHESSI instrument should be able to acquire better data, it has yet to observe many flares with strong γ-ray spectra. Therefore, at present, the signal-to-noise ratio of γ-ray spectra does not sufficiently constrain a more detailed choice of function to describe the accelerated particle energy and, even with less noisy data, it is not clear whether the observed lines actually can provide enough information to define the accelerated ion energy distribution. An investigation of the information content of a γ-ray spectrum with regards to constraining the accelerated ion energy would be a useful exercise (Section 7.3).

In order to fix the slope of the power-law spectrum, at least two γ-ray lines are required that sample the accelerated particles at different energy ranges. Figure 2.3 shows the typical energy ranges of the prompt nuclear line excitation cross-sections in the examples of the ^{16}O 6.13 MeV line and ^{12}C 4.44 MeV line cross-sections. Most of the brighter lines have cross-sections that peak for incident protons in the 10-12 MeV range and do not extend below about 6 or 7 MeV, much like the ^{16}O cross-section. The ^{24}Mg line at 1.37 MeV and the ^{20}Ne line at 1.63 MeV are sensitive down to much lower energies. In particular, ^{20}Ne has a resonance down near its cut-off energy at about 3 MeV. So pairing up ^{24}Mg and ^{16}O or, better, ^{20}Ne and ^{16}O can give a relative measure of the numbers of accelerated protons at $\sim$ 3 MeV and $\sim$ 11 MeV, allowing the slope of the proton spectrum to be deduced (Share & Murphy 1995; Ramaty, Mandzhavidze, &

Kozlovsky 1996b). Of course, such a measurement would also require accurate values for the relative abundances of ^{16}O, ^{24}Mg and ^{20}Ne.

Solar flares apparently release energy in various forms and the partitioning of energy between bulk heating, mechanical energy and accelerated particles represents a clue to the nature of the primary energy release process. Observations in the X- and γ-ray domains have a prominent role to play here, as direct signatures of accelerated particles at the flare site (e.g. the recent review of Vilmer & MacKinnon 2003). Specifically, electron-ion bremsstrahlung in the 10s to 100s of keV photon energy range yields information on the distribution of electrons of similar energies, while various line features in the 0.4 - 7 MeV photon energy range bear witness to the presence of ions of energies upwards of a few MeV.

It has been clear for some time that accelerated electrons may embody several tenths of all the energy manifested in a flare (e.g. Hoyng et al. 1976; Lin & Hudson 1976). More recently we have seen claims for a similar, or even greater energy manifested as ions $>$ 1 MeV (Ramaty et al. 1995; Murphy et al. 1997). These have followed particularly from the finding (Share & Murphy 1995) that the 1.63 MeV line from de-excitation of ^{20}Ne nuclei is stronger than expected, a finding that may be understood in terms of a fast ion distribution that declines steeply, as a power-law with energy. The total energy content of such a distribution is determined by the lowest energy for which the power-law form remains valid. The strong 1.63 MeV line, whose threshold energy for proton excitation is lower than most other deexcitation lines, thus points to a high total ion energy, typically to a rough equipartition of energy between electrons and ions (Vilmer & MacKinnon 2003).

Nonetheless some uncertainty over flare ion energy remains, arising from various sources. First, there is the continuing lack of a readily observable, unambiguous diagnostic for ions below 1 MeV.nucleon^{-1}, although the energy manifested as ions above this energy already seems substantial. The central role played by the 1.63 MeV line focuses attention on the source region ^{20}Ne abundance, a quantity which appears to vary significantly with position in the solar atmosphere (Schmelz et al. 1996). Unease over the role of the ^{20}Ne abundance is underlined by the large values implied by interpretation of γ-ray lines (Meyer 1993). Further, it is generally assumed that all accelerated species have the same

distribution in energy per nucleon. Difficult or impossible to verify at the flare site, this assumption is not always borne out even by measurements of flare-associated energetic particles in the interplanetary medium. In the two events studied by VanHollebeke et al. (1990), for instance, α particles consistently displayed a steeper energy distribution than protons, in the 1 to 100 MeV.nucleon^{-1} energy range. The kinematically broadened lines produced by heavier accelerated particles yield little model-independent information on particular species. Some of the consequences of relaxing this assumption will be the main focus of Chapter 5, and I refer to it for brevity as Assumption A:

> Assumption A: the energy distributions of all accelerated species, expressed in energy/nucleon, are identical.

At this point we also introduce a little notation. Let Φ_ϵ denote the fluence (cm^{-2}s^{-1}) of photons in a line at photon energy ϵ (MeV), e.g. $\Phi_{2.223}$ denotes the photon fluence in the neutron capture line, while Φ_{4-7} denotes the total (de-excitation) line fluence in the 4 - 7 MeV range.

Assumption A impacts on the form of deduced energy distribution and the total ion energy content in various ways. First, given a particular value of energy power-law index, deduced from ratios of narrow line fluences, it immediately implies that a large fraction of the total ion energy resides in heavier ion species. For example, in the flare of 4 June 1991 analyzed by Murphy et al. (1997), the total energy in ions, 10^{33} ergs, is about seven times greater than that found in protons alone. At the very least, the consequences for secondary flare emissions and the flare thermal phase have never been investigated in any detail.

The resolvable, narrow lines are produced by interactions involving both fast protons and α particles (e.g. Ramaty et al. 1979). For diagnostic purposes one selects two lines whose production cross-sections have significantly different dependence on exciting species energy. For instance, the photon flux in the 4-7 MeV photon energy range is dominated by various (broad and narrow) de-excitation lines, produced by fast ions of energies above a few MeV.nucleon^{-1}, while production of the neutrons needed to produce the 2.223 neutron capture line tends to be dominated by ions of rather higher energies, typically 50 MeV and above. Thus a measured value of the ratio $\Phi_{2.223}/\Phi_{4-7}$ may be used, with Assumption A,

as a diagnostic of the steepness of the fast ion distribution (e.g. Ramaty 1986). In practice one assumes e.g. a power-law form $E^{-\delta}$ in particle energy E and deduces δ.

By studying the $\alpha - \alpha$ lines at 0.429 and 0.478 MeV, Murphy et al. (1991) found strong evidence for an over-abundance of fast α-particles in some events (see also Share & Murphy 1998). However, neutron production and deexcitation line production cross-sections do not have the same energy-dependences for α's and protons. Thus the possibility of a different fast α-particle abundance forces re-examination of the diagnostic use of $\Phi_{2.223}/\Phi_{4-7}$ - Ramaty et al. (1996b) - with its implications now depending also on the assumed value of α/p, the abundance of fast α's relative to fast protons. The measured values of $\Phi_{0.429}$ and $\Phi_{0.478}$ may corroborate any assumed value of α/p. Relaxing Assumption A, however, would open up the possible parameter space still further. For instance instead of asking, 'given Assumption A and a value of α/p, what single value of δ is consistent with an observed value of $\Phi_{2.223}/\Phi_{4-7}$?', one might instead have asked, 'given two, not necessarily identical values of δ, one for protons and one for α's, what value of α/p is consistent with an observed value of $\Phi_{2.223}/\Phi_{4-7}$?'

As already mentioned, the 1.63 MeV line of ^{20}Ne includes contributions from lower energy protons than most other deexcitation lines. As long as its abundance relative to other species is known with some confidence, its fluence relative to any other, strong deexcitation line then gives another diagnostic for δ, in the 1 - 20 MeV energy range. The 6.13 MeV line of ^{16}O includes only a small spallation contribution from other target species, so $\Phi_{1.63}/\Phi_{6.13}$ gives a good diagnostic (Ramaty et al. 1996b; see also MacKinnon & Toner 2003, where the effects of ion containment in a warm target region are dealt with).

The importance of the lower threshold energy for proton excitation of the 1.63 MeV line was pointed out by Share & Murphy (1995), in the course of trying to understand its surprisingly high observed intensity. They also noted that this line is not distinguished, relative to other lines, for excitation by α's as it is for excitation by protons. So high values of α/p, suggested by the $\alpha - \alpha$ lines, might appear inconsistent with this interpretation of the unexpectedly high values of $\Phi_{1.63}$. In later work (Ramaty et al. 1995, 1996b) it became clear that a high value of α/p is not inconsistent with the observed fluence of $\Phi_{1.63}$, but, along

with Assumption A, it does force δ, and thus the total fast ion energy content, to higher and higher values (for instance, compare the values of $\Phi_{1.63}/\Phi_{6.13}$ for the cases $\alpha/\mathrm{p} = 0.1$ and 0.5 shown in Figure 5.1 in Chapter 5).

Assumption A may well be justified, as it sometimes is for flare-associated particles in the interplanetary medium (Reames et al. 1997). We have seen, however, that its invocation is not justified *a priori* at the flare site. Moreover, if it does not actually apply, its use with diagnostics based on the 1.63 MeV line may over-estimate flare ion total energy content.

In Chapter 5 I investigate the interpretation of observed narrow nuclear line fluences without making Assumption A. Having considered how this affects the properties of some key line diagnostics, I apply these to the flares in the SMM/GRS data set and evaluate the implications to the role of fast ions in the flaring process (see also Toner & MacKinnon 2004).

The exact relationship between the photons we observe and the accelerated particles that provide the energy to produce them is, of course, very sensitive to the nature of the target medium through which they travel and deposit their energy.

Chapter 3

Source Model

3.1 Introduction

In this chapter I consider the region from which the flare γ-ray (and neutron) emission emerges. Fast ions are deposited by the flare explosion into an ambient medium. Interactions between the fast ions and nuclei within the target region excite the nuclei which de-excite in a short time ($\lesssim 10^{-11}$ s) to emit γ-ray photons (Kozlovsky et al. 2002). This work attempts to link the observed γ-ray line spectrum back to the energy put into the fast ions by the flare. The details of how the flare gets its energy in the first place are beyond the scope of this thesis. Somehow changes in the solar magnetic field (see Section 1.3) release large amounts of energy which is transmitted to the ions by one of the methods considered in Section 2.5. The distribution of the fast ions with energy can give clues as to which of these mechanisms might be in operation, or rule them all out. There are a range of diagnostics for these energy distributions and I consider those that can be derived from the γ-ray nuclear lines, in the contexts of different types of source region (Sections 3.2 and 3.3 and Chapter 4).

3.2 Thick and Thin Targets

Consider a charged test particle passing through a region full of target nuclei. Will the test particle use up all of its useful energy before it leaves the target region? By 'useful energy' I mean sufficient energy to excite the required energy state of the target nucleus for emission in the γ-ray line of interest. In the thick target, the effect on the emission of γ-rays is that all of the energy in the test particles that can be is converted into γ-rays. This does not necessarily mean that all of the particle energy has gone into γ-rays as there are more efficient mechanisms for removing particle energy, particularly coulomb scattering on electrons. In

contrast to the thick target, in the thin target, only a negligible amount of the available energy is converted to γ-rays and the test particles emerge with their energy distribution unchanged by γ-emission. The choice of thick or thin target then has consequences for how we model the transfer of energy from fast ions to the γ-emitting nuclei in the target and for how we interpret a particular set of deexcitation lines. I will discuss, in more detail, the mechanisms of energy loss in the next section (3.3) and in Chapter 4.

There are two kinds of interactions that we need to consider here that involve the ions in a solar flare. There is an acceleration mechanism and then the accelerated ions can interact with ambient nuclei to produce the γ-ray line spectrum. Clearly some of the ions escape during the acceleration mechanism and are detected as SEPs. However, if the ions that go on to stimulate the γ-ray emission also escape, they would include spallation products from these nuclear reactions. Expected enrichments in exotic species like deuterium, lithium and beryllium are not observed in SEPs. So it is unlikely that the γ-ray emission region is a thin target, since we see no evidence of ions emerging from this region (e.g. Hua & Lingenfelter 1987c,and references therein).

On another line of evidence, MacKinnon and Brown (MacKinnon & Brown 1989, 1990) investigated the limb-brightening of the γ-ray continuum emission from solar flares (e.g. Rieger et al. 1983; Vestrand et al. 1987). The continuum arises mainly from high-energy electron bremsstrahlung which is most efficient at high source densities. Strong beaming of the bremsstrahlung emission from these relativistic electrons provides a preferential direction for observation: the electrons have to be moving towards us in the line of sight. This will confine detectable γ-ray flares to the limb by one of three possible mechanisms. One possibility is that the electrons seen on the limb have little or no component of their velocity along a vertical section of magnetic flux and are trapped orbiting the field lines and lose all of their energy in bremsstrahlung emission (i.e. a thick target) which we see since the line of sight lies perpendicular to this field at the limb, such a situation on the disk will produce very little emission and go unseen. Secondly, we have electrons bottled in a nonuniform magnetic field. Their motion is all perpendicular to the field at the mirror points. If the field is vertical at these points, the electrons will only have motion in the line of sight

when the flare occurs at the limb. Maximum bremsstrahlung emission occurs at the mirror points and so we detect limb flares preferentially. This is also a thick target since the electrons are bottled until they produce all of their potential γ-ray bremsstrahlung emission, deep in the atmosphere where the field is strongest and the density highest. Thirdly, as we look at events closer to the centre of the disk, the electrons have to be injected more parallel to the field in order to produce emission in the dense part of the source. However, if the pitch angle is too small, the electrons escape the field and we get no returning electrons coming back up out of the source to produce emission in our direction. So disk flares lose their continuum emission in our direction. The limb-brightening effect implies that the continuum source is deep in the densest part of the atmosphere where thick target effects can provide the maximum emission. Otherwise we do not detect the flare in γ-rays at all as is the case for disk flares. Although the accelerated electrons are a different population of charged particles than the ions that stimulate the line emission, they must all be moving along the same field lines and are likely to be producing emission in similar regions of the solar atmosphere.

Ramaty et al. (1995) tried to model the brightest γ-ray emission lines and the neutron capture line at 2.22 MeV and match up their models with nineteen actual SMM spectra. Modelling nuclear excitation and neutron production puts strong restraints on the parameters. They found difficulty in fitting a thick target unless there was enhanced ^{20}Ne abundance in the target (but see Chapter 4 and the effects of a warm target), otherwise the parameters of the model were quite reasonable in light of other sources of abundance measurements such as impulsive and gradual flare abundances. They found that a model of downward-streaming isotropically distributed fast ions moving into a thick target fitted the data well with a range of power-law energy distributions with index (δ, see Equation 2.5.1) between 3 and 5. The thin target presented even more difficulty, with only impulsive flare abundances producing results even near to the observed spectra, in all nineteen flares. Again a downward, isotropic stream of fast ions gave the best results, but it is difficult to square this geometry with thin target conditions. So they concluded that, with the best available set of data (the SMM flares), it is difficult to produce a physically realistic model with a thin target. In this work, I use a thick target model throughout.

Once we have decided whether the target is thick or thin, we then need to decide whether it is 'warm' or 'cold,' by which we mean how the energy of the target particles (giving a 'temperature' although this energy may not be thermal) compares with the energy of the test particles.

3.3 Cold Neutral Targets

As a test particle passes through the target region, it will lose energy. In terms of the γ-ray spectrum we are interested in the energy lost to heavy ions in the target but energy will also be lost in coulomb interactions with lighter particles, the most common being hydrogen atoms. The exact form of the coulomb energy loss rate depends on the relative energy of the test particle and the target hydrogen atoms and, also, the ionization state of the hydrogen.

There are indirect arguments that ions slow down in a medium where they have much more energy than the larger number of ambient particles that they encounter, a 'cold target.' For example, assuming that the target material is located in or near the photosphere, we can assume low ionization (a neutral target) and a temperature of $T = 5780K$ (Lang 2001; Golub & Pasachoff 2001). To produce prompt γ-ray lines we need test particles of energy $\gtrsim 1$ MeV. For a cold target, we need the test particles to have kinetic energy $E \gg \frac{m}{m_e} kT$, where m is the mass of the target particle, m_e is the mass of the electron and k is the Boltzmann constant (Emslie 1978). For a beam of protons entering the photosphere, this limit is $\sim 9 \times 10^{-4}$ MeV. Since we need a proton of at least 1 MeV energy to excite the target, we can assume, in this case, that the target is 'cold.' However, we do not have any direct information about conditions in the γ-ray emitting region. This is a difficulty in deciding what we believe the observed γ-ray line fluences are telling us, since this depends very much on whether the source region is 'cold' or 'warm.'

Assuming photospheric conditions, we can start to model the line emission from a cold, neutral, thick target. Observations (eg. Murphy et al. (1991, 1997)) show that the lines take the form of a narrow peak over a broader component. The narrow peak results from light accelerated particles striking heavier ambient particles so that the excited particle experiences little recoil and produces

little doppler broadening. Conversely the broader component results from emission from heavier accelerated ions as they encounter lighter ambient ions. These heavy ions leave the collisions with sufficient velocities to spread their emission by doppler broadening. The lightest particles involved are protons, or hydrogen ions, and α-particles, or helium ions, (^{3}He is also a component) while the heavier particles start with carbon ions. The intervening elements, lithium and beryllium are not abundant and only show up in the γ-ray spectrum as fusion reaction products of helium. For simplicity here, we will only model the narrow component and derive total photon yields as this is adequate to answering many questions. The narrow line's shape and the broad component await future work.

Consider a test particle (either a proton or an α-particle) of mass m and energy E passing through a region with hydrogen density n_H . With m in gm and E in MeV, the test particle will have velocity v cm s^{-1}. The main process by which target particles are excited to appropriate energies for prompt deexcitation to produce γ-rays is by Coulomb interaction. Deflection of the charged test particle in the electric field of the target transfers energy to the target particle (see, e.g. Dendy 1994). A smaller proportion of emission in each γ-ray line is produced by spallation when a heavier nucleus is forced to emit an α-particle and transmutes to the excited state of a lighter nuclear species. We proceed here to describe the Coulomb process, but spallation is handled in mathematically the same way, except that the source particle is not the same nucleus as the type that eventually emits the γ-ray photon.

The probability that the particle will excite a target particle to the appropriate energy depends on the appropriate cross-section σ (see section 2.3) and whether the incident particle has enough energy. Effectively the test particle traces out a cylinder given by the cross-section multiplied by the path length and the path length increases at rate v cm s^{-1}. Within this cylinder the test particle will emit photons in interactions with $n_H a_x v\sigma$ targets per second where a_x is the relative abundance of the appropriate target particle. The test particle's energy must be above E_{th} the threshold energy for exciting the line of interest and some energy will be lost as it passes through the target. So, in fact, it will emit photons until v has reduced to the point where the particle energy drops below E_{th}. Given this, the photon yield, $\phi(E)$, for a given test particle with initial energy E can be

calculated by integrating the emissivity over this effective life of the test particle and changing variable from time to the energy of the test particle (e.g. Ramaty 1986; Brown 1971).

$$\phi(E) = \int_{E_{th}}^{E} \frac{\sigma(E')n_H a_x v(E')}{|\frac{dE'}{dt}|} dE' \tag{3.1}$$

It is convenient to express this in terms of column depth X_H gm cm^{-2} of hydrogen in the target region rather than in time t s.

$$\frac{n_H v(E)}{\frac{dE}{dt}} = \frac{1}{\bar{m}\frac{dE}{dX_H}} \tag{3.2}$$

where $\bar{m}$ is the mean mass of particles in the target region, taken to be mainly hydrogen and helium nuclei ($\bar{m} = \frac{m_H + a_{He} m_{He}}{1+a_{He}}$). So 3.1 changes like this.

$$\phi(E) = \int_{E_{th}}^{E} \frac{\sigma(E')a_x}{\bar{m}|\frac{dE'}{dX_H}|} dE' \tag{3.3}$$

This assumes that the incident ions slow down systematically. This will be the case if if they are moving through a neutral medium of much less energetic ambient particles. Otherwise they will tend to lose energy diffusively and we need to approach the energy loss in a different way. Barkas & Berger (1964) give empirical energy-loss rates for particles passing through a cold, neutral medium and Murphy (1985) summarizes these results.

For protons, the energy-loss rate is

$$\frac{dE}{dX} = \left\{ \begin{array}{ll} 702.9E^{-0.836}, & E < 160\ MeV \\ 114.2E^{-0.480}, & 160 < E < 1000\ MeV \\ 4.15, & E > 1000\ MeV \end{array} \right\} MeV gm^{-1} cm^2 \tag{3.4}$$

and, for α-particles, it is

$$\frac{dE}{dX} = \left\{ \begin{array}{ll} 8959(1 - \exp(-1.993E^{\frac{1}{2}}))^2 E^{-0.836}, & E < 640\ MeV \\ 889E^{-0.480}, & 640 < E < 4000\ MeV \\ 16.6, & E > 4000\ MeV \end{array} \right\} MeV gm^{-1} cm^2 \tag{3.5}$$

In a thick target (see section 3.2) all accelerated particles that start with energy above E_{th} can contribute to emission in our chosen line. $N(E)dE$ is the

number of test particles between energies E and $E+dE$. However we cannot hit target particles with unlimited energies and there will be a maximum energy E_{max} above which the target particle will be destroyed in some way. E_{max} may not be high enough to destroy the particles. It may, instead, reflect a limitation of the acceleration mechanism. Values for E_{max} are suggested by observations. Vilmer et al. (2003) studied the 1990 May 24 solar flare and found that $E_{max} \simeq 2$ GeV for consistency with the observed energy of neutrons emitted by the flare. Kocharov et al. (1998) also studied neutron emission, but in the 1991 June 15 flare (see chapter 6). This flare showed a maximum cut-off energy greater than 10 GeV. The π^0 emission from the 1988 December 16 and 1989 March 6 flares indicated to Alexander et al. (1994) that these flares had a high-energy cut-off for protons between 500 and 800 MeV. The sensitivity of the model to the choice of E_{max} depends on the slope of the power law. The cut-off is less critical for steeper accelerated particle spectra.

Accepting that there is an upper limit E_{max} for the proton's energy, the total photon yield from the target region, using 3.3, is Φ.

$$\Phi = \int_{E_{th}}^{\infty} \frac{\sigma(E')a_x}{\bar{m}|\frac{dE'}{dX_H}|} \int_{E'}^{\infty} N(E)H(E_{max}-E)dEdE' \tag{3.6}$$

where $H(E)$ is the Heaviside step function.

The exact form of the integrand of Φ depends on the test particle type and the distribution $N(E)$. The test particle type fixes the choice of $\frac{dE'}{dX_H}$ (3.4 or 3.5). If we choose a power law distribution for the test particles as in Section 2.5 the distribution for a beam of protons is $N_p(E)$.

$$N_p(E) = \frac{N_0(\delta-1)}{E_0}\left(\frac{E}{E_0}\right)^{-\delta} \tag{3.7}$$

where δ is the power-law index and there are N_0 protons with energy above E_0. For α-particles this modifies to $N_\alpha(E)$.

$$N_\alpha(E) = r_p^\alpha \frac{N_0(\delta-1)}{4E_0}\left(\frac{E}{4E_0}\right)^{-\delta} \tag{3.8}$$

where r_p^α is a parameter giving the abundance of test α-particles relative to test protons, so that $r_p^\alpha N_0$ gives the number of α-particles with energies above $4E_0$. The power-law index δ may, or may not, be the same for protons and α-particles.

Expressing the accelerated ion energies in MeV.nucleon^{-1} simplifies the computation in situations where there are a variety of fast ions.

Substitution of the appropriate distribution (3.7 or 3.8) into equation 3.6, using an appropriate choice of 3.4 or 3.5, produces a model for total emission from a flare in a given γ-ray line. Therefore, for a beam of protons, the total photon yield is

$$\Phi = \left\{ \begin{array}{ll} \frac{a_x N_0}{\bar{m}(E_0^{1-\delta} - E_{max}^{1-\delta})} \int_{Eth}^{Emax} \frac{\sigma(E) E^{\zeta(E)} (E^{1-\delta} - E_{max}^{1-\delta})}{K(E)} dE & \delta \neq 1 \\ \frac{a_x N_0}{\bar{m} \log(\frac{E_{max}}{E_0})} \int_{Eth}^{Emax} \frac{\sigma(E) E^{\zeta(E)} \log(\frac{E_{max}}{E})}{K(E)} dE, & \delta = 1 \end{array} \right\} \quad (3.9)$$

where

$$K(E) = \left\{ \begin{array}{ll} 702.9, & E < 160\ MeV \\ 114.2, & 160 < E < 1000\ MeV \\ 4.15, & E > 1000\ MeV \end{array} \right\}$$

and

$$\zeta(E) = \left\{ \begin{array}{ll} 0.836, & E < 160\ MeV \\ 0.480, & 160 < E < 1000\ MeV \\ 0, & E > 1000\ MeV \end{array} \right\}$$

For a beam of α-particles, the total photon yield is

$$\Phi = \left\{ \begin{array}{ll} \frac{a_x r_p^{\alpha} N_0}{\bar{m}((4E_0)^{1-\delta} - E_{max}^{1-\delta})} \int_{E_{th}}^{E_{max}} \frac{\sigma(E) E^{\zeta(E)} (E^{1-\delta} - E_{max}^{1-\delta})}{K(E)} dE, & \delta \neq 1 \\ \frac{a_x r_p^{\alpha} N_0}{\bar{m} \log(\frac{E_{max}}{4E_0})} \int_{E_{th}}^{E_{max}} \frac{\sigma(E) E^{\zeta(E)} (E^{1-\delta} - E_{max}^{1-\delta})}{K(E)} dE, & \delta = 1 \end{array} \right\} \quad (3.10)$$

where

$$K(E) = \left\{ \begin{array}{ll} 8959(1 - \exp(-1.993 E^{\frac{1}{2}}))^2, & E < 640\ MeV \\ 889, & 640 < E < 4000\ MeV \\ 16.6, & E > 4000\ MeV \end{array} \right\}$$

and

$$\zeta(E) = \left\{ \begin{array}{ll} 0.836, & E < 640\ MeV \\ 0.480, & 640 < E < 4000\ MeV \\ 0, & E > 4000\ MeV \end{array} \right\}$$

δ is not necessarily the same for protons and α-particles. Numerical evaluation of these equations allows the modelling of γ-ray line fluences assuming we have some information about the initial fast ion energy distribution and the abundances of fast ion species and ambient nuclei.

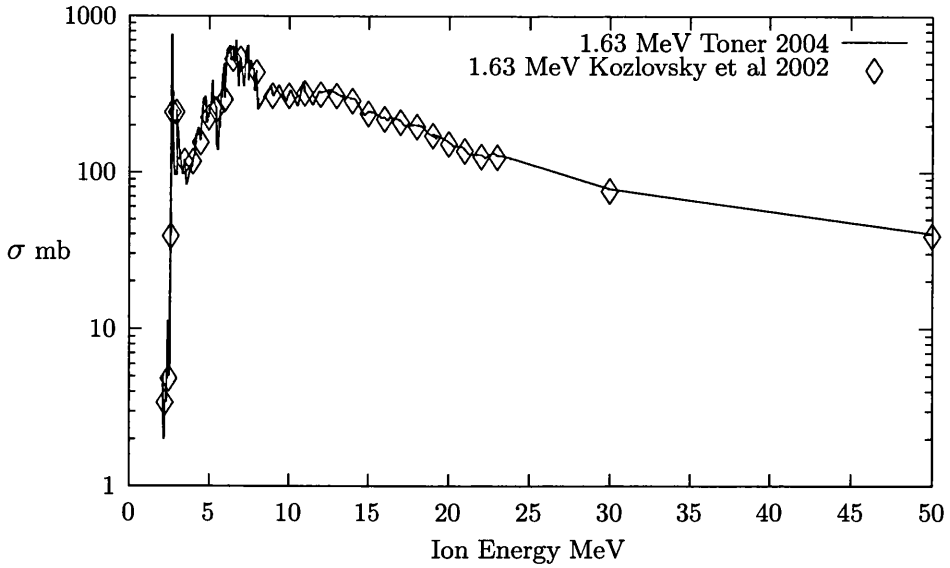

Figure 3.1: A comparison between the cross-sections used in this present work (Toner 2004) with the coarser cross-sections used by Kozlovsky et al. (2002) in Monte Carlo simulations. These show the cross-section for excitation of 1.63 MeV ^{20}Ne by fast protons. Note that my methods allow finer energy resolution but that the coarser resolution is necessary for the computational intensity of a Monte Carlo approach.

3.4 Software

In order to use equations 3.9 and 3.10 in practice a numerical method is required. For the work presented here, I gather the constant terms together and evaluate the remaining integral by a simple trapezoidal rule. The size of the increment in energy used to calculate each step of the integration is dictated by the energy-resolution of the excitation cross-section and, in fact, varies with energy, needing to be finer at lower energies where there is more structure in the cross-section. For this reason, I do not always use the published digitizations in Kozlovsky et al. (2002) which are useful for the fast integrations required for Monte Carlo simulations and prefer my own digitizations of the original cross-sections published in graphical form by Dyer et al. (1981, 1985); Seamster et al. (1984) and others. My own digitizations are listed in Appendix B and Figure 3.1 allows a comparison to be made of the proton-excitation cross-section of ^{20}Ne that leads to emission at 1.63 MeV.

The software I have developed allows a choice of target models: the cold,

neutral target model described here and the warm, ionized target described in Chapter 4. In its simplest form, a number of model parameters are provided by the user and a set of line fluences are calculated based on this input. Alternatively, modified versions allow an exploration of one or more parameters by setting ranges of values and calculating sets of line fluences as these parameters vary through the given ranges. The required parameters are the relative abundances of the target species which are listed in the program as parameters); the slope of the (assumed) power law distribution of the accelerated ions, specified by δ in Equations 3.9 and 3.10, which can either be a single power law or separate power laws for protons and α-particles (this distribution is also defined by a maximum energy cut-off, usually 1 GeV, and also there is a minimum threshold energy set by the reaction cross-section); a normalization energy E_0 and the number of accelerated protons N_0 above this energy (these are used to deduce total proton numbers from observed spectra); r_p^α, the ratio of α-particles to protons above the normalization energy E_0 in the accelerated ion population (this is actually the parameter $F_{0,\alpha}/F_{0,p}$ defined precisely in Section 5.2.1, other authors quote α/p which is equivalent); and a flag which specifies whether to use a cold, neutral target or a warm, ionized one. When a warm, ionized target is chosen, the target temperature must also be specified and the method of calculating the Coulomb logarithm (see Appendix A). There are further data which are read in from files as the program runs. It is convenient to store reaction cross-sections (σ in Equations 3.9 and 3.10) in this way. This allows σ from different sources to be compared and their differences evaluated in terms of their effects on the calculated line fluences.

All fluences are set to zero and then calculation of a set of line fluences proceeds reaction by reaction. The reactions included are listed in Table 3.1. Proton-induced nuclear excitations are taken one by one and then alpha-induced excitations, the fluences from each reaction contributing to a line being summed to derive the final modelled value. Table 3.1 also includes a ^{3}He-induced reaction for the 1.02 MeV complex which is dealt with similarly and then the fluence added into the final value. The calculation is modified for the parameters of a ^{3}He nucleus in the same way as the α-particle version was deduced.

The appropriate equation is chosen from 3.9 and 3.10, with a modification for warm-target energy loss if that target model is required (see Section 4.4). The

Photon Energy (MeV)	proton excitations	α-particle excitations	^3He excitations
0.429		$^4He(\alpha,n)^7Be^*$	
0.478		$^4He(\alpha,p)^7Li^*$	
		$^4He(\alpha,n)^7Be(\epsilon)^7Li^*$	
0.847	$^{56}Fe(p,p')^{56}Fe*$	$^{56}Fe(\alpha,\alpha')^{56}Fe^*$	
	$^{28}Si(p,x)^{27}Al^*$		
0.931	$^{56}Fe(p,x)^{55}Fe*$		
1.02 complex		$^{56}Fe(\alpha,n)^{59}Ni^*$	
		$^{56}Fe(\alpha,x)^{58}Ni^*$	
		$^{56}Fe(\alpha,x)^{58}Co^*$	$^{16}O(^3He,p)^{18}F^*$
1.369	$^{24}Mg(p,p')^{24}Mg^*$	$^{24}Mg(\alpha,\alpha')^{24}Mg^*$	
	$^{28}Si(p,x)^{24}Mg^*$		
	$^{56}Fe(p,x)^{55}Fe^*$	$^{56}Fe(\alpha,n)^{59}Ni^*$	
1.634	$^{20}Ne(p,p')^{20}Ne^*$	$^{20}Ne(\alpha,\alpha')^{20}Ne^*$	
	$^{24}Mg(p,x)^{20}Ne^*$	$^{24}Mg(\alpha,x)^{20}Ne^*$	
	$^{28}Si(p,x)^{20}Ne^*$		
	$^{14}N(p,p')^{14}N^*$	$^{14}N(\alpha,\alpha')^{14}N^*$	
	$^{16}O(p,x)^{14}N^*$		
1.779	$^{28}Si(p,p')^{28}Si^*$	$^{28}Si(\alpha,\alpha')^{28}Si^*$	
	$^{32}S(p,x)^{28}Si^*$		
4.438	$^{12}C(p,p')^{12}C^*$	$^{12}C(\alpha,\alpha')^{12}C^*$	
	$^{14}N(p,x)^{12}C^*$	$^{14}N(\alpha,x)^{12}C^*$	
	$^{16}O(p,x)^{12}C^*$	$^{16}O(\alpha,x)^{12}C^*$	
6.129	$^{16}O(p,p')^{16}O^*$	$^{16}O(\alpha,\alpha')^{16}O^*$	
	$^{20}Ne(p,x)^{16}O^*$		
	$^{16}O(p,x')^{15}O^*$	$^{16}O(\alpha,x')^{15}O^*$	

Table 3.1: The line fluences modelled with the software used in this work, together with the nuclear excitation reactions that contribute to each. The reactions are given in the standard notation where the first nucleus is the target, the bracketed particles are, first, the incident ion and, second, the ejected particle and the last nucleus, marked with an asterisk, is the resultant excited nucleus. This excited nucleus de-excites almost instantly to produce the observed photon. Any intermediate reactions, such as in the second reaction for the 0.478 MeV line, list in the middle. The ^3He-induced reactions complicate the interpretation of the 1.02 MeV complex as discussed in Chapter 5. For more details of all of these reactions see the summary in Kozlovsky et al. (2002) and the discussion in Section 2.3.

calculation process divides into two parts: the evaluation of the integral part of the equation and normalization according to the target particle abundance and the energy limits of the accelerated ion distribution. The integral is evaluated by a simple application of the trapezoidal rule. Each trapezium is created between adjacent energies in the digitized cross-section σ for the nuclear excitation and so the energy resolution varies according to the detail in the cross-section. For example, the integral part of Equation 3.9, when $\delta \neq 1$, would be evaluated like this.

$$Integral = \sum_{i=0}^{m} \left(\frac{\sigma(E_i) E_i^{\zeta(E_i)} (E_i^{1-\delta} - E_{max}^{1-\delta})}{K(E_i)} + \frac{\sigma(E_{i+1}) E_{i+1}^{\zeta(E_{i+1})} (E_{i+1}^{1-\delta} - E_{max}^{1-\delta})}{K(E_{i+1})} \right) \frac{E_{i+1} - E_i}{2} \quad (3.11)$$

where $E_0 = E_{th}$ and $E_m = E_{max}$.

The values at which $\sigma(E)$ is given in the cross-section file provide the sequence of E_i. The resulting number is multiplied by the energy-independent terms that complete Equation 3.9 to produce a photon yield from this accelerated ion population. Care has to be taken at this point over units, as the nuclear physics that provides the cross-sections works in millibarns and the astrophysics of the solar flare works in cm^2, for example.

It is then convenient, for comparison with observations, to adjust the total photon yield to the photons observed per unit area at the Earth. This is just a matter of simple geometry and produces line fluences that can be compared directly with SMM/GRS and CGRO data.

The set of line fluences can then be written to a file for further analysis and comparison with observed spectra. Sometimes we also want to investigate some of the parameters and these are output along with the corresponding line fluences.

3.5 A Cold Target Application: ^{24}Mg 1.37 MeV Line

The 1.63 MeV line due to excited ^{20}Ne has drawn attention to itself by its anomalous brightness in SMM flare spectra. For example, Share & Murphy (1995) (see Section 2.4.2) find, in a sample of nineteen X-class flares observed with the SMM GRS instrument, that the high 1.63 MeV line intensity implies either an excess in the abundance of ^{20}Ne or a very steep ('soft') energy spectrum for the accelerated

protons in those flares. This would be the case if the accelerated ions include few alpha particles. However, the evidence, from observations of lines arising solely from alpha-alpha interactions (^{7}Li at 478 keV and ^{7}Be at 429 keV, Murphy et al 1990), has been interpreted as indicating that alphas are probably over-abundant (Murphy et al 1991). For now, take this conclusion at face value but see Chapter 5 where I will take a more critical look at it.

In Chapter 4 I investigate a mechanism by which the cross-section for excitation of ^{20}Ne to produce the line at 1.63 MeV, which has a particular sensitivity to lower-energy protons ($\approx$ 2 MeV), might be fed a supply of accelerated ions which do not excite other species in the γ-emission spectrum, without having to invoke a steep proton spectrum. Among nuclear species detected in solar flares, the nuclear excitation cross-section of ^{20}Ne to collisions with protons is particularly sensitive to lower energy collisions; hence the expected enhancement due to a steep spectral slope in the exciting protons. It is of interest to see if there are any other lines that have a similar sensitivity to low-energy protons to provide a check on results obtained with the 1.63 MeV line. The cross-section for proton excitation of the 1.37 MeV line due to excited ^{24}Mg has an incident particle energy threshold only slightly greater than that of the 1.63 MeV line, and thus may offer a consistency check on the idea of a steep, low energy proton distribution (R.S.McIntosh, private communication to A.L.MacKinnon). Figure 2.3 shows the two cross-sections compared with more typical species and Figure 3.2 allows a clearer comparison between ^{20}Ne and ^{24}Mg. Full digitizations of these cross-sections are also given in Appendix B. The 1.37 MeV line due to ^{24}Mg also has a lower-energy sensitivity, although it lacks the little 'spike' at 3 MeV If this interpretation of the observed fluence of the 1.63 MeV line is correct, we should see some correlation with the 1.37 MeV line over a number of flare events.

In the next section I quantify this assertion, demonstrating that, in the absence of abundance variations, the ratio of the fluxes in the 1.37 and 1.63 MeV lines should not vary by more than a factor of two, irrespective of the fast proton energy distribution. Section 3.5.2 discusses the role of fast alpha's, possibly over-abundant, at least in some flares (Share & Murphy 1998), but still making Assumption A (see Chapters 4 and 5).

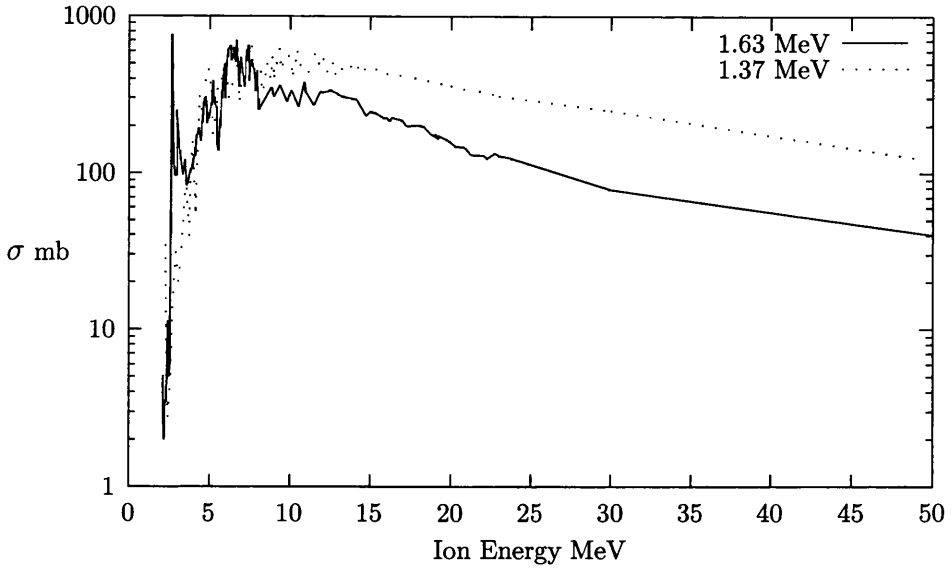

Figure 3.2: The excitation cross-sections of ^{20}Ne at 1.63 MeV and ^{24}Mg at 1.37 MeV showing how they both have fairly low-energy sensitivity to proton excitation.

3.5.1 The 1.37 MeV ^{24}Mg Line and Proton Excitation

Line fluences depend on the availability and energy of exciting particles, specified by the energy spectrum of accelerated ions (protons and alpha particles) and the probability of successful collisions on the target species, summed up in the collision cross-section σ (Section 2.3). Values for σ are summarized in Ramaty et al. (1979) and Kozlovsky et al. (2002) for a range of solar flare species including ^{24}Mg and ^{20}Ne. The cross-sections used in this work are listed in Appendix B.

Assuming a power-law distribution in energy per nucleon of the accelerated ions (spectral index δ), the line fluence is integrated over a suitable range of accelerated ion energies, from the lowest exciting energy determined by the cross-section up to the highest significant exciting energy determined by the power law, using Equations 3.9 and 3.10. The resulting fluences are normalized to an accelerated ion spectrum where there is one particle above an energy of 1 MeV.nucleon^{-1}.

The method described in Section 3.4 is used to calculate separately the fluence contributions from proton- and α-excited emission, assumed for now to share the same accelerated ion energy spectrum (Assumption A). A total line fluence is then summed from these. For clarity I begin with an accelerated particle population consisting only of protons.

If the 1.63 MeV and 1.37 MeV lines were only indicators of steep proton spectrum slopes, then we could be confident of using their values as a probe of the accelerated particle energy spectrum. However they are also clearly dependent on the relative abundances of ^{20}Ne and ^{24}Mg. This complicates the analysis of these lines. Variations in the relative abundance of Ne and Mg from flare to flare can be inferred from observations in other wavelengths: Widing & Feldman (1995) find a variation of a factor of 1.5 in EUV data; soft X-rays reveal variations between factors of 2.5 and 3 (McKenzie & Feldman 1992; Saba & Strong 1993). However, neither of these data are guaranteed to originate in the same region as the γ-rays.

The line fluences resulting from this analysis could be used to fit actual data and recover information about relative abundances in the ambient medium excited by the flare, if we can be confident that their relative dependences on accelerated ion energies are closely matched. This section does not set out to do this as we are interested in the first step of showing how the relative fluences of the 1.37 and 1.63 MeV lines are affected by changes in the proton spectrum, irrespective of the species abundances. I take the relative abundances preferred by Murphy et al. (1991) and Ramaty et al. (1996b) for consistency with other analyses and as these are the best available for the flare γ-ray source region.

Figure 3.3 shows the ratio of the 1.37 and 1.63 MeV lines (^{24}Mg and ^{20}Ne respectively) for a number of values of accelerated particle spectrum index δ. The α/p ratio in the accelerated particles is set at 0.0 for the curve marked 'protons,' that is they are all protons. It can be seen that, although the ratio of 1.37 MeV to 1.63 MeV emission decreases monotonically with accelerated particle spectrum index δ, this ratio does not vary by more than a factor of two across the whole range of δ investigated.

3.5.2 The 1.37 MeV ^{24}Mg Line and Combined Proton and α-particle Excitation

Figure 3.3 shows a very simple model when all of the incident particles are protons. In reality, the α-particles in the accelerated ions are significant, particularly at low energies. The α cross-sections are also given in Ramaty et al. (1979) and Kozlovsky et al. (2002). Inclusion of the α-induced emission alters the picture

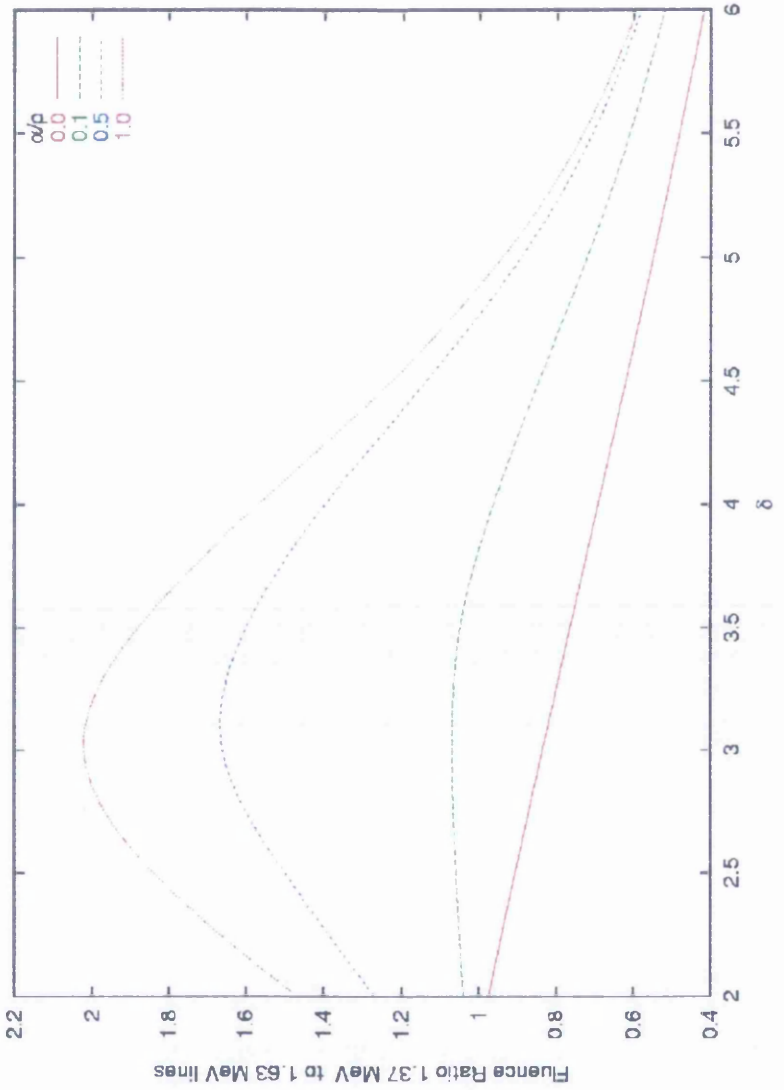

Figure 3.3: Comparison of the fluences of the ^{24}Mg and ^{20}Ne line emission at 1.37 and 1.63 MeV respectively. These are calculated for various values of the relative α-particle abundance in the accelerated ions given relative to the protons as α/p, and for accelerated particle spectral slopes δ. The ratio of the two fluences is given for each combination of α/p and δ.

somewhat.

The other curves show what happens when we add α-particles with the same energy spectrum as the protons. The proportion of αs is set by the ratio α/p. The line fluence due to the α-collisions is calculated as for the protons and then the two fluences combined in proportion to the α/p ratio.

Introduction of the α-particles seems to enhance the ^{24}Mg emission, especially in the mid-range of δ ($\approx$3) as well as removing the small downward trend except at extremely high values of δ. This is likely to be because the ^{24}Mg abundance is higher, while the two species have almost the same coverage of α-particle energies in their cross-sections (see Figure 2.4). However, with very soft spectra, this α-effect is minimized because there are almost no particles available to excite emission except at the low-energy end, where the cross-sections are sensitive only to protons. Again, the variation in the line ratio due to changes in the accelerated α/proton ratio, even at its maximum (when $\delta \approx 3$), is not likely to be more than a factor of two between flares.

3.5.3 Correlation Between the 1.37 MeV and 1.63 MeV Line Fluences

Having modelled the 1.63 MeV and 1.37 MeV lines using a thick target model and excitation cross-sections measured by Dyer et al. (1981) extended beyond 30 MeV using the cross-sections published by Ramaty et al. (1979), 1000 flare events were simulated by randomly varying the ^{24}Mg, in a uniform distribution, by a percentage around a canonical value taken from the Case 1a fit to SMM data made by Murphy et al. (1991). At the same time ^{20}Ne abundance is kept at exactly the value from this same fit while the proton spectral slope is varied over a specified range, again randomly from a uniform distribution. There are no other accelerated particles in this model.

The Pearson's moment correlation coefficient, r, can be used to test the relationship between the 1.63 MeV fluence, $\Phi_{1.63}$, and the 1.37 MeV fluence, $\Phi_{1.37}$, over all 1000 modelled flares.

$$r = \frac{\sum_i^{1000}(\Phi_{1.63} - \overline{\Phi}_{1.63})(\Phi_{1.37} - \overline{\Phi}_{1.37})}{\sqrt{\sum_i^{1000}(\Phi_{1.63} - \overline{\Phi}_{1.63})^2}\sqrt{\sum_i^{1000}(\Phi_{1.37} - \overline{\Phi}_{1.37})^2}} \tag{3.12}$$

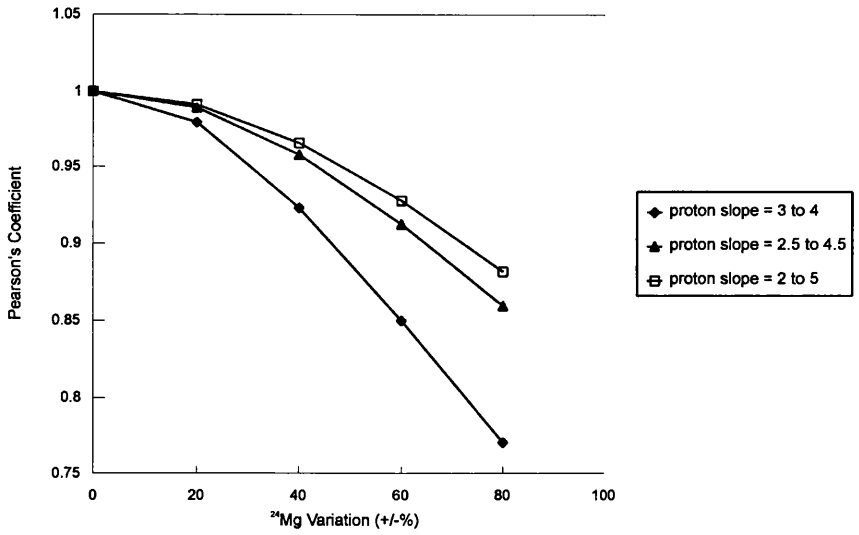

Figure 3.4: Pearson's correlation coefficient of the fluences in the 1.37 and 1.63 MeV lines in 1000 simulated flares, in three different ranges of accelerated proton power laws. A Monte Carlo simulation has produced these fluences while varying relative abundances of the ambient ^{24}Mg and ^{20}Ne and the power law index of the accelerated protons. The accelerated ion population in this example consists only of protons.

where the overline (e.g. $\overline{\Phi}_{1.63}$) represents a mean from the 1000 simulated results.

With this high number of events, the Pearson's coefficient is significant to a level of less than 10^{-39}. This says that the probability of the measured coefficient arising purely by chance is less than 10^{-39}. Fewer events yield essentially the same correlations but with a higher probability of these arising by chance.

The graph in Figure 3.4 shows how the correlation weakens with increasing variability in the ^{24}Mg abundance. However, quite large variations in abundance still result in quite acceptable correlations, especially if we restrict the range to those observed in the EUV and X-rays.

Curiously, the correlation drops off less sharply when a wider range of spectral slopes is allowed. This is due to the increasing influence of the variation in slope as compared with the influence of the fixed range of variation in relative abundance. However, in all cases a correlation of better than 0.8 arises even when the variation in Mg abundance is as much as $\pm 80\%$. This translates to a variation in relative

abundance $^{20}Ne/^{24}Mg$ of a factor of 5, much more than observed in EUV or X-rays.

3.5.4 The 1.37 MeV-to-1.63 MeV Fluence Ratio as a Diagnostic

Clearly the fluences of the 1.63 MeV and 1.37 MeV lines are not strongly enough affected by abundance variations to hide their relationship to the slope of the energy spectrum of the accelerated ions. If a strong correlation between the 1.63 MeV and 1.37 MeV lines is observed in a large sample of flares, then it can be assumed that protons dominate the accelerated ions. A poor correlation would indicate that something else is happening, most likely that there is a large component of α-particles in the accelerated ions because the low-energy sensitivity of these lines is particularly a feature of their proton cross-sections. Figure 3.3 shows how the variation of the line ratio becomes progressively broader as the proportion of α-particles increases. Also see Chapter 5 for a more complete discussion of the effects of the α-particle component in the accelerated ion population.

Share & Murphy (1995) present fluxes for the brightest lines in γ-ray spectra recorded in 19 flares by the SMM GRS instrument and Murphy et al. (1997) does the same for the 4 June 1991 flare as recorded by the OSSE instrument on CGRO (see Sections 1.10.4 and 1.10.6). This represents the best available data set of flare γ-ray spectra to date. The flux ratios derived from these data for 1.37 MeV and 1.63 MeV have a range spanning 0.33 ± 0.14 up to 2.36 ± 1.47. This is outside the range expected when the accelerated ions are only protons and there is not much flare-to-flare variation in abundances. Either there is quite substantial variation in abundances or there is a large accelerated α-particle population in these flares. Calculation of Pearson's coefficient between the 1.63 MeV and 1.37 MeV line fluences for the SMM flares finds $r = 0.915$ with a significance level of better than 10^{-6}. This means that the two lines are totally uncorrelated in this data set, further evidence that the picture is more complicate than the simple model developed here.

Chapter 4

Warm Ionized Targets

4.1 Feeding the Low-energy Sensitivity of ^{20}Ne

This chapter and Chapter 5 focus on physical reasons why the 1.63 MeV emission from^{20}Ne could be enhanced without calling for extra ^{20}Ne in the flare region or demanding excessive accelerated ion-energies. Both approaches attempt to arrange protons into an energy distribution that will feed large numbers into the 3 MeV spike in the excitation cross-section (Figures 2.3 and B.3). In Chapter 5 I separate the α-particle energy-distribution from the proton distribution so that the protons can develop a steep power law while the α-particles can maintain a flatter distribution; while, in this chapter, I consider what would be the effect on the overall accelerated ion spectrum of passing the ions through a region in which energy loss would be by a warm target mechanism, rather than the usual cold target (see Section 3.3. In a warm target situation, the test particle is injected with an energy that is low compared to the energies of the ambient particles (especially electrons) in the target region and its energy loss rate is less than in the case of a cold target. The reason for attempting to apply this here is that the slower ions in the distribution (i.e. the important ones at around 3 MeV) may experience warm target conditions at temperatures that would still be cold with respect to the faster ions. This would reduce the energy-loss rate for the slower ions and keep the population high at the cross-section spike.

4.2 Why Warm Targets?

Emslie et al. (1997) pointed out that the cold target assumption may be valid for very high-energy ions ($E \gtrsim 10$ MeV) but it may not hold for ions with energies around 1 MeV. These particles may lose a substantial part of their energy while passing through the corona, high up in the loop, where the plasma is hot and

ionized. Observational evidence that there is something different happening at these energies comes from the 1.63 MeV ^{20}Ne line, which has a cross-section sensitive to protons in this lower-energy range (See Sections 2.3 and 3.5). It also implies a low relative abundance of accelerated α-particles in the 1 MeV range, which calls into question the usual practice of applying the same energy distribution to protons and α-particles. Ramaty, Mandzhavidze, & Kozlovsky (1996b) confirm that the abundance of ^{20}Ne derived from this data is much higher than is found by other methods for either the corona or the photosphere, unless a steep energy-spectrum is inferred for the protons. The consequence is that there is a lot more of the flare energy contained in accelerated ions. However this may not be the case if we can relax the cold, neutral target assumption and allow at least some proportion of the accelerated ions to lose energy in a hot, ionized plasma, perhaps somewhere in the corona (MacKinnon & Toner 2003).

The obvious place for a γ-ray warm target would be the corona and there are flares in which a significant fraction of observed γ-ray line production does appear to take place in the corona (Barat et al. 1994; Vestrand & Forrest 1993). However there are strong arguments against a nearly isotropic, coronally trapped population in other flares. For example, the temporal behaviour appears to need rapid precipitation of the ions (Hua et al. 1989); and red-shifted γ-ray lines show significant anisotropy (Share et al. 2002). There is no clear justification for a universal warm target model for all flares, but we can say that, in some flares, there could be a coronal, warm-target origin for the γ-ray lines, or a warm-target component to the γ-ray source. This is enough motivation for considering warm target effects when interpreting γ-ray line fluxes from at least some events and such a treatment is explored here.

4.3 Proton Containment in the Corona

In what follows we assume the usual picture of a low-lying, flaring magnetic loop, as described in Section 1.3. The loop extends up into a comparatively tenuous (typically n_H is in the range 10^{10} to 10^{11} cm^{-3}) coronal region where particle acceleration takes place. Both ends of the coronal field lines are anchored in a denser, cooler chromospheric region. It is this region where most of the γ-ray

producing ions are thought to stop and produce most of their radiation. Warm target conditions can only be expected in the corona, so we should identify any factors which will detain the fast protons in the corona.

First, and most trivially, protons which are given large pitch angles θ at the time of their acceleration will spend a time $1/\mu$ longer in the corona, where $\mu = \cos\theta$ (ignoring any effects of magnetic field inhomogeneity). Barring the *a priori* unlikely circumstance of a concentration at large pitch angles, however, this will increase coronal residence times by a factor only of order unity.

Pressure balance arguments at least suggest magnetic field strength will increase from corona to chromosphere. The resulting trapping, in a coronal magnetic bottle, has often been discussed. Denote by B_0 the magnetic field strength at the apex of the loop, and by B_1 the field strength at a footpoint, i.e. at the depth in the atmosphere beyond which collisions will prevent all but a negligible fraction of incident protons from mirroring and returning. Provided the variation in magnetic field, as the ions pass between these two points, is small compared to the cyclotron motion of the ions (e.g. Dendy 1994), the magnetic moment, M, induced by the motion of an accelerated ion around the magnetic field lines is an approximate constant of the ion motion.

$$M = \frac{mv^2 \sin^2\theta}{2B} \tag{4.1}$$

With no non-magnetic forces acting, the ion energy must be a constant too, and so $\sin^2\theta/B$ is also an approximate constant of the ion motion (the first adiabatic invariant). In the absence of pitch-angle scattering, any protons with pitch angles greater than $\theta_0 = \sin^{-1}(B_0/B_1)^{1/2}$ are trapped in the corona. For an isotropic distribution, a fraction $\mu_0 = \cos\theta_0$ of all accelerated protons are trapped in this way. Only a modest field strength variation is needed to trap a significant fraction of all protons: $\mu_0 = 0.5$, for instance, implies just $B_0/B_1 = 0.75$.

These considerations apply to ions produced in a coronal loop by some unspecified mechanism. More effective trapping may occur naturally in more involved geometries (e.g. Lau et al. (1993)). In particular, ions accelerated in reconnection near a coronal null may be much more effectively trapped because they begin to move adiabatically at very low field strengths (Fletcher & Martens 1998).

While binary collisions are ineffective at scattering fast ions (Emslie 1978),

other mechanisms for more effective pitch-angle scattering may well operate. The discussion of stochastic acceleration in Chapter 2 defines the resonance condition in Equation 2.5.1. When $\lambda = 0$, the ions are in resonance with the wave and it follows from Equation 2.5 that the ion is moving parallel to the field at the Alfvén speed. So the Alfvén speed represents a minimum speed for ions that will interact with the accelerating wave (e.g. Kennel & Petschek 1966). A proton moving at the Alfvén speed has energy E (in keV) given by

$$E = 25B_2^2/n_{10} \tag{4.2}$$

where n_{10} and B_2 measure ambient density and field strength in units of 10^{10} cm^{-3} and 100s of G, respectively. Thus all protons of interest for γ-ray production may potentially interact with Alfvén waves, as has been discussed in detail elsewhere (e.g. Miller & Ramaty (1987)). The relative magnitudes of scattering τ_s and loop transit τ_l times determine the regime in which scattering takes place, and thus its effects on coronal containment (Kennel & Petschek 1966; Bespalov et al. 1987)): weak ($\tau_s \gg \tau_l$), in which scattering reduces residency times by allowing particles to trickle into the loss cone; moderate ($\tau_s \simeq \tau_l$), in which the distribution remains close to isotropic and a fraction $(1-\mu_0)$ of particles can precipitate; strong ($\tau_s \ll \tau_l$), in which scattering actually increases coronal residency times, even for particles inside the loss cone, by impeding the free flow of particles out of the loop.

Hua et al. (1989) carried out studies of proton turbulent transport in converging loops, treating scattering with a Monte Carlo method. Restricting their simulations to cases in which the isotropisation length was at least twice the loop length, they confirmed the existence of the weak and moderate regimes, finding a saturation of the precipitated flux as scattering time reduces to the point that the distribution is close to isotropic. Situations with still shorter mean free paths were (Monte Carlo) simulated by Kocharov et al. (1999), confirming the existence of the strong regime with its enhanced containment.

The strong regime might arise in flares in (at least) one of two ways. First, Alfvén turbulence might itself be the means by which ions are accelerated to γ-ray producing energies. In this case, the turbulent energy density needed to accelerate protons fast enough implies scattering in the strong regime, and indeed effective

containment in the acceleration region (Smith & Brecht 1991). Second, and most importantly, very modest anisotropies of the large numbers of protons needed to produce observed γ-ray fluxes are adequate to result in unstably growing waves (Tamres et al. 1989; Bespalov et al. 1987). Even if produced isotropically, such anisotropies will inevitably occur as protons travel away, with different parallel velocities, from a localized source region. The number of protons involved in the June 7, 1980 flare, for instance, evidently implies turbulent propagation of protons in the strong scattering regime (Smith & Brecht 1991), with coronal residency times many times greater than loop transit times. Kocharov et al. (2000) have also drawn attention to the possible role of self-generated Alfvén turbulence in containing ions in warm target regions.

It seems clear that a variety of factors point to typical coronal residency times substantially greater than the loop transit times used in Emslie et al. (1997), and thus to the possibility, at least that large numbers of γ-ray producing protons slow down mostly in a warm target region. In the chapter 5 I explore the consequences of this possibility quantitatively, in the limit that the containment mechanism has no significant influence on ions' evolution in energy. Before doing this I also note that other coronal containment mechanisms have been proposed, in the presence of which a more elaborate re-evaluation of radiative yields would be necessary - e.g. Spicer & Emslie (1988).

4.4 γ-ray Line Flux in a Target of Arbitrary Temperature

In this section we assume for illustration that all protons slow down in a fully ionized plasma characterized by a single, ambient temperature T. We will consider the effect of T on the yields of various γ-ray lines. Emslie et al. (1997) found that implausibly high values of T, in excess of 10^8 K, would be necessary to yield a significant enhancement of ^{20}Ne line flux, even with perfect coronal trapping. First we look briefly at how this conclusion was reached and argue that it deserves to be revisited.

The energy loss rate of a proton in a fully ionized hydrogen plasma of temperature T (K) is given by (e.g. Trubnikov (1965); Tamres et al. (1986)):

$$\frac{dE}{dt} = -f(E)n\Theta(E,T) \tag{4.3}$$

where

$$f(E) = \frac{2\pi e^4 Z^2 \Lambda (2m)^{1/2}}{m_e E^{1/2}} \tag{4.4}$$

where m and Z are the mass (gm) and charge (multiples of the elementary charge e) of the incident fast ion, m_e is the electron mass, Λ is the Coulomb logarithm (dependent on energy and species, and given for fast particles e.g. by Emslie (1978); see also the Appendix), n (cm^{-3}) is the ambient particle density and $\Theta(E,T)$ is the ratio of the true energy loss rate to that experienced in a cold target (i.e. a source region in which $T \to 0$). $\Theta \to 1^-$ as $E/kT \to \infty$ and the details of its evaluation can be found in Tamres et al. (1986). For a test particle of type i, where i stands for proton or α-particle,

$$\Theta(E,T) = \psi(x_e) + \frac{m_e}{m_i}(\psi(x_p) - \psi'(x_p) - \psi'(x_e)) \tag{4.5}$$

where $\psi(x)$ is the incomplete gamma function $P(3/2,x)$, m_e, m_p and m_i are the masses of the electron, proton and the test particle, respectively, and

$$\begin{aligned} x_p &= \frac{E}{kT}\frac{m_p}{m_i} \\ x_e &= \frac{E}{kT}\frac{m_e}{m_i} \end{aligned} \tag{4.6}$$

with k being the Boltzmann constant. Press et al. (1992) provides a convenient method of evaluating the incomplete gamma function numerically which is used in the code behind this work. The energy-loss rates derived in this way tend to the empirical results of Barkas & Berger (1964) for the cold target case when the temperature approaches 0 K, as discussed in Appendix A.

We need not carry out any drastic reconsideration of the ions' energy evolution in the case that we appeal to interaction with Alfvén waves for coronal containment. For typical loop lengths $\sim 10^9$ cm and proton energies of a few MeV, values of $\tau_s \sim 1$ s are in the strong scattering regime. Changes of proton energy due to interaction with Alfvén waves take place on a time of order $\left(\frac{c}{v_A}\right)^2$ longer (e.g. Kulsrud & Pearce (1969)), easily in the 10^3 to 10^4 s regime for typical field strengths and densities and much longer than collisional slowing down times.

If we inject a population of protons with energy distribution $F(E)$ (i.e. the number of protons with energies between E and $E + dE$ is $F(E)dE$), then the standard thick target formalism for γ-ray line production (e.g. Ramaty (1986)) tells us that the total number of photons Φ_k produced in line k is

$$\Phi_k = a_k \int_{E_k}^{\infty} \frac{v(E)\sigma_k(E)}{f(E)} \Psi(E) dE \tag{4.7}$$

where E_k and σ_k are the threshold energy and cross-section (as a function of incident proton energy) for production of line k, a_k is the abundance relative to hydrogen of the target nuclei and $\Psi(E)$ is the total number of protons injected above energy E, i.e.

$$\Psi(E) = \int_{E}^{\infty} F(E) dE$$

The dominant, direct excitation cross-section for the particular line of interest, the 1.63 MeV line, has its threshold near 2 MeV and its maximum value at 6.4 MeV. Cross-sections generally climb steeply from threshold so one might expect the total (proton-excited) yield of 1.63 MeV photons to be dominated by protons about 6 to 7 MeV. Inspection of the integrand of Equation (4.4) for the particular case of this line is instructive, however. Even for hard injected spectra, the contribution from protons immediately above threshold is significant compared to that from protons of 6 to 7 MeV. Thus it is important to include the *full* proton energy range all the way from threshold.

Emslie et al. (1997) carried out detailed calculations only for the case where no non-collisional factors lengthen coronal lifetimes. They did consider a source region characterized by a single temperature, but discussed such a source only semi-quantitatively, basing rough arguments on the enhancement of proton lifetime expected for protons of energies around the maximum of the 1.63 MeV line cross-section. Since even protons immediately above the *threshold* of the cross-section can make a significant contribution, particularly for power-law ion distributions which fall off steeply with energy, a more detailed discussion is needed.

Now we ask the following question: for protons of a given energy E, what does the source temperature T have to be to reduce the energy loss rate by one

order of magnitude, i.e. to give $\Theta(E) = 0.1$? The factor of 0.1 is quite arbitrary but serves to make our point. In the 'warm target' regime, $\frac{m_p}{m_e} \gg \frac{E}{kT} \gg 1$, a simple, analytical approximation for Equation 4.4, exists (Tamres et al. 1986):

$$\left(\frac{dE}{dt}\right)_{warm} = -\frac{4\pi e^4 n\Lambda}{\sqrt{2m_p}E^{3/2}}\left(1 + 0.01756\left(\frac{E}{kT}\right)^{3/2}\right)E \tag{4.8}$$

and, similarly, there is an approximation for cold target conditions:

$$\left(\frac{dE}{dt}\right)_{cold} = -\frac{2\pi e^4 n\Lambda\sqrt{2m_p}}{m_e E^{3/2}}E \tag{4.9}$$

By definition (see Equation 4.4) $\Theta(E,T)$ is found by dividing Equation 4.8 by Equation 4.9.

$$\Theta(E,T) = \frac{m_e}{m_p}\left(1 + 0.01756\left(\frac{E}{kT}\right)^{3/2}\right) \tag{4.10}$$

Substituting our condition that the warm target should decrease energy loss to one-tenth, i.e. $\Theta(E,T) = 0.1$ into Equation 4.10 gives us a simple analytical expression relating E and kT.

$$kT = 2.1E$$

where kT has been expressed in keV and E in MeV. As found by Emslie et al. (1997), such a reduction of proton energy loss rate at 7 MeV needs very high temperatures (about 2×10^8 K). Nearer the threshold of the cross-section however, at 2 - 3 MeV, a more acceptable temperature of 7×10^7 K will do. Several observations exist suggesting flare temperatures in the range 10^7 to 10^8 K (e.g., Tsuneta et al. (1997); Warren & Reeves (2001)).

Thus a complete assessment of the influence of warm target effects on γ-ray line yields must consider the contribution of all proton energies above threshold, not just those in the vicinity of the cross-section maximum. Also 'gradual phase' flare conditions can extend the lifetime of trapped protons near threshold by up to an order of magnitude.

4.5 Role of α Particles

As pointed out by Share & Murphy (1995), too many α particles in the accelerated population complicates the interpretation of the 1.63 MeV line. The cross-section

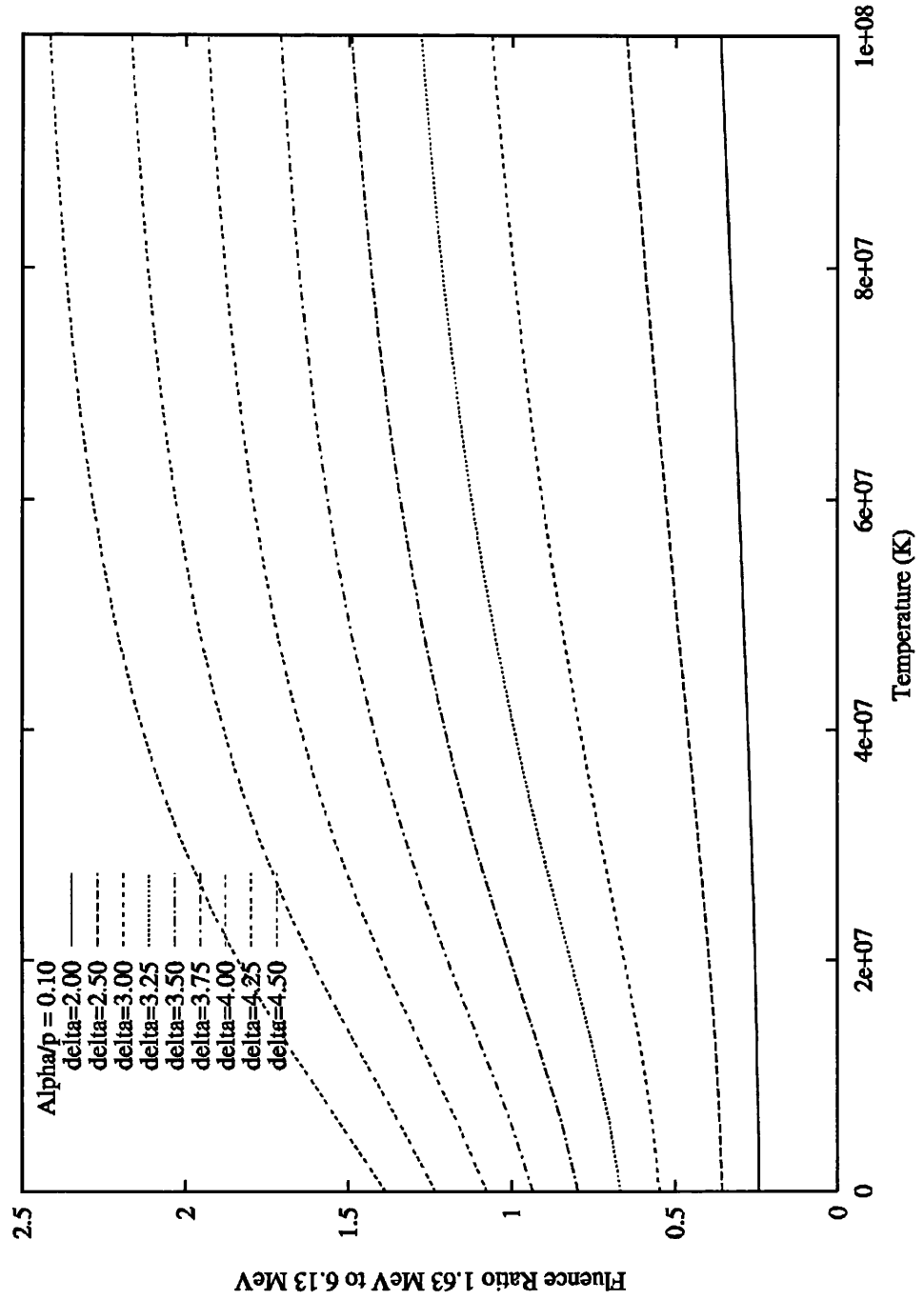

Figure 4.1: Dependence of the ratio of line fluxes $\Phi_{1.63}/\Phi_{6.13}$ on T for injected ion energy distributions characterized by various values of ion energy spectral index δ. The fast α-particle abundance relative to protons is $\alpha/p = 0.1$.

data presented in Ramaty et al. (1979); see also Dyer et al. (1981, 1985); Seamster et al. (1984) clearly show that this line's threshold when excited by α's, rather than protons, is not significantly different from that of other de-excitation lines. So, if α's are over-abundant in the fast ion distribution - as appears to be the case in at least some flares (Murphy et al. 1991; Share & Murphy 1998) - assuming an injected fast ion distribution extending steeply to low energies helps less with understanding the observed 1.63 MeV line flux. For example, Murphy et al. (1997) used the ratio $\Phi_{1.63}/\Phi_{6.13}$ to deduce δ values of 4.0 and 4.4 assuming a relative abundance ratio α/p of 0.1 and 0.5 respectively. Clearly the assumption of identical energy distributions for protons and α's, combined with the deleterious effect of α's on the 1.63 MeV flux relative to other lines, combine to push the deduced ion distribution to steeper forms. Larger and larger values for the total ion energy content follow immediately. This is further complicated by the assumption that fast protons and α-particles share the same energy spectrum. This effect is investigated separately in Chapter 5.

In general, thresholds for excitation by alphas are of the same order as thresholds for protons when expressed in MeV.nucleon^{-1}. It follows immediately that warm target effects will be of a similar order of magnitude and thus we include them explicitly in these calculations. As summarized above, inclusion of alphas in cold target calculations softens the deduced ion spectrum, increasing the total ion energy. The precise magnitude of this effect in the warm target case will depend on the detailed forms of the cross-sections and would have to be calculated by combining the warm target approach given here with the separated ion energy distributions described in Chapter 5. However, this starts to introduce many more parameters than the current state of the data might support.

4.6 Results

In Fig. 4.1 we show the ratio $\Phi_{1.63}/\Phi_{6.13}$ as a function of T, calculated as described in the previous section. We assume that $F(E)$ has power-law dependence on E, $F(E) \sim E^{-\delta}$, up to $E = E_{max}$, and that it is zero for $E > E_{max}$. We adopted $E_{max} = 1$ GeV throughout; as long as $\delta > 2$ and $E_{max} \gg 100$ MeV its value has no important influence on the results. We have assumed $\alpha/p = 0.1$, a range of

values of δ and the same target isotopic abundances as Ramaty et al. (1996b). In particular the assumed $^{20}Ne/^{16}O$ abundance ratio is 0.14. At the larger δ's the results of Figures 4.1, 4.2 and 4.3 scale roughly linearly with $^{20}Ne/^{16}O$ abundance ratio. Spallation reactions on other species contribute up to 30% of the 1.63 MeV flux at the hardest δ, however, complicating the effects of abundance variations.

In common with all previous work, we assume that proton and α distributions are characterized by the same value of δ, and that the abundance ratio α/p refers to the relative numbers of particles above the same energy *per nucleon.* These assumptions will be submitted to scrutiny in Chapter 5. Cross sections come from Dyer et al. (1981, 1985); Seamster et al. (1984), as far as we know the most recent, published measurements (see also Kozlovsky et al. (2002)). We include contributions to the total line fluence from both direct excitation of e.g. ^{20}Ne nuclei for the 1.63 MeV line, as well as the various spallation type channels which can contribute to the lines (listed in Kozlovsky et al. (2002)).

Ramaty et al. (1996b) previously calculated $\Phi_{1.63}/\Phi_{6.13}$ assuming ions slow down in a cold, neutral target. We checked that our numerical evaluation of Equation (4.4) gives the same results when the same energy-loss rate $f(E)$ (empirically derived in Barkas & Berger (1964)) is used. These are similar to our ionized medium results in the case ($T \rightarrow 0$) but not identical because of differences in the energy-dependence of Λ in the neutral and ionized cases; see the Appendix. They also give us reference results for discussion of the warm target case.

We see that temperatures in excess of 10^7 K lead to enhanced values of $\Phi_{1.63}/\Phi_{6.13}$. Warm target effects have least influence on $\Phi_{1.63}/\Phi_{6.13}$ for the hardest injected spectra.

Figure 4.2 shows similar results, now assuming $\alpha/p = 0.5$. As anticipated, a greater relative α abundance in the fast ion distribution does make $\Phi_{1.63}/\Phi_{6.13}$ slightly less dependent on T, but a significant variation remains.

The ratio $\Phi_{1.63}/\Phi_{6.13}$ does not increase indefinitely with source temperature. In fact a maximum value occurs at a temperature weakly dependent on δ but generally around 4 - 5×10^8 K. Figure 4.3 shows the *maximum* value of $\Phi_{1.63}/\Phi_{6.13}$ as a function of δ, for a range of abundances of fast α-particles relative to protons. The range of δ consistent with a given, observed $\Phi_{1.63}/\Phi_{6.13}$ is bracketed by the

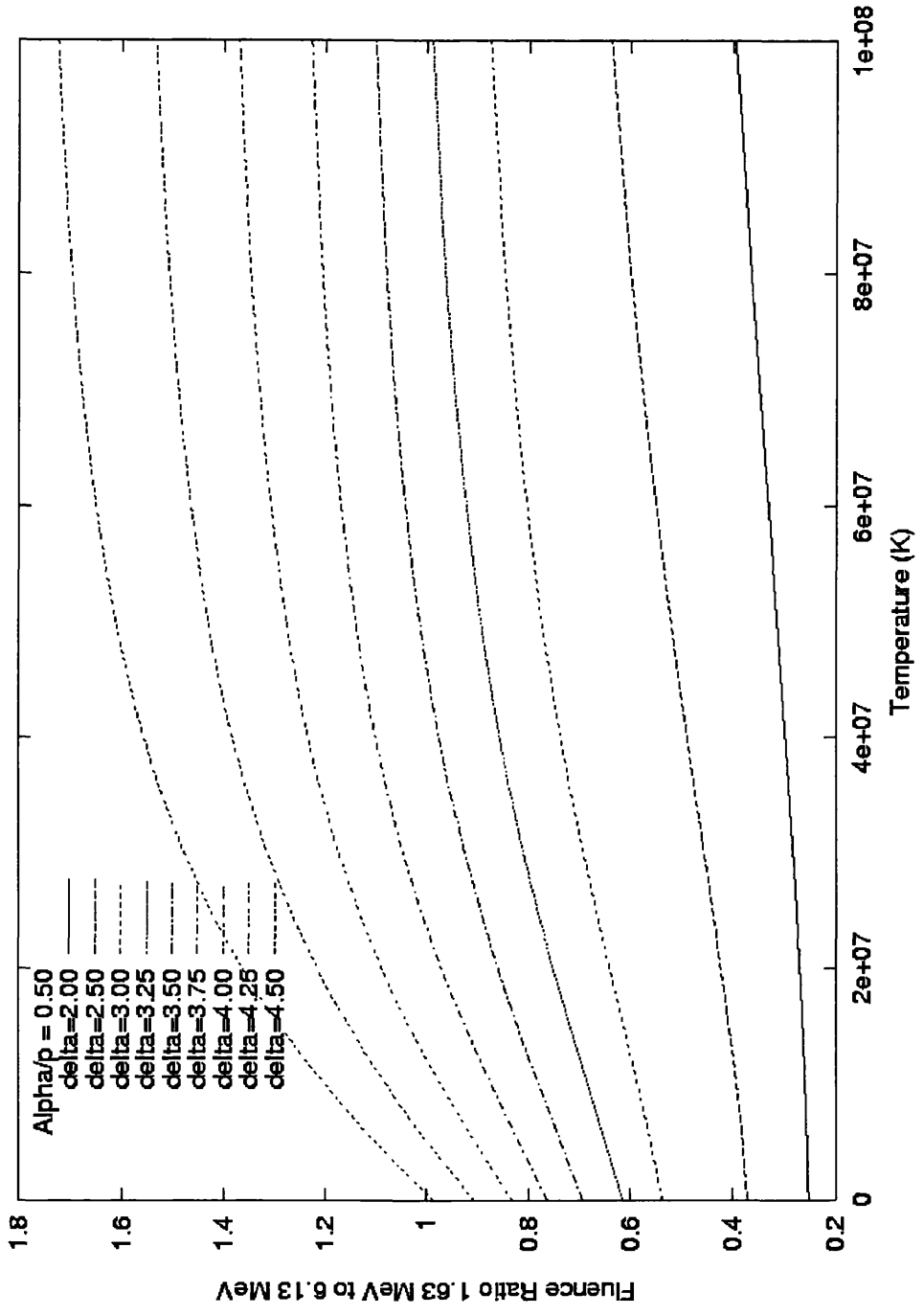

Figure 4.2: As Figure 4.1 except α's are over-abundant: $\alpha/p = 0.5$.

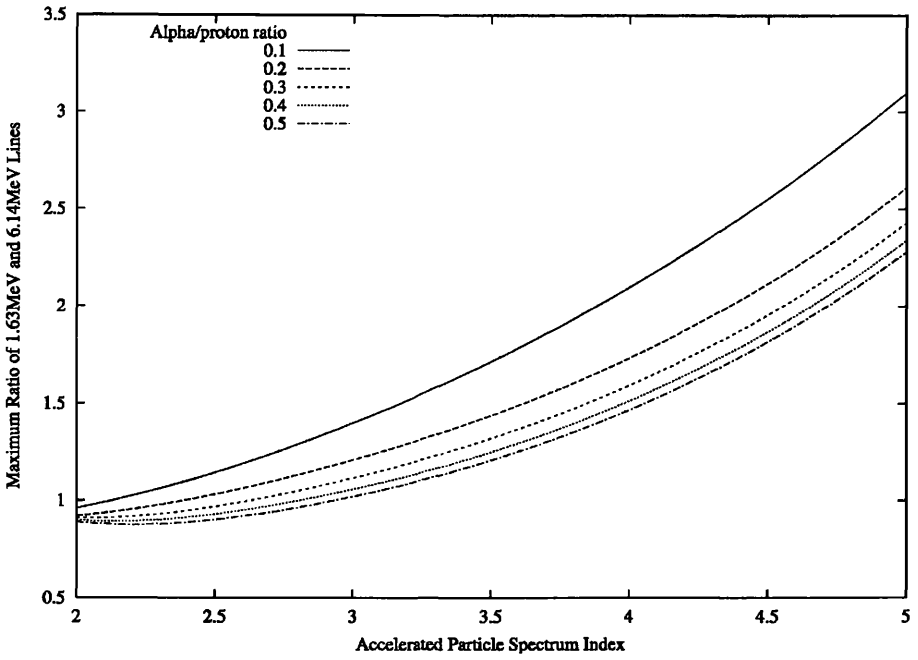

Figure 4.3: The maximum value of $\Phi_{1.63}/\Phi_{6.13}$ enhanced by the warm target model as it depends on the accelerated particle spectrum index delta, for a range of values of fast α-particle abundance relative to protons.

values obtained assuming a cold target (e.g. Ramaty et al. (1996b); the extreme left-hand edges of Figures 4.1 and 4.2), and the maximum possible warm target enhancement (Figure 4.3). The α/p ratio may be established from, say, analysis of $\alpha - \alpha$ lines such as the ^{7}Be and ^{7}Li lines in the 0.4 - 0.5 MeV range (Murphy et al. 1990a). With given α/p, measured values lying above the curve of Figure 4.3 demand relative abundances of ^{20}Ne and ^{16}O that differ significantly from the values assumed here.

4.7 Examples of Applications

At first sight it might seem that such a contained source would allow us to interpret measurements of $\Phi_{1.63}/\Phi_{6.13}$ in terms of a flatter ion distribution than that found for a cold target, and thus one containing fewer ions and less energy in total. However, the Coulomb logarithm Λ tends to be greater in an ionized target (Appendix A). Specific examples are necessary to see whether these two effects conspire to imply increased or decreased ion numbers, compared to a cold, neutral target.

Share & Murphy (1995) found values of $\Phi_{1.63}$ and $\Phi_{6.13}$ in 19 flares observed by SMM between 1981 and 1989. Most values of the fluences in these lines lay in the range 10 - 30 photons.cm^{-2}, with most associated values of $\Phi_{1.63}/\Phi_{6.13}$ in the range 1.0 to 1.4. Taking a typical value of $\Phi_{1.63} = 18$ photons.cm^{-2} and $\Phi_{1.63}/\Phi_{6.13} = 1.4$, representing the high end of the observed range, we now give some illustrations of how a warm target source could influence deductions of flare ion energy distribution and total content.

First we discuss the reference case of a cold, neutral target. We illustrate the influence of fast α abundance by considering two cases, with fast α to proton abundances (denoted α/p) of 0.1 and 0.5 (i.e. the number of α's above 1 MeV.nucleon^{-1} is 0.1 or 0.5 times the number of protons above 1 MeV). The above combination of $\Phi_{1.63}$ and $\Phi_{6.13}$ are produced for $\delta \simeq 4.4$ ($\alpha/p = 0.1$) or $\delta \simeq 5.3$ ($\alpha/p = 0.5$). Denote by N_p the number of protons above 1 MeV. Corresponding values of N_p are 7×10^{36} and 9×10^{36} for $\alpha/p = 0.1$ and 0.5, respectively, with numbers of alphas implied by α/p. Note how assuming a greater abundance of fast α's forces us to a steeper energy distribution, and thus to greater numbers of accelerated ions.

Now compare with the case of a fully ionized but cold target. Our illustrative line fluences are produced by $\delta \simeq 4.5$ and $N_p \simeq 2.7 \times 10^{37}$ (α/p = 0.1); and $\delta \simeq 5.4$ and $N_p \simeq 3.6 \times 10^{37}$ (α/p = 0.5). The ion energy distributions are close to those found assuming a neutral target, but the different values of Λ mean significantly greater numbers of ions are needed.

Next we consider the influence of a high temperature, contained source. With α/p = 0.1, a temperature of just 2×10^7 K, quite in line with inferences from other data, lets us interpret the adopted fluences as resulting from $\delta \simeq 4$ and $N_p \simeq 6.4 \times 10^{36}$ K. No more ions are needed than in the neutral target case, but the ion energy distribution is harder. An even hotter source would imply a still harder distribution, with correspondingly reduced ion numbers and energy, e.g. for $T = 6 \times 10^7$ K and $\delta = 3.5$, $N_p \simeq 10^{36}$, almost an order of magnitude down on those found in the neutral target.

Observations of the Li and Be formation lines give independent information on flare α acceleration, often appearing stronger than expected and indicating an enhanced fast α abundance, e.g. α/p = 0.5 (Murphy et al. 1991; Share & Murphy

N_α/N_p	δ	$T(K)$	N_p	*proton energy(ergs)*	$p+\alpha$ *energy(ergs)*
0.1	4.5	0	2.7×10^{37}	5.5×10^{31}	7.7×10^{31}
0.5	5.4	0	3.4×10^{37}	6.5×10^{31}	1.9×10^{32}
0.1	4.0	2×10^7	6.0×10^{36}	1.5×10^{31}	2.1×10^{31}
0.1	3.5	6×10^7	1×10^{36}	2.7×10^{30}	3.8×10^{30}
0.5	4.5	2×10^7	4.5×10^{36}	1×10^{31}	3.1×10^{31}

Table 4.1: Illustrative sets of parameters consistent with $\Phi_{1.63} = 18$ cm^{-2} and $\Phi_{6.13}/\Phi_{1.63} = 1.4$

1998). It is clear from Figure 4.3 that we then need $\delta > 4$ to obtain such a high $\Phi_{1.63}/\Phi_{6.13}$ but, again, allowing even moderate source temperatures results in a reduction of fast ion numbers: just $T = 2 \times 10^7$ K lets us reduce δ to 4.5, and N_p to $\simeq 4.5 \times 10^{36}$, for example. In this case ion numbers and energies are comparable to those deduced assuming a neutral target (more precisely, smaller by a factor of about two). Although the overall importance of fast ions in the flare process is little changed, we still reach significantly different conclusions about the products of the ion accelerator.

All of the above examples rest on our assumed value for the source ^{20}Ne/^{16}O abundance ratio, a quantity that can evidently vary significantly, even within a single active region (e.g. Schmelz et al. (1996)). Other possibilities are opened up if we felt it necessary to insist on a different, particular value for this abundance ratio. And in a real event, other quantities like the observed α - α line fluences would enter the discussion in a more crucial way.

Table 4.1 summarizes the properties of the above examples. Energies quoted there are those in ions above 1 MeV.nucleon^{-1} kinetic energy.

4.8 ^{20}Ne Abundance and Partial Trapping

Ramaty et al. (1996b) deduced δ in several flares from the ratio $\Phi_{2.223}/\Phi_{4.44}$. They found consistency with the values of δ deduced from $\Phi_{1.63}/\Phi_{6.13}$ only by assuming an enhanced ^{20}Ne abundance, ^{20}Ne/^{16}O = 0.25 as opposed to the more standard value of 0.14. Might a warm target enhancement of $\Phi_{1.63}$ reconcile its observed

brightness with the standard ^{20}Ne abundance, even if containment is not perfect as assumed in the foregoing?

Figures 4.1, 4.2 and 4.3 together show that the necessary enhancement is certainly possible in principle for a fully contained source. We have also investigated a partial trapping situation in which some ions (possibly those accelerated with pitch angles inside the loss cone) precipitate immediately, while the remainder produce a trapped, warm target yield over a longer period. In such a situation there would be an impulsive component to γ-ray line emission, as observed, but event-integrated fluences would also include a more gradual, warm target component. The total thick-target yield in any line is then just a linear combination of the warm, ionized and cold, neutral target yields. Suppose for illustration that 0.5 of all accelerated ions are trapped in a coronal warm target, while the remainder precipitate to the cold, neutral atmosphere. Combining the calculations of the warm and cold target yields, we find that $\Phi_{1.63}/\Phi_{6.13}$ can still be enhanced significantly, for instance by 43% for $\delta = 3.75$ and $T = 6 \times 10^7$ K. If we interpreted this fluence increase solely as resulting from a ^{20}Ne abundance enhancement, we would deduce $^{20}\mathrm{Ne}/^{16}\mathrm{O} = 0.20$ as opposed to the value of 0.14 used in these calculations. Of course larger fractions of trapped ions would lead to larger apparent ^{20}Ne abundance enhancements.

Suppose now that all ions are contained in a warm target for a period of time significantly shorter than their warm target stopping times but longer than their loop transit times (so that we do not simply revert to the results of Emslie et al. (1997). Ions will produce only some fraction of their warm, thick target line yields before precipitating. Might the precipitated distribution nevertheless be softened such as to produce enhanced 1.63 MeV flux from the cold neutral target?

A detailed discussion of this question will be presented elsewhere along with a study of warm target line flux temporal evolution. Here we give an approximate treatment containing the essential features.

For few MeV protons in 10^7 to 10^8 K plasmas, the 'warm target' energy loss rate approximation of Tamres et al. (1986) applies (Equation 4.8 and see also MacKinnon (1989)), and we have approximately

$$\frac{dE}{dt} = -0.1nT^{-3/2}E \tag{4.11}$$

Here we have set $\Lambda = 25$ as a representative value for the few MeV energy range (Appendix A). This expression does not hold exactly for all ion energies of possible interest, but serves our semi-quantitative purposes here.

Consider now the evolution of the proton distribution in a homogeneous, confined warm target region. Let $N(E,t)$ denote the number of protons in the region per unit proton energy E at time t. Solving the continuity equation

$$\frac{\partial N}{\partial t} + \frac{\partial}{\partial E}\left[\frac{dE}{dt}N\right] = 0 \tag{4.12}$$

with the energy loss rate of Equation 4.11 and initial condition

$$N(E, t=0) = AE^{-\delta} \tag{4.13}$$

we find

$$N(E,t) = AE^{-\delta}e^{(1-\delta)K't} \tag{4.14}$$

Here $K' = 0.1nT^{-3/2}$.

Equation 4.14 has one slightly surprising feature: protons in the appropriate energy range trapped in a warm target region retain the same energy distribution. Trapping them in a warm target region for some period of time before precipitation will make no important difference to the form of the precipitated energy distribution, only to the numbers of protons found above any given energy. While this evolved distribution is softer than that obtained by letting protons evolve in a cold target, it is not different from the injected distribution.

Suppose that all ions are injected into a fully contained warm target, but that containment breaks down after some time t. Because the form of the ion distribution does not change, we may then apply the same linear combination of warm and cold target yields described above to calculate the resulting line fluence ratios. Specifically, after a time t, a fraction $1 - e^{(1-\delta)K't}$ of the warm target yield has been produced, and a fraction $e^{(1-\delta)K't}$ of the neutral target yield from the same energy distribution will subsequently be produced. The results quoted above, for the case that half the ions are trapped in a warm target region and the other half precipitate immediately to the neutral atmosphere, will apply if trapping ceases at a time $\ln 2/(1-\delta)K'$. For example, such a situation applies

after 130 s, scaling in inverse proportion to density, with $\delta = 3.5$, $n = 10^{10}$ cm^{-3}, $T = 6 \times 10^7$ K. Particularly with coronal densities rather higher than this, breakdown of coronal containment after just a few 10s of seconds will result in an admixture of cold and warm target line yields apparently implying a significantly higher ^{20}Ne abundance. At the upper end of the acceptable range this effect apparently offers a possible explanation of the apparent high ^{20}Ne abundance found e.g. in Ramaty et al. (1996b) which remains consistent with impulsive phase time profiles.

4.9 Conclusions and Discussion

We have reconsidered the possible role of warm target effects in the interpretation of flare de-excitation γ-ray line fluxes. Our key finding is that temperatures of just a few $\times 10^7$ K, no higher than flare coronal temperatures diagnosed by other means, are high enough to preferentially increase the coronal lifetimes of significant numbers of the protons which can excite the 1.63 MeV line of ^{20}Ne. This effect is lessened when fast alphas are overabundant but still occurs to a significant degree. Effective coronal trapping of flare protons is a necessary precondition for warm target effects to be significant, however; otherwise we revert to the situation treated in detail by Emslie et al. (1997), in which warm target effects were shown to be unimportant. When other factors indicate that such trapping may be occurring, deductions of proton (ion) energy distribution, and/or ^{20}Ne abundance, need to respect this possibility. It should also be considered in any comprehensive attempt to determine the partitioning of flare energy between mass motion, bulk heating and the acceleration of ions and/or electrons. Trapping of ions in a warm target region for long enough for them to produce at least half of their total, warm target line yield may remove the need for an anomalously high ^{20}Ne abundance.

We recalled various factors that might contain a significant fraction of flare-accelerated protons in the corona. Most important is the possibility that the proton distribution itself drives unstably growing Alfvén waves. Protons will inevitably become anisotropic as they travel away from a localized flaring region, and only a modest anisotropy is needed for unstable wave growth with typical

γ-ray producing proton numbers Tamres et al. (1989). This self-containing behaviour seems difficult to avoid in large flares. At least in one SMM flare its occurrence seems almost inescapable (Smith & Brecht 1991), unless MHD turbulence plays no role in ion acceleration.

We also need, however, to acknowledge that various other findings argue against a coronally contained, nearly isotropic ion distribution, at least in some flares. Observations of red-shifted lines argue that the fast ion pitch-angle distribution is significantly anisotropic, consistent with precipitation of most ions into the photosphere (Share et al. 2002; Smith et al. 2003). An ion population self-contained via MHD turbulence would still exhibit some residual anisotropy (Kulsrud & Pearce 1969) but detailed discussion of the magnitude of this effect lies outside the scope of this chapter.

The magnitude of fast ion stopping times, easily in excess of 100 s for γ-ray producing ions in coronal conditions, also constitute a potential difficulty for any model which involves coronal production of γ-rays. Deexcitation γ-ray lines exhibit at least a component that is clearly impulsive in nature (e.g. Chupp (1984)), suggesting ions stop on shorter timescales, and detailed modelling apparently requires rapid ion precipitation (Hua et al. 1989). For the modest temperatures suggested in section 3.3, warm target effects are not significantly worse off in this respect. The relative contributions to total flare γ-ray line fluences of impulsive and gradual components remain uncertain, apparently, so any further discussion is probably premature at this point. We note that sources with partial containment or containment that ceases to be effective at some point might allow warm target effects to be important for interpreting line fluences without contradicting observed temporal behaviour. The warm target source studied here will display a characteristic sort of behaviour, with lines sensitive to lower energy ions decaying more gradually than in a cold target source. Detailed modelling of the expected temporal behaviour may yield tests of these ideas, and will be carried out elsewhere.

So far all detected solar γ-rays have been from large flares. No doubt we are seeing only the large event end of the distribution of γ-ray flare sizes. Conclusions about the likelihood of proton self-containment also rest, thus far, on analyses of large flares. In more modest events fast protons may be sufficiently dilute not to

drive unstable Alfvén wave growth, and proton containment in hot regions may only occur to a lesser degree. A dependence on flare size of $\Phi_{1.63}/\Phi_{6.13}$ would argue strongly in favour of the scenario outlined here.

Chapter 5

Unravelling α-particle and Proton Energies

5.1 Introduction

In this chapter I investigate the interpretation of observed narrow nuclear line fluences without making Assumption A (see Section 2.5.4). I concentrate particularly on the use of the deexcitation line diagnostic $\Phi_{1.63}/\Phi_{6.13}$. In subsection 5.2 I allow protons and α's to have different values of δ and show how we may still, in principle constrain all the parameters describing the proton and α distributions. In subsection 5.3 I apply these procedures to some of the best-observed γ-ray events in the SMM/GRS dataset. Subsection 5.4 gives a concluding discussion, in particular considering some implications of our findings for particle acceleration and the overall role of fast ions in the flaring process.

5.2 Diagnosis of Fast Proton and α Distributions: Method

5.2.1 Calculation of Line Fluences

Consider the production of narrow, nuclear de-excitation lines consequent to the injection of a population of fast protons and α particles into the solar atmosphere during a flare. Assume a thick target source, i.e. one from which no particles escape, so that the number of particles necessary to produce a given set of lines will be minimized. Let $F_i(E)$ denote the energy distribution of particles of species i (i = protons or α's), i.e. $F_i(E)\mathrm{d}E$ is the total (flare-integrated) number of particles of species i with energies between E and $E + \mathrm{d}E$ (measured in MeV.nucleon^{-1}). The fluence at Earth Φ_ϵ (cm^{-2}) in a narrow line at energy ϵ, resulting from

de-excitation of nuclear species X is given by (see Chapter 3)

$$\Phi_\epsilon = \frac{a_X}{4\pi D^2} \sum_i \int_{E_{0i}}^{\infty} \frac{\sigma_{i,\epsilon}(E)}{|\mathrm{d}E_i/\mathrm{d}N|} \Psi_i(E) \mathrm{d}E \tag{5.1}$$

where a_X is the abundance relative to hydrogen of (target) species X, D is the Astronomical Unit, $\sigma_{i,\epsilon}$ is the cross-section for production of the line at ϵ by fast particles of species i and energy E (MeV.nucleon^{-1}), $\mathrm{d}E_i/\mathrm{d}N$ is the rate at which fast particles of species i lose energy per unit hydrogen column depth N (cm^{-2}), and $\Psi_i(E)$ is the cumulative distribution of species i at energy E, i.e.

$$\Psi_i(E) = \int_E^{\infty} F_i(E) \mathrm{d}E$$

In deriving Equation 5.1, spatially homogeneous abundances a_X are assumed. For narrow lines, the index i sums over protons and α particles.

In what follows we assume power-law energy distributions for the accelerated particles, so that

$$\Psi_i(E) = F_{0,i} \left(\frac{E}{E_0} \right)^{1-\delta_i} \tag{5.2}$$

$F_{0,i}$ is the total number of particles of species i injected at energies $\geq E_0$ and we allow for the possibility $\delta_\alpha \neq \delta_p$. We always adopt the same E_0 (in MeV.nucleon^{-1}) for both species, so that $F_{0,\alpha}/F_{0,p}$ measures the abundance of α particles relative to protons in the accelerated ion population (this quantity is a precise equivalent of the abundance of fast α's relative to fast protons, previously denoted α/p). We use the empirically derived energy loss rates of Barkas & Berger (1964) (see also Appendix A and MacKinnon & Toner (2003)), appropriate to a cold, neutral medium (i.e. the chromosphere or photosphere).

The procedure described below employs numerical calculations of line fluences using Equations 5.1 and 5.2. Cross-section data come from Kozlovsky et al. (2002), or in some cases from our own digitizations of the original measurements cited by them. We will also use a standard set of source abundances: $a_{^{20}Ne} = 1.90 \times 10^{-4}$, $a_{^{16}O} = 1.39 \times 10^{-3}$, $a_{^{56}Fe} = 1.88 \times 10^{-4}$, $a_{^4He} = 0.1$. In this we follow previous discussions of the significance of ratios of pairs of lines (e.g. Ramaty et al. 1996b).

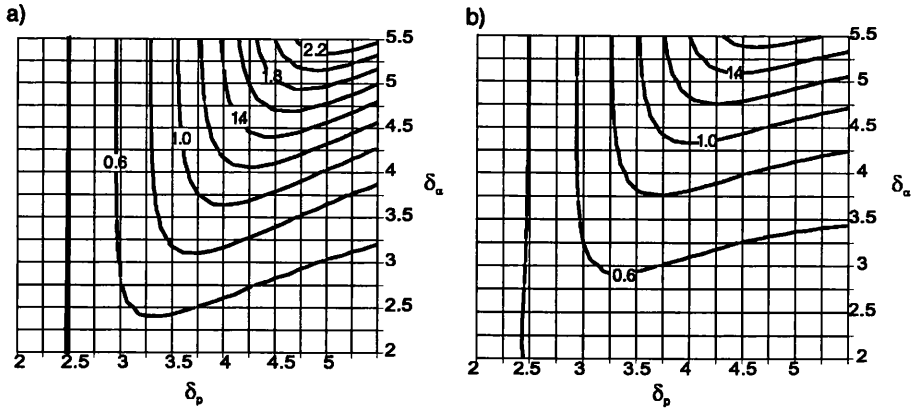

Figure 5.1: Contours of constant $\Phi_{1.63}/\Phi_{6.13}$ for (a) $F_{0,\alpha}/F_{0,p} = 0.1$ (b) $F_{0,\alpha}/F_{0,p} = 0.5$. Each contour is labelled with the value of $\Phi_{1.63}/\Phi_{6.13}$ it represents.

5.2.2 De-excitation Line Ratio Diagnostics Without Assumption A

As reviewed in Section 2.5.4, key diagnostics include the 1.63 MeV line from ^{20}Ne, any deexcitation line with a higher threshold for proton excitation (we follow Ramaty et al. (1996b) and use the 6.13 MeV line of ^{16}O, for which spallation contributions from other species are minimized), and the lines from the α fusion reactions that make ^{7}Li and ^{7}Be, at 0.429 and 0.478 MeV, giving a single feature in the 0.4 to 0.5 MeV photon energy range.

Because the 1.63 MeV line is not similarly distinguished from other lines when excited by α-particles, a given, observed value of $\Phi_{1.63}/\Phi_{6.13}$ implies larger and larger values of δ for larger and larger values of the α/p relative fast α abundance (Ramaty et al. 1996b). Moreover, the large, observed values of $\Phi_{0.4-0.5}$ (Murphy et al. 1991; Share & Murphy 1997, 1998), the spectral feature resulting from α fusion reactions forming ^{7}Li and ^{7}Be, together with Assumption A, have been taken to imply large α-particle numbers, possibly α/p as high as 0.5.

I have calculated $\Phi_{1.63}/\Phi_{6.13}$ without making Assumption A, for values of δ_p and δ_α lying between 2 and 6. I show contours of $\Phi_{1.63}/\Phi_{6.13}$ in $(\delta_p, \delta_\alpha)$ space, assuming $F_{0,\alpha}/F_{0,p} = 0.1$ (Fig. 5.1(a)) and 0.5 (Fig. 5.1(b)). A measured value of $\Phi_{1.63}/\Phi_{6.13}$ constrains δ_p and δ_α to lie along a single curve in $(\delta_p, \delta_\alpha)$ space. Figures 5.1 provide a possible starting point for interpretation of the 1.63 and 6.13 MeV lines in a way that can generalize the approach of, e.g., Ramaty et al. (1996b).

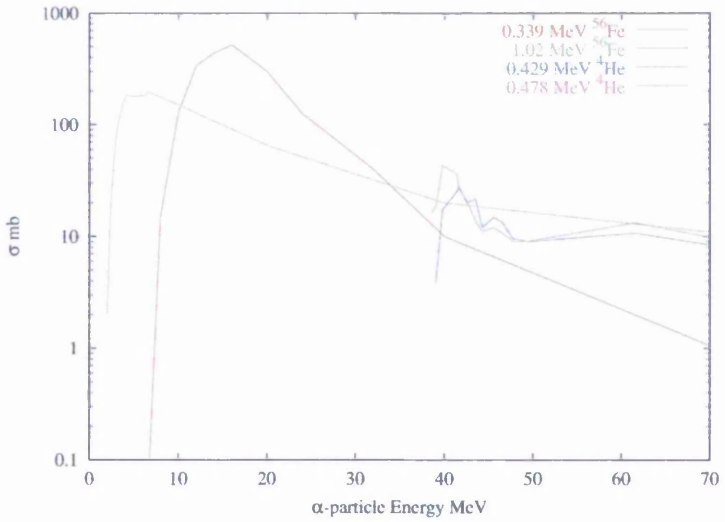

Figure 5.2: A comparison plot of the nuclear excitation cross-sections for interactions between α-particles and ^{56}Fe nuclei, giving rise to the 0.339 and 1.02 MeV lines, and for the $\alpha - \alpha$ fusion reactions that produce the spectral feature between 0.4 and 0.5 MeV.

However, a closer look at the details of production of $\Phi_{0.4-0.5}$, taken with the information in Figures 5.1, proves rewarding. It is easy to see from Equation 5.1 that the photon yield per injected particle in any one line falls off monotonically with δ. In these calculations, then, with fixed $F_{0,\alpha}/F_{0,p}$, α-particles become irrelevant to the value of $\Phi_{1.63}/\Phi_{6.13}$ in the limit $\delta_\alpha \gg \delta_p$, and *vice versa*. As a consequence there are wide ranges of values for δ_p and δ_α separately that are excluded for any observed $\Phi_{1.63}/\Phi_{6.13}$. In particular, a given, measured value of $\Phi_{1.63}/\Phi_{6.13}$ implies *minimum* values of both δ_p and δ_α. Comparing Figs. 5.1 (a) and (b) we see that an increased proportion of α particles increases the minimum δ_α required to satisfy any specific observation.

The cross-sections for the 0.429 and 0.478 MeV lines, which merge to give the 0.4 to 0.5 MeV feature, both have thresholds around 10 MeV.nucleon^{-1} (Kozlovsky et al. 2002). This is significantly higher than typical threshold energies for direct excitation of deexcitation lines in α-particle collisions with heavier nuclear species as shown in Figure 5.2. Assuming a value of the source ^{4}He, detailed calculation (Figure 5.3) shows that a measured value of $\Phi_{0.4-0.5}$ tells us, to within a

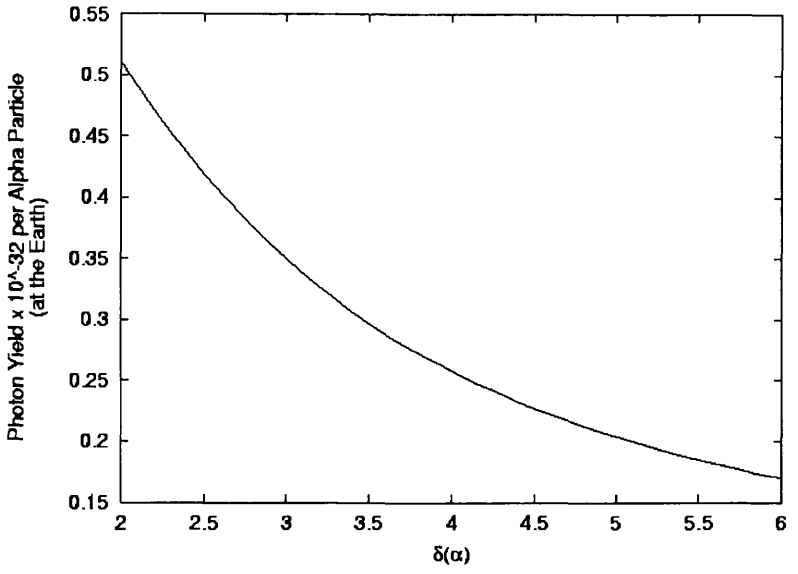

Figure 5.3: Total yield of photons in the two lines at 0.429 and 0.478 MeV, as a function of α particle energy spectral index δ_α. The yield is normalized to one α above 10 MeV.nucl^{-1}.

factor of three, the number of α-particles above 10 MeV.nucleon^{-1}. The number of α's above 1 MeV.nucleon^{-1} then follows only with an assumption about the α energy distribution. A power-law in energy, with δ_α deduced from $\Phi_{1.63}/\Phi_{6.13}$ with Assumption A, is one possibility. A value of δ_α deduced in this way depends on the number of fast α's we believe present however (Ramaty et al. 1996b). Assumption A thus couples the interpretation of these various features in a way we might prefer to avoid, if possible.

Other narrow line features, excited only in α-Fe spallation reactions, have lower energy thresholds. Specifically, lines at 0.339, 0.999 and 1.05 MeV all have diagnostic potential (Mandzhavidze et al. 1997; Share & Murphy 1998). The last two of these, together possibly with lines excited by fast ^{3}He at 0.937 and 1.042 MeV due to $^{16}O(^3He,p)^{18}F^*$ reactions, may be unresolvable in scintillator data, combining to form a feature at an energy of about 1.02 MeV (Share & Murphy 1998). The cross-sections for these ^{56}Fe features are compared with the $\alpha - \alpha$ cross-sections in Figure 5.2. Estimates of the fluences in these lines were

obtained from SMM/GRS data and interpreted in the framework of Assumption A (Share & Murphy 1998).

In fact, as long as we are prepared to proceed with an adopted set of target abundances, we can interpret such a set of line fluences without invoking Assumption A. Because the features at 0.339 and 1.02 MeV have lower α-particle energy thresholds than the lines at 0.429 and 0.478 MeV, $\Phi_{1.02}/\Phi_{0.4-0.5}$ or $\Phi_{0.339}/\Phi_{0.4-0.5}$ can give an estimate of δ_α. Any of the fluences involved, e.g. $\Phi_{0.4-0.5}$ then fixes $F_{0,\alpha}$. We can then calculate the α-particle contributions to $\Phi_{1.63}$ and $\Phi_{6.13}$ and subtract these from the observed values to determine the contributions to these lines that must be attributed to protons only. The ratio of these proton-only contributions then tells us δ_p and the absolute value of either one fixes $F_{0,\alpha}$.

We have numerically calculated $\Phi_{1.63}/\Phi_{6.13}$, assuming only fast protons are present. The following approximate expression, a numerical fit to the results of these calculations, is valid to within a few percent over the range $2 < \delta_p < 6$:

$$\delta_p = 1.1266 \left(\ln \frac{\Phi_{1.63}}{\Phi_{6.13}} - \ln \frac{a_{^{20}Ne}}{a_{^{16}O}} \right) + 1.3075 \tag{5.3}$$

Similarly, we find

$$\delta_\alpha = 0.4588 \left(\ln \frac{\Phi_{1.02}}{\Phi_{0.4-0.5}} + \ln \frac{a_{^4\mathrm{He}}}{a_{^{56}\mathrm{Fe}}} \right) + 1.7617. \tag{5.4}$$

in the case that ^{3}He makes no contribution to $\Phi_{1.02}$. These expressions allow this process to be carried out rapidly.

It may be that newer data (from RHESSI, for example) will provide detections of the 0.339 MeV line, which is not complicated by nearby lines stimulated by other accelerated ions. Given abundances of ^{4}He and ^{56}Fe, the ratio $\Phi_{0.339}/\Phi_{0.4-0.5}$ can be used to calculate δ_α more cleanly.

$$\delta_\alpha = 0.8099 \left(\ln \frac{\Phi_{0.339}}{\Phi_{0.4-0.5}} + \ln \frac{a_{^4\mathrm{He}}}{a_{^{56}\mathrm{Fe}}} \right) + 0.6359 \tag{5.5}$$

In practice the lines at 0.339, 0.999 and 1.05 MeV are not yet always clearly evident in data. Such deductions of their fluences as exist are mostly at the 1 - 2 sigma level (Share & Murphy 1998). Thus it is sometimes necessary, and possibly always desirable, to use only a measurement of $\Phi_{0.4-0.5}$ to constrain the α-particle population. Instead of deducing a single value of δ_α, one starts by assuming a range of values of δ_α. For each assumed δ_α we may carry out the

last three of the four steps described above. Some ranges of δ_α will lead to α-particle contributions to $\Phi_{1.63}$ or $\Phi_{6.13}$ that exceed the measured values, so we may eliminate these cases. With this restricted subset of the possible line fluences the problem is under-determined but we may still delineate forbidden and allowed regions of the parameter space.

We have seen that a set of measurements of $\Phi_{0.4-0.5}$, $\Phi_{1.63}$, $\Phi_{6.13}$ and $\Phi_{1.02}$ (or, even better, $\Phi_{0.999}$ or $\Phi_{1.05}$) allow deduction of separate energy spectral indices and numbers for α's and protons. In this procedure dealing only with a set of fluences, as opposed to carrying out a complete fit of the complete γ-ray spectrum, a set of abundances must be assumed. Such an assumption is also necessary in the interpretation of a single line ratio using Assumption A (e.g. Ramaty 1986; Ramaty et al. 1996b). In the next section I shall apply this procedure to sets of line fluences obtained from real data.

5.3 Application to Flares Observed by SMM/GRS

Share & Murphy (1995, 1997, 1998) studied γ-ray data obtained by the GRS instrument on SMM, and also from OSSE on the *Compton Observatory* (Murphy et al. 1997). They were able to obtain estimates of narrow line fluences in 19 SMM flares. Here we illustrate our procedure by giving results for a few of these flares. We concentrate on the flare of 27 April, 1981 from which a particularly high quality spectrum was obtained (Murphy et al. 1990b, 1991; Share & Murphy 1995, 1997), but also give results for the other events, here and in Appendix C.

For the 27 April, 1981 event Share & Murphy (1997) found $\Phi_{1.63} = 19.5 \pm 2.4$ cm^{-2}, $\Phi_{6.13} = 14.5 \pm 1.1$ cm^{-2} and $\Phi_{0.429} + \Phi_{0.478} = 37.8 \pm 10.2$ cm^{-2}. This gives three fluence measurements to constrain our model which has four parameters: δ_α, N_α, δ_p and N_p. So the data do not fully constrain the problem.

Having fixed E_0, I start by choosing a value for δ_α. This allows me to use $\Phi_{0.429}+\Phi_{0.478}$ to deduce $F_{0,\alpha}$ using equations 5.1 and 5.2. $\Phi_{1.63}$ and $\Phi_{6.13}$ depend on the distribution of α-particles thus found and also on the distribution of protons. However, using the chosen value of δ_α and the corresponding $F_{0,\alpha}$, I can calculate the contribution to $\Phi_{1.63}$ and $\Phi_{6.13}$ due to excitation in α-particle interactions and subtract this from the measured line fluences, leaving a measure of the proton-

excited contribution to each line. If this remaining fluence is not negative, we have a physical solution. Equation 5.3 can be used to define the relationship between the ratio of the proton-induced fluences and the index δ_p of the proton distribution. I then use this δ_p to calculate the expected fluence per proton and derive $F_{0,p}$ from the measured proton-induced fluences. $\frac{F_{0,\alpha}}{F_{0,p}}$ follows.

Table 5.1 illustrates the results of this approach for a range of δ_α. Errors are calculated, for each δ_α, via simple linear propagation of errors at each step. These are probably only indicative, but give some sense of likely uncertainties without undertaking a full map of confidence regions in the full parameter space. There is a summary of results of this kind for all of the SMM X-class flares in Appendix C.

Consider first the 27 April 1981 flare. Values of $\delta_\alpha < 3.5$ yield consistent explanations of the three fluences. $\Phi_{0.4-0.5}$ constrains only the number of α's above 10 MeV.nucleon^{-1}. Small δ_α (e.g. 2.5) then results only in small numbers of α's above 1 MeV.nucleon^{-1}, as the flat α energy distribution is extrapolated to lower energies. Because $F_{0,\alpha}/F_{0,p}$ is so small in consequence, α's have little influence on $\Phi_{1.63}/\Phi_{6.13}$. δ_p and $F_{0,p}$ are then almost independent of the assumed δ_α. In particular, values of δ_p in the range 4.2 - 4.5 are favoured, similar to previous deductions (Ramaty et al. 1996b, - with no Ne/O abundance enhancement). As we consider an increasing sequence of δ_α values, however, extrapolation to 1 MeV of the $\Phi_{0.4-0.5}$ data point implies greater and greater numbers of α's. For $\delta_\alpha >\sim 3$, the α contribution to $\Phi_{6.13}$ starts to become comparable to the proton contribution, and if we let δ_α increase to 3.5, there are sufficient α's in the 1 to 10 MeV.nucleon^{-1} energy range to account completely for $\Phi_{6.13}$. The proton energy distribution becomes extremely steep so that protons continue to account for some of $\Phi_{1.63}$. Naturally, uncertainties associated with the proton energy distribution also become very large. A picture with only very modest numbers of protons would be consistent with the data in this limit.

For comparison, I also show deductions of α and proton numbers and total energy using Assumption A and $\alpha/p = 0.5$ (see Figure 5.4). As anticipated, ion energy distributions are softer and total ion energy content greater using Assumption A, except possibly in the limit when α's dominate in forming the observed line spectrum and proton energy content is consequently only poorly constrained.

Flare	δ_α	$F_{0,\alpha}$	δ_p	$F_{0,p}$	$\frac{F_{0,\alpha}}{F_{0,p}}$	Ion Energy (erg)
1981	2.125	$(1.1 \pm 0.3) \times 10^{34}$	$4.35^{+0.66}_{-0.56}$	$(6.8^{+14}_{-4.5}) \times 10^{36}$	$0.0016^{+0.0031}_{-0.0011}$	$(1.6^{+1.8}_{-0.8}) \times 10^{31}$
April 27	2.250	$(1.5 \pm 0.4) \times 10^{34}$	$4.35^{+0.68}_{-0.58}$	$(6.8^{+14}_{-4.6}) \times 10^{36}$	$0.0022^{+0.0045}_{-0.0015}$	$(1.6^{+1.8}_{-0.8}) \times 10^{31}$
	2.375	$(2.1 \pm 0.6) \times 10^{34}$	$4.37^{+0.71}_{-0.60}$	$(6.9^{+16}_{-4.7}) \times 10^{36}$	$0.0030^{+0.0065}_{-0.0021}$	$(1.6^{+1.9}_{-0.8}) \times 10^{31}$
	2.500	$(2.9 \pm 0.8) \times 10^{34}$	$4.4^{+0.7}_{-0.6}$	$(7.1^{+17.7}_{-4.9}) \times 10^{36}$	$0.0041^{+0.0132}_{-0.0032}$	$(1.6^{+1.9}_{-0.8}) \times 10^{31}$
	2.625	$(4.0 \pm 1.1) \times 10^{34}$	$4.44^{+0.84}_{-0.67}$	$(7.4^{+21}_{-5.3}) \times 10^{36}$	$0.0055^{+0.0141}_{-0.0041}$	$(1.7^{+2.6}_{-0.9}) \times 10^{31}$
	2.750	$(5.6 \pm 1.5) \times 10^{34}$	$4.49^{+0.95}_{-0.72}$	$(7.8^{+28}_{-5.8}) \times 10^{36}$	$0.0071^{+0.0210}_{-0.0056}$	$(1.8^{+3.5}_{-1.0}) \times 10^{31}$
	2.875	$(7.8 \pm 2.1) \times 10^{34}$	$4.57^{+1.15}_{-0.80}$	$(8.6^{+41}_{-6.6}) \times 10^{36}$	$0.0091^{+0.0317}_{-0.0075}$	$(1.9^{+5.0}_{-1.1}) \times 10^{31}$
	3.000	$(1.1 \pm 0.3) \times 10^{35}$	$4.7^{+1.5}_{-0.9}$	$(9.7^{+78.7}_{-7.9}) \times 10^{36}$	$0.011^{+0.065}_{-0.010}$	$(2.2^{+7.3}_{-1.3}) \times 10^{31}$
	3.125	$(1.5 \pm 0.4) \times 10^{35}$	$4.85^{+2.57}_{-1.07}$	$(1.2^{+?}_{-1.0}) \times 10^{37}$	$0.0129^{+0.0766}_{-0.0129}$	$(2.6^{+?}_{-1.5}) \times 10^{31}$
	3.250	$(2.1 \pm 0.6) \times 10^{35}$	$5.11^{+?}_{-1.33}$	$(1.6^{+?}_{-1.4}) \times 10^{37}$	$0.0133^{+0.1240}_{-?}$	$(3.4^{+?}_{-?}) \times 10^{31}$
	3.375	$(2.9 \pm 0.8) \times 10^{35}$	$5.59^{+?}_{-1.81}$	$(2.8^{+?}_{-2.6}) \times 10^{37}$	$0.0105^{+0.2095}_{-?}$	$(5.7^{+?}_{-?}) \times 10^{31}$
	3.500	$(4.0 \pm 1.1) \times 10^{35}$	$7.1^{+?}_{-3.3}$	$(1.5^{+?}_{-1.5}) \times 10^{38}$	$0.0027^{+0.48}_{-?}$	$(5.6 \pm ?) \times 10^{32}$
A	5.2	4.4×10^{36}	5.2	8.8×10^{36}	0.5	5.5×10^{31}
1986	2.5	$(3.8 \pm 58) \times 10^{32}$	$3.4^{+0.7}_{-0.8}$	$(5.4^{+20}_{-4.8}) \times 10^{35}$	$0.0007^{+0.100}_{-0.0029}$	$(1.5^{+1.6}_{-1.0}) \times 10^{30}$
February 6	3.0	$(1.4 \pm 22) \times 10^{33}$	3.4 ± 0.9	$(5.4^{+27}_{-5.0}) \times 10^{35}$	$0.0027^{+0.60}_{-0.0089}$	$1.5^{+1.9}_{-1.1} \times 10^{30}$
	3.5	$(5.3 \pm 81) \times 10^{33}$	$3.4^{+1.2}_{-1.3}$	$(5.4^{+53}_{-5.3}) \times 10^{35}$	$0.0099^{+7.5}_{-0.023}$	$(1.5^{+2.7}_{-1.1}) \times 10^{30}$
	4.0	$(1.9 \pm 30) \times 10^{34}$	$3.4^{+2.2}_{-2.3}$	$(5.3^{+241}_{-5.3}) \times 10^{35}$	$0.037^{+1150}_{-0.048}$	$(1.5^{+?}_{-2.2}) \times 10^{30}$
A	4.1	4.3×10^{35}	4.1	8.6×10^{35}	0.5	6.1×10^{30}
1989	2.5	$(9.4 \pm 4.9) \times 10^{33}$	$4.5^{+4.3}_{-1.5}$	$(2.6^{+?}_{-2.4} \times 10^{36}$	$0.0037^{+0.12}_{-0.0037}$	$(5.8^{+?}_{-4.4}) \times 10^{30}$
May 3	3.0	$(3.6 \pm 1.9) \times 10^{34}$	$5.0^{+?}_{-2.2}$	$(4.1^{+?}_{-4.1}) \times 10^{36}$	$0.0086^{+1.3}_{-?}$	$(9.0 \pm ?) \times 10^{30}$
	3.375	$(9.5 \pm 5.0) \times 10^{34}$	$7.5^{+?}_{-5.7}$	$(7.7^{+?}_{-7.7}) \times 10^{37}$	$0.0012^{+180}_{-?}$	$(1.5 \pm ?) \times 10^{32}$
A	5.2	1.4×10^{36}	5.2	2.8×10^{36}	0.5	1.8×10^{31}
1989	2.5	$(1.4 \pm 0.5) \times 10^{34}$	$5.3^{+?}_{-2.2}$	$(6.3^{+?}_{-6.2}) \times 10^{36}$	$0.0022^{+0.21}_{-?}$	$(1.3 \pm ?) \times 10^{31}$
November 15	2.875	$(3.8 \pm 1.5) \times 10^{34}$	$7.3^{+?}_{-4.5}$	$(6.4^{+?}_{-6.4}) \times 10^{37}$	$0.00059^{+1.8}_{-?}$	$(1.2 \pm ?) \times 10^{32}$
A	5.2	1.4×10^{36}	5.2	2.7×10^{36}	0.5	1.7×10^{31}

Table 5.1: Solutions for SMM/GRS flare spectra, choosing a range of values for δ_α and using the fluences given in Share & Murphy (1997). Above the largest δ_α shown for each flare, there was insufficient line fluence to accommodate the α-induced emission, except in the case of the 1986 February 6 flare for which solutions were possible throughout the range of δ_α investigated. Linear propagation of the quoted observation error bars led to the errors quoted here. A '?' in the error indicates that the value was not obtainable by this method. A more complete statistical treatment of errors is beyond the scope of the present work. For comparison, the last line for each flare, labelled 'A', gives the result which would have been obtained from $\Phi_{1.63}$, $\Phi_{6.13}$ and Assumption A with $\alpha/p = 0.5$

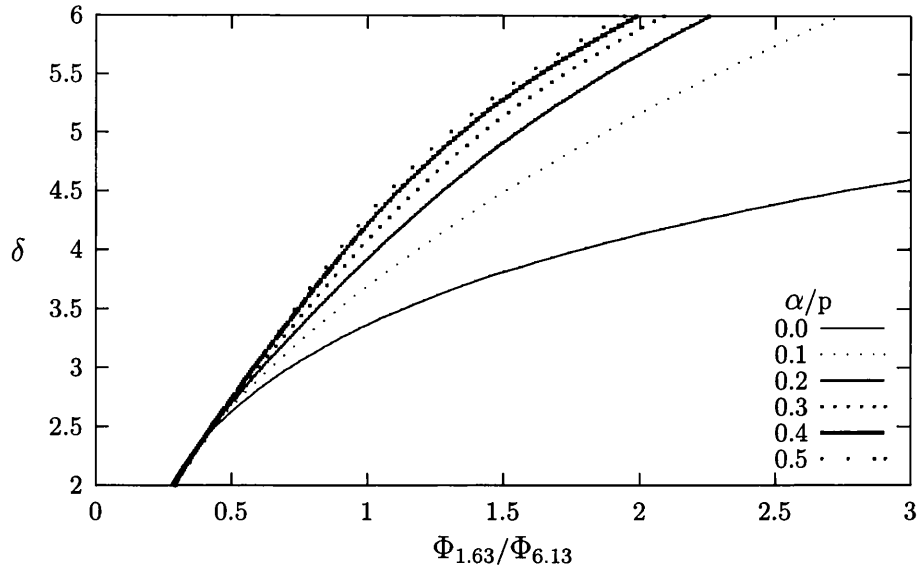

Figure 5.4: The accelerated particle power law index δ as a function of the fluence ratio of the 1.63 and 6.13 MeV lines making Assumption A. The curves show different assumed values for α/p.

The steep slope required for the accelerated proton distribution is partly a consequence of the choice of the abundance ratio of ^{20}Ne to ^{16}O. The calculations here make use of 'standard' photospheric abundances, but the abundance of ^{20}Ne is problematic as it is often found to vary by up to a factor of 3 in many different flare-associated measurements (Murphy et al. 1991; McKenzie & Feldman 1992; Saba & Strong 1993; Widing & Feldman 1995; Schmelz et al. 1996) and has not been measured in the photosphere (it is too cool to excite ^{20}Ne emission Sheeley, Jr. 1996) where various estimates are employed.

Ramaty et al. (1996b) find the value of 0.25 for the ^{20}Ne to ^{16}O abundance ratio to be consistent with the proton distributions deduced from the ratio between the neutron capture line at 2.12 MeV and the ^{12}C line at 4.44 MeV, across a sample of 9 flares from the SMM data set. This value would reduce the δ_p values derived here by 0.7, bringing the range for the 27 April 1981 flare down to 3.5 to 3.8, within the error bars of the δ_α value. This allows us to bring consistency between nuclear de-excitation lines, neutron capture and $\alpha - \alpha$ fusion lines, a quite satisfying position. However, to be completely sure of this result, the analysis of Ramaty et al. (1996b) would have to be repeated without Assumption A. This would also necessitate a complete treatment of the 2.22 MeV neutron capture lines.

The flares of 3 May 1989 and 15 November 1989 behave similarly, as do any other flares in which $\Phi_{0.4-0.5}$ is well-determined. Interpretations appear to be favoured in which α-particles have harder energy distributions than protons. Note that the largest acceptable δ_α is significantly smaller than the smallest acceptable δ_p. Only by adopting different target elemental abundances, specifically a smaller $^{16}O/^{4}He$ relative abundance or larger $^{20}Ne/^{16}O$, could we avoid this conclusion. Moreover, for the softest α-particle distributions, protons make almost no contribution to most observed deexcitation lines.

In the flare of 6 February 1986, on the other hand, $\Phi_{0.4-0.5}$ is comparatively small. The best estimate comes with such a large uncertainty that this is more or less a non-detection: 0.5 ± 7.6 photons cm^{-2} (Share & Murphy 1997). Nonetheless we include this particular event for illustrative purposes: the number of α particles is always small and the interpretation of $\Phi_{1.63}/\Phi_{6.13}$ is almost independent of any assumption made about α's. Share & Murphy (1998) reanalyzed these data, revising $\Phi_{0.4-0.5}$ upwards, but the accompanying error remains large. Fluences of the strong lines are almost unaffected by this reanalysis (Share 2004), and the limit illustrated by this event needs no reconsideration in consequence.

Although the results shown in Table 5.1 have large error bars, modelling this data with Assumption A in place is also fraught with problems. Table 5.2 shows a more sophisticated best-fit approach. Rather than just ignore the 0.4 to 0.5 MeV lines and calculate δ from the ratio of the 1.63 and 6.13 MeV line fluences, as shown in Figure 5.4, I have modelled all three fluences, fixing δ_p to have the same value as δ_α. The rest of the modelling goes exactly as described in Section 5.2.2. For each set of parameters derived, I have calculated the χ^2 statistic and repeated over narrower ranges of δ attempting to minimize χ^2. The values shown in Table 5.2 represent the best fits giving δ to better than one decimal place. The 67% error bars for the 1986 February 6 flare are set from the χ^2 values of the neighbouring solutions in δ. The other flares cannot be modelled to that level of confidence while maintaining Assumption A. The only reason that 1986 February 6 can be modelled is because it is proton-dominated and there is no detection of the $\alpha - \alpha$ feature between 0.4 and 0.5 MeV. Clearly Assumption A creates problems for these flares.

In principle α-Fe lines combined with $\Phi_{0.4-0.5}$ may fix δ_α at the outset. Share

Flare	δ_α	$F_{0,\alpha}$	δ_p	$F_{0,p}$	$\frac{F_{0,\alpha}}{F_{0,p}}$	Ion Energy (erg)
1981 April 27	3.6±?	(5.2±?) × 10^{35}	3.6±?	(5.8±?) × 10^{35}	0.90±?	(2.9±?) × 10^{30}
1986 February 6	$3.4^{+0.5}_{-0.4}$	$(4.1^{+9.1}_{-2.7}) \times 10^{33}$	$3.4^{+0.5}_{-0.4}$	$(5.1^{+10.9}_{-3.6}) \times 10^{35}$	$0.008^{+0.001}_{-0.000}$	$(1.4^{+2.6}_{-0.9}) \times 10^{30}$
1989 May 3	3.6±?	(1.5±?) × 10^{35}	3.6±?	(1.3±?) × 10^{35}	1.19±?	(7.3±?) × 10^{29}
1989 November 15	3.3±?	(1.2±?) × 10^{35}	3.3±?	(2.9±?) × 10^{34}	3.98±?	(4.1±?) × 10^{29}

Table 5.2: An analysis of the same group of flares in Table 5.1 except that we make Assumption A and assume the protons and α-particles have the same energy distributions. Only the 1986 February 6 data provided a good enough fit to set meaningful error bars at the usual 67% confidence level. The 1981 April 27 fit is only 0.002% confident, while the 1986 May 3 and 1989 November 15 fits are 18% and 14% confident respectively. The 1986 February 6 fit is in excellent agreement with the fit with Assumption A relaxed, but this is not surprising since the relaxed fit does not rule out two identical energy spectra. This is the flare with a non-detection of $\Phi_{0.4-0.5}$ and so there is no more to go on than the ratio of the 1.63 and 6.13 MeV line fluences. The other flares present more of a problem as Assumption A is ruled out by our separate energy spectra in these cases and so we now have difficulty in making a good fit with Assumption A restored.

& Murphy (1998) obtained estimates of $\Phi_{1.02}$ for the 19 SMM flares, both separately and summed, and the OSSE flare of 4 June 1991. Determination of $\Phi_{0.339}$ proved difficult for instrumental reasons. Concentrating on the 27 April 1981 flare, for which $\Phi_{1.02}$ is best-determined, and assuming first that the contribution of fast ^{3}He to this feature is negligible, we find that the measured value of $\Phi_{1.02}/\Phi 0.4-0.5$, 0.14 ± 0.06, implies $\delta_\alpha = 3.5 \pm 0.2$. This is exactly the limit discussed above, in which protons make almost no contribution to most deexcitation lines.

The progress made above has been under the assumption that fast ^{3}He nuclei are not over-abundant at the flare site - as they sometimes are in the interplanetary medium. For instance we assumed that all of the measured 1.02 MeV fluence was due to fast α's, neglecting possible contributions from unresolved lines produced primarily by fast ^{3}He (see Section 2.5.4). ^{3}He can also directly excite any of the abundant target nuclei. So its contributions to e.g. $\Phi_{1.63}$ and $\Phi_{6.13}$ may also need to be considered. A complete discussion of the consequences of a ^{3}He overabundance is probably not possible at this time: to the best of my knowledge,

laboratory measurements of some of the necessary cross-sections are still lacking. With some assumptions, however, I can illustrate the consequences of such an overabundance for the findings above, in particular for the interpretation of $\Phi_{1.02}$ and $\Phi_{0.4-0.5}$.

Qualitatively, if some of the measured 1.02 MeV fluence is attributed to ^{3}He (Tatischeff et al. 2003), we must need fewer α-particles above the α-excitation threshold of ~ 2 MeV. Since the number of α's above 10 MeV is almost fixed by $\Phi_{0.4-0.5}$, the inevitable consequence is a harder deduced α-particle distribution. To illustrate the possible effects of ^{3}He on deduced energy distributions, suppose that ^{3}He is indeed overabundant ($F_{0,^3He}/F_{0,\alpha} = 1$) and that accelerated ^{3}He and α-particles have the same energy distribution (I adopt this limited version of Assumption A only for illustrative purposes, and in the absence of any clear resolution of lines excited by only ^{3}He). With these assumptions, we can evaluate both α-particle and ^{3}He contributions to $\Phi_{1.02}$ as a function of δ_α, and thus deduce values of δ_α and $F_{0,\alpha}$ from $\Phi_{0.4-0.5}$ and $\Phi_{1.02}$. Cross-sections for ^{3}He excitation are large and the result is consequently very different from that found above: $\delta_\alpha = 0.54$ and there are 6.6×10^{32} α's above 1 MeV.nucleon^{-1}. If we further neglect ^{3}He contributions to $\Phi_{1.63}$ and $\Phi_{6.13}$, we can subtract off the α contributions as above and deduce $\delta_p = 5.6$ and 3.5×10^{37} protons above 1 MeV. Uncertainties in these deduced quantities are once again very large.

Clearly some uncertainty remains in this process, as long as there is no measurement of lines produced only by ^{3}He. The possibility of ^{3}He contributions will however only strengthen the qualitative conclusion, that α's appear to have harder energy distributions than protons. Clear measurements of α-only features $\Phi_{0.339}$, $\Phi_{0.999}$ or $\Phi_{1.05}$ would allow deductions uncomplicated by ^{3}He.

5.4 Summary and Discussion

The use of ratios of pairs of nuclear lines has been advocated e.g. in Ramaty (1986) ($\Phi_{2.223}/\Phi_{4-7}$) or Ramaty et al. (1996b) ($\Phi_{1.63}/\Phi_{6.13}$). These ratios give information on the ion energy distribution without the need for detailed, lengthy fitting of the γ-ray spectrum, but it is necessary to adopt a set of target abundances, as well as Assumption A, in order to use these. In this work we have

continued to adopt a set of abundances but have shown that useful constraints may be obtained without Assumption A if there is also an estimate of $\Phi_{0.4-0.5}$, and that measurement of the fluence in one further α-excited line allows deduction of δ_p and δ_α. We applied these procedures to interpret line fluences obtained from GRS/SMM data by Share & Murphy (1997) and Share & Murphy (1998), finding α energy distributions routinely significantly harder than those of protons. Uncertainties on derived quantities are large, but this finding seems fairly robust, open to revision only via adoption of a different set of source region elemental abundances. If the abundance of ^{20}Ne is higher than assumed, it may be possible to fix its value combining this analysis with analysis of the 2.22 MeV feature, constraining the solution by neutron production conditions.

The measured photon fluence from the 0.429 and 0.478 MeV lines tells us, to within a factor of three, the number of α particles at energies above 10 MeV.nucleon^{-1}. The number of α's above 1 MeV.nucleon^{-1} then follows only with a specific assumption about the form of the α energy distribution. If one invokes Assumption A, large observed values of $\Phi_{1.63}/\Phi_{6.13}$ then imply steep α-particle distributions, characterized by δ in the range 4 to 5, and thus large numbers of α's above 1 MeV.nucleon^{-1}. Without Assumption A, however, the α energy distribution may be characterized by smaller values of δ_α, with correspondingly reduced total numbers of α's above 1 MeV.nucleon^{-1}.

The largest values of δ_α are obtained when α's account for almost all deexcitation line fluences. Among the three or four line features considered, only the 1.63 MeV line continues to require a proton contribution. At least in the case of the 27 April 1981 flare, this appears to be the limit consistent with the observed value of $\Phi_{1.02}$. The proton distribution then becomes very steep, to minimize the proton contribution to $\Phi_{6.13}$. The total number and energy content of protons becomes particularly ill-defined, however: $\Phi_{1.63}$ gives us an energy-weighted measure of the number of protons above 2 MeV energy but the results of Table 5.1, for example, have been obtained assuming $E_0 = 1$ MeV, a very significant extrapolation with such steep energy distributions. While much of our preferred region of parameter space involves only modest numbers of fast α's, at least compared to protons, it is quite possible that α numbers and energy content are in fact dominant, compared to protons, in this regime. Such a situation

might be consistent with the turbulent cascade acceleration mechanism of Miller & Roberts (1995). As the turbulent cascade proceeds, particles of progressively higher gyrofrequencies are able to interact resonantly with waves. Protons may only be accelerated at the end of this process, after much of the energy of the cascade has been damped by heavier species, particularly α's. Away from our α-dominated cases, the occurrence of harder α-particle energy distributions might also be understandable in these terms.

Apart from those cases with the largest δ_α, in which α's account for most of the observed deexcitation line fluences, our preferred regions of parameter space appear deficient in fast α's. Distributions expressed in energy per nucleon may not be the correct comparison, however. Consider an acceleration process taking place in two stages (e.g. Heyvaerts 1981), in which ions first fall freely through a potential drop, then develop a more extended range of energies e.g. interacting with MHD turbulence. Minimum ion energies in such a situation would scale with charge, not atomic weight. Parameters in Table 5.1 may be consistent with the cosmic ^{4}He abundance if appropriate minimum energies are adopted.

A comment is necessary on the relationship between the suggestions here and previous deductions from γ-ray line data. In some previous analyses (e.g. Murphy et al. 1997), interpretation of $\Phi_{1.63}/\Phi_{6.13}$ proceeds with Assumption A and one or two assumed values of α/p (typically 0.1 or 0.5). Of course values of δ_p $(= \delta_\alpha)$ can be obtained in this way but here I go further and make explicit use of a simultaneous value of $\Phi_{0.4-0.5}$, and further still with a value of $\Phi_{1.02}$. The more complete, and time-consuming alternative is a fit to the complete γ-ray line spectrum, obtaining best values of target, and possibly accelerated particle, abundances together with δ_p, $F_{0,p}$, etc. (Murphy et al. 1991). So far such a procedure has been carried out with Assumption A. A variety of sets of parameters yield statistically acceptable, though not equally good fits, varying according to which quantities (e.g. fast particle abundances) are held fixed. We note that the smallest χ^2 values of Murphy et al. (1991) actually occurred for $\alpha/p = 1$ but this value was considered unreasonable. Above we saw that large observed values of $\Phi_{0.4-0.5}$, resulting in large, deduced α/p values, may become easier to understand when Assumption A is dropped. Presumably a procedure like that of Murphy et al. (1991), but in the extended parameter space used here would lead to further

possibilities for acceptable fits, at least as good as those found here.

The neutron capture line at 2.223 MeV, when compared with de-excitation lines, gives a further, important window on flare ion distributions. Its interpretation involves detailed, complex calculations of neutron production and transport, beyond the scope of the present work. Throughout much of our preferred region of parameter space, the small values of $\frac{F_{0,\alpha}}{F_{0,p}}$ and harder α-particle energy distributions will minimize the role of α's in both neutron capture and deexcitation line production. Murphy et al. (1997), for instance, adopted Assumption A and found reasonable consistency between values of δ_p using both $\Phi_{1.63}/\Phi_{6.13}$ and $\Phi_{2.223}/\Phi_{4.44}$, whether $\frac{F_{0,\alpha}}{F_{0,p}}$ values of 0.1 or 0.5 were adopted. The procedure described here would give similar results for δ_p to those found in the case $\frac{F_{0,\alpha}}{F_{0,p}}$ $= 0.1$, with the minimized role of α's suggesting that consistency with the neutron capture line would be unaffected. Clearly a more detailed study is needed, however, particularly to address the allowed regime in which α's dominate in deexcitation line production.

All of the discussion here assumes uninterrupted, power-law energy distributions for both protons and α's, but of course this assumption also may not be justified. In particular, the cases with largest δ_α require very steep proton distributions, possibly not best described by power-laws. Observable signatures do not appear to allow much further discussion of this possibility, however.

Finally, all of this is probably only an exploratory exercise until a more complete analysis of a full spectrum has been carried out, simultaneously fitting both accelerated particle energy distributions and source region abundances, and taking proper account of electron bremsstrahlung and broad/unresolved contribution to the observed spectrum. A slightly extended version of the work of Murphy et al. (1991) would be necessary, and RHESSI has undoubtedly now supplied the best data (Smith et al. 2003; Share et al. 2003) for this purpose. It remains to be seen, however, how far variability of δ_p and δ_α may be masked by variability in source elemental abundances. On the other hand, line widths and shapes may further discriminate between the allowed regions of parameter space.

I have at least shown here that interpretations of existing data may be possible which do not invoke Assumption A. Even in the resulting, enlarged parameter space, not all possibilities are consistent with the data. Resolution of this matter

		00:27:20 to 00:32:56 UT	00:32:56 to 00:43:20 UT
Species	Line Energy keV	Flux ph.cm^{-2}s^{-1}	Flux ph.cm^{-2}s^{-1}
^{56}Fe	847	0.0238 ± 0.0048	$0.0011^{+0.0029}_{-0.0011}$
^{24}Mg	1369	0.0291 ± 0.0076	0.0231 ± 0.0051
^{20}Ne	1634	0.0250 ± 0.0065	0.0317 ± 0.0044
^{28}Si	1779	0.0188 ± 0.0055	0.0159 ± 0.0035
^{14}C	4438	0.0705 ± 0.0115	0.0281 ± 0.0071
^{16}O	6129	0.0320 ± 0.0082	0.0184 ± 0.0056

Table 5.3: γ-ray line emission as measured by RHESSI for the 23 July 2002 flare (Shih 2004). The emission has been divided into two parts over the time that γ emission was detected.

is an important one for a clear determination of flare fast ion numbers and energy content and for a fuller understanding of the flare particle accelerator.

5.5 An Application to the RHESSI Flare of 23 July 2002

In an early investigation of data gathered with the RHESSI satellite, Shih (2004) has made a first attempt to derive time profiles for the 23 July 2002 flare. These time series are produced by dividing the data into two time periods, 00:27:20UT to 00:32:56UT and 00:32:56UT to 00:43:20UT, and then integrating the flux detected in each period. Table 5.3 shows the results.

As expected, most of the lines decrease in flux as the flare progresses, except the ubiquitous 1.63 MeV ^{20}Ne line. It actually increases in flux by 27% between the two halves of the gamma-emission period. Perhaps the stream of accelerated ions may have encountered a region of enhanced ^{20}Ne abundance later in the flare. Soft X-ray data reveals variations in abundances across an active region of as much as an order of magnitude (del Zanna 2003). Alternatively, the abundances may be altered as a result of the flare process itself by chromospheric evaporation, when the chromosphere is overheated by the impulsive stage of the flare and chromospheric material is ejected into the corona. This may produce changes in the flare region during the later stages. As already discussed in Section 2.4.2 the relative abundance of ^{20}Ne could vary considerably from flare to flare and Ramaty

et al. (1996b) found a general 33% overabundance of ^{20}Ne relative to ^{16}O in the SMM/GRS dataset, when applying Assumption A (Chapter 5); an enhancement of similar size to what we see here.

Considering just the flux ratio of the 1.63 MeV line to the 6.13 MeV line in Table 5.3, we find a ratio of 0.78 in the first half of the flare and 1.72 in the second half. We can analyze this ratio in a cold, thick target γ-ray source. Keeping Assumption A, with no enhancement of ^{20}Ne over the usual deduced photospheric values (^{20}Ne:^{16}O = 0.14) and the α to proton ratio at 0.1, this would imply that the fast proton spectrum started with an index δ_p of 3.5 and this changed to 4.9 in the latter half of the flare. With more α-particles, the sensitivity to protons is lessened and we start with δ_p at 3.9, changing to 5.6 in the second half. It would appear to be more reasonable to assume less α-particles and then most of the line enhancement might be due to some change in the supply of fast protons to the flare site with time. Lin et al. (2003), in a preliminary analysis of this same flare, derive parameters for the fast ions from the fluences of the 2.22 MeV neutron recapture line and the nuclear deexcitation lines. They assume α-particle to proton ratio enhancement to 0.5 and ^{3}He and ^{20}Ne enrichment, 'impulsive flare' abundances after Ramaty et al. (1996b), consistent with the γ-ray emission originating in the impulsive phase of the flare. They find δ_p values between 3.4 and 4.0, within the range of values implied by the time series. Adopting these same 'impulsive flare' parameters, the time series for the 1.63 MeV and 6.13 MeV fluxes give δ_p starting at 3.1 and rising to 4.5 in the second half of the flare. Notice that assuming enhanced ^{20}Ne has hardened the derived fast ion spectrum.

Without Assumption A, Equation 5.3 can provide an estimate for δ_p assuming very few α-particles, at least in the energy range 2 to 10 MeV. Without the abundance enhancements as before, Equation 5.3 reveals that δ_p moves from 3.2 to 4.1 through the course of this flare, a not-unlikely range of values. Unfortunately Table 5.3 does not provide the α-excited lines to allow investigation of δ_α with time. Share et al. (2003) present line fluxes from this flare in their analysis of the 0.511 MeV positron annihilation line emission. They have a flux for the 0.4 to 0.5 MeV feature of 0.143 ± 0.032 γcm^{-2}s^{-1} for the period 00:24:20UT to 00:43:20UT, close to the whole period of the time series by Shih

(2004). Averaging the fluxes in Table 5.3 over time, the 1.36 MeV line has a flux of 0.029 ± 0.005 $\gamma\text{cm}^{-2}\text{s}^{-1}$ and the 6.13 MeV line has 0.023 ± 0.006 $\gamma\text{cm}^{-2}\text{s}^{-1}$. With these values and the analysis set out in Section 5.2.2 (Toner & MacKinnon 2004), I find that $\delta_\alpha \lesssim 3$ or there is not enough emission left to be produced by proton-excitation.

So again we see a harder energy spectrum for fast α-particles than for protons. This allows the 1.63 MeV line to react strongly to changes in the proton spectrum. However, detailed modelling of the evolution of the protons through the history of the impulsive phase would be necessary to see if it is possible to enhance the 1.63 MeV line as the other lines diminish without introducing an enhancement in ^{20}Ne.

Chapter 6

Solar Flare Neutron Emission

6.1 Another Neutral Emission

Previously in this thesis, I have discussed the nuclear deexcitation γ-ray lines, proposing innovations and refinements in their interpretation and exploring their implications. Now I would like to give some attention to direct solar flare neutrons, specifically as detected by the COMPTEL instrument on the Compton Gamma Ray Observatory.

Direct solar flare neutrons are a valuable diagnostic of high-energy ion acceleration in these events, and COMPTEL improved over all previous cosmic neutron detectors in its capacity for neutron energy measurement (see Sections 1.7 and 1.10.6). Neutrons detected from a flare begin in the nuclear reactions between accelerated ions and the ambient nuclei, and so the information we can take from these neutrons gives another measure of the conditions in the flare which complements the deexcitation lines and extends the range of accelerated ions that we can investigate to tens and hundreds of MeV energies. Lockwood et al. (1997) discuss the relationships between the γ-ray emission and the production of neutrons in solar flares.

Previous studies of COMPTEL neutron data have worked with an incomplete model of the instrumental response, applying energy-by-energy detection efficiencies (e.g. Kocharov et al. 1998). Ignoring off-diagonal elements of the response matrix in this way essentially underestimates the overall detector efficiency, and may overestimate the number of neutrons as a result. Here I employ statistical regularization techniques with the full (Monte-Carlo-simulation-derived) response matrix to produce improved estimates of neutron numbers and energy distribution. These techniques are applied to data from the well-observed 15 June 1991 flare, as previously summarized in Toner et al. (2001) and discussed by Kocharov

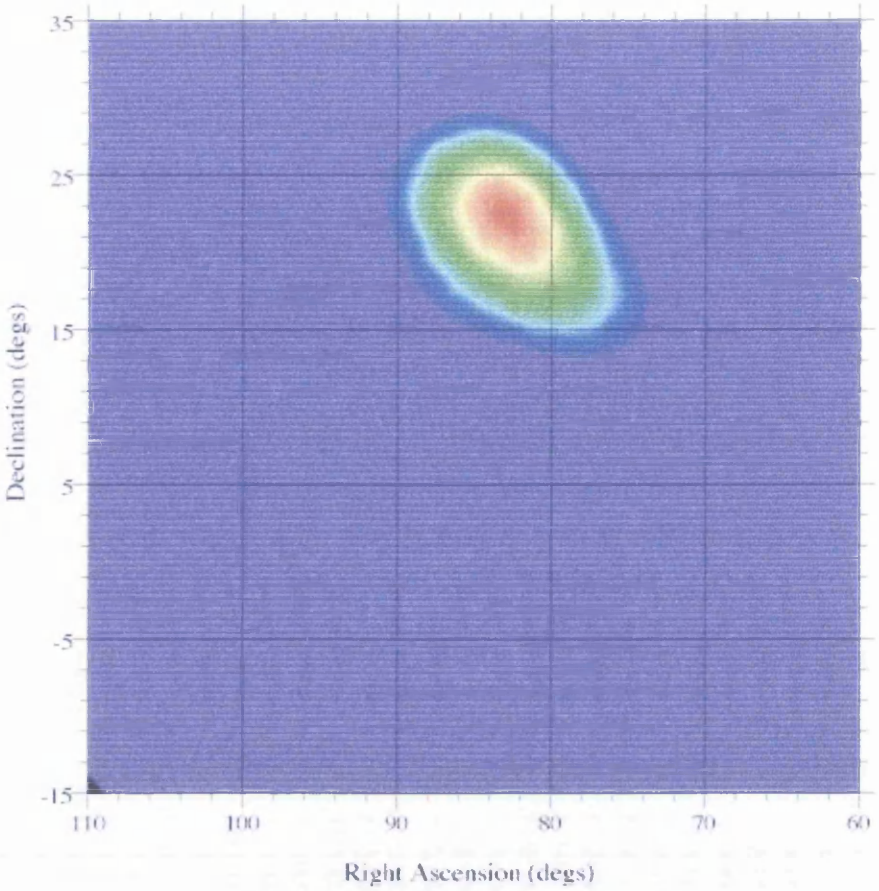

Figure 6.1: An image of the neutron source of the 15 June 1991 solar flare made with COMPTEL, on board the CGRO. This was made from the same data-set analyzed here to obtain the neutron emissivity spectrum, but the reduction was to trace each neutron back to its point of origin. This is the first image of an astrophysical object produced in particles other than photons (Arndt et al. 1998; McConnell 1994).

et al. (1998). Figure 6.1 shows the neutron source as seen by COMPTEL, the first ever image of a solar flare in neutrons.

6.2 Solar Flares and Energetic Neutrons

Solar flare hard X-ray and γ-ray observations reveal the presence of electrons of energies sometimes in excess of 10 MeV; and of ions of energies sometimes exceeding 1 GeV/nucleon. Fast neutrons, secondary products of various nuclear reactions involving the accelerated ions, are a further, useful diagnostic of the accelerated ion distribution. Ions at 10 to 30 MeV.nucleon^{-1} reveal themselves by

the nuclear de-excitation lines discussed in Sections 1.5 and 2.2 and ions at more than 300 MeV.nucleon^{-1} by very high-energy continuum resulting from decay of secondary pions. Fast neutrons fill the diagnostic gap between these ranges. Flare secondary neutrons were first detected by SMM (Chupp et al. 1982), but with no energy discrimination. Early assumptions such as impulsive neutron production were found not to be justified. Chupp et al. (1987) showed that the majority of neutrons in the 1982 June 3 flare were produced after the impulsive phase.

COMPTEL could measure neutron energies and has provided the first neutron spectra and images from the Sun 6.1. For example, Lockwood et al. (1997) found that neutrons with energies above 200 MeV follow the same intensity-time profile as pion-decay γ-rays and that these neutrons are produced over time-scales from 10 to 70 minutes. Neutrons in the 10 to 100 MeV energy-range were found to be more complicated in their relationship with γ-emission due to the presence of higher-energy neutrons. However, the 2.22 MeV neutron capture feature has a similar time profile to these lower-energy neutrons, and they have production times extending from minutes up to hours.

6.3 COMPTEL

The COMPTEL instrument is shown in Figure 6.2.The front detector array (D1) was made up of seven Ne213A detectors, each 27.6 cm in diameter and 8.5 cm deep. Ne213A is a liquid organic scintillator with a low density and low atomic number. This maximizes the probability that an incident photon will scatter in the front detectors. The rear array (D2) is made of fourteen NaI detectors, each 28 cm in diameter and 7.5 cm deep. These dense detectors are more likely to stop the photon that was scattered in the front detectors, thus measuring the total scattered photon energy. Photon energies and arrival directions are deduced from Compton scatter events in the D1 array, and scattered photon energy measured in D2 as described in Section 1.10.6. COMPTEL performs the same trick with neutrons, via elastic scatters on D1 detector protons. Time-of-flight to D2 reveals the scattered neutron energy. The incident neutron's energy and angle of incidence to the detector axis θ are given by simple kinematics. This results in neutron imaging and spectroscopy in the energy range 10 to 120 MeV

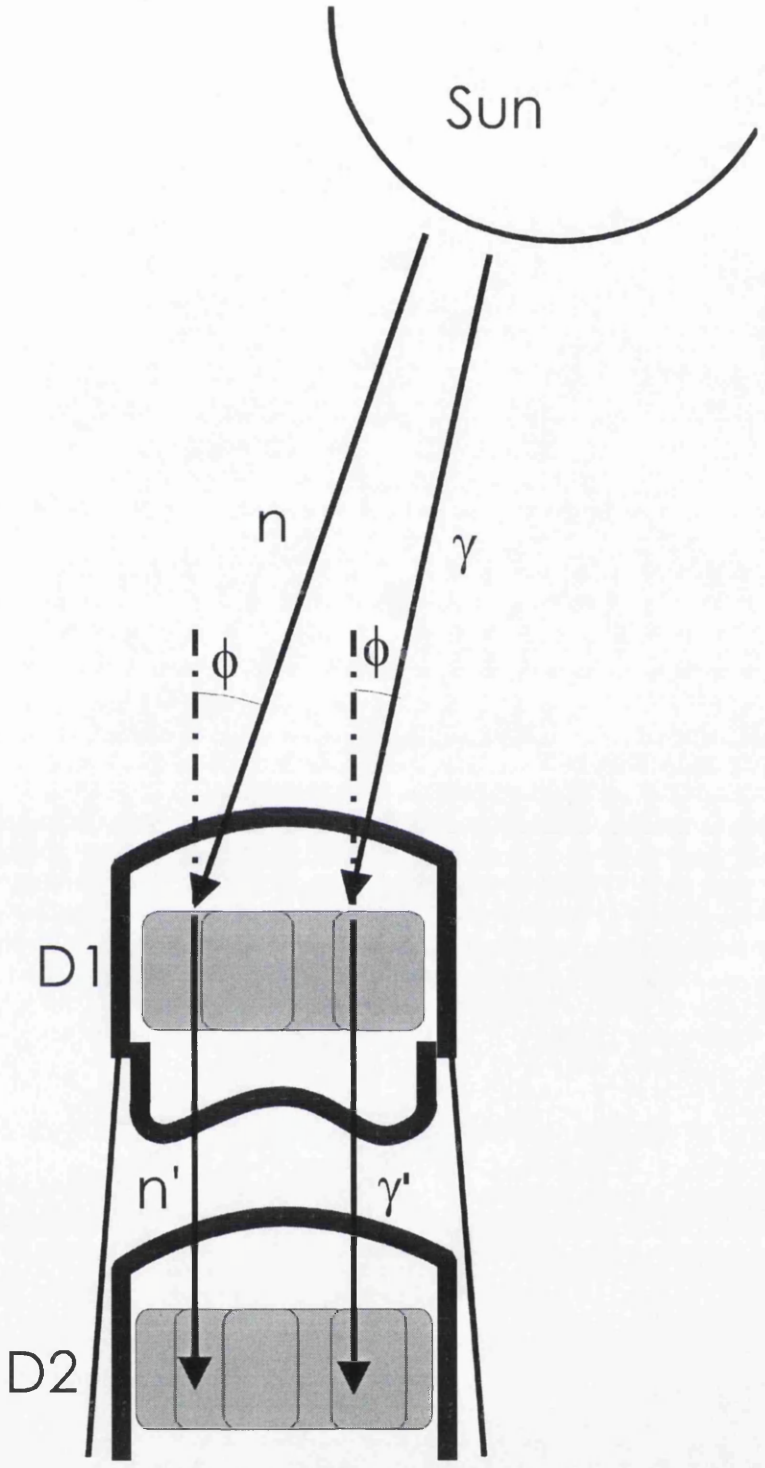

Figure 6.2: How COMPTEL worked. Path nn' shows how a solar neutron enters the front detector array D1 at angle ϕ to the instrument axis, interacts to deposit energy in D1 and produce secondary neutron n' which travels on to be detected by the back array D2. Path $\gamma\gamma'$ shows the similar path of a high-energy photon. The telescope length was 2.61 m. After McConnell (1994).

(as in Figure 6.1).

6.4 COMPTEL Neutron Response

6.4.1 Principles

If E_1 is the energy of the scattered proton in D1 by collision with the solar neutron, and E_2 the scattered neutron energy derived from the time-of-flight, the incident neutron's energy E is simply the sum of these two detected energies.

$$E = E_1 + E_2 \tag{6.1}$$

The angle of incidence to the detector axis ϕ comes from simple kinematics.

$$tan^2(\phi) = \frac{E_1}{E_2} \tag{6.2}$$

However neutrons may scatter more than once in D1 or they may scatter inelastically on carbon nuclei. Some, but not all of these misleading events may be identified and excluded. Even with 'clean', single elastic scatter events, instrument geometry and D1 scattered proton energy resolution combine with the above to give finite neutron energy resolution.

6.4.2 Simulation

Work at University of California, Riverside uses the Los Alamos codes LAHET (Los Alamos High Energy Transport) and MCNP (Monte Carlo Nuclear Particle) to simulate neutron transport in COMPTEL (O'Neill 1993, 1994). The LAHET code can simulate the transport of high-energy particles through a system of arbitrary geometry, using the MCNP code to handle the transport of photons and low-energy neutrons (Prael & Lichtenstein 1989; Brown & Nagaya 2002). This software is capable of simulating any spacecraft high-energy particle experiment, modelling Coulomb scattering, nuclear elastic scattering and nuclear interactions. LAHET simulates the transport of protons, pions and muons through the instrument and all neutrons above a pre-selected cut-off energy. The parameters of neutrons below this energy are output to a neutron file. Together with a γ-photon file produced from LAHET output by the PHT code (PHoTon), this neutron data is processed by MCNP as a coupled neutron-photon problem to give a complete

picture of γ-ray transport through the system. Alternatively the neutrons and photons can be analyzed separately.

The results of these simulations are summarized in an instrumental neutron response matrix (supplied by Bhattacharya 1999). The matrix elements in full generality would represent the probability of a neutron incident on COMPTEL with energy E, at angle ϕ to the instrument, giving the signal in the instrument appropriate to a neutron of energy E', at angle ϕ'. In practice, flare neutron numbers do not justify a full deconvolution in (E, ϕ)-space. Instead the Monte Carlo simulations are carried out assuming a point neutron source at the Sun's position, and a detector response matrix $\mathbf{H}$ calculated.

In this case a 6×6 matrix was created by simulating the passage of ~ 180000 neutrons through the COMPTEL instrument. The neutrons are injected at six different energies (13, 22, 32, 50, 77 and 100 MeV) and then detected in six energy bins (8.5 to 17.5, 17.5 to 26.5, 26.5 to 37.5, 37.5 to 62.5, 62.5 to 91.5 and 91.5 to 108.5 MeV). The matrix gives the number of neutrons originating with a given energy that are then detected in a particular energy bin. Once normalized, the diagonal gives the probability that a given neutron will be detected at its true energy. The off-diagonal elements give the probabilities that it will be detected in another energy bin due to a misleading detector signal. Even when inelastic-scattering events are excluded from the data, there are still significant non-diagonal elements. For example, 35% of neutrons injected at 32 MeV are actually detected in the 8.5-to-26.5 MeV energy range.

Let x_i be the number of neutrons measured in the ith energy bin, of which there are n bins in all; f_j be the number of neutrons incident on the instrument at the jth injection energy, of which there are m levels; and ϵ be the vector representing data (Poisson) noise. Then

$$\mathbf{x} = \mathbf{H}\mathbf{f} + \epsilon \tag{6.3}$$

6.5 Statistical Regularization

We aim to find an estimator $\hat{\mathbf{f}}$ of $\mathbf{f}$, knowing $\mathbf{x}$. The difficulties of doing this in the presence of non-zero ϵ are well-known (e.g. Craig & Brown 1986): straightforward inversion of $\mathbf{H}$ can amplify even very modest noise levels giving rise to unphysical oscillations and spurious features. One is forced to adopt a statistical regularization approach, in which both smoothing and deconvolution are carried out, with the deduced $\mathbf{f}$ being a compromise between (spurious) exact data fit, and some measure of 'smoothness.' In practice, one finds $\hat{\mathbf{f}}$ that minimizes the expression

$$\sum_{i=1}^{m} \left[x_i - \sum_{j=1}^{n} H_{ij} \hat{f}_j \right]^2 + \lambda \Phi(\hat{\mathbf{f}}) \tag{6.4}$$

where $\Phi(\hat{\mathbf{f}})$ is the adopted smoothness measure, and the Lagrange multiplier λ is chosen to find the desired compromise between smoothness and exact data fit (according to some pre-chosen criterion).

6.5.1 GUIPS

The Glasgow University Inverse Problem Software (GUIPS) consists of automatic methods for finding estimators $\hat{\mathbf{f}}$ with various choices of Φ and strategies for choosing λ (i.e. the degree of compromise between data fit and smoothness). In this Chapter, I employ GUIPS to estimate true neutron energy distributions incident on COMPTEL. Neutron numbers are not great (typically a few hundred across the whole energy range). So Poisson noise levels are serious. Because of this it is particularly important to test the robustness of results obtained by any particular choice of $\hat{\mathbf{f}}$ and prescription for choosing λ. I tested a number of GUIPS subroutines with simulated data. This was data with a known $\mathbf{f}$ and added Poisson noise. By manipulating the test data and trying to retrieve $\mathbf{f}$, it was possible to confirm the strengths and weaknesses in the regularization methods and to ensure that there were no problems with the computer codes.

In the end, I used maximum entropy and quadratic regularizations, although I had to rewrite some of the quadratic regularization code due to incompatibilities with my FORTRAN compiler. The former regularization method is well-known, at least in its global variant (see, e.g. Groetsch 1993; Craig & Brown 1986). I

also employ a local version which attempts to equalize neighbouring data points and is less prone to over-smoothing. Quadratic regularization minimizes first or second derivatives across the reconstruction, thus acting against sharp features. I use the simple χ^2 choice of Lagrangian multiplier, and also the 'Bayesian' choice, again less prone to over-smoothing. Details of these methods are to be found in Thompson (1992) and Thompson & Craig (1992). The GUIPS code speeds up the development of regularization software as the investigator only has to write the code that passes the particular data and response matrix for a given problem to the GUIPS subroutines.

6.5.2 Quadratic Regularization

In quadratic regularization, we attempt to find a source function $\hat{\mathbf{f}}$ that minimizes a derivative. Thus nth order quadratic regularization minimizes the nth derivative of $\hat{\mathbf{f}}$. The simplest forms of smoothing function that arise from this approach are those of first and second order (Thompson 1992; Thompson & Craig 1992).

$$\begin{aligned} \Phi(\hat{\mathbf{f}}) &= \sum_{i=1}^{n-1}(\hat{f}_i - \hat{f}_{i+1})^2 \\ \Phi(\hat{\mathbf{f}}) &= \sum_{i=1}^{n-2}(\hat{f}_i - 2\hat{f}_{i+1} + \hat{f}_{i+2})^2 \end{aligned}$$

In a more general form we can define a smoothing matrix $\mathbf{C}$ for each order of quadratic regularization. This gives a general form for Φ.

$$\Phi(\hat{\mathbf{f}}) = \hat{\mathbf{f}}^{\mathbf{T}}\mathbf{C}\hat{\mathbf{f}} \tag{6.5}$$

For example, the first order quadratic regularization smoothing matrix is given by

$$\mathbf{C} = \begin{bmatrix} 1 & -1 & 0 & \dots & 0 & 0 & 0 \\ -1 & 2 & -1 & \dots & 0 & 0 & 0 \\ 0 & -1 & 2 & \dots & 0 & 0 & 0 \\ \vdots & \vdots & \vdots & \ddots & \vdots & \vdots & \vdots \\ 0 & 0 & 0 & \dots & 2 & -1 & 0 \\ 0 & 0 & 0 & \dots & -1 & 2 & -1 \\ 0 & 0 & 0 & \dots & 0 & -1 & 1 \end{bmatrix}$$

Quadratic regularization has the major advantage that the minimization expression reduces to an analytical form.

$$\hat{\mathbf{f}} = \frac{\mathbf{H}^T\mathbf{x}}{\mathbf{H}^T\mathbf{H} + \lambda\mathbf{C}} \tag{6.6}$$

Equation 6.6 provides a fairly quick way of obtaining estimates of $\hat{\mathbf{f}}$, providing that there are relatively few data points (less than 100 or so). So that a range of values can be tried in order to find the optimum combination of $\hat{\mathbf{f}}$ and λ. Since this method is essentially linear, it is restricted to problems of small dynamic range. It also has a disadvantage in that it does not guarantee a positive set of elements for the solution, which in most problems would be unphysical.

6.5.3 Maximum Entropy Regularization

Entropy methods take their name from Boltzmann statistical mechanics. If we consider a phase space containing N particles which we subdivide into s congruent cells, we can define the statistical state of the system when each cell i contains N_i particles (after Groetsch 1993) so that equation 6.7 holds.

$$\sum_{i=1}^{s} N_i = N \tag{6.7}$$

W is the number of possible distributions of particles among the cells in this system and is given by Equation 6.8.

$$W = \frac{N!}{\prod_{i=1}^{s} N_i!} \tag{6.8}$$

We can then find the state with the maximum number of distributions, or maximum entropy, by maximizing Equation 6.8 under constraint Equation 6.7. It is more computationally efficient to exploit the fact that W being a maximum is equivalent to $\frac{\ln W}{N}$ being a maximum. Provided all of the N_i are large, we can also use Stirling's approximation for $n!$, $\lim_{n\to\infty} \frac{n!}{n(\ln n - 1)} = 1$. So Equation 6.8 becomes Equation 6.9.

$$\ln W \approx -\sum_{i=1}^{s} N_i \ln\left(\frac{N_i}{N}\right) \tag{6.9}$$

Clearly $\frac{N_i}{N}$ is the probability p_i that a given particle occupies the ith cell in phase space. If we define $H \equiv \frac{\ln W}{N}$, the entropy function, then we have Equation 6.10.

$$H = -\sum_{i=1}^{s} p_i \ln p_i \tag{6.10}$$

This expression gives us the mathematical form that is used in maximum entropy regularization. It comes into regularization by way of Shannon information theory which shows that the entropy function is a natural uncertainty function. The entropy function measures the disorder of a system and so, by maximizing this in our solution, we make the least assumptions about the missing information. For maximum entropy regularization we define Φ in this way (Thompson 1992).

$$\Phi(\hat{\mathbf{f}}) = \sum_{i=1}^{n} \hat{f}_i - m_i - \hat{f}_i \ln(\frac{\hat{f}_i}{m_i}) \tag{6.11}$$

where $\mathbf{m}$ is a prior estimate for $\hat{\mathbf{f}}$. The solution will be smoothed towards $\mathbf{m}$, which is often taken as flat, but some knowledge of the data may suggest a different prior. In effect, we are maximizing the probabilities that elements of $\hat{\mathbf{f}}$ match elements in $\mathbf{m}$. We can also take a maximum entropy approach which does not require $\mathbf{m}$. In this case we maximize the probabilities that elements of $\hat{\mathbf{f}}$ match values with their neighbours.

$$\Phi(\hat{\mathbf{f}}) = \sum_{i=1}^{n-1} (\hat{f}_i - \hat{f}_{i+1})(\ln(\hat{f}_i) - \ln(\hat{f}_{i+1})) \tag{6.12}$$

There are a number of advantages to maximum entropy techniques. They are more efficient than quadratic techniques in problems where the data has a high dynamic range, say greater than one order of magnitude. However, quadratic approaches are faster when the dynamic range is low, and the maximum entropy solutions are identical to quadratic when the source function is completely flat. This is where the main disadvantage lies. The smoothing function is nonlinear and so the solution can only be obtained iteratively. The slowness of this process can also limit the choice of λ if computing power is at a premium (see Section 6.5.4). A major advantage is that maximum entropy methods ensure that the solution is always positive, avoiding nonphysical results. We choose the

global form, Equation 6.11, over the local form, Equation 6.12, when we are sure that adjacent data values are independent, which is usually not the case, and vice versa. However it is always a good idea, when computing power allows, to use a number of regularization methods and compare their results to avoid artifacts introduced by any one method.

6.5.4 The Lagrangian Multiplier λ

To provide an automatic method of choosing the best Lagrangian multiplier, and therefore amount of smoothing of our solution, we start with a first estimate of λ and then refine it according to some statistical scheme. I used two methods in investigating the COMPTEL neutron data: the χ^2 and Bayesian methods (as in Thompson 1992; Thompson & Craig 1992). Both start by calculating χ^2, or the residual sum of squares.

$$\chi(\lambda)^2 = \sum_{i=1}^{n} \left(x_i - \sum_{i=1}^{n} H_{ij} \hat{f}_j \right)^2 \tag{6.13}$$

where H_{ij} is an element of matrix $\mathbf{H}$, while x_i and $\hat{f}_j$ are elements of the vectors $\mathbf{x}$ and $\hat{\mathbf{f}}$. An initial value of λ is used to get an estimate of $\hat{\mathbf{f}}$ and an iterative process then refines λ to some optimal value.

The χ^2 method optimizes λ so that

$$\chi(\lambda)^2 \;=\; n\sigma^2 \tag{6.14}$$

where σ^2 is the noise variance. It is often useful to substitute $\frac{x_i}{\sigma_i}$ for x_i and $\frac{h_{ij}}{\sigma_i}$ for h_{ij}, particularly in situations where the noise is not uniform. It also simplifies the noise variance which becomes 1. In general, this method will tend to oversmooth $\hat{\mathbf{f}}$, and it is the oldest method of choosing λ (Thompson & Craig 1992).

Alternatively, we can use a Bayesian method. This uses a slightly different optimizing function for λ.

$$\chi(\lambda)^2 + \lambda \hat{\mathbf{f}}^T \mathbf{C} \hat{\mathbf{f}} = n\sigma^2 \tag{6.15}$$

Again, we start with an estimate of λ and iterate until this constraint is achieved. In contrast to the χ^2 method, the Bayesian approach will tend to undersmooth $\hat{\mathbf{f}}$. This method is one of a number of approaches developed by Gull (1988) using

a Bayesian approach to finding λ. Essentially, this involves taking into account what we believe about $\mathbf{f}$. $\hat{\mathbf{f}}$ is our best estimate of $\mathbf{f}$, given the data $\mathbf{x}$. We are trying to maximize the probability $P(\mathbf{f}|\mathbf{x})$ that we have found the 'true' $\mathbf{f}$, given we have these particular data. Bayes theorem states

$$P(\mathbf{f}|\mathbf{x}) = P(\mathbf{x}|\mathbf{f})P(\mathbf{f}) \tag{6.16}$$

where $P(\mathbf{x}|\mathbf{f})$ is the probability that this data will arise given the actual form of the signal and $P(\mathbf{f})$ is the unconditional probability that this form of the signal will occur and is defined by our prior beliefs about the phenomenon being observed (Titterington 1985). So a Bayesian approach recognizes that maximizing $P(\mathbf{f}|\mathbf{x})$ depends on what the error distribution will allow (described by $P(\mathbf{x}|\mathbf{f})$) and how well we understand the characteristics of the signal we are trying to find (defined by $P(\mathbf{f})$).

Clearly, Equation 6.15 explicitly requires *a priori* values for λ and $\hat{\mathbf{f}}$ in order to apply the constraint. So the optimization being carried out links the two processes of finding the required degree of smoothing and of finding the best fit to our data. In effect, the number of degrees of freedom, n, in the problem have been split between obtaining a fit to the data and finding the smoothing function (Thompson & Craig 1992). However, it can be argued that Equation 6.14 also requires *a priori* λ and $\hat{\mathbf{f}}$ to begin the iterative process that leads to the final choice of λ. Indeed, there is also a Bayesian justification for the χ^2 approach, but this is based on the assumption that $\mathbf{f}$ is flat and uniform (Titterington 1985), rather than having some expected structure. Therefore we reserve the term 'Bayesian' for the second method which allows us to say something explicit based on our prior knowledge of the problem.

6.6 15 June 1991 Solar Flare

This X12+ flare was one of the sequence of large events produced by AR 6659. It has been discussed by several authors, in particular Kocharov et al. (1998). It produced detectable neutron emission as well as γ-rays to photon energies in excess of 1 GeV Kocharov et al. (1994). The CGRO was in orbital darkness during the flare's impulsive phase (which peaked at 08:20UT), but it was still

producing γ and neutron emissions when spacecraft night ended some 40 minutes later. This was a target of opportunity for CGRO and the Sun was 15° from the axis of COMPTEL.

Kocharov et al. (1998) (also Rank 1995) analyzed COMPTEL neutron data from the period 08:59UT to 09:30UT, deducing the source neutron energy distribution at the Sun. In the absence of a full deconvolution procedure, they applied energy-by-energy detection efficiencies, given by the diagonal elements of the energy response matrix. However, the neutron energy distribution incident on the instrument in a restricted time period like this has a rather complex relationship to that released from the flare. Firstly, neutrons of different energies have different Sun-Earth travel times. So temporal and energy evolution are convolved in the actual measured energy distribution. Secondly, the β-decay of free neutrons, with an e-folding time of 930 s, further complicates interpretation.

6.6.1 Previous Neutron Analysis

Kocharov et al. (1998) assumed a source neutron population separable in energy and time. Ideally, the CGRO γ-ray flux should have been a proxy for the neutron production time-dependence. The same population of accelerated ions are assumed to produce the neutrons and the γ-rays (e.g. the neutron production code of Hua & Lingenfelter 1987c), and in particular the 2.22 MeV flux results from deuterium formation by neutron capture on hydrogen, although the neutrons result from higher energy ions (up to a few hundred MeV) than do the prompt deexcitation lines ($\approx$ 10 to 30 MeV). As already mentioned the COMPTEL γ-ray record is missing for the first part of the flare. GAMMA-1 observed the γ-ray flux early in the flare (Akimov et al. 1991) and the time profile of these two data sets follows closely the high-frequency (8.4 GHz Magun 1998) microwave time profile, which originates in gyrosynchrotron emission from accelerated electrons (Murphy 1985). So they adopted this flux as a marker for the time-dependence and hence deduced the source neutron energy distribution.

In absence of a full deconvolution procedure, they applied energy-by-energy detection efficiencies, given by the diagonal elements of the energy response matrix $\mathbf{H}$. This procedure clearly underestimates the overall neutron detection efficiency of the instrument. Full deconvolution might also significantly revise the

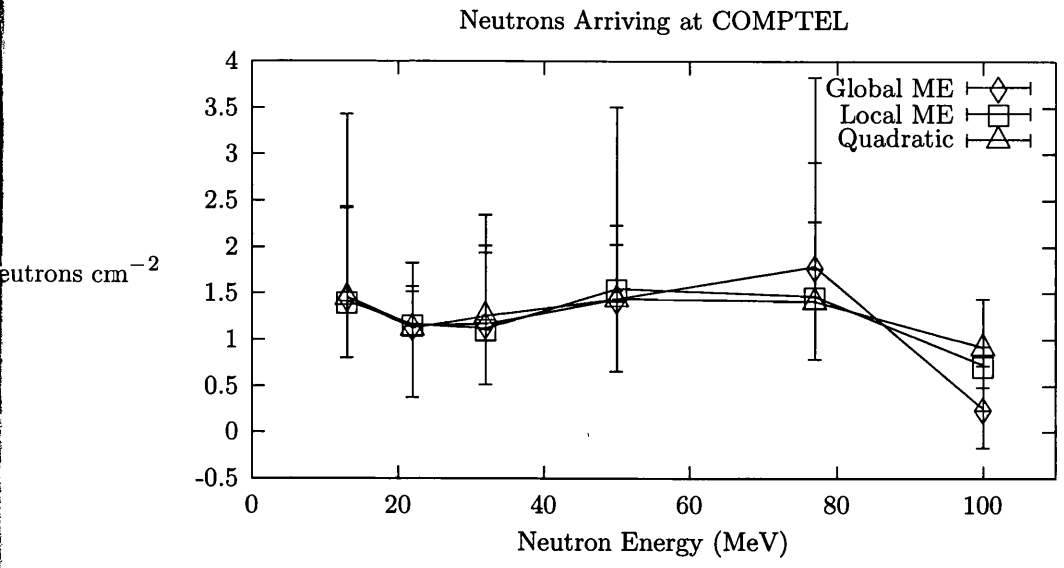

Figure 6.3: Maximum entropy and quadratic regularised solutions for the energy spectrum of neutrons arriving at the COMPTEL instrument during 15 June 1991 solar flare, using a Bayesian method for choosing the smoothing parameter. Error bars are set at the 66.7% confidence level.

form of the energy distribution.

6.6.2 Solutions to the Inverse Problem

Figures 6.3 and 6.4 show various inversions of the COMPTEL data that reconstruct likely energy spectra for the neutrons arriving at COMPTEL over the whole observation period. Assigning confidence limits to such an inversion is a lengthy process. Assuming the main source of noise is due to Poisson noise in the detector, a distribution of data sets around the measured data set was created by a Monte Carlo method. 1000 of these sets were inverted as described above and the results sorted so that median values could be extracted and values at given percentiles of the distribution. The error bars in the figures are taken from the 66.7 percentiles to allow comparison with the Kocharov et al. (1998) results which show traditional 1 σ error bars.

In order to complete the comparison of these inversions with the results of Kocharov et al. (1998), I have to repeat their method for restoring the time of emission at the Sun for our detected neutrons.

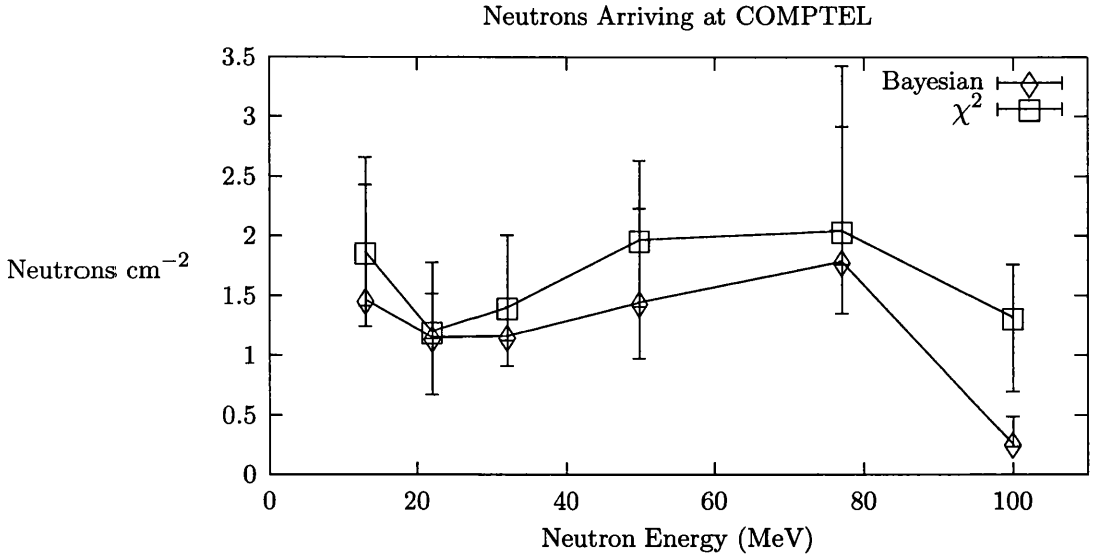

Figure 6.4: As 6.3 except that both solutions use global maximum entropy as the smoothing function and differ only in the method of choosing the smoothing parameter, either Bayesian or χ^2.

6.6.3 Neutron Emissivity

The detected neutrons arrived at COMPTEL between 09:02UT and 09:37UT. However the neutrons were produced at the Sun during the time that the microwaves and γ-rays were detected, between 08:12UT and 09:25UT. Since neutron energy depends on velocity, we have to adjust each neutron's emission time according to its time-of-flight which will introduce an energy-dependence to the time. The time correction for the difference between neutron transit times and photon transit times is given by this relativistic formula.

$$\Delta T(E) = \frac{R}{c}\left[\frac{\gamma}{\sqrt{\gamma^2 - 1}} - 1\right] \tag{6.17}$$

where R is 1 AU, c the speed of light, and γ is the Lorentz factor for a neutron. We use this to match up neutrons with photons. Effectively we adjust the detection times of the neutrons to pretend that they arrive with the photons that were emitted with them. In particular, if $T_0(E)$ is the time when photons were detected that were emitted along with neutrons of energy E MeV, which start to arrive at COMPTEL at time $T_0^{\oplus}$, then

$$T_0(E) \;=\; T_0^{\oplus} \;-\; \Delta T(E) \tag{6.18}$$

In this way we can use the time profile of electromagnetic data to deduce the time profile of the neutron production and, for this reason, we will call this adjusted time the neutron emission time. However, this time differs from the true emission time by the travel time for photons arriving from the Sun.

Neutron production is assumed to follow γ-ray production (See Section 6.2), but we take the 8.4 GHz emission as a proxy for this, since the γ-ray emission is not completely recorded. Even so, this data only spans the gradual phase of the flare, and so neutrons from the impulsive phase cannot be included. Optical and radio data places the start of the gradual phase at 08:26UT, in terms of the photon detection time. Therefore we only include neutrons with photon-matched emission times (using Equation 6.17) that start after 08:26UT. Kocharov et al. (1998) estimate that this amounts to about 12% of all of the flare neutrons detected by COMPTEL. A further assumption is that the energy spectrum of the neutrons is constant throughout the flare, mainly because we lack information to deduce any variation. So the derived neutron spectrum will be a time-averaged version for the gradual phase of the flare. This spectrum is $f(E)$ in neutrons.sr^{-1}.MeV^{-1}.

Consider one COMPTEL energy channel, detecting neutrons in the energy range E_i to E_{i+1}. Define the time limits for neutron emissivity at the Sun (using photon-matched times) to be T_s at 08:26UT and T_f at 09:25UT. Then the start time for emission of neutrons of energy E will be $T_0^{\bigstar}(E)$ which is the later of T_s or $T_0(E)$ (see Equation 6.18). Neutrons of this energy stop at time $T_1 E$. Not all neutrons survive the flight to Earth as some will suffer β-decay on the way with e-folding time τ (930 s), so that a neutron with velocity v will have a survival probability $P(E) = \exp(-\frac{R}{v\tau\gamma})$. COMPTEL has an effective area for neutron detection $A(E)$. So the number of neutrons of energy E detected will depend on how many neutrons are emitted in that timespan $f(E)$, their survival probability $P(E)$, and the detection area $A(E)$ divided by R^2. We integrate this over E_i to E_{i+1} to get the total neutrons detected in this energy bin. However, without the time information, we need to normalize $f(E)$ according to the time profile of the microwave emission. We create a weighting factor W, based on the microwave emission $j_{mw}(t)$.

$$W(t_0, t_1) = \frac{\int_{T_s}^{T_f} j_{mw}(t)dt}{\int_{t_0}^{t_1} j_{mw}(t)dt} \tag{6.19}$$

This gives us the observed number of neutrons in energy channel E_i to E_{i+1} as N_i.

$$N_i = \frac{1}{R^2} \int_{E_i}^{E_{i+1}} \frac{f(E)A(E)P(E)}{W(T_0^{\star}(E), T_1(E))} dE \tag{6.20}$$

Equation 6.20 can be used to deduce the average $f(E)$ over the energy bin, $< f(E) >_i$.

$$< f(E) >_i = N_i R^2 \left[\int_{E_i}^{E_{i+1}} \frac{A(E)P(E)}{W(T_0^{\star}(E), T_1(E))} dE \right]^{-1} \tag{6.21}$$

Then the neutron emissivity at the Sun during the gradual phase is ε_i.

$$\varepsilon_i = \frac{< f(E) >_i}{T_f - T_s} \tag{6.22}$$

Figure 6.5 shows the result of applying this process to the COMPTEL neutron data recovered by a local maximum entropy method and compares this with the emissivity deduced by Kocharov et al. (1998).

6.6.4 Results and Conclusions

In Figure 6.3 we can see neutron energy distributions incident on the instrument reconstructed using a variety of smoothness measures and a Bayesian smoothing parameter strategy. As expected the quadratic regularization is smoother, the maximum entropy solutions less smooth. However they are all very similar and the dip at 20 MeV seems to be real, interpretable in terms of lower energy neutrons still arriving from the impulsive phase. Figure 6.4 shows how slight variations are introduced if a χ^2 approach is adopted for choosing λ. The low-energy dip is less pronounced when χ^2 is adopted but is still consistent with the Bayesian results.

Figure 6.5 compares a local maximum entropy solution with the diagonal-elements-only approach of Kocharov et al. (1998). The shape of my maximum entropy inversion is a little less sloped at the lower energy end but is otherwise similar to the previous emissivity. The most obvious difference is that I deduce fewer neutrons in total emitted at the Sun.

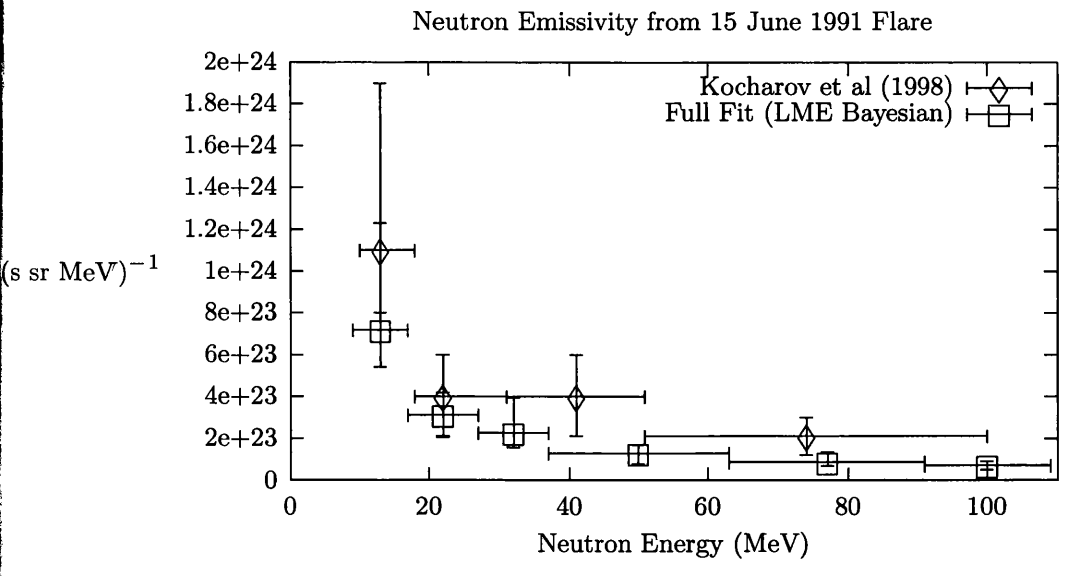

Figure 6.5: A comparison of a diagonal-elements-only inversion by Kocharov et al. (1998) with the full inversion with local maximum entropy smoothing function. Both of these data sets have been converted to source neutron energy distributions at the Sun (after Kocharov et al. (1998)).

In spite of the low neutron count rates, the form of the neutron energy distribution is broadly consistent across the various methods, and with previous results. Total neutron numbers are revised by this more complete treatment, however, to 73% of the result of Kocharov et al. (1998). They already had difficulty with their value in reconciling the inferred proton numbers with the proton spectra implied by the higher energy (200 MeV) γ-ray observations from GAMMA-1 (Akimov et al. 1991). This forced the adoption of a complex accelerated proton spectrum that softens above $\sim$ 200 MeV and then hardens again above $\sim$ 1 GeV to produce enough protons for the high-energy γ-emission. My fuller treatment of the instrument response significantly strengthens this conclusion.

Although a full calculation of neutron production and transport is beyond the scope of this thesis, the following comments can be made. Again, a more sophisticated approach to the accelerated ions may solve this problem. Neutron production is much higher in interactions with α-particles than with protons (e.g. the cross-sections for neutron production in Hua & Lingenfelter 1987c). Assumption A, that the accelerated protons and α-particles have exactly the same energy distributions (Chapter 5 and Toner & MacKinnon (2004)), is inherent in

the proton-number argument. Therefore, it might require too many α-particles in an α-poor flare. A reduced number of α-particles, relative to protons, would reduce the implied neutron emission. Relaxing Assumption A in the neutron-production calculations may provide further evidence that these high-energy flares are proton-dominated, and this is why we see fewer neutrons than have hitherto been expected.

Chapter 7

Future Work

7.1 Summary

In this thesis we have seen that there is further refinement necessary in the analysis of γ-ray spectra from solar flares, particularly in using diagnostics of the accelerated ion energy distribution. Particularly I have looked at the role of the 1.63 MeV line due to deexcitation of ^{20}Ne. This line is often used to investigate the energy distribution of accelerated protons, as the ^{20}Ne cross-section for proton excitation is sensitive to protons with energies as low as 3 MeV, whereas most other species have a lower-energy threshold nearer 7 MeV. However, problems have arisen in previous analyses as ratios of the 1.63 MeV line fluence with either of the 4.44 MeV ^{12}C or the 6.13 MeV ^{16}O line have implied either that there is a very steep proton energy spectrum, implying high proton numbers and a large component of flare energy in the ions, or that ^{20}Ne is enhanced in the target region.

Although the 1.63 MeV line provides a probe of the lower-energy protons, this sensitivity necessitates consideration of the mechanism of energy-loss in the target region. A fresh look at the effects of a warm target on this line fluence reveals the possibility that some of the protons could become trapped in a higher-temperature region, providing a gradual, warm component in each integrated line fluence. The increased lower-energy component of the proton spectrum can enhance the emission in the 1.63 MeV line, avoiding the necessity of invoking an actual enhanced ^{20}Ne abundance (MacKinnon & Toner 2003, and Chapter 4). Observations revealing the time-variation of individual lines would test for this warm target component.

While 1.63 MeV emission probes lower-energy accelerated protons, it doesn't prefer lower-energy α-particles. Until now, analyses of the accelerated ion energies

has made the assumption that all ions have the same energy distribution. There is no physical reason for supposing this, it just reduces the number of parameters that have to be considered in modelling the γ-ray spectrum, an important consideration given its complexity (Murphy et al. 1991). When the accelerated protons and α-particles are allowed to have different energy spectra, we see that the two types of ions can have very different distributions, especially when we can constrain the model with line fluences excited only by α-particles. The 0.4 to 0.5 MeV feature, which probes higher-energy α-particles, when detected, demands a hard α-particle spectrum. However, this does not imply that the protons follow suit. As we have seen, the protons can still have a steeper spectrum as indicated by the 1.63 MeV fluence alongside this hard α-particle distribution. We also see a variety of accelerated particle mixes ranging from proton-dominated flares right through to α-dominated flares (Toner & MacKinnon 2004, and Chapter 5). It may be necessary to obtain better cross-sections for α-particle excitation of nuclei if, indeed, the α-particles have harder spectra. These cross-sections are not so well defined by the data above a few tens of MeV.nucleon^{-1}, unlike cross-sections for proton excitation (Kozlovsky et al. 2002).

Protons and α-particles are not the whole story, however. The 4 to 7 MeV continuum is produced partly by very broad lines resulting from the interaction of heavy ions (e.g. ^{12}C, ^{16}O) with ambient protons and α-particles (Murphy et al. 1990b, 1991). This emission is relatively easily distinguished from the narrow emission lines and it is fortunate that the solar abundances of intermediate species such as lithium and beryllium are very low, providing a distinct break between light and heavy ions. Yet there is still some difficulty if ^{3}He is present in the accelerated ion population in sufficient quantity as may be the case. Share & Murphy (1998) illustrate the complexity of handling relative helium isotope abundances in interpreting the 1.02 MeV line feature. The SEP record already has a large number of ^{3}He-rich events amongst impulsive flares (Meyer 1985a, 1993; Zhang 1995; Litvinenko 1996, and references therein) and nuclear physics investigations are beginning to provide reactions with ^{3}He that could significantly contribute to the narrow emission line spectrum (e.g. Tatischeff et al. 2003). Neutron recapture is strongly affected by the amount of ambient ^{3}He encountered and Hua & Lingenfelter (1987a) used the time profile of the 2.22 MeV neutron

recapture line to calculate the ambient ^{3}He/H abundance ratio. They derived a figure of $(2.3 \pm 1.2) \times 10^{-5}$, in the range of values previously derived from solar wind, coronal and meteorite data. If the ambient ^{3}He is as scarce as that, then enhancements in the accelerated ions must arise from the acceleration or transport mechanisms. Share & Murphy (1998) analyzed the known ^{3}He-excited narrow lines, in the SMM/GRS data and one CGRO/OSSE spectrum, and found that either ^{3}He or α-particles are enhanced in the accelerated ions but this makes Assumption A and a more flexible study is needed. As seen in Section 5.3 (and Toner & MacKinnon 2004) ^{3}He interactions could produce a component of most of the narrow emission lines and a full investigation of the accelerated ion energies would need to include a separate ^{3}He energy spectrum, further increasing the number of parameters. At present this awaits a complete set of ^{3}He cross-sections.

More direct observations of the accelerated ion population can be made through the solar flare neutron emission and much of this data remains in the COMPTEL archive awaiting reduction. Careful interpretation of the instrument response matrix is necessary to derive an accurate measure of the detected neutron numbers and energy distribution and this matrix has to be carefully constructed for each set of observations. A long and expensive job is still to be done in converting this data source into useful information. However, similar data inversion techniques to those described in Chapter 6, may help to sort out the use of the γ-ray line spectrum in analyzing the fast ion energy. Expression of the modelling process in a matrix that converts the fast ion and ambient nuclei parameters into a set of line fluences would allow the degeneracy of the problem to be investigated and perhaps point to the parameters that can be deduced with present data.

As always the quality of instrumentation is continuously developing. The SMM/GRS database of γ-ray flares remains a valuable resource while spectra from CGRO/OSSE and other recent space missions are starting to be published. At present RHESSI is gathering spectra at unprecedented resolution but may lack the sensitivity of the earlier instruments, although it is emerging that the γ-ray emission lines do not necessarily correlate in brightness with the total flare energy as estimated from GOES data (e.g Hudson et al. 2003). Time will reveal if there are some big γ-ray flares for RHESSI as its mission continues and we await future developments in γ-ray instruments.

7.2 Temporal Behaviour of Flare γ-ray Spectra

In this present work, I have concentrated on investigating line fluences only. This has allowed a wider exploration of the parameter space in γ-ray nuclear deexcitation lines. However there is a lot more that can be derived from these lines when studied in more detail. Line shapes yield information about the geometry of the incident ion flow and of the source region (e.g. Murphy et al. 1988; Share & Murphy 1997; Hua & Lingenfelter 1987c,b). Time series of emission in individual lines also give information about the production of the lines. For example, the time profiles of the bright narrow lines between 1 and 7 MeV may indicate the occurrence of mirroring and pitch-angle scattering of the accelerated ions (Hua et al. 1989). The time profile of the 2.22 MeV neutron recapture line has been used to derive parameters affecting neutron recapture rates (Hua & Lingenfelter 1987a), particularly ^{3}He abundance.

As touched upon in Section 5.5 where I attempted a preliminary analysis of the data derived from RHESSI observations of the 23 July 2002 flare by Shih (2004), improvements in instrumentation are beginning to produce γ-ray line data with some resolution in time. The ^{20}Ne 1.63 MeV line has already shown itself to be interesting in this respect, with a different time history from the other lines in this flare, either as a result of variations in abundance across the active region or perhaps due to changes in the proton energy spectrum throughout the flare. It is clear that interesting work can be done, but that previous simplifications like Assumption A will have to be abandoned as suggested here.

My discussion in Section 5.5 assumed a cold, neutral target region. Another line of enquiry would be to use the time-history of a γ-ray spectrum to investigate whether there is some temperature variation over the life of the accelerated ion stream. Share et al. (2003) find ambiguity in their analysis of the 0.511 MeV positron annihilation feature in this same flare. This feature is formed, when a positron decays to positronium, out of a narrow line at exactly 0.511 MeV due to emission of two photons from the positronium singlet spin state and a continuum due to emission of three photons with different energies from the triplet spin state. The exact ratio of the line emission to the continuum emission (the $3\gamma/2\gamma$ ratio) depends on the temperature and density of the source region. Share et al.

(2003) find that it is not possible to distinguish between a source in quiet solar atmosphere conditions at $\sim$ 6000 K derived from the $3\gamma/2\gamma$ ratio and a hot, thermal source at between 400,000 and 700,000 K derived from the shape of the narrow line. This might indicate that a component of the fast ions was trapped for a time in the hot corona. Detailed modelling would be necessary to determine whether the injection of this hotter material towards the end of the impulsive stage would enhance 1.63 MeV emission in the way seen in Table 5.3. This might add strength to the idea in Chapter 4 and (MacKinnon & Toner 2003) that there may be a warm target component responsible for enhancement of the 1.63 MeV emission in some flares. Future work on the evolution of the ions over time should be carried out, even if just to rule out these effects and confirm a change in ^{20}Ne abundance during the flare.

7.3 Inversion Techniques

As we saw in Chapter 6, there is a lot that can be done with the CGRO/COMPTEL neutron data. However, instrument response matrices are required for each flare and this work is yet to be done.

The kind of inversion techniques described in Chapter 6 (Toner et al. 2001), might also provide a way forward in the analysis of the γ-ray spectra. Assuming nothing about the mechanisms of ion acceleration or the detailed shape of the accelerated ion distributions, one could construct a vector of ion numbers within energy bins. To some extent these bins can be defined according to the ranges of energies to which the various line-producing interactions are sensitive. For example, the $\alpha - \alpha$ feature between 0.4 and 0.5 MeV samples α-particles with energies above $\sim$ 10 MeV.nucleon^{-1}, and the 1.63 MeV line is uniquely sensitive to protons with energies above $\sim$ 3 MeV. A matrix transformation applied to such a vector, containing information about the excitation cross-sections and target nuclei abundances, a kind of source response matrix, would produce a vector of γ-ray line fluences.

Once such a model has been created, the matrix would then reveal details of exactly how the line fluences constrain the source model. Particularly, the degeneracy of the matrix could be investigated to help select the most important

lines and, also, show which lines really just sample exactly the same accelerated ion energies. These degenerate groups of lines might prove useful in the tricky task of subtracting the continuum (e.g. Murphy et al. 1991).

If a group of lines was identified which allowed an invertible source response matrix to be created, it might be possible to apply, say, a maximum entropy technique to invert a set of measured line fluences directly into a fast ion distribution. More realistically, this may prove to be a much larger task. It may be necessary to include bremsstrahlung continuum approximation and values for the broad line components into the inversion. The most satisfactory approach would probably have to include the continuum fit in the inversion too.

7.4 Neutron Production

An implication of the work in Chapter 6 is that neutron production in the absence of Assumption A (5) should be investigated. The differing cross-sections for neutron production reactions involving protons and α-particles (Hua & Lingenfelter 1987c) would result in quite different rates of production depending on the mix of accelerated ions over the > 10 MeV.nucleon^{-1} energy range. This would be a major piece of work, expanding the original Hua & Lingenfelter (1987c) calculations.

7.5 Conclusion

Some progress has been made here in opening up the parameter space for modelling γ-ray line emission from solar flares. Rather than increasing the complexity of the problem to intractability, some new constraints have been found; for example, the 0.4 to 0.5 MeV feature can constrain the fast α's while the α-excited emission from the deexcitation lines constrains the fast protons.

The possibility of more complex behaviour in the history of the fast ions has also been investigated. It may be possible that some of the fast ions spend some time trapped in a hotter region such as the corona and this may explain some of the enhanced emission that is often seen in the 1.63 MeV line due to ^{20}Ne.

Careful data inversion techniques are often necessary when using the advanced instrumentation that has been developed to detect and image γ-rays and neu-

trons. This kind of technique may help to disentangle the large number of parameters necessary to model the production of these radiations in solar flares.

To take this work further, there are a number of possible avenues of investigation. A major goal would be to move beyond forward modelling and properly invert the γ-ray spectrum through a source response matrix. This might, if the information is there in the detectable lines, reveal the actual shape of the fast ion distributions and a direct count of ion numbers and ion energy in the range ~ 2 to ~ 100 MeV, or even higher energies if we can include the 0.511 MeV and 2.22 MeV features.

In the meantime, as newer data provides more detail, the line shapes will start to provide more information about the nature of the fast ion velocity distribution and the source region, but it is necessary to start widening the parameter space to reveal the complexity of the fast ion population. Greater sensitivity and finer time resolution demands that we start to look at the time variation of all of the lines in the γ-spectrum. This could put in perspective the various competing parameters of varying species abundance, fast ion energy distributions and the nature of the source region.

As a consequence, tighter observational restraints on the fast ion energy distribution and the geometry of the ion flow will help to resolve our picture of the acceleration mechanisms. This still remains a fruitful and exciting branch of solar physics.

Appendix A

The 'Effective Coulomb Logarithm'

The rate of loss of energy, and thus the penetrating power, of fast ions is a well-studied topic. A recent review (Weaver & Westphal 2002) summarizes results in the energy range appropriate here as well as concentrating on effects that become important for heavy ions at relativistic energies.

Equations 4.4 and 4.4 summarize the rate at which the energy E of a fast proton changes in an ionized medium. An expression of this form also applies in the case of energy loss in a neutral medium, via the introduction of an 'effective Coulomb logarithm', given explicitly by e.g. Mott & Massey (1949); Emslie (1978). For protons in the nonrelativistic regime, its value is given numerically by

$$\Lambda_{neutral} = 5 + \ln E \tag{A.1}$$

Here E is measured in MeV. It is easy to verify that the energy loss rate given by Equations 4.4, 4.4 and A.1 is in excellent agreement with the empirical findings of Barkas & Berger (1964), at least for the energy range needed here (see also Weaver & Westphal (2002)). Comparison of the radiative properties of ionized and neutral targets may thus be carried out via comparison of the effective Coulomb logarithms.

Discussions of fast electron stopping carried out to understand deka-keV X-rays (Brown 1971) generally set the Coulomb logarithm equal to a constant. This habit would be a bad one here: Λ varies from 5 to almost 10 in the relevant 1 - 100 MeV energy range, and its energy-dependence is key to theoretical understanding of the empirical (Barkas & Berger 1964) results.

For protons in an ionized medium, in the absence of too strong a magnetic

field (Emslie 1978),

$$\Lambda_{ionised} = \ln \frac{m_e v^3}{e^2 \nu_p} \tag{A.2}$$

Here ν_p is the plasma frequency. Numerically,

$$\Lambda_{ionised} = 23.2 + \frac{3}{2} \ln E + \frac{1}{2} \ln n_{10} \tag{A.3}$$

where n_{10} measures ambient density in units of 10^{10} cm^{-3}. In a medium of 10^{10} cm^{-3} density, $\Lambda_{ionised}$ varies from 23.2 to 30.1; it takes values in excess of four times larger than $\Lambda_{neutral}$, but varies less over the relevant energy range.

Appendix B

γ-ray Nuclear Excitation Cross-sections

I digitized a number of cross-sections for important reactions leading to the γ-ray spectra investigated here, in finer resolution than the published cross-sections of Ramaty et al. (1979); Kozlovsky et al. (2002). These are based on the same sources as the Ramaty et al. (1979); Kozlovsky et al. (2002) cross-sections, particularly Dyer et al. (1981); Seamster et al. (1984); Carlson et al. (1985); Dyer et al. (1985); Lesko et al. (1988); Neu et al. (1989). These finer cross-sections are useful when a detailed line-by-line approach is being made to modelling the spectrum. When the more computationally intensive approach of modelling entire spectra and fitting them to data is adopted, computer time can be reduced by using the less-detailed cross-sections of Kozlovsky et al. (2002) which are available in electronic form.

Figures B.1 to B.6 show all of the cross-sections I have digitized where these are significantly different in energy resolution from those of Ramaty et al. (1979); Kozlovsky et al. (2002). Tables B.1 to B.8 list the actual digitizations for use in coding γ-ray spectrum models. The columns run in pairs, the first listing the accelerated ion energy (in MeV, not MeV.nucleon^{-1}) and the second the corresponding cross-section value in millibarns.

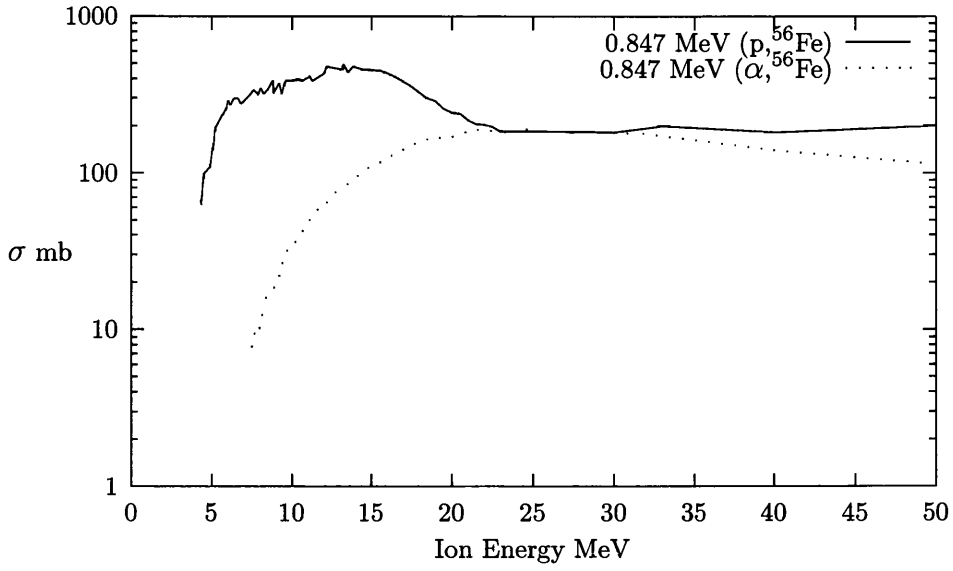

Figure B.1: Cross-sections for the 0.847 MeV excitation of ^{56}Fe.

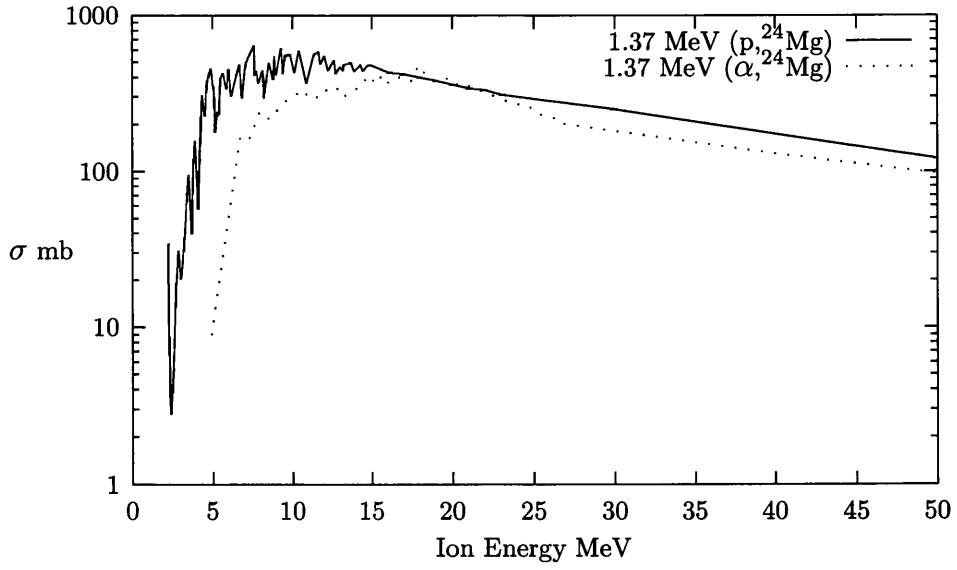

Figure B.2: Cross-sections for the 1.37 MeV excitation of ^{24}Mg.

α energy MeV	Cross-section mb	MeV	mb	MeV	mb
7.523076923	7.793495401	12.78461538	76.53467947	22.61538462	185.2322216
7.753846154	10.0910651	13.52307692	85.33012114	23.63076923	180.2625506
7.984615385	10.22922001	14.12307692	95.13634374	24.6	190.3389017
8.4	15.80588791	14.72307692	106.0695072	25.70769231	182.730492
8.723076923	17.86358019	15.36923077	113.5319534	26.72307692	182.730492
9	18.86212207	15.96923077	126.5791587	31.84615385	177.6927822
9.323076923	23.76754101	16.56923077	133.6547051	40	140
9.461538462	27.98017289	17.16923077	145.0164678	80	60
9.738461538	32.49458716	17.67692308	153.1226266	160	20
10.06153846	32.93946457	18.27692308	159.4982438	185.5384615	26.56148829
10.33846154	38.25402747	18.73846154	170.7196315	400	7
10.75384615	43.82604532	19.70769231	166.1393247	1000	0.4
11.4	55.97981979	20.63076923	180.2625506		
12.18461538	65.01179032	21.6	187.7682018		
proton energy MeV	Cross-section mb	MeV	mb	MeV	mb
4.369747899	63.09573445	9.579831933	369.2391073	17.94117647	332.01205
4.579831933	99.11830032	9.663865546	389.3898397	18.44537815	302.5305457
4.915966387	108.7773468	10.04201681	389.3898397	18.99159664	286.874739
5.12605042	145.7006665	10.46218487	394.5970609	19.49579832	257.9517399
5.294117647	195.1572166	10.67226891	389.3898397	19.95798319	244.6028644
5.756302521	238.1897546	11.17647059	416.1316699	20	242.6
5.924369748	254.5477314	11.34453782	389.3898397	20.54621849	238.1897546
6.092436975	290.7110492	12.10084034	433.0504174	21.00840336	217.0393407
6.218487395	272.0291125	12.18487395	475.2510411	21.51260504	205.8076617
6.428571429	298.5382619	13.19327731	456.6835671	21.97478992	203.0917621
6.680672269	298.5382619	13.27731092	494.5734166	22.4789916	197.7670094
6.890756303	275.6668955	13.57142857	438.8415015	22.98319328	185.0579267
7.43697479	314.8305899	13.86554622	475.2510411	30	180.8
7.68907563	336.4519711	14.45378151	456.6835671	33	199
7.941176471	314.8305899	14.83193277	456.6835671	40	182.2
8.109243697	345.5107295	15.16806723	450.6570338	50	202
8.319327731	319.0407473	15.50420168	450.6570338	70	120
8.529411765	340.9512662	15.84033613	438.8415015	100	48
8.865546218	389.3898397	16.21848739	421.6965034	200	25
8.895	321.2	16.51260504	410.6402716	1000	10
9.243697479	374.1768573	16.97478992	384.2513346		
9.411764706	319.0407473	17.43697479	359.5582274		

Table B.1: Digitized cross-section for 0.847 MeV excitation of ^{56}Fe by α-particles and protons.

α energy MeV	Cross-section mb	MeV	mb	MeV	mb
4.914992272	9.011837656	14.32766615	346.9565168	21.93199382	315.5133078
6.723338485	164.4788344	14.74497682	413.9004268	22.39567233	311.260329
7.326120556	164.4788344	15.11591963	376.390373	22.9057187	290.8400589
8.021638331	250.5077799	15.44049459	419.5558528	23.46213292	279.2366988
8.531684699	215.7685843	15.85780526	356.5027369	23.97217929	271.7594631
9.551777434	279.2366988	16.32148377	402.8172451	24.48222566	253.930652
10.0618238	298.8422814	16.87789799	397.3874481	24.94590417	257.4002932
10.61823802	333.1143335	17.43431221	381.5332715	25.45595054	230.9179856
11.08191654	294.8140206	17.94435858	480.5392654	25.82689335	221.7052776
11.45285935	290.8400589	18.40803709	408.3212335	26.42967543	218.7167892
11.87017002	333.1143335	18.87171561	376.390373	26.89335394	201.6130613
12.38021638	328.6241007	19.42812983	386.7464413	40	130
12.7511592	346.9565168	19.9381762	397.3874481	80	40
13.12210201	298.8422814	20.44822257	346.9565168	160	13
13.58578053	315.5133078	20.91190108	351.6972389	400	3
13.91035549	333.1143335	21.42194745	346.9565168	1000	0.4
proton energy MeV	Cross-section mb	MeV	mb	MeV	mb
2.257	34.3	7.666	409.039	15.801	382.255
2.3	10.415	7.794	437.7	16.014	392.751
2.385	3.572	7.922	367.034	16.525	387.468
2.428	2.799	8.177	443.669	16.567	352.419
2.555	4.318	8.262	295.521	16.695	333.833
2.598	5.22	8.433	392.751	17.206	316.228
2.726	17.191	8.603	494.445	17.717	299.551
2.896	30.778	8.816	387.468	18.228	279.936
3.066	20.225	8.901	543.618	18.825	268.789
3.279	33.383	9.029	414.617	19.165	247.809
3.45	72.248	9.327	614.095	19.676	237.942
3.535	94.726	9.455	420.271	20.187	241.186
3.748	39.811	9.583	551.032	20.698	231.583
3.833	108.466	9.881	558.546	21.252	222.361
3.918	156.357	9.923	536.305	21.678	202.247
4.131	57.388	10.179	431.811	22.274	199.526
4.216	112.964	10.434	589.642	22.743	205.005
4.302	179.036	10.945	367.034	30	150
4.387	307.776	11.414	566.163	40	116
4.557	228.467	11.67	581.709	50	89
4.685	367.034	11.797	487.793	60	68
4.813	414.617	12.053	551.032	70	57
4.94	455.852	12.266	443.669	80	53
5.111	329.342	12.649	514.95	90	44
5.196	179.036	12.777	420.271	100	39
5.366	241.186	12.99	462.068	200	24
5.451	231.583	13.203	443.669	300	18
5.537	387.468	13.245	481.23	400	15
5.664	426.002	13.714	494.44	500	14
5.92	338.386	13.927	437.7	600	13
6.048	449.719	14.31	481.23	700	12
6.218	303.636	14.48	437.7	800	11
6.729	481.23	14.736	474.756	900	10
6.857	295.521	15.119	414.617	1000	9
7.112	494.445	15.204	437.7		
7.624	639.562	15.588	426.002		

Table B.2: Digitized cross-sections for 1.369 MeV excitation of ^{24}Mg by α-particles and protons.

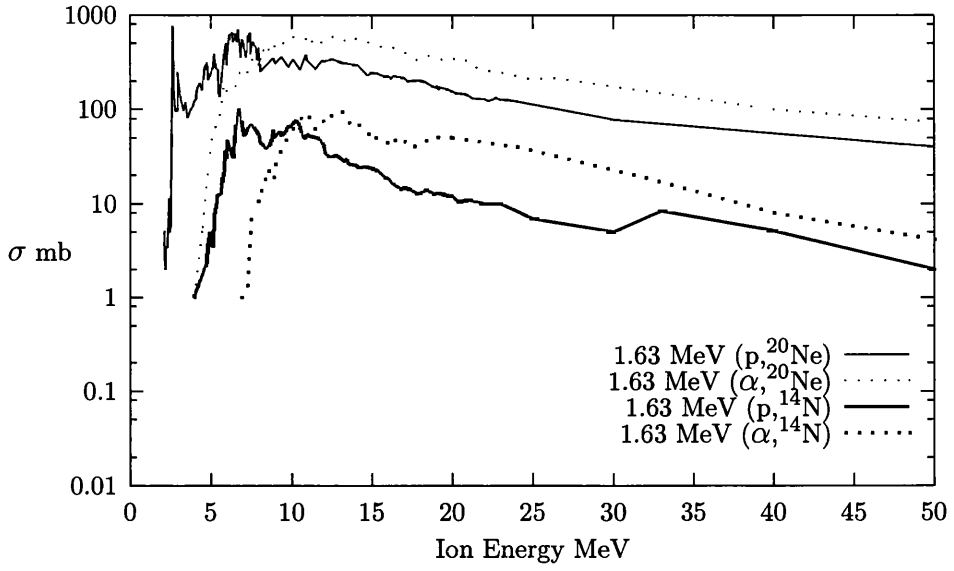

Figure B.3: Cross-sections for the 1.63 MeV emission.

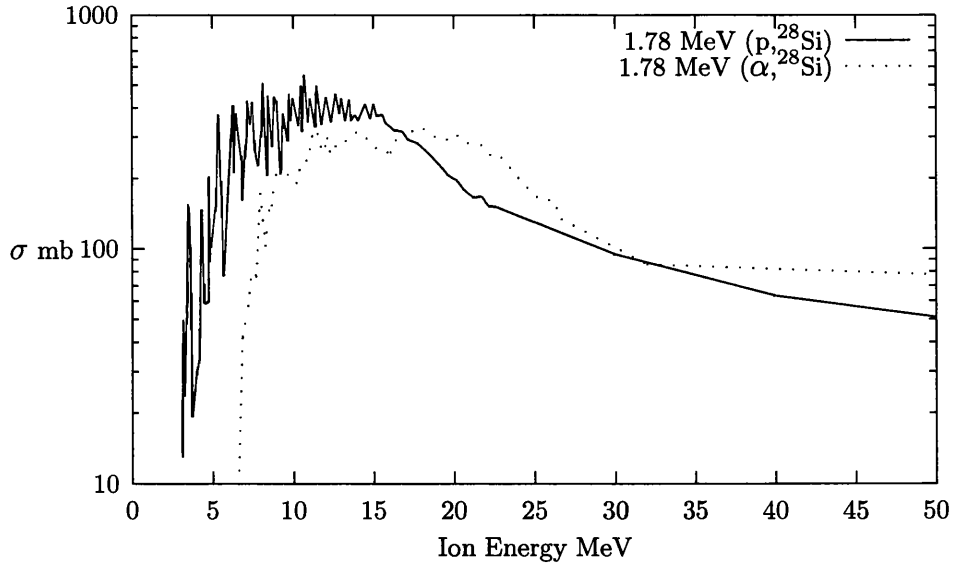

Figure B.4: Cross-sections for the 1.78 MeV excitation of ^{28}Si.

α energy MeV	Cross-section mb	MeV	mb	MeV	mb
4	1	10.29096478	595.865072	18	353
4.50229709	5.64260033	10.70444104	587.8016072	18.37672282	374.94235
4.869831547	27.78350176	11	546	19	354
5	38	11.0719755	472.6680128	19.5712098	322.7570517
5.099540582	51.29312649	11.39356815	572.0005544	20	337
5.558958652	87.26265097	11.80704441	505.9900908	20.35222052	359.9258324
5.834609495	189.7171137	12	556	21	318
5.972434916	167.8232283	12.12863706	572.0005544	21.31699847	281.6463595
6	151	12.45022971	587.8016072	22	271
6.294027565	158.9217841	12.77182236	587.8016072	22.37366003	252.5613347
6.569678407	179.6544048	13	590	23	249
6.84532925	259.5381373	13.18529862	556.6242592	23.38437979	242.4462017
7	234	13.50689127	505.9900908	24	226
7.30474732	252.5613347	13.82848392	556.6242592	24.44104135	211.5649828
7.534456355	336.2228452	14	564	25	212
7.856049005	359.9258324	14.42572741	519.967658	25.4517611	214.4672321
8	272	15	514	26	212
8.177641654	441.5403669	15.11485452	505.9900908	26.37059724	217.4092944
8.407350689	369.8684926	15.71209801	453.7375626	40	100
8.728943338	519.967658	16	465	80	30
9	460	16.21745789	459.9619362	160	10
9.050535988	429.6710515	16.81470138	418.1208024	400	2
9.418070444	485.7250845	17	411	1000	0.4
9.831546708	587.8016072	17.32006126	369.8684926	1600	0.4
10	580	17.82542113	336.2228452		
proton energy MeV	Cross-section mb	MeV	mb	MeV	mb
2.137	5.08	5.513	150.131	11.923	329.342
2.179	2.478	5.598	138.413	12	326
2.222	1.995	5.726	219.37	12.564	338.386
2.25	3.5	5.855	338.386	13	318
2.35	3.43	5.94	443.669	13.291	307.776
2.436	6.141	5.983	501.187	14	296
2.479	11.296	6	300	14.145	295.521
2.5	5	6.197	614.095	14.744	231.583
2.564	6.058	6.368	648.283	15	246
2.607	55.103	6.41	521.972	15.342	241.186
2.62	40	6.5	550	15.812	222.361
2.65	171.907	6.538	630.957	16	225
2.692	762.699	6.667	514.95	16.197	213.507
2.735	329.342	6.709	703.168	16.325	225.393
2.75	250	6.752	566.163	17	215
2.778	154.254	6.838	474.756	17.265	199.526
2.821	112.964	6.88	357.224	17.778	202.247
2.906	96.018	7	550	18	202
2.991	97.327	7.094	468.369	18.333	196.842
3	250	7.222	357.224	18.761	176.628
3.205	125.893	7.35	597.683	19.231	165.062
3.376	97.327	7.479	648.283	19	177
3.5	120	7.521	387.468	19.744	162.841
3.632	82.727	7.65	521.972	20	157
3.846	102.746	7.692	481.23	20.256	148.111
3.974	109.945	7.821	455.852	20.769	146.119
4	120	7.906	333.833	21	141
4.145	129.349	8	450	21.282	131.113
4.231	169.595	8.12	251.189	21.795	129.349
4.359	191.581	8.889	352.419	22	129
4.5	160	9	320	22.265	124.199
4.615	231.583	9.06	307.776	22.735	132.901
4.701	295.521	9.402	362.096	23	128
4.829	307.776	9.872	283.753	23.291	127.609
4.872	207.801	10	320	23.889	122.528
5	230	10.128	338.386	30	78
5.171	279.936	10.556	265.173	50	40
5.256	387.468	10.94	382.255	80	24
5.385	276.17	11	330	100	19
5.5	260	11.538	268.789	300	7
				1000	3

Table B.3: Digitized cross-sections for 1.634 MeV excitation of ^{20}Ne by α-particles and protons.

α energy MeV	Cross-section mb	MeV	mb	MeV	mb
6.885245902	1	11.7585693	73.61987469	17	46
7.242921013	1.358328854	12	76	17.07898659	40.35629891
7.511177347	9.665441016	12.11624441	71.15685565	17.61549925	40.81665761
7.868852459	9.236708572	12.42921013	86.29002427	18	45
8	14	12.74217586	91.32530536	18.10730253	44.69369958
8.137108793	13.58328854	13	92	18.59910581	48.93900918
8.494783905	23.68013841	13.05514158	95.56427437	19	52
8.807749627	17.63215596	13.23397914	91.32530536	19.09090909	50.63298105
8.986587183	21.87265374	13.32339791	83.40311399	19.4485842	52.38558796
9	27	13.68107303	67.23357536	20	50
9.433681073	39.90113244	13.90461997	70.35429904	24	40
9.746646796	51.21056954	14	72	32	19
10	61	14.48584203	62.10169419	40	8
10.01490313	61.401268	14.97764531	49.49727393	80	0.6
10.41728763	73.61987469	15	54	100	0.124374681
10.81967213	92.36708572	15.55886736	44.69369958	250	1.85E-06
11	83	16	45	500	1.67E-14
11.13263785	82.46243555	16.09538003	40.81665761	1000	1.35E-30
11.44560358	60.70874172	16.58718331	51.79474679		
proton energy MeV	Cross-section mb	MeV	mb	MeV	mb
4	1	8.83105802	49.068451	14	26
4.778156997	2.312023118	8.895	61.3	14.20648464	24.29509441
4.906143345	3.812530329	8.959044369	54.6725185	14.67576792	24.62574809
5	5	9	50	15	24
5.034129693	4.606860781	9.300341297	59.29173094	15.40102389	22.40234814
5.162116041	3.468306077	9.428327645	52.49966785	15.87030717	18.79198265
5.290102389	7.911134124	9.513651877	54.6725185	16	19
5.418088737	9.955040996	9.684300341	58.49561181	16.33959044	16.19546218
5.460750853	12.35880605	9.726962457	65.17634761	16.85153584	14.34021864
5.674061433	12.5270081	10	67	17	15
5.716723549	16.86575825	10.1109215	68.79761542	17.36348123	14.34021864
5.887372014	22.10154839	10.19624573	75.62567708	17.83276451	12.87031099
5.93003413	36.44549353	10.45221843	73.60843648	18	13
6	30	10.62286689	61.74569077	18.38737201	13.95770741
6.100682594	47.7595983	10.79351536	49.73626746	18.89931741	12.69749936
6.399317406	30.5719328	10.83617747	49.068451	19	13
6.56996587	58.49561181	11	55	19.36860068	12.87031099
6.783276451	101.8187565	11.1774744	52.49966785	19.88054608	12.02914704
7	65	11.47610922	50.41317283	20	12.3
7.124573379	52.49966785	11.77474403	49.068451	20.39249147	10.50815376
7.167235495	54.6725185	11.98805461	42.28857899	21	11
7.295221843	61.74569077	12	41	22	10
7.551194539	70.68301538	12.07337884	38.99402296	23	10
7.764505119	63.4378326	12.11604096	34.06352814	25	7
7.849829352	59.29173094	12.37201365	31.83724069	30	5
8	54	12.58532423	31.83724069	33	8.36
8.020477816	53.21418281	12.79863481	32.70974088	40	5.2
8.063139932	45.86148793	13	31	50	2
8.19112628	42.86412211	13.13993174	29.75645654	70	1
8.276450512	42.28857899	13.26791809	28.57384528	120	0.3
8.447098976	38.47044426	13.48122867	29.75645654	200	0.011381636
8.660409556	41.72076379	13.60921502	26.34775643	500	1.53E-07
				1000	1.15E-15

Table B.4: Digitized cross-sections for 1.635 MeV excitation of ^{14}N by α-particles and protons.

α energy MeV	Cross-section mb	MeV	mb	MeV	mb
6.6	11.41368132	11.03076923	265.3153495	19.61538462	291.9755832
6.830769231	42.43485986	11.26153846	316.9495204	20.12307692	308.3961239
7.2	57.33447519	11.53846154	308.3961239	20.63076923	284.0961488
7.430769231	82.94913876	11.86153846	251.1886432	21.13846154	280.2365337
7.707692308	76.41318761	12.13846154	295.9968768	21.69230769	276.4293537
7.938461538	171.2629287	12.36923077	244.4099104	22.2	251.1886432
8.261538462	103.2431832	12.6	272.6738966	22.75384615	254.6481903
8.446153846	145.3370155	13.29230769	288.0089213	23.21538462	231.3963135
8.676923077	153.5106865	14.07692308	321.3147727	23.67692308	213.1635142
8.861538462	210.267561	14.76923077	284.0961488	24.18461538	193.6995951
9.092307692	201.8136305	15.41538462	258.1553847	24.69230769	178.4370968
9.369230769	207.4109512	16.06153846	258.1553847	25.15384615	166.6411209
9.692307692	207.4109512	16.66153846	321.3147727	25.70769231	159.9412169
10.01538462	201.8136305	17.35384615	316.9495204	26.16923077	162.1440401
10.2	191.0680709	17.90769231	330.2264693	26.72307692	133.8852313
10.47692308	231.3963135	18.46153846	312.6435727	32	85.8
10.8	234.5832667	19.06153846	291.9755832	1000	0.4
proton energy MeV	Cross-section mb	MeV	mb	MeV	mb
3.146	13.045	8.418	205.642	15.221	367.754
3.231	49.736	8.461	450.423	15.561	372.759
3.316	23.647	8.759	273.149	15.774	343.719
3.444	57.71	8.844	444.375	16.284	321.255
3.529	154.819	9.014	420.985	16.794	316.941
3.614	135.243	9.269	208.441	17.177	292.249
3.699	83.131	9.311	226.052	17.772	280.634
3.784	19.307	9.439	377.833	18.24	262.293
4.082	30.572	9.694	288.325	18.75	241.859
4.209	33.606	9.779	456.553	19.303	220.022
4.379	146.67	9.906	353.139	19.685	205.642
4.549	58.496	10.034	438.408	20.238	194.818
4.762	59.292	10.374	334.551	20.706	177.228
4.804	202.881	10.544	495.127	21.216	165.645
4.847	87.75	10.629	316.941	21.726	167.899
4.974	107.476	10.714	551.675	22.194	152.74
5.23	150.689	10.969	348.397	22.704	150.689
5.4	372.759	11.097	438.408	30	95
5.612	170.184	11.395	330.059	40	63
5.74	76.655	11.48	495.127	50	51
6.335	409.755	11.82	339.104	60	42
6.378	211.277	12.075	444.375	70	38
6.463	377.833	12.415	348.397	80	34
6.845	238.611	12.67	456.553	90	32
6.888	161.226	12.925	377.833	100	31
7.058	262.293	13.053	438.408	200	20
7.143	300.258	13.265	353.139	300	16
7.185	426.714	13.52	432.522	400	14
7.398	339.104	13.648	353.139	500	12
7.526	420.985	13.861	372.759	600	11
7.653	262.293	14.073	353.139	700	10
7.866	226.052	14.498	415.332	800	9
8.078	316.941	14.838	357.945	900	9
8.163	508.696	15.009	415.332	1000	8

Table B.5: Digitized cross-sections for 1.779 MeV excitation of ^{28}Si by α-particles and protons.

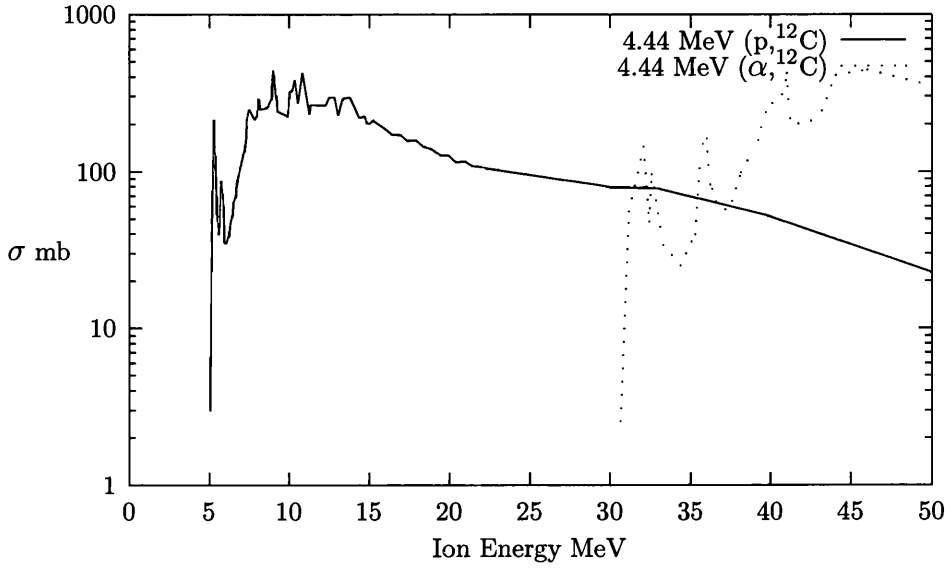

Figure B.5: Cross-sections for the 4.44 MeV excitation of ^{12}C.

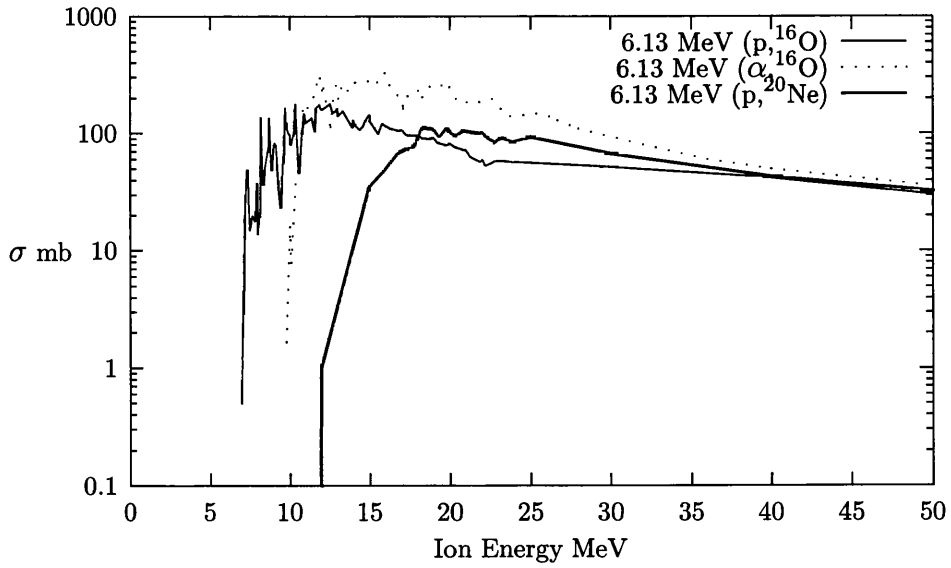

Figure B.6: Cross-sections for the 6.13 MeV emission.

α energy MeV	Cross-section mb	MeV	mb	MeV	mb
30.63	2.56	41.19	219.82	71.28	330.23
31.16	55.97	41.73	200.81	73.97	382.52
32.06	143.05	42.99	214.9	76.48	443.08
32.42	47.78	43.34	260.44	79.52	423.49
32.6	96.3	43.52	291.62	81.85	291.62
33.31	34.03	44.06	409.37	86.15	248.93
34.39	25.08	46.03	443.08	90.27	266.4
35.28	39.87	51.4	322.85	94.39	243.36
35.64	143.05	52.48	357.43	98.33	266.4
36	161.99	53.55	365.6	102.45	294.93
36.18	86.01	54.63	428.3	106.75	219.82
36.36	77.69	55.7	365.6	112	272.31
36.9	52.89	56.96	468.85	120	382
37.61	64.83	58.39	418.73	128	242.33
38.15	98.5	59.46	357.43	140	276
39.22	158.37	60.9	353.41	144	217.6
39.58	229.99	62.33	361.49	160	265
40.12	272.49	63.76	404.76	200	264
40.84	319.22	65.55	308.58	280	263
41.01	423.49	68.42	285.1	400	292
				800	272
proton energy MeV	Cross-section mb	MeV	mb	MeV	mb
5.094	2.996	8.219	247.809	15.068	202.247
5.223	50.802	8.69	254.614	15.24	210.634
5.308	213.507	8.947	291.545	15.967	186.461
5.437	102.746	9.033	437.7	16.396	171.907
5.522	52.909	9.118	387.468	16.952	169.595
5.651	39.275	9.247	283.753	17.38	156.357
5.822	87.333	9.289	241.186	17.937	158.489
5.908	66.608	9.974	222.361	18.408	144.153
5.993	35.242	10.103	320.54	18.921	138.413
6.122	34.768	10.274	324.911	19.435	127.609
6.293	38.747	10.402	382.255	20	126.1
6.378	45.585	10.616	272.455	20.377	114.505
6.507	52.909	10.873	420.271	20.976	116.066
6.55	63.096	11.344	231.583	21.404	108.466
6.721	69.371	11.387	265.173	21.875	107.007
6.764	80.516	12.329	261.606	22.389	104.147
6.849	89.731	12.543	295.521	22.945	102.746
7.277	136.551	12.885	295.521	30	79.3
7.363	162.841	13.099	228.467	33	78.4
7.406	213.507	13.399	291.545	40	51.7
7.534	247.809	13.827	295.521	50	22.6
7.92	213.507	14.384	219.37	100	10.1
8.048	225.393	14.726	222.361	200	7
8.134	291.545	14.854	202.247	1000	4

Table B.6: Digitized cross-sections for 4.438 MeV excitation of ^{12}C by α-particles and protons.

α energy MeV	Cross-section mb	MeV	mb	MeV	mb
9.789473684	1.663218333	13.98496241	275.5889917	21.56390977	179.3421978
10	16	14	269	22	191
10.10526316	7.916386781	14.61654135	288.337946	22.55639098	196.3190107
10.37593985	36.83704453	15	276	23	170
10.64661654	59.89824188	15.2481203	251.7572562	23.54887218	138.2779283
10.82706767	156.5895169	15.87969925	333.9885571	24	143
11	144	16	288	24.54135338	143.0483376
11.05263158	163.8334658	16.5112782	219.817464	25	148
11.41353383	175.3325384	17	200	25.62406015	147.9833198
11.59398496	237.9206176	17.05263158	163.8334658	26	143
11.86466165	315.6324667	17.63909774	269.4274858	26.66165414	129.2090586
12	231	18	231	28	110
12.13533835	243.3615965	18.18045113	191.9297906	32	80
12.36090226	153.0885526	18.67669173	248.9270046	36	60
12.54135338	114.0993427	19	252	40	50
12.85714286	278.7223849	19.26315789	243.3615965	60	25
13	219	19.80451128	278.7223849	80	20
13.03759398	194.111995	20	242	120	15
13.26315789	257.5146636	20.48120301	183.4435537	200	10
13.53383459	222.3167458	21	184	400	6
				1000	1.809562359
proton energy MeV	Cross-section mb	MeV	mb	MeV	mb
7	0.5	10.623	45.929	16.809	105.102
7.167	4.572	10.708	58.637	17	107
7.253	25.974	10.836	112.481	17.278	96.883
7.381	49.153	10.922	147.557	17.79	95.577
7.551	14.89	11	122	18	97
7.722	20.07	11.391	136.018	18.302	90.527
7.85	17.763	11.604	103.685	18.771	89.307
8	38	11.647	134.184	19	92
8.02	13.725	11.689	164.479	19.241	83.448
8.191	20.904	11.903	176.027	19.795	79.039
8.234	137.876	12	160	20	82
8.404	36.466	12.073	162.262	20.307	75.885
8.447	48.491	12.543	178.432	20.776	72.858
8.703	73.853	12.713	149.573	21	72
8.746	136.018	12.969	157.917	21.288	62.754
8.916	48.491	13	163	21.843	57.067
9	69	13.055	139.76	22	59
9.044	82.323	13.353	155.788	22.227	53.323
9.172	79.039	13.951	112.481	22.782	57.847
9.343	33.161	14	130	23	58
9.471	23.302	14.121	117.155	30	52
9.556	36.964	14.377	106.538	40	42
9.642	64.481	14.59	115.576	50	30
9.727	164.479	14.761	128.831	60	23
9.855	109.469	14.974	143.605	70	15
10	97	15	128	80	15
10.026	82.323	15.316	110.965	85	10
10.154	80.118	15.529	99.549	90	14
10.282	99.549	15.785	120.379	100	7.5
10.367	178.432	16	115	200	4.5
10.41	149.573	16.297	109.469	400	3.5
				1000	3

Table B.7: Digitized cross-sections for 6.129 MeV excitation of ^{16}O by α-particles protons.

proton energy MeV	Cross-section mb	MeV	mb	MeV	mb
11.95560807	0.1	19	108	23	90
12	1	19.35897436	93.01774682	23.33333333	90.52697242
15	35	19.82905983	112.4813578	23.84615385	84.58793988
15.85470085	47.19221198	20	103	25	93
16.32478632	57.06700347	20.2991453	95.57705281	30	67
16.79487179	69.00805764	20.81196581	105.1020052	40	43
17	71	21	104	50	32
17.26495726	73.85320578	21.28205128	102.2876457	70	23
17.82051282	77.97313398	21.75213675	100.9088538	100	15
18	93	22	101	198.0596252	8.024848831
18.29059829	112.4813578	22.30769231	91.76390903	200	8
18.84615385	109.4693983	22.82051282	83.44773213	1000	5

Table B.8: Digitized cross-section for production of 6.129 MeV ^{16}O by spallation reaction on ^{20}Ne by protons.

Appendix C

Ion Energies from the 19 SMM/GRS-observed Flares

Tabulated here are models calculated according to the methods shown in Chapter 5 and in MacKinnon & Toner (2003). A range of values is chosen for the slope of the α-particle energy spectrum and then the other parameters derived to fit the measured fluences for the 1.63 MeV and 6.13 MeV lines and the 0.5 MeV $\alpha - \alpha$ feature. Above the largest δ_α shown for each flare, there was insufficient line fluence to accommodate the α-induced emission, except in the cases of the 1982 December 7 and 1986 February 6 flares for which solutions were possible throughout the range of δ_α investigated. Linear propagation of the quoted observation error bars led to the errors quoted here for selected flares. A '?' in the error indicates that the value was not obtainable by this method. Error bars have not been propagated for this larger set of models and a more complete statistical treatment of errors is beyond the scope of the present work. The reader should be wary of any numbers quoted here without errors and consult the original data (Share & Murphy 1997) to check for the quality of the line detections. For example, the flare of September 9, 1989, shows an interesting pattern in which a steeper α-particle distribution is followed by a flatter proton distribution. The ratio of α-particles to protons also rises to very large values. However, in the original spectrum, the $\alpha - \alpha$ lines are only given by an upper limit and the 1.63 MeV line is only barely detected (1.9 ± 1.1 photons.cm^{-2}). So the interesting result is probably an artifact of the poor data.

Flare	δ_α	$F_{0,\alpha}$	δ_p	$F_{0,p}$	$\frac{F_{0,\alpha}}{F_{0,p}}$	Ion Energy (erg)
1981	2.5	4.5×10^{33}	4.7	5.9×10^{36}	0.00075	1.3^{31}
April 10	3.0	1.7×10^{34}	4.9	7.5×10^{36}	0.0023	1.6×10^{31}
	3.5	6.3×10^{34}	5.4	1.5×10^{37}	0.0043	3.2×10^{31}
	3.8	1.4×10^{35}	6.8	9.3×10^{37}	0.0015	1.8×10^{32}
1981	2.5	$(2.9 \pm 0.8) \times 10^{34}$	$4.4^{+0.7}_{-0.6}$	$(7.1^{+17.7}_{-4.9}) \times 10^{36}$	$0.0041^{+0.0132}_{-0.0032}$	$(1.6^{+1.9}_{-0.8}) \times 10^{31}$
April 27	3.0	$(1.1 \pm 0.3) \times 10^{35}$	$4.7^{+1.5}_{-0.9}$	$(9.7^{+78.7}_{-7.9}) \times 10^{36}$	$0.011^{+0.065}_{-0.010}$	$(2.2^{+7.3}_{-1.3}) \times 10^{31}$
	3.5	$(4.0 \pm 1.1) \times 10^{35}$	$7.1^{+?}_{-3.3}$	$(1.5^{+?}_{-1.5}) \times 10^{38}$	$0.0027^{+0.48}_{-?}$	$(5.6\pm?) \times 10^{32}$
1982	2.5	2.2×10^{33}	5.3	2.0×10^{37}	0.00011	4.1×10^{31}
June 3	3.0	8.3×10^{33}	5.4	2.3×10^{37}	0.00037	4.7×10^{31}
	3.5	3.1×10^{34}	5.7	3.3×10^{37}	0.00093	6.8×10^{31}
	4.0	1.1×10^{35}	6.7	1.3×10^{38}	0.00091	2.5×10^{32}
1982	2.5	1.4×10^{34}	5.0	6.6×10^{36}	0.0021	1.4×10^{31}
July 9	2.95	4.7×10^{34}	7.1	1.1×10^{38}	0.00042	2.2×10^{32}
1982	2.5	6.2×10^{33}	4.7	1.3×10^{36}	0.0050	2.8×10^{30}
November 26	2.9	1.8×10^{34}	7.0	2.6×10^{37}	0.00072	4.9×10^{31}
1982	2.5	2.0×10^{33}	4.1	1.2×10^{37}	0.00016	2.9×10^{31}
December 7	3.0	7.5×10^{33}	4.1	1.2×10^{37}	0.00061	2.9×10^{31}
	3.5	2.8×10^{34}	4.1	1.2×10^{37}	0.0023	2.9×10^{31}
	4.0	1.0×10^{35}	4.1	1.3×10^{37}	0.0081	3.0×10^{31}
1984	No	Solutions				
April 24						
1986	2.5	$(3.8 \pm 58) \times 10^{32}$	$3.4^{+0.7}_{-0.8}$	$(5.4^{+20}_{-4.8}) \times 10^{35}$	$0.0007^{+0.100}_{-0.0029}$	$(1.5^{+1.6}_{-1.0}) \times 10^{30}$
February 6	3.0	$(1.4 \pm 22) \times 10^{33}$	3.4 ± 0.9	$(5.4^{+27}_{-5.0}) \times 10^{35}$	$0.0027^{+0.60}_{-0.0089}$	$(1.5^{+1.9}_{-1.1}) \times 10^{30}$
	3.5	$(5.3 \pm 81) \times 10^{33}$	$3.4^{+1.2}_{-1.3}$	$(5.4^{+53}_{-5.3}) \times 10^{35}$	$0.0099^{+7.5}_{-0.023}$	$(1.5^{+2.7}_{-1.1}) \times 10^{30}$
	4.0	$(1.9 \pm 30) \times 10^{34}$	$3.4^{+2.2}_{-2.3}$	$(5.3^{+241}_{-5.3}) \times 10^{35}$	$0.037^{+1150}_{-0.048}$	$(1.5^{+?}_{-2.2}) \times 10^{30}$
1988	2.5	7.7×10^{34}	4.2	1.6×10^{37}	0.0047	3.8×10^{31}
December 16	3.0	2.9×10^{35}	4.4	2.1×10^{37}	0.014	5.0×10^{31}
	3.5	1.1×10^{36}	5.4	8.6×10^{37}	0.013	1.8×10^{32}
1989	2.5	6.2×10^{34}	4.5	3.8×10^{37}	0.0016	8.6×10^{31}
March 6	3.0	2.3×10^{35}	4.7	4.8×10^{37}	0.0048	1.1×10^{32}
	3.5	8.6×10^{35}	5.3	1.2×10^{38}	0.0074	2.5×10^{32}
	3.6	1.1×10^{36}	5.6	1.9×10^{38}	0.0059	3.9×10^{32}
1989	2.5	2.1×10^{34}	4.6	1.7×10^{37}	0.0012	3.8×10^{31}
March 10	3.0	8.0×10^{34}	4.8	2.4×10^{37}	0.0035	5.1×10^{31}
	3.5	3.0×10^{35}	5.7	7.3×10^{37}	0.0041	1.5×10^{32}
	3.65	4.4×10^{35}	6.7	3.0×10^{38}	0.0015	5.8×10^{32}
1989	2.5	1.0×10^{34}	4.2	3.3×10^{36}	0.0031	7.7×10^{30}
March 17	3.0	3.9×10^{34}	4.3	4.0×10^{36}	0.0010	9.2×10^{30}
	3.8	3.1×10^{35}	6.4	7.1×10^{37}	0.0047	1.3×10^{32}
1989	2.5	$(9.4 \pm 4.9) \times 10^{33}$	$4.5^{+4.3}_{-1.5}$	$(2.6^{+?}_{-2.4} \times 10^{36}$	$0.0037^{+0.12}_{-0.0037}$	$(5.8^{+?}_{-4.4}) \times 10^{30}$
May 3	3.0	$(3.6 \pm 1.9) \times 10^{34}$	$5.0^{+?}_{-2.2}$	$(4.1^{+?}_{-4.1}) \times 10^{36}$	$0.0086^{+1.3}_{-?}$	$(9.0\pm?) \times 10^{30}$
	3.375	$(9.5 \pm 5.0) \times 10^{34}$	$7.5^{+?}_{-5.7}$	$(7.7^{+?}_{-7.7}) \times 10^{37}$	$0.0012^{+180}_{-?}$	$(1.5\pm?) \times 10^{32}$
1989	2.5	1.8×10^{34}	5.2	2.1×10^{37}	0.00086	4.4×10^{31}
August 16	3.0	6.7×10^{34}	6.2	8.4×10^{37}	0.00081	1.7×10^{32}
	3.1	8.7×10^{34}	7.1	2.6×10^{38}	0.00030	5.0×10^{32}
1989	No	Solutions				
August 17						
1989	2.5	4.0×10^{33}	2.8	2.3×10^{34}	0.17	1.0×10^{29}
September 9	3.0	1.5×10^{34}	2.7	1.7×10^{34}	0.89	1.1×10^{29}
	3.5	5.5×10^{34}	2.5	5.4×10^{33}	10.3	1.7×10^{29}
	3.7	9.3×10^{34}	2.2	9.3×10^{34}	101	2.5×10^{29}
1989	2.5	$6.1 \times 10^{3}4$	4.4	1.9×10^{37}	0.0033	4.3×10^{31}
October 19	3.0	2.3×10^{35}	4.6	2.8×10^{37}	0.0086	6.1×10^{31}
	3.45	7.6×10^{35}	5.9	1.7×10^{38}	0.0048	3.3×10^{32}
1989	No	Solutions				
October 24						
1989	2.5	$(1.4 \pm 0.5) \times 10^{34}$	$5.3^{+?}_{-2.2}$	$(6.3^{+?}_{-6.2}) \times 10^{36}$	$0.0022^{+0.21}_{-?}$	$(1.3\pm?) \times 10^{31}$
November 15	2.875	$(3.8 \pm 1.5) \times 10^{34}$	$7.3^{+?}_{-4.5}$	$(6.4^{+?}_{-6.4}) \times 10^{37}$	$0.00059^{+1.8}_{-?}$	$(1.2\pm?) \times 10^{32}$

Table C.1: Solutions for SMM/GRS flare spectra, choosing a range of values for δ_α and using the fluences given in Share & Murphy (1997).

Bibliography

Akimov, V. V., Afanassyev, V. G., & Belaousov, A. S. 1991, in Proc. 22nd Internat. Cosmic Ray Conf., Dublin, 73

Alard, J. P. 1974, Nuovo Cimento Lett., 10, 841

Alexander, D., Dunphy, P. P., & MacKinnon, A. L. 1994, Sol.Phys., 151, 147

Anders, E. & Grevesse, N. 1989, Geochim.Cosmochim.Acta, 53, 197

Arellano, H. F. & von Geramb, H. V. 2002, Phys.Rev.C, 66, 4602

Arndt, M. B., Young, C. A., & McConnell, M. L. 1998, COMPTEL Neutron Image of the Sun, Internet, http://www.gro.unh.edu/comptel

Arnold, J. R., Metzger, A. E., Anderson, E. C., & van Dilla, M. A. 1962, J.G.R., 67, 4878

Bame, S. J., Asbridge, J. R., Feldman, W. C., Fenimore, E. E., & Gosling, J. T. 1979, Sol.Phys., 62, 179

Bame, S. J., Asbridge, J. R., Feldman, W. C., Montgomery, M. D., & Kearney, P. D. 1975, Sol.Phys., 43, 463

Barat, C., Trottet, G., Vilmer, N., et al. 1994, Ap.J., 425, L109

Barkas, W. H. & Berger, M. J. 1964, Tables of Energy Losses and Ranges of Heavy Charged Particles, Tech. Rep. SP-3013, NASA

Bespalov, P. A., Zaitsev, V. V., & Stepanov, A. V. 1987, Sol.Phys., 114, 127

Bhattacharya, D. 1999, private Communication

Breneman, H. H. & Stone, E. C. 1985, Ap.J.Lett., 299, 57

Brown, F. B. & Nagaya, Y. 2002, The MNCP5 Random Number Generator, Tech. Rep. LA-UR-02-3782, Los Alamos, american Nuclear Society, 2002 Winter Meeting

Brown, J. C. 1971, Sol.Phys., 18, 489

Brown, J. C., Karlicky, M., MacKinnon, A. L., & van den Oord, G. H. J. 1990, Ap.J.Supp., 73, 343

Cane, H. V., von Rosenvinge, T. T., Cohen, C. M. S., & Mewaldt, R. A. 2003, Geophys.Res.Lett., 30, 592

Carlson, R. F., Cox, A. J., Nasr, T. N., et al. 1985, Nuc.Phys.A, 445, 57

Cattaneo, F. & Hughes, D. W. 2001, A.&G., 42, 18

Centre, S. E. 2004, GOES X-ray Flux Plot, Internet, www.sec.noaa.gov

Chuchkov, E. A., Ermakov, S. I., Kadobnov, V. B., et al. 1991, Sov.Astron.Lett., 17, 58

Chupp, E. L. 1984, A.R.A.&A., 22, 359

Chupp, E. L., Debrunner, H., Flückiger, E., et al. 1987, Ap.J., 318, 913

Chupp, E. L. & Dunphy, P. P. 2004, New Astron. Rev., 48, 113

Chupp, E. L., Forrest, D. J., Higbie, P. R., et al. 1973, Nature, 241, 333

Chupp, E. L., Forrest, D. J., Ryan, J. M., et al. 1981, Ap.J., 244, L171

—. 1982, Ap.J., 263, L95

Cliver, E. W., Forrest, D. J., Cane, H. V., et al. 1989, Ap.J., 343, 953

Covington, J. & Myers, D. 2000, The Trace Educational CD-ROM, CD-ROM, NASA

Craig, I. J. D. & Brown, J. C. 1986, Inverse Problems in Astronomy (Adam Hilger)

Datlowe, D. W., Elcan, M. J., & Hudson, H. S. 1974, Sol.Phys., 39, 155

Deb, P. K. & Amos, K. 2003, Phys.Rev.C, 67, 7602

del Zanna, G. 2003, private communication to A. MacKinnon

Dendy, R. O. 1994, Plasma Dynamics, 2nd edn. (Oxford: O.U.P.)

Dennis, B. R. 1988, Sol.Phys., 118, 49

Dolan, J. & Fazio, G. 1965, Rev.Geophys., 3, 319

Dyer, P., Bodansky, D., Leach, D. D., Norman, E. B., & Seamster, A. G. 1985, Phys.Rev.C, 32, 1873

Dyer, P., Bodansky, D., Seamster, A. G., Norman, E. B., & Maxson, D. R. 1981, Phys.Rev.C, 23, 1865

Emslie, A. 2003, Ap.J., 595, L119

Emslie, A. G. 1978, Ap.J., 224, 241

Emslie, A. G., Brown, J. C., & MacKinnon, A. L. 1997, Ap.J., 485, 430

Enge, H. E. 1979, Nucl.Instrum.Methods, 162, 161

Evenson, P., Meyer, P., Yanagita, S., & Forrest, D. J. 1984, Ap.J., 283, 439

Feldman, U., Schühle, U., Widing, K. G., & Laming, J. M. 1998, Ap.J., 505, 999

Fletcher, L. & Martens, P. C. H. 1998, Ap.J., 505, 418

Forman, M. A., Ramaty, R., & Zweibel, E. G. 1986, in The Physics of the Sun, ed. P. A. Sturrock, T. E. Holzer, D. Mihalas, & R. K. Ulrich, Vol. 2 (Dordrecht: Reidel), 249

Forrest, D. J. & Chupp, E. L. 1983, Nature, 305, 291

Galloway, R. K. and, M. A. L., Kontar, E., & Helander, P. 2004, Ap.J., in preparation

Golub, L. & Pasachoff, J. M. 2001, Nearest Star: the Surprising Science of Our Sun (Harvard)

Groetsch, C. W. 1993, Inverse Problems in the Mathematical Sciences, 1st edn. (Braunschweig, Wiesbaden: Vieweg)

Guessoum, N. & Gould, R. J. 1989, Ap.J., 345, 356

Gull, S. F. 1988, in Maximum Entropy and Bayesian Methods, ed. J. Skilling (Dordrecht: Kluwer), 53–73

Heyvaerts, J. 1981, in Solar Flare Magnetohydrodynamics, ed. E. R. Priest (Gordon and Breach), 429

High Energy Astrophysics Science Archive Research Centre. 2004, HEASARC Archive, Internet, http://heasarc.gsfc.nasa.gov

Hoyng, P., Brown, J. C., & van Beek, H. F. 1976, Sol.Phys., 48, 197

Hua, X.-M. & Lingenfelter, R. E. 1987a, Ap.J., 319, 555

—. 1987b, Ap.J., 323, 779

—. 1987c, Sol.Phys., 107, 351

Hua, X.-M., Ramaty, R., & Lingenfelter, R. 1989, Ap.J., 341, 516

Hudson, H. S., Bai, T., Gruber, D. E., et al. 1980, Ap.J., 236, L91

Hudson, H. S., Lin, R. P., & Smith, D. M. 2003, A.G.U., Fall Meeting 2002, Abstracts

Hurford, G. J., Schwarz, R. A., Krucker, S., L. R. P., & Smith, D. M., V. N. 2003, Ap.J., 595, L77

Institute of Space and Astronautical Science. 2004, The Yohkoh Observatory, Internet, http://isass1.solar.isas.jaxa.jp/ yohkoh

Kahler, S. W., Sheeley, N. R., J., Howard, R. A., et al. 1984, J.Geophys.Res., 89, 9683

Kanbach, G., Bertsch, D. L., Fichtel, C. E., et al. 1993, A.&A.Supp.Ser., 97, 349

Kane, S. R., McTiernan, J., Loran, J., et al. 1992, Ap.J., 390, 687

Kennel, C. F. & Petschek, H. E. 1966, J.G.R., 71, 1

King, C. H., Austin, S. M., Rossner, H. H., & Chien, W. 1977, Phys.Rev.C, 16, 1712

King, C. H., Rossner, H. H., Austin, S. M., et al. 1975, Phys.Rev.Letters, 35, 988

Kocharov, G. E., Chuikin, E. I., Kovaltsov, G. A., Usoskin, I. G., & Kocharov, L. E. 1994, High Energy Solar Phenomena - A New Era of Spacecraft Measurements, ed. J. M. Ryan & W. T. Vestrand (AIP)

Kocharov, L., Debrunner, H., Kovaltsov, G., et al. 1998, A.&A., 340, 257

Kocharov, L., Kovaltsov, G. A., & Torsti, J. 1999, Ap.J., 519, 422

—. 2000, Ap.J., 543, 422

Kozlovsky, B., Murphy, R. J., & Ramaty, R. 2002, Ap.J.S., 141, 523

Kulsrud, R. & Pearce, W. M. 1969, Ap.J., 156, 445

Kunz, S., Bochsler, P., Geiss, J., Ogilvie, K. W., & Coplan, M. A. 1983, Sol.Phys., 88, 359

Lang, K. R. 2001, The Cambridge Encyclopedia of the Sun (Cambridge, U.K.: CUP)

Lau, Y.-T., Northrop, T. G., & Finn, J. M. 1993, Ap.J., 414, 908

Leikov, N. G., Akimov, V. V., Volzhenskaya, V. A., et al. 1993, A.&A.Supp.Ser., 97, 345

Lentners, G., Ramaty, R., Mandzhavidze, N., & Miller, J. 1999, Bull.Am.Astron.Soc., 32, 876

Lesko, K. T., Norman, E. B., Larimer, R. M., et al. 1988, Phys.Rev.C, 37, 1808

Lin, R. P. & Hudson, H. S. 1976, Sol.Phys., 50, 153

Lin, R. P., Krucker, S., Hurford, G. J., et al. 2003, Ap.J., 595, L69

Lindstrom, R. M., Evans, J. C., Finkel, R. C., & Arnold, J. R. 1971, Earth&Plan.Sc.Lett., 11, 254

Lingenfelter, R. E. & Ramaty, R. 1967, High Energy Reactions in Astrophysics (New York: W.A.Benjamin)

Litvinenko, Y. E. 1996, A.I.P.Conf.Proc., Vol. 374, High Energy Solar Physics, Greenbelt 1995 (Woodbury,N.Y.: A.I.P.), 498–504

l'Observatoire de Paris. 2004, Solar Atmospheric Temperature, Internet, www.lesia.obspm.fr/solaire

Lockwood, J. A., Debrunner, H., & Ryan, J. M. 1997, Sol.Phys., 173, 151

MacKinnon, A. L. 1989, A.&A., 226, 284

—. 1991, Vistas in Astronomy, 34, 331

MacKinnon, A. L. & Brown, J. C. 1989, A.&A., 215, 371

—. 1990, A.&A., 232, 544

MacKinnon, A. L. & Toner, M. P. 2003, A.&A., 409, 745

Magun, A. 1998, unpublished microwave data referenced by Kocharov et al.

Mandzhavidze, N., Ramaty, R., & Kozlovsky, B. 1997, Ap.J., 489, L99

Marsch, E., von Steiger, R., & Bochsler, P. 1995, A.&A., 301, 261

Mason, G. M., Wiedenbeck, M. E., Miller, J. A., et al. 2002, Ap.J., 574, 1039

McConnell, M. 1994, in High Energy Solar Phenomena - A New Era of Spacecraft Measurements, ed. J. M. Ryan & W. T. Vestrand (AIP), 21–25

McDonald, F. B. & Van Hollebeke, M. A. I. 1985, Ap.J., 290, L67

McKenzie, D. & Feldman, U. 1992, Ap.J., 389, 764

Mechau, D. V. 1962, SAO Sp.Rep.

Meliorensky, A. S., Pissarenko, N. F., Shamolin, W. M., & Likin, O. B. 1975, A.&A., 41, 379

Mercer, D. J., Austin, S. A., Brown, J. A., et al. 2001, Phys.Rev.C, 63

Meyer, J. P. 1985a, Ap.J.S, 57, 151

—. 1985b, Ap.J.S, 57, 173

—. 1993, Element Fractionation at Work in the Solar Atmosphere (C.U.P.), 26–62

Miller, B. 1962, SAO Sp.Rep.

Miller, J. A., Cargill, P. J., Emslie, A. G., et al. 1997, J.Geophys.Res., 102, 14631

Miller, J. A. & Ramaty, R. 1987, Sol.Phys., 113, 195

Miller, J. A. & Roberts, D. A. 1995, Ap.J., 452

Morimoto, K. 1996, Phd thesis, Graduate School of Science, Rikkyo University, Japan

Mott, N. F. & Massey, H. S. W. 1949, Theory of Atomic Collisions, 2nd edn. (Oxford)

Murphy, R. J. 1985, PhD dissertation, University of Maryland

Murphy, R. J., Hua, X. M., Kozlovsky, B., & Ramaty, R. 1990a, Ap.J., 351, 299

Murphy, R. J., Kozlovsky, B., & Ramaty, R. 1988, Ap.J., 331, 1029

Murphy, R. J. & Ramaty, R. 1984, Adv.Sp.Res., 4, 127

Murphy, R. J., Ramaty, R., Kozlovsky, B., & Reames, D. V. 1991, Ap.J., 371, 793

Murphy, R. J., Share, G. H., DelSignore, K. W., & Hua, X.-M. 1999, Ap.J., 510, 1011

Murphy, R. J., Share, G. H., Grove, J. E., et al. 1997, Ap.J., 490, 883

Murphy, R. J., Share, G. H., Letaw, J. R., & Forrest, D. J. 1990b, Ap.J., 358, 298

NASA Goddard Space Flight Centre. 2004, The Yohkoh Satellite, Internet, http://hesperia.gsfc.nasa.gov/ sftheory/yohkoh.htm

National Space Science Data Centre. 2004, NSSDC Archive, Internet, http://nssdc.gsfc.nasa.gov

Neu, R., Welte, S., Clement, H., Hauser, H. J., & Staudt, G. 1989, Phys.Rev.C, 39, 2145

Noci, G., Spadaro, D., Zappalá, R. A., & Zuccarello, F. 1988, A.&A., 198, 311

O'Neill, T. 1993, AIP Conf.Proc., Vol. 280, Compton Symposium, St. Louis (AIP), 1112

—. 1994, AIP Conf.Proc., Vol. 304, Compton Symposium, Maryland (AIP), 536

Parkinson, J. H. 1977, A.&A., 57, 185

Pelaez, F., Mandrou, P., Niel, M., et al. 1992, Sol.Phys., 140, 121

Peterson, L. E. & Winckler, J. R. 1959, J.Geophys.Res., 64, 697

Phillips, A. 2004, ScienceNASA, http://science.nasa.gov/headlines/y2004/17mar_ulysses.htm

Prael, R. E. & Lichtenstein, H. 1989, User Guide to LCS: The LAHET Code System, Vol. LA-UR-89-3014 (Los Alamos), http://www-xdiv.lanl.gov/XCI/PROJECTS/LCS/ lahet-doc.html

Press, W. H., Teukolsky, S. A., Vetterling, W. T., & Flannery, B. P. 1992, Fortran Numerical Recipes, Vol. 1, Numerical Recipes in Fortran 77: The Art of Scientific Computing, 2nd edn. (Cambridge: Cambridge University Press)

Prince, T. A., Ling, J. C., Mahoney, W. A., Riegler, G. R., & Jacobson, A. S. 1982, Ap.J., 255, L81

Ramaty, R. 1974, in The Physics of the Sun, ed. P. A. Sturrock, T. E. Holzer, D. Mihalas, & R. K. Ulrich, Vol. 2 (Dordrecht: Reidel), 333–334

Ramaty, R. 1986, in The Physics of the Sun, ed. P. A. Sturrock, T. E. Holzer, D. Mihalas, & R. K. Ulrich, Vol. 2 (Dordrecht: Reidel)

Ramaty, R. 2002, http://lheawww.gsfc.nasa.gov/users/ ramaty/ViewPubs/ramaty.html

Ramaty, R., Kozlovsky, B., & Lingenfelter, R. E. 1979, Ap.J.S., 40, 487

Ramaty, R. & Mandzhavidze, N. 1994, in High Energy Solar Phenomena - A New Era of Spacecraft Measurements, ed. J. M. Ryan & W. T. Vestrand (AIP), 26–44

Ramaty, R. & Mandzhavidze, N. 1997, Ap.J., 479, 458

Ramaty, R., Mandzhavidze, N., & Hua, X. M., eds. 1996a, High Energy Solar Physics, AIP Conf.Proc.374 (New York: AIP)

Ramaty, R., Mandzhavidze, N., & Kozlovsky, B. 1996b, in High Energy Solar Physics, ed. R. Ramaty, N. Mandzhavidze, & X. M. Hua, AIP Conf.Proc.374 (New York: AIP), 172–183

Ramaty, R., Mandzhavidze, N., Kozlovsky, B., & Murphy, R. L. 1995, Ap.J., 455, L193

Rank, G. 1995, Phd thesis, Max Planck Institut

Reames, D. V. 1995, Adv.Sp.Res., 15, 41

—. 1999, Sp.Sci.Rev., 90, 413

Reames, D. V., Barbier, L. M., von Rosenvinge, T. T., et al. 1997, Ap.J., 483, 515

Reames, D. V., Cane, H. V., & von Rosenvinge, T. T. 1990, Ap.J., 357, 259

Rieger, E., Reppin, C., Kanbach, G., et al. 1983, 18th Int. Cosmic Ray Conf. Papers, 10, 338

Ryan, J. M., Forrest, D. J., Chupp, E. L., et al. 1981, Ap.J., 244, L175

Ryan, J. M. & Vestrand, W. T., eds. 1994, High Energy Solar Phenomena - A New Era of Spacecraft Measurements (AIP)

Saba, J. & Strong, K. 1993, Adv.Sp.Res., 13, 391

Sanahuja, B., Domingo, V., Wenzel, K.-P., Joselyn, J. A., & Keppler, E. 1983, Sol.Phys., 84, 321

Schmelz, J. T., Saba, J. L. R., Ghosh, D., & Strong, K. T. 1996, Ap.J., 473, 519

Seamster, A., Norman, E. B., Leach, D. D., Dyer, P., & Bodansky, D. 1984, Phys.Rev.C, 29, 394

Share, G. H. 2004, Private Communication

Share, G. H. & Murphy, R. J. 1995, Ap.J., 452, 933

—. 1997, Ap.J., 485, 409

—. 1998, Ap.J., 508, 876

Share, G. H., Murphy, R. J., Kiener, J., & de Séréville, N. 2002, Ap.J., 573, 464

Share, G. H., Murphy, R. J., Skibo, J. G., et al. 2003, Ap.J., 595, L85

Sheeley, Jr., N. R. 1996, Ap.J., 469, 423

Shih, A. Y. 2004, Private Communication

Slobodrian, R. J. & Conzett, H. E. 1982, Z.Phys., 308, 15

Slocum, P. L., Stone, E. C., Leske, R. A., et al. 2003, Ap.J., 594, 592

Smith, D. F. & Brecht, S. H. 1991, Ap.J., 373, 289

Smith, D. M., Share, G. H., Murphy, R. J., et al. 2003, Ap.J., 595, L81

Spadaro, D., Zuccarello, F., & Zappalá, R. A. 1996, A.&A., 308

Spicer, D. S. & Emslie, A. G. 1988, Ap.J., 330, 997

Spitzer, L. 1956, Physics of Fully Ionized Gases (New York: Interscience)

Sturrock, P. A., Holzer, T. E., Mihalas, D., & Ulrich, R. K., eds. 1986, The Physics of the Sun, Vol. 2 (Dordrecht: Reidel)

Talon, R., Vedrenne, G., Melioransky, A. S., et al. 1975, in Solar Gamma-, X- and EUV Radiation, ed. S. R. Kane (IAU), 315–339

Tamres, D. H., Canfield, R. C., & McClymont, A. N. 1986, Ap.J., 309, 409

Tamres, D. H., Melrose, D. B., & Canfield, R. C. 1989, Ap.J., 342, 576

Tatischeff, V., Duprat, J., Kiener, J., et al. 2003, Phys.Rev.C, 68

Terekhov, O. V., Syunyaev, R. A., Kuznetsov, A. V., et al. 1993, Astron.Lett., 19, 65

Thompson, A. M. 1992, software documentation for GUIPS, University of Glasgow

Thompson, A. M. & Craig, I. J. D. 1992, A.&A., 262, 359

Titterington, D. M. 1985, A.&A., 144, 381

Toner, M. P. & MacKinnon, A. L. 2004, Sol.Phys., 223, 155

Toner, M. P., Ryan, J. M., MacKinnon, A. L., et al. 2001, in IAU Symp., Vol. 203, Recent Insights into the Physics of the Sun and Heliosphere - Highlights from SOHO and Other Space Missions, ed. P. Brekke, B. Fleck, & J. B. Gurman (ASP), 573–576

Trottet, G., Schwartz, R. A., Hurley, K., et al. 2003, A.&A., 403, 1157

Trubnikov, B. A. 1965, Rev.Plasma Phys., 1, 205

Tsuneta, S., Masuda, S., Kosugi, T., & Sato, J. 1997, Ap.J., 478, 787

VanHollebeke, M. A. I., McDonald, F. B., & Meyer, J. P. 1990, Ap.J.S., 73, 285

Veck, N. J. & Parkinson, J. H. 1981, Mon.Not.R.Astr.Soc., 197, 41

Vestrand, W. T. & Forrest, D. J. 1993, Ap.J.Lett., 409, 69

Vestrand, W. T., Forrest, D. J., Chupp, E. L., Rieger, E., & Share, G. H. 1987, Ap.J., 322, 1010

Vilmer, N. 1994, Ap.J.Sup., 90, 611

Vilmer, N. & MacKinnon, A. L. 2003, in Energy Conversion and Particle Acceleration in the Solar Corona, ed. K.-L. Klein, Lecture Notes in Physics Series (Springer)

Vilmer, N., MacKinnon, A. L., Trottet, G., & Barat, C. 2003, A.&A., 412, 865

Volodichev, N. N., Mamontova, N. A., Nechaev, O. I., & Savenko, I. A. 1983, in 18th International Cosmic Ray Conference, Vol. 10 (Bombay: Tata Institute of Fundamental Research), 303–306

von Rosenvinge, T. T., McDonald, F. B., Trainor, J. H., Van Hollebeke, M. A. I., & Fisk, L. A. 1978, IEEE Trans., GE-16, 12

Warren, H. P. & Reeves, K. K. 2001, Ap.J.Lett., 554, 103

Weaver, B. A. & Westphal, A. J. 2002, Nucl.Instr.Meth.B, 187, 285

Weiss, N. 2001, A.&G., 42, 10

—. 2002, A.&G., 43, 9

Widing, K. & Feldman, U. 1995, Ap.J.

Wieler, R. & Baur, H. 1995, Ap.J., 453, 987

Wild, J. P., Smerd, S. F., & Weiss, A. A. 1963, Ann.Rev.Astron.Astrophys., 1, 291

Yoshimori, M., Okudaira, K., Hirasima, Y., & Kondo, I. 1983, Sol.Phys., 86, 375

Yoshimori, M., Suga, K., Morimoto, K., et al. 1994, Ap.J.Sup., 90, 639

Zastenker, G. N., Borodkova, N. L., & Ivanov, K. G. 1985, Kosmichem.Issle., 23, 134, in Russian

Zhang, T. X. 1995, Ap.J., 449, 916